Mobility Prediction of Multi-Body Vehicle Dynamics Handling Simulations on Deformable Terrain

By

Justin C. Madsen

A dissertation submitted in partial fulfillment of

the requirements for the degree of

Doctor of Philosophy

(Mechanical Engineering)

at the

UNIVERSITY OF WISCONSIN–MADISON

2014

Date of final oral examination: 05/06/2014

The dissertation is approved by the following members of the Final Oral Committee:

Dan Negrut, Associate Professor, Mechanical Engineering

Roxann Engelstad, Professor, Mechanical Engineering

Robert Rowlands, Professor, Mechanical Engineering

Darryl G. Thelen, Professor, Mechanical Engineering

Zhiguang Qian, Associate Professor, Statistics

To my new boss

ACKNOWLEDGMENTS

I would like to thank my advisor, Professor Dan Negrut, for his guidance and support. His leadership by example continues to inspire me as my work and life has grown and changed so much in the years we have worked together. I would like to thank the other committe members, for lending their expertise and insight to shape one of the most important projects I have worked on up to this point in my life. From the time the first word of this thesis was written, to the last simulation analyzied, I was lucky enough to be surrounded by my good friends and colleagues in the Simulation-Based Engineering Lab, whose constant ideas and support have inspired me more than the many cups of coffee we shared in conversation. I thank my family last, only to make them think I may have forgotten to mention them as they near the end of the page. The unwaivering love and support of my mother and father is something I never forget. To Josh and Michelle, if you read this, thank you for always being there; if you don't read this, thank you anyway. Finally, to my lovely wife and beautiful daughter, whom I love dearly and without none of this would be possible.

DISCARD THIS PAGE

TABLE OF CONTENTS

Page

Page

DISCARD THIS PAGE

LIST OF TABLES

DISCARD THIS PAGE

LIST OF FIGURES

Figure Page

Figure Page

Figure Page

Figure Page

Figure Page

Figure Page

ABSTRACT

Mobility of wheeled vehicles on deformable ground concerns a wide variety of industries, including: agriculture, forestry, mining, recreation, and military. The field of terramechanics is dedicated to studying vehicle-ground interaction when the ground is not rigid. Current trends in computer power and cost have led to the emergence of simulation as a powerful tool for design and analysis, especially early on in the design process, when changes can be made relatively cheaply. Commercial off-the-shelf software (COTS) is available to build models of entire vehicle systems. Vehicle mobility can be analyzed and understood by running simulations of driving maneuvers, for example, a lane change over a range of speeds, vehicle weights, driver aggressiveness, etc. Flexible tire models are also available and allow high-fidelity mobility and Noise-Vibration-Harshness (NVH) simulations to be run on non-flat rigid roads. The existing software available to run these types of multibody dynamic vehicle simulations on soft soil typically relies on semi-empirical methods, which (i) limit the mobility scenarios that can be analyzed, and (ii) have difficulty handling transient effects. On the other end of the spectrum are complex discrete and continuum mechanics approaches that can incorporate many important features such as constitutive elastic/plastic material laws. This includes strain hardening or softening of the material due to non-uniform, non-steady loading. Approaches drawing on Finite Element Analysis (FEA) or Discrete Element Methods (DEM) have been applied to the tire/soil mobility problem by a number of researchers, but are not readily incorporated into a multibody vehicle dynamics package. Further, the simulation times are

typically long, taking hours or days to run and sometimes require a supercomputer. This is unlike COTS vehicle dynamics software, which typically runs at near real time on a modern workstation.

This thesis focuses on building a framework to extend vehicle dynamics mobility simulation on deformable terrain to allow for general driving maneuvers. First, a deformable terrain model with a stress/strain relationship informed from soil mechanics is discussed and described in the context of a three-dimensional description of the terrain surface. The flexibility characteristics of the tire is shown to have a significant effect on the contact pressure, which is included in the novel tire/soil contact patch model that considers the tire geometry and is calibrated using experimental data based on the inflation pressure. Classic terramechanics approaches are based on pressure-sinkage relationships, which involves curve fitting experimental data of flat plate tests. These methods were originally devised with tracked vehicles in mind, and served as a good first approximation. The relationship is defined for two-dimensional steady-state motion on flat, homogeneous soil, and is ill-suited for vehicle dynamics because: i) a real vehicle and tire operates in 3-dimensions, ii) after the first wheel disturbs virgin soil, the second wheel will immediately encounter a non-flat surface, iii) dynamics is inherently non-steady-state. In the case of vehicles with pneumatic tires, further complications arise: iv) the contact patch stress of a pneumatic tire is not uniform nor flat along the width, v) strain hardening and the the influence of iv) leads to a non-homogeneous soil, and vi) the inflation pressure has a large impact on the contact patch area and stress.

The above shortcomings provide the motivation for developing a terrain model that considers the soil deformation caused by the combination of a general set of normal and shear stresses on the surface, rather than assuming all soil deformation being due to the pressure-sinkage relationship specified by Bekker. Elasticity solutions proposed by Boussinesq, Cerruti and Frolich are first extended to calculate the stress field in the terrain. The solution to the stress field is a major computational bottleneck, and a High Performance Computing (HPC) approach levering parallel computing in the form of both CPUs and Graphics Processor Units (GPU) is used. A semi-logarithmic soil model is used that relates soil dry bulk density to applied pressure, which captures the compression-rebound volumetric strain due to the loading cycle of a vehicle. This soil model

includes rebound and a term for time-dependent (e.g., viscous, strain rate) effects. Bulk density is implemented in a way in which the vertical strain can be found. The second major effort is to quantify the tire/terrain contact patch, both in shape, size and the normal and shear stress distributions, which is used as the boundary condition at the surface of the terrain model. A tire model, constructed to relate the normal pressure to the tire belt radial deflection, is calibrated using manufacturer data for static load/deflection tests at a number of tire inflation pressures. The contact area is based on assuming a tire with the undeflected shape of a torus. The radial dimension of the torus section is also calibrated using available maximum contact width data that is also measured during tire load/deflection testing. These solution methods were developed into a C/C++ library, and an API was developed to allow easy integration to vehicle dynamics simulation software via the Standard Tire Interface (STI). Using an open source dynamics simulation software package, Chrono, the developed tire/terrain model was incorporated into a virtual testing environment that included a single tire soil testing bin as well as a full vehicle model.

The new tire/terrain model is validated at two different levels: static load/deflection tests used in the deformable tire model parameter identification, and a tire testing rig in a multibody dynamics engine. Under certain driving conditions, single wheel performance is simulated and compared against experimental and analytical results found in the literature. In-plane wheel performance is analyzed: drawbar pull, motion resistance, thrust, torque and the normal and shear stress in the contact patch. These tests are run over a range of wheel weights, widths and slip rates.

A demonstration of the technology developed includes testing a number of variations of the deformable tire model during parameter identification to find a best fit according to the measured contact area and total wheel loads vs. wheel deflection. Using a torus shaped tire yields a better definition of contact area than a cylinder shaped tire, and pressure as a function of square root is the functional form that leads to the best fit model according to the minimum Least Squares error. Validation of the resulting in-plane mobility prediction model uses the torus shaped tire with fitted parameters and compares it to both simplified two-dimensional methods and experimental results available in the literature. Analysis of overall tire drawbar pull, torque, sinkage and contact

stress distribution as a function of slip rates is performed using a dynamic tire testing rig. The soil response is validated using experimental data only. It is shown that the newly developed model predicts higher drawbar pull than the two-dimensional methods, but less than the experimentally reported values due to the lack of lugs in the current model. Wheel torque shows good agreement with both the two-dimensional model and the experimental results.

A demonstration of a dynamically driven wheel is shown and the contact stress distribution at different combinations of wheel velocity and spin rate show the need for mobility prediction models to consider these variables separately and not combined into a single slip ratio. Additional features of the model include repeated loading effects and allowing out-of-plane tire/soil motion, e.g. turning and lane change scenarios. Analysis of the computational speedup achieved from the parallel CPU/GPU implementation includes a scaling analysis and a comparison of CPU only vs. combined CPU/GPU simulation times.

Future work includes integrating a structural or lumped-mass type tire model into the terrain model, as soft strain-hardening soil becomes a nearly rigid surface after a certain number of vehicle passes. For highly transient effects and very dry and non-cohesive soils that tend to flow, continuum or discrete mechanics approaches are needed to capture the complicated localized shear failure that dominates the mobility response.

Chapter 1

Introduction

1.1 Background

Since World War II, there has been considerable research done to understand how vehicles operate on unprepared or off-road terrain, driven by both agricultural and military interests. Unprepared terrain can be hard or soft, depending on a wide variety of reasons: soil material composition (i.e., sand, silt and clay percentages), moisture content, previous loading history, homogeneity, etc. Soil can be prone to strain hardening due to plastic volumetric compaction, which is commonly seen in agricultural clays and silts. On the other hand, a soil with a low cohesive strength and low porosity may be nearly incompressible and extremely susceptible to shear or distortional plastic failure, which is the case for dry sand. Early methods to quantify the vehicle-soil interaction were purely empirical in nature. Bulk vehicle properties are combined with simple soil strength test results to calculate a mobility index, which was used to determine if traversing a particular type of terrain was feasible or not. Semi-empirical parametric methods approximated a vehicle's contact footprint in soft soil with a rigid plate, and vertical pressure sinkage tests were run from which parameters for the analytical model were identified. These parametric methods are typically coupled with a shear stress model based upon the shear displacement of the soil-tire interface and combine to form a traction prediction model. Under a number of assumptions it is possible to predict a vehicle's thrust, sinkage, torque, motion resistance, and slip rate. With the emergence of more powerful computers came an effort to model vehicle traction with physics-based methods such as Finite Element Analysis (FEA) or Discrete Element Methods (DEM), which were much more complex but have the potential for lifting several assumptions that limit the applicability of the

semi-empirical methods. Due to the complexity of coupling a structural tire model with a continuum or discrete mechanics-based soil model, the application of this type of modeling methodology to vehicle mobility prediction remains an active area of research.

Consider the flip side of the coin, the prediction of vehicle mobility on rigid terrain. Driven by the automotive, mining, military and other interests, there exists a number of commercial solutions for modeling and simulating vehicle dynamics on rigid terrain. Pneumatic tires can be virtually tested under a wide variety of operating conditions as there also exist a number of tire modeling software packages. These tire models are both empirical and physics-based in nature, depending on the type of maneuver and the frequency of interest. Combining high-fidelity vehicle and tire models allow arbitrary driver maneuvers on road surfaces that are non-uniform and non-flat in nature. For example, one can analyze the vibrational harshness on a passenger due to encountering a very rough road surface at moderate speed [1]. The effects of describing the road surface as a non-Gaussian, non-stationary function along the path length on the force inputs to the front suspension were investigated in [2]. Road surfaces were described in one-dimension (straight and flat), two-dimensions(flat with curves), and three-dimensions (curves with rolling hills), and the driver steering input was designed to attempt to follow the center-line with throttle and braking based on a specified constant velocity throughout the simulation.

At the time of this work, the tools to model the tire-terrain interaction effects when the ground is not rigid are either limited to steady-state effects, not applicable to vehicles with tires, or are too computationally expensive and difficult to integrate with existing vehicle dynamics software packages. Simulation of a truck modeled using commercial software performing a lane change on soft soil is currently feasible, but the available solutions are based off of the semi-empirical Bekker relations [3, 4, 5] limiting their accuracy. This is the case when repeated loading changes the relative displacement of the tire and soil during contact, which has a large impact on the contact patch size, shape, and pressure distribution which affects mobility [6].

1.2 Terramechanics Methods

1.2.1 Empirical Methods

Early empirical methods utilized simple soil measurement techniques such as the cone penetrometer test to determine if vehicle mobility was possible over a given terrain. For both wheeled and tracked vehicles, a vehicle cone index is calculated for a single pass and for 50 passes. These methods were pioneered in WWII by the U.S. Army Waterways Experiment Station(WES) [7] and were subsequently used as a basis for the NATO Reference Mobility Model (NRMM), which correlates vehicle performance with a terrain measurement parameter, rating cone index (RCI) for fine-grain soils, cone index (CI) for coarse-grain soils and its derivatives [8]. Numerics for specific soils were developed, and were typically related to drawbar pull and drawbar efficiency at 20% slip. There are a number of other empirical methods that relate data from cone penetrometer tests to a set of numerics to determine average tractive ability in soft soil, for both tracked and wheeled vehicles.

1.2.2 Semi-Empirical Parametric Methods

Semi-empirical parametric methods were first developed by Bekker [9] and Reece [10] to characterize the pressure-sinkage relationship in soft soils due to a flat plate being vertically depressed, in an effort to simulate the footing of a tracked vehicle. Provided the terrain is flat and can be idealized as isotropic and homogeneous in the vertical direction, these methods proved to be accurate under steady-state operating conditions. Janosi and Hanamoto developed methods to determine the tractive performance of tracked vehicles on soft soil based on the slip displacement and soil shear strength [11, 12]. Wong and Reece combined these approaches to solve the 2-D plastic equilibrium between a homogeneous soft soil loaded by a rigid circular wheel that is driven with at a constant forward velocity and slip rate [13]. These methods have been shown to be accurate when predicting steady-state drawbar pull, motion resistance or wheel torque, for driven [13] and towed wheels [14] in homogeneous sand.

Multi-pass effects are included in these semi-analytical models by modifying the pressure-sinkage relation with a method that characterizes the effect of soil hardening using bulk density, moisture content, hardpan depth, and a dynamic penetrometer measurement [15]. The effect of the wheel curvature seen in small vehicles with rigid wheels can be used as a modifier to the Bekker equations [16], as can the wheel width [17]. To describe the elastic tire flattening effect, the contact shape was described with a larger diameter circle, and the pressure during unloading-reloading is described by a linearly elastic model [3]. Harnisch further described the effect of the tire tread by considering an interlocking of soil in the negative recessed area of the tire, where the shear was based on the shear strength of the soil only. In the positive areas (e.g., under a lug), the shear strength of the soil as well as the coulomb friction limit is considered. The multipass effect is considered by storing the soil deformation as well as the soil compaction for each individual wheel. These types of approaches has been experimentally validated by several authors [18, 19].

Semi-empirical parametric methods rely on a number of simplifying assumptions to find the tractive performance of wheeled vehicles on deformable terrain: the wheel is two dimensional and circular, operating at a steady-state forward velocity and slip rate, on flat and homogeneous soil. Implementation and identification of the soil parameters is relatively straightforward; however, the numerous assumptions limit their applicability when used in a multibody dynamics framework. A number of researchers have extended and incorporated soft soil into multibody dynamics software using these types of semi-empirical methods for vehicles with rigid wheels, pneumatic tires or tracks.

When the vehicle wheel is considered rigid, it is typical that the application is related to small rovers with very stiff metal wheels. A rigid cylinder shaped wheel was used by Trease [20], Chan [21], Schmid [19], Harnisch [3] and Azimi [22]. Rigid traction geometry was used by Rubinstein [23] and Slattegren [4], which is typical for tracked vehicles with rigid tracks. Vehicles with rigid traction elements are more readily applied to tracked vehicles and planetary rovers, as their wheels are less flexible than tires [24, 25]. With the exception of Azimi, who uses an incremental strain assumption with plasticity theory, most approaches involve an extension of the Bekker or Wong methods to describe the stress-strain relationship between the wheel and soil. Slattegren

incorporated the effect of grousers as an additional horizontal force on the track shoe rigid bodies, and provided an iterative equilibrium solution method for the entire vehicle-soil system.

1.2.3 Finite Element Methods

A second class of approaches draw on fully resolved Direct Numerical Simulation (DNS) methods, which are the focus of much present day research in the form of continuum based methods, discrete particle approaches, or sometimes a combination of both. Finite Element Analysis (FEA) approaches are the most commonly developed continuum models for terramechanics. Constitutive material models for the soil and tire lead to the solution of a three-dimensional boundary value problem to find the stress-strain of the wheel and soil. Hambleton studied the indentation [26] of a non-frictional clay soil due to a small rigid wheel, assuming rigid-perfectly plastic or elastic-perfectly plastic material models. Simulations were carried out with ABAQUS/Explicit using a Arbitrary Lagrangian-Eulerian mixed-formulation due to the necessary remeshing which stems from large element deformations. The Mohr-Coulomb yield criteria is approximated with a Drucker-Prager cap model, with both associated and non-associated flow rules. Purely friction materials with cohesions near zero caused numerical instabilities. Large values of the sand internal friction angle caused associated flow simulations to become unstable. Small-scale experiments were carried out, and the force-sinkage response curves closely matched the simulation results for frictionless clay, but deviated for sand if the dilatation angle was not small. An analytical rigid footing method was developed where the contributions of the bearing capacity in conjunction with the surcharge, cohesion and weight effects are superimposed to approximate the indentation force.

Rolling was also considering in the same simulation framework, where are rigid wheel of varied width and diameter was driven with a longitudinal velocity until a steady slip rate was obtained [27]. Vertical force was compared with sinkage for soil of varying friction angle. An analytical approach that simplified the problem to either an inclined force or an inclined footing was developed and slightly underestimated the force at a given sinkage. Small scale experimental tests confirmed the results of the numerical FEA simulations.

To describe the lateral tire flattening effects in a 2-D ring elastic tire model, Fervers considered the equilibrium between the tension forces in the carcass and the inflation pressure [28]. The extracted load-deflection curve for a given inflation pressure could then be used to connect the nodes of an elastic ring tire model to the rim. The model was validated on rigid roads with wheel load-deflection tests at various inflation pressures. A step climb test was also run to validate the wheel height as it traversed the obstacle. Using an extended Abaqus model for soil Drucker-Prager Cap plasticity, a clay soil with high cohesion and a sand with low cohesion and high internal friction were simulated. It was noticed that on clay soil, the tire with high inflation pressure caused more sinkage, while the wheel center both had approximately the same height for both inflation pressures. The tire at higher inflation pressure also generated larger and deeper stress patterns in the soil, which is seen in the higher rolling resistance measured. The tire at higher inflation pressure also created a large soil wedge in front of the tire, and in both cases the pressure in the soil were about equal. Comparing the two soils in terms of compaction, the sand saw lower compaction throughout, but at greater depth; the clay soil saw large compaction near the surface.

A fully three-dimensional tire-soil model was developed by Shoop, who analyzed the vehicle mobility and soil deformation with an elastic tire and Drucker-Prager cap and crushable foam soil models [29]. Soil material model validation was performed for plate sinkage tests, to produce results similar to experiments performed in snow. The tire was modeled using a number of abstractions of the tire carcass and tread, ranging from a simple rigid cylinder, to a treaded tire with straight ribs. Soil/Tire contact was calculated by finding a normal component based on penalty or kinematic contact methods, and forces lateral to the surface were found using the Janosi-Hanamoto shear stress-displacement equation. A rigid wheel was simulated in the soil; however, limited results for the deformable tire on soil or snow were provided.

A fully three-dimensional hyperelastic tire on soft soil is presented by Xia, where compaction density was seen to increase at higher tire angular velocities [30]. Compaction of the terrain is analyzed in [6], and four wheels are simulated illustrating the effects of repeated loading leading to differences in front and rear contact patch attributes.

1.2.4 Discrete Element Methods

Discrete Element Methods (DEM) consider the soil as a system of rigid bodies that interact through friction and contact. Some examples of the use of DEM to calculate vehicle mobility include [31], where a tracked vehicle was driven on a granular bed of spheres to test a collision detection method to include complex contact geometry, shown in Figure 1.1.

Combinations of a flexible FE tire model with discrete terrain was investigated by Nakashima [33], where the entire bed of particles sat on top of a flexible foundation. Other work included studying the performance of a lugged wheel used on a rover on sloped terrain, represented by a two-dimensional bed of particles [34]. The maximum slope traversal angle was found by calibrating the model using small-scale experiments in a sloped test-bed filled with regolith simulant. Three-dimensional DEM was used by Knuth [35] to study the digging-in motion of a rover wheel, where the shape complexity of the particles was increased and calibrated with experimental sinkage-torque data.

1.2.5 Summary

Benefits of DNS methods include representing the tire as a structural model to capture the belt dynamics when calculating the contact patch shape and pressure distribution. The complicated stress-strain field in the soil can be accurately computed for any shape of tire under a wide range of operating conditions, provided the solution is numerically stable. Two problems become immediately apparent when using DNS with a multibody vehicle dynamics model. First, simulation times are prohibitively long and cannot realistically be used in the design cycle. Second, accurate constitutive material models and validation of system level characteristics is still an active area of research [36, 37]. In the case of FEA models, soils with large dilation angles or very low cohesiveness tend to cause numerical instabilities due to extremely large volumetric strains [26]. Difficulty with describing the entire tire/soil system using DNS methods has lead many researchers to embrace a tire model that is either two-dimensional [28] , or represented with a simplified lumped mass-spring representation [38].

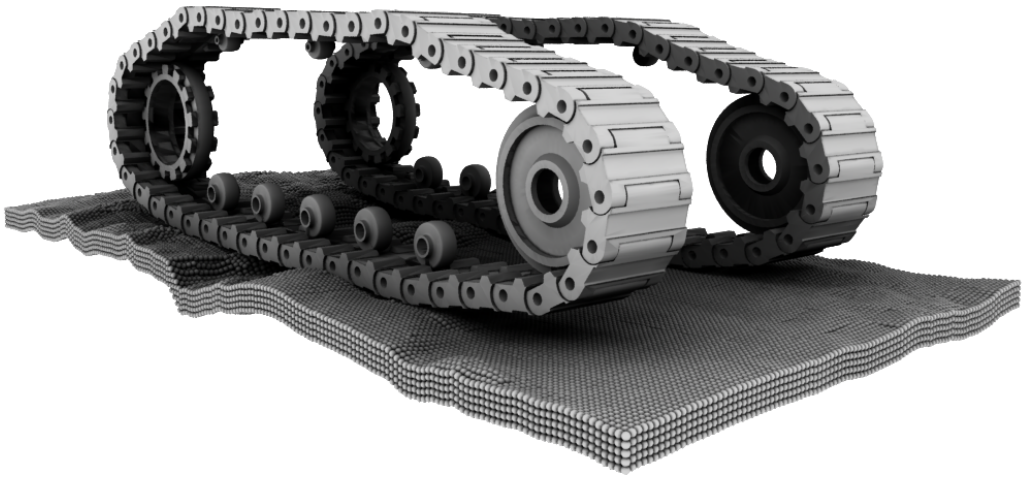

Figure 1.1: Tracked vehicle on a particle terrain, also from [32]

1.3 Motivation

Existing semi-empirical terramechanics simulation methods are applicable for general purpose vehicle mobility simulations on off-road conditions, granted the actual vehicle and terrain do not stray too far from the model assumptions. Modifications can be made to incorporate these relations into multibody dynamics software to perform mobility simulations. However, there are still a number of assumptions inherent in the semi-empirical models that limit the ability of a general purpose vehicle dynamics simulation for mobility studies. Traction geometry is typically assumed to be simple and is described in two-dimensions; however, most vehicles use specialized wheels or tracks to enhance mobility in off-road terrains, and most commercially available terramechanics software does not consider tread geometry effects on tractive performance. Soil flow effects (e.g. bulldozing, slip sinkage, rutting) are also generally ignored, or dealt with in an ad-hoc manner [39, 33]. High wheel slips, low vehicle weight, low soil cohesive strength, or non-homogeneous soil composition and properties can all cause classical terramechanics approaches to lose accuracy to a degree where they lose their predictive capability. Finite Element (FE) approaches have attempted to capture more complex aspects of vehicle loading on deformable soil. Typical vehicle dynamics simulations for mobility or component fatigue analysis purposes require many simulation runs with time-lengths in the 10s to 100s second range, which makes most Direct Numerical Simulation (DNS) methods infeasible.

Rather than relying on the classic pressure-sinkage equations which are only defined for two-dimensional steady-state motion on flat, homogeneous soil, both the previous soil deformation effects on the terrain, as well as any repeated loading-unloading effects that cause hardening of the soil should be considered in a 3-D Cartesian space. This is the motivation for developing a terrain model that considers the soil deformation caused by the combination of a general set of normal and shear stresses on the surface, rather than assuming all soil deformation is due to the pressure-sinkage relationship specified by Bekker. The objectives of the work are twofold: (i) calculate the normal and shear stress distribution in the tire contact patch, and (ii) determine the response of a strain hardening soil due to the stresses at the surface caused by repeated vehicle loads.

Two problems became evident when attempting to incorporate soft soil into the tire model. First, simulation times were extremely long for even short simulations, due to the complexity of solving the non-linear equations of motion. Second, the contact model was difficult to accurately describe. In purely frictional material, it is assumed that the friction between the tire and soil is larger than the internal friction of the soil, and a no-slip boundary condition is assumed at the contact interface. However, if the soil has a large enough shear strength, the tire-terrain interface may experience slip, and the static friction limits the maximum shear stress. Finally, the calculation of the normal force distribution in the contact patch was prohibitively expensive, since even when using simple Bekker/Reece pressure sinkage equations to model the soil plastic strength, the equilibrium between the tire elastic normal forces and the terrain plastic strength leads to a system of non-linear equations which must be iteratively solved for. This led to the adoption of a simpler elastic tire model, which does not include the belt dynamics and is calibrated based on quasi-static wheel load-deflection experimental data.

To address (ii), a terrain database with two distinct layers has been developed to a) describe the soil surface geometry, required to find the soil-tire collision area , and b) track the changes in the subsoil states (i.e., bulk density) due to vehicle loading, which impacts the soil surface geometry in subsequent simulation time steps. The surface geometry of the terrain is described by tracking the height at discrete coordinates on an equidistantly spaced grid in the global x and y directions. The surface coordinate height is calculated at each time step by summing the vertical plastic strain component of a number of subsoil nodes directly below the point at the surface. Vertical compaction of the soil can be calculated by a semi-logarithmic stress and bulk-density relationship whose parameters can be found by using USCS soil classification codes with other commonly available soil material metrics by using the methods described by Ayers and Bozdech [40]. Although the soil near the contact patch tends to flow due to local plastic shear failure, the soil not in this flow zone will experience volumetric plastic strain that tends to increase the bulk density of the soil, as shown by Wulfsohn [41]. By assuming that any change in the terrain surface geometry is caused by soil volumetric strain, the terrain surface can be accurately described by tracking the compaction of the soil.

In order to find the volumetric plastic strain in the soil, the maximum principal stress of the soil in the area affected by the vehicle loading must be known. If only the soil plastic strain in the vertical direction is considered, then the maximum principal stress simplifies to the vertical normal stress. The three-dimensional vertical stress field can be calculated with the Boussinesq and Cerruti equations, using the Frolich modification. The latter is needed to avoid numerical singularities near the surface, since the stress model assumes a semi-infinite half-space, which is no longer the case when considering a non-flat terrain surface geometry. Contact patch forces at the tire and terrain interface, used as the input to the soil stress field calculation, are found by first computing the contact area between the soil surface and tire geometry, then by considering the elasticity of the tire and the strength of the soil at the current time step. Similar to methods proposed in [3, 20, 38], classical terramechanics methods by Wong, Reece and Bekker are utilized to calculate the maximum normal stress for a given soil depth.

1.4 Document Overview

This work focuses on extending the capability of large wheeled vehicle mobility simulation on soft, deformable soil. Rather than assuming that soil deformation is the result of the pressure-sinkage relationship specified by Bekker or Reece, the plastic strain of the soil is inferred from soil mechanics relationships derived from uniaxial loading-unloading tests. A history of the soil stress and strain is maintained at a number of discrete points in the volume of soil affected by vehicle loads. This allows incorporation of multi-pass effects that cause hardening of the soil that affects future loads. A terrain database maintains the surface profile of the ground as it is deformed by the tires. The tires apply normal and shear stress on the area of the ground they are in contact with, which is determined by running a collision detection function at each simulation step. An elastic tire is developed, which is used to calculate the normal and shear stress based on: (1) the surface profile of the terrain, (2) the soil state, (3) the local tire radial deflection, (4) the inflation pressure of the tire, and (5) the bearing capacity of the soil. The tire model requires parameters to be identified for the elastic pressure-displacement relationship, a process carried out based on available manufacturer data for load-deflection tests at various inflation pressures. The

shape of the tire is derived from that of an undeflected tire, as the contact surface is shown to have curvature in both the lateral and longitudinal directions [42]. The shape of the tire is also calibrated based on maximum contact area width data taken during the load/ deflection tests. Based on the contact area and normal and shear stress calculated by the contact patch model, the stress at any point in the soil volume around the contact area can be calculated based on elasticity theories. Computation of the stress field is a major computational bottleneck, and a parallel CPU/GPU approach is leveraged to reduce the computation time by an order of magnitude. The soil stress-strain relationship derives the model parameters from a technique described and experimentally validated by Ayers [40]. A tire testing rig is modeled in a multibody dynamics modeling and simulation software, Chrono, where in-plane testing is carried out and mobility and contact patch results are compared to analytical methods and experimental results reported in the literature by Wong [13, 14], and Wulfsohn [42, 41]. The deformable terrain model is developed, implemented and tested with the final demonstration of technology by performing full-vehicle non-steady-state maneuvers on non-flat, deformable terrain in near real-time speed.

The document is organized as follows. Chapter 2 provides a review of multibody dynamics software for vehicle mobility analysis, followed by a review of literature on terramechanics and soil mechanics methods. Soil stress and strain models are presented in Chapter 3 to include volumetric strain in terms of compression and rebound of soil due to applied stress cycles. Soil model parameters are readily derived from available soil material types and measured strengths. Chapter 4 describes the tire model developed to find the contact patch area and normal and shear stress distributions, which requires fitting collision geometry and elastic constants with static tire load/deflection test data. The resulting contact model includes the local equilibrium between the elastic surface of the tire and plastic surface of the terrain model. Chapter 5 outlines a co-simulation framework that draws on a dynamics engine that performs the tire testing bin simulations. Chapter 6 describes the tire and soil model parameter identification used for the validation and calibration experiments carried out on a single tire. Validation is carried out based on the in-plane mobility performance such as drawbar pull and wheel torque as a function of slip rate. Both analytical and

experimental results are compared and show good agreement in most circumstances, and large differences are readily explained by differences in the models. The motivation for developing the tire contact and terrain models is based on the fact that multibody mobility simulations such as those in [43]cannot be performed on soft soil using classical empirical methods. Chapter 7 presents some examples where the developed models are used to perform out-of-plane turns and maneuvers, investigate repeated loading effects, incorporate non-flat terrain surface and complex tire geometry. Also, a simple full vehicle model is built in Chrono and initial tests have been run on the terrain using four tires to propel the vehicle down an incline slope. Directions of immediate work and thoughts on future developments are discussed. Chapter 8 provides a summary of the paper and contributions to the field, and lists the specific accomplishments of this work.

1.5 Specific Contributions

The specific contributions of the author are summarized as follows:

- Developed and implemented a deformable terrain database for use in multibody vehicle mobility simulations to allow for transient and out-of-plane driving scenarios such as braking or lane-change maneuvers.
  - Developed a method to approximate the vertical stress field due to an arbitrary normal and shear stress distribution applied to the soil surface.
  - Developed a method to track plastic volumetric strain based on loading-unloading cycles. Collaboration with University of Tennessee yielded a method to identify the soil model parameters based on soil mechanical experimental data.
  - Implemented the above algorithms in the context of a terrain database that is integrated to existing computer software that runs vehicle mobility simulations.
  - Accelerated the computational bottlenecks by leveraging parallel CPU/GPU hardware support in key locations of the algorithms.

- Developed and implemented a contact patch model to complement the deformable terrain database for vehicles with pneumatic tires. Specifically considered non-uniform normal and shear stress in the lateral tire direction, to better describe non-planar travel.
  - Developed a method to calculate normal stress for soil-tire contact based on the contact geometry, elastic tire effects and the bearing capacity of the soil.
  - Developed a method to calibrate the normal stress model parameters based on the tire inflation pressure from readily available manufacturer tire load-deflection test data. Also calibrated tire contact geometry cross-section dimension based on related test data.
  - Implemented these models into the vehicle simulation framework in a similar way as the terrain database model.
- Validated results of single wheel in-plane mobility against analytical results and experimental data.
- Demonstrated out-of-plane mobility effects of the combined tire/soil model.
- Demonstration of technology includes analysis of repeated-loading effects a single wheel.

Chapter 2

Literature Review

A review of literature is performed to assess the state of the art in terms of experimental and analytical approaches to modeling tire/soil interaction in the context of large wheeled vehicle mobility. The order of review is from the top down; beginning with the vehicle itself and the tools used to model and simulate mobility scenarios, then moving to the tires and finally the terrain. First, a survey of software tools currently available to perform multibody vehicle dynamics simulation is presented, with an emphasis on the ability to include soft soil effects on mobility. Standard tire coordinate systems and terminology according to the Society of Automotive Engineers (SAE) standard J670 and the Standard Tire Interface (STI) are discussed. The classical Bekker/Reece pressure-sinkage methods are described which leads to the seminal work by Wong to calculate the in-plane steady-state mobility of a rigid wheel on sand, which is used as a basis for comparison against the newly developed models. Experimental and analytical methods to calculate the contact patch area and pressure distribution of a tire in soft soil are presented and used as a basis when developing the deformable tire/soil contact model developed in Chapter 4.1. Soil mechanics methods to evaluate stress and strain due to the types of loads expected from a wheeled vehicle are reviewed, and appropriate models for calculating stress and strain are selected. Methods to extract soil model parameters from readily available soil mechanical test data are presented. Repeated loading, time-dependent and hysteresis effects on the loading characteristics of a soft soil are also reviewed. Soil flow effects are discussed and tend to dominate the physics when the soil cohesiveness trends towards zero, placing a limit on the type of soils that can be accurately simulated without the use of very complex Finite or Discrete Element methods.

2.1 Multibody Vehicle Dynamics Software

There are multiple commercial CAE software tools available for the modeling and simulation of vehicle dynamics at varying degrees of accuracy, including MSC/ADAMS, Modelica, CarSim, and LMS VirtualLab. Tire simulation software options are just as numerous, e.g. Pacejka/Magic Tire formula tire [44], CDTire [45], FTire [1], and vary from empirical to lumped-mass linear elastic approaches. A good overview of the different types of tire models used for different simulation purposes, and some validation experiments is given in [46]. Therein, the consensus is that depending on the type of application, the tire model should be chosen based on the expected response frequencies, with structural tire models needed if the response reaches the the range of 60Hz. Another review of tire models and their applications is given by Ammon [47], with similar conclusions reached.

Soft soil effects are typically based on simple elastic equations or modified Bekker-type relationships [4, 3], using rigid or simplified traction elements. Most models will consider the wheel rigid, which is mostly applicable to small unmanned rover type vehicles, [48, 20, 25]. More complicated tire models can be simulated on soft soil, for example using a lumped mass-spring approach [38]; however, most rely on a finite element approach, [28, 30]. All Finite Element approaches are carried out using ABAQUS, Marc, or other structural mechanics software, and currently have not been integrated to a multibody vehicle dynamics environment. Chan proposed a lumped mass-spring tire which was exercised dynamically on a Bekker-type soil but limited the developed model to two-dimensional in-plane motion [38]. Out-of-plane motion is included in the models with rigid wheels for rover simulation, but no literature was found for vehicles running on tires.

2.1.1 Tire Coordinate System and the Standard Tire Interface

The coordinate system used to describe the wheel and tire assembly are described according to SAE vehicle dynamics terminology outlined in standard J670 [49]. Due to a large number of tire models being used with commercial vehicle simulation software, the need for compatibility led to

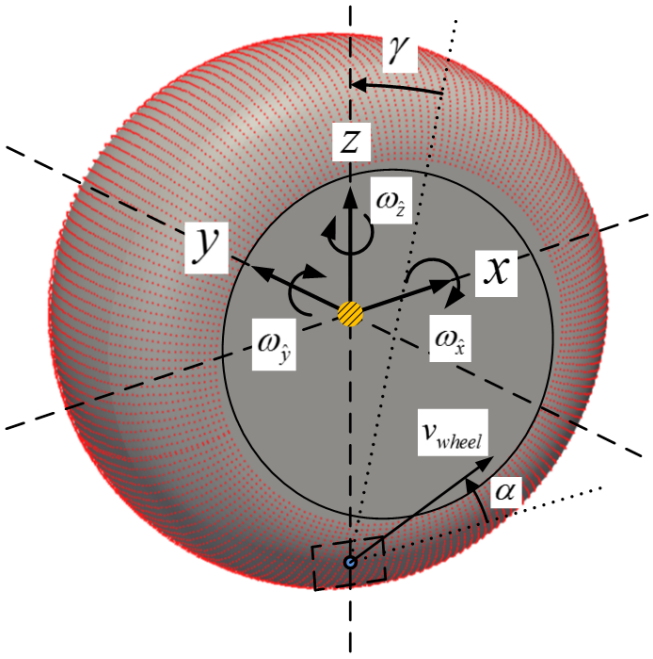

Figure 2.1: Standard Tire Inteface Coordinate System

the development of the Standard Tire Interface by a consortium of industry and academic partners [50]. It provides the standard coordinate system in which to define the wheel local positions, rotational velocities and angles with respect to the velocity of the vehicle, shown in Figure 2.1.

The the relative angle of rotation about the vertical axis between the wheel heading and the direction of wheel velocity is defined as the slip angle, α. The relative angle between the vertical and the current wheel XZ plane is defined as camber, γ.

2.2 Empirical Terramechanics Models

Bekker introduced parametric empirical methods that assume the soil to be an ideal elastoplastic material with a stress-strain relationship whose stress increases linearly in the elastic range and remains constant once the plastic deformation occurs [12, 51]. The vertical pressure was measured as a plate was pressed into the terrain (called a bevameter), and pressure was assumed a function of the sinkage raised to a power. Janosi-Hanamoto developed methods that relate the shear stress to the shear displacement for tracked vehicles [11]. Wong and Reece combined the two models and

solved for the contact angles of a two-dimensional wheel in soft soil by assuming that the weight of the wheel was in equilibrium with the contact normal and shear stress. Drawbar pull, motion resistance, sinkage and driving torque could be analyzed at a given tire slip rate. Towed wheels can be analyzed at a given slip rate directly by assuming the driving torque is zero [13]. Driven wheels require additional test data to form a linear relationship between the slip rate and the ratio of the angles of maximum pressure and initial contact, respectively [13].

Introduced in 1.2.2, these semi-empirical methods are reviewed in-depth as they form the basis for the majority of existing methods applied to vehicle mobility simulation on soft soil.

2.2.1 Vertical Pressure-Sinkage Relations

Bekker proposed an empirical pressure-sinkage relationship for terrains under the assumption that the terrain is homogeneous in the depth range of operation [9]. If a flat plate with is placed on the surface of the soil, the vertical pressure applied to the plate as a function of displacement from the surface is

$$p_z = \left(\frac{k_c}{b} + k_\varphi \right) z^n, \tag{2.1}$$

where p_z is the uniform plate pressure measured at sinkage depth z, b is the width of the shorter edge of the plate, and n, k_c, and k_φ are the soil material parameters experimentally obtained for each soil type. Cohesive soil is dependent on the plate width, frictional soils are not, which is why the cohesive soil parameter, k_c is divided by the plate width. A common technique for measuring the response of the terrain to obtain these types of soil parameters is known as the Bevameter technique [12]. Example values for the pressure-sinkage parameters of sand, clay and snow are given in Table 2.1.

The pressure-sinkage relationship of these three different types of soil is plotted in Figure 2.2 with a plate width of b=10 cm.

In order for Equation 2.1 to be accurate, the mechanical properties of the soil n, k_c, k_φ, must remain fairly constant in the range of interest, the soil must be homogeneous in the vertical direction, and the test apparatus plate size and aspect ratio must closely resemble that applied by the vehicle

Table 2.1: Bekker model parameters for various soils and snow [52]

Terrain type	Moisture content %	n	$k_c[\frac{kN}{m^{n+1}}]$	$k_\varphi[\frac{kN}{m^{n+2}}]$
Dry sand	0	1.1	0.99	1528.4
Loam	46	0.73	41.6	2471
Clay	38	0.5	13.19	692.0

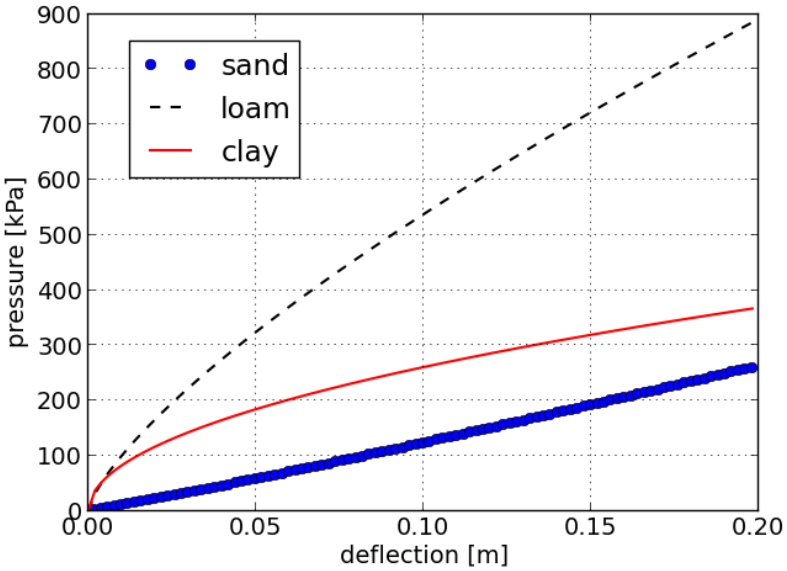

Figure 2.2: Pressure/sinkage relations of sand, loam and clay soils

running gear. When dealing with stratified soils, Equation 2.1 can still be applied by determining the mechanical properties of each sublayer of soil; however, the soil must still be homogeneous within the depth range of each layer. Reece proposed a modified version of equation (2.53) that resembles Terzaghi's bearing capacity equation

$$p = \left(ck_c' + \gamma_s b k_\varphi'\right)\left(\frac{z}{b}\right)^n, \tag{2.2}$$

where n, $k_\varphi{}'$, and $k_c{}'$ are pressure-sinkage parameters, c is cohesion, γ_s is specific weight, and the other parameters are the same as those in Equation 2.1. The pressure-sinkage parameters in Equation 2.2 have the advantage of being dimensionless, as well as producing results that generally agree more closely with experimental values. Factors that can lead to inconsistencies between measured data and results using Equations 2.1 or 2.2 include: instrumentation error, localized random homogeneities in the soil, form effects from experimental plate size, critical plate size, deformation rate and plate size effect due to stratification of soil [9]. Error from instrumentation can be reduced to acceptable levels where the other sources of error greatly outweigh its contribution. Localized non homogeneities in an otherwise homogeneous soil can cause a large spread in the measured load vs. sinkage curves depending on soil conditions.

For a 95% confidence interval assuming a normal distribution, one can expect a 20% spread of loads in sandy soils, and a 5-10 % load spread in cohesive soils, assuming the soil is allowed to consolidate [9]. Form effects from experimental plate size have been shown to not contribute significantly to inconsistencies between the theory and measurements, where derived values for k_c and k_ϕ obtained experimentally only varied by a few percent when considering various plate aspect ratios [53]. The size of the plate has almost no effect on measured n, k_c, k_φ values in homogeneous soils, as long as the soil is deformed with the same pattern; i.e., localized or general shear failure as defined by Terzaghi [54]. Deformation rate can have an effect on the agreement between measured and calculated values. This effect is minimal in dry soils, but can have an overall effect in moisture saturated soils due to hydrodynamic and viscous forces present during deformation. However, the effect of the deformation rate from field measurements is insignificant [55], likely due to the noise from the non-homogeneity of the soil [55]. Stratified soil usually falls into two categories,

a soft top layer resting upon a hard bottom layer, or vice versa. Examples of soft soil layered upon a hard base include: a plowed field, snow resting upon ice, or loose soil dislodged from a vehicles movement settling on top of a packed soil base. A hard top layer resting on top of a weak sublayer usually involves either organic soils (e.g., muskeg) or an ice crust forming on top of fresh, unpacked snow. Stratified soil can be considered as set of homogeneous soils and can be represented by a family of p_z curves that are valid for various amounts of sinkage.

2.2.2 Shear Stress-Displacement Relations

Bekker noticed that shear stress is a function of shear displacement, hence terrain that has just come into contact with the vehicle running gear exerts no shear stress since the shear displacement is initially zero [51]. In reality, the maximum shear stress can be reached quickly depending on the type of soil and whether grousers, hubs or treads are present on the tire. The tractive force of a vehicle is typically associated with the shearing of the terrain. For example, the maximum soil shear stress according to the Mohr-Coulomb failure criteria is defined as

$$\tau_{max} = (c + \sigma \tan(\varphi)) \,. \tag{2.3}$$

For most distributed soils, i.e. terrains composed of sand, clay or fresh snow, the shear stress-shear displacement relationship proposed by Janosi and Hanamoto [11] can be used,

$$\begin{aligned} \tau &= \tau_{\max} \left(1 - e^{-j/K}\right) && (2.4) \\ &= (c + \sigma \tan \varphi) \left(1 - e^{-j/K}\right), && (2.5) \end{aligned}$$

where j is the shear displacement and K is the shear deformation modulus, which is a measure of the magnitude of the shear displacement required to develop the maximum shear stress [18]. Shear stress initially increases with shear displacement at a rate determined by K, and then reaches a constant value for any increase in shear displacement, as shown in Figure 2.3. Equation 2.5 can be used to determine the approximate tractive force of a vehicle on a given terrain. For example, the tractive force of a tracked vehicle with a track length in contact with the terrain, l, and track width

b, can be computed by integrating the shear stress τ calculated by Equation 2.5 over the length of the track multiplied by the track width as follows

$$F = b\int_0^l \tau dx \tag{2.6}$$

$$= b\int_0^l (c + \sigma \tan\varphi)(1 - e^{-j/K})dx. \tag{2.7}$$

This equation depends on the normal pressure distribution along the length of the track, which assumes the stress value along the width to be constant. The shear stress/shear displacement relationship has been shown to deviate from that in Equation 2.5 when the soil does not behave as a perfectly plastic medium. This occurs in the case when there is a top layer of soil that is stronger in shear initially. Nevertheless, after experiencing a certain maximum applied load the surface yields and the supported shear lessens and becomes equal to that of the homogenized soil beneath the surface. Examples of this type of soil behavior include: ice on top of a layer of snow, hard dried out clay or certain organic materials. This phenomenon was first noted by Kacigin and Guskov [56], and Wong suggested a the following equation to capture this effect [57]

$$\tau = \tau_{\max}\left(\frac{j}{K_w}\right)e^{\left(1-j/K_w\right)}, \tag{2.8}$$

where K_r is the ratio of residual shear stress as slip is increased, $j \to \infty$ to the maximum obtained shear stress τ_{max}, and K_w is the shear displacement where τ_{max} occurs. Equation 2.8 is plotted for various shear displacement ratios in Figure 2.3

2.2.3 Repetitive Loading and Hysteresis

Tires or tracks of off-road vehicles have a tendency to encounter the same section of terrain multiple times. For example, a wheeled vehicle traveling in a straight line will encounter the same terrain twice as the rear tires pass over terrain already encountered by the front tires. Due to the elastoplastic nature of the soil there will be a certain amount of permanent plastic deformation

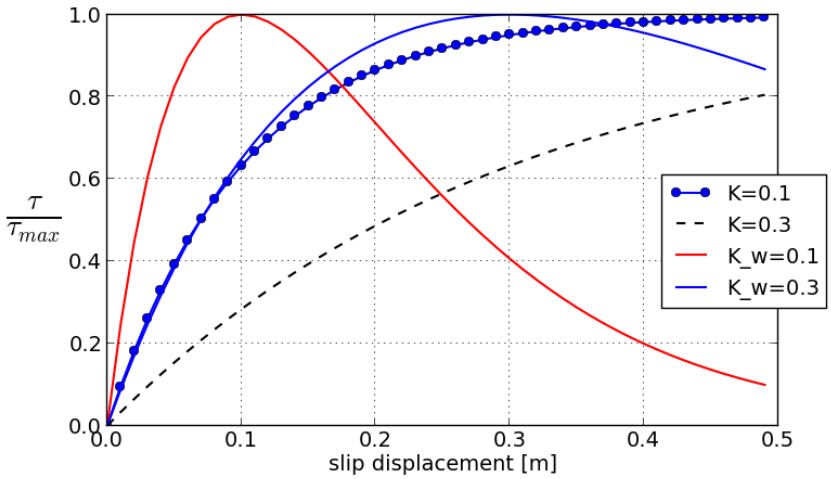

Figure 2.3: Shear stress/displacement relations

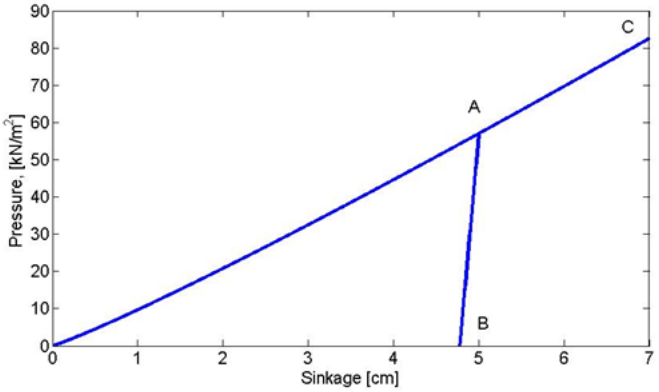

Figure 2.4: Repetitive loading of a sandy soil

as well as elastic deformation which rebounds when an element of soil is initially loaded then unloaded. This element of soil will then experience reloading when successive wheels or tracks travel over it.

When dealing with exclusively vertical loading, experimental observations have shown that the unloading/reloading cycle can be approximated by a linear pressure-sinkage relationship which is assumed to be the average response of the terrain [12, 57]

$$p = p_u - k_u(z_u - z), \tag{2.9}$$

where p and z are the pressure and sinkage, respectively during either unloading or reloading; p_u and z_u are the pressure and sinkage when unloading begins, and k_u is the average slope of the unloading-reloading line. The degree of elastic rebound is represented by the k_u parameter. As the soil behavior becomes more plastic and less elastic, the slope approaches a vertical line. Experimental measurements have shown that the value of k_u is dependent on z, and an approximate relationship can be expressed as

$$k_u = k_0 + A_u z_u, \tag{2.10}$$

where k_0 and A_u are soil specific parameters and z_u is the depth of sinkage where unloading begins. Figure 2.4 illustrates the repetitive loading behavior of a sandy terrain.

As the soil is initially loaded along the curve O-A, it follows the pressure-sinkage relationship of Equation 2.1. Curve A-B represents the response of the terrain as it is unloaded to zero pressure as given by Equation 2.9. As the terrain is reloaded, it follows the same curve A-B, and then resumes the pressure-sinkage relationship given by Equation 2.1 along curve A-C once point A is reached during reloading.

2.3 In-Plane Steady-State Traction Performance

Wong and Reece predicted the performance of a driven cylindrical rigid wheel on homogeneous soil that is in an active state of plastic failure which allows for the weight, W, drawbar pull, D, and torque, T to be stated as:

$$W = rb\left(\int_{\theta_2}^{\theta_1}\sigma\left(\theta\right)\cos\theta d\theta + \int_{\theta_2}^{\theta_1}\tau\left(\theta\right)\sin\theta d\theta\right) \tag{2.11}$$

$$D = rb\left(-\int_{\theta_2}^{\theta_1}\sigma\left(\theta\right)\sin\theta d\theta + \int_{\theta_2}^{\theta_1}\tau\left(\theta\right)\cos\theta d\theta\right) \tag{2.12}$$

$$T = r^2 b\left(\int_{\theta_2}^{\theta_1}\tau\left(\theta\right)d\theta\right). \tag{2.13}$$

Terms in the equation correspond to Figure 2.5, where the angle from the vertical is defined as θ, $\sigma(\theta)$ is the normal contact stress and $\tau(\theta)$ is the shear stress. Each integral is swept over the start of the contact angle at the front of the wheel, θ_1, to the end of the contact θ_2 near the bottom of the wheel.

It is assumed that $\sigma(\theta)$ could be described as symmetric about a maximum value of normal stress, $\sigma(\theta_m)$, that is found empirically. Then, the following symmetry relationship holds

$$\frac{\theta_R - \theta_2}{\theta_m - \theta_2} = \frac{\theta_1 - \theta_F}{\theta_1 - \theta_m}, \tag{2.14}$$

where θ_R and θ_R

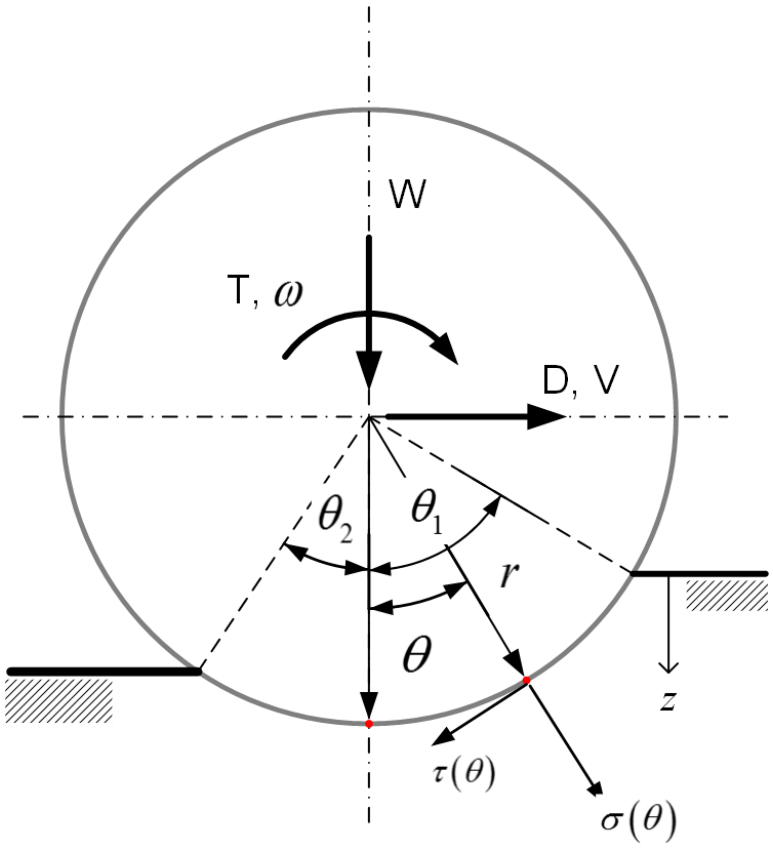

Figure 2.5: Repetitive loading of a sandy soil

Next, the Reece pressure/sinkage relation can be described in radial coordinates, for the two zones on either side of the maximum normal stress. Zone 1 is near the front of the tire, in the θ_1 region, and Zone 2 is underneath the tire near the θ_2 region and are expressed in polar coordinates, respectively:

$$\sigma_1(\theta) = (k_1 + k_2 b)\left(\frac{r}{b}\right)^n (\cos\theta - \cos\theta_1)^n \tag{2.15}$$

$$\sigma_2(\theta) = (k_1 + k_2 b)\left(\frac{r}{b}\right)^n \left(\cos\bar{\theta} - \cos\theta_1\right)^n, \tag{2.16}$$

where k_1 and k_2 are the soil cohesion and frictional constants, respectively, n is the soil exponent, found empirically with flat plate pressure-sinkage tests, and

$$\bar{\theta} = \theta_1 - \left(\frac{\theta - \theta_2}{\theta_m - \theta_2}\right)(\theta_1 - \theta_m)\,. \tag{2.17}$$

A typical assumption is that the soil has no rebound, thus $\theta_2 = 0$ and $\sigma\,(\theta < 0) = 0$. Shear stress is derived from the Janosi-Hanamoto shear slip/stress empirical relationship, Equation 2.5. The slip displacement is found by assuming for a driven wheel that the relative velocity between the wheel and soil can be described as a function of the slip rate i and tangential absolute velocity v_j along the wheel as

$$j = \int_0^t v_j dt = \int_\theta^{\theta_1} r\omega\,(1 - (1-i)\cos\theta)\frac{d\theta}{\omega} = r\left[\theta_1 - \theta - (1-i)(\sin\theta_1 - \sin\theta)\right]. \tag{2.18}$$

The first assumption that is made describes that the point of maximum normal stress, σ_n, can be inferred from experiments as a linear function of the slip,

$$\frac{\theta_M}{\theta_1} = c_1 + c_2 i, \tag{2.19}$$

where c_1 and c_2 are constants found by running trials at various slip ratios, i.

Towed wheels have a fundamentally different failure pattern in the soil, due to the necessity at steady-state conditions that the driving torque is zero. Thus, any positive shear stress must be

balanced by negative shear stress to result in zero torque. The point where the tire shear stress switches signs can be reduced to the point on the rim where the absolute velocity of the soil relative to the wheel has an angle of $\frac{\pi}{4} - \frac{\phi}{2}$ with the radial normal direction. For a given slip rate i the relation between the absolute velocity and the tire radial normal direction, α, is related to the angle θ. If this transition point is assumed to yield the maximum normal stress, the inflection angle, θ_0 is

$$\tan\left(\frac{\pi}{4} - \frac{\phi}{2}\right) = \frac{\cos\theta_0 - \frac{1}{1+i}}{\sin\theta_0}. \tag{2.20}$$

Another substantial difference between driven and towed wheels is the calculation of the slip displacement, which differs due to the two different zones of shear stress (positive and negative). The relative velocity of the soil with respect to the rim surface is found as the sum of the point on the rim surface by the velocity of the soil.

$$V_r = V_j + V_s = r\omega\left(1 - (1+i)\cos\theta\right) + K_v r\omega(1+i). \tag{2.21}$$

Slip displacement in the front region ($\theta > \theta_0$) is found by integrating the relative slip velocity with time

$$\begin{aligned} j_1 &= \int_0^t V_r dt = \int_\theta^{\theta_1} r\omega\left(1 + K_v(1+i) - (1+i)cos\theta\right)\frac{d\theta}{\omega} && (2.22)\\ &= r\left[(\theta_1 - \theta)(1 + K_v(1+i)) - (1+i)(\sin\theta_1 - \sin\theta)\right]. && (2.23) \end{aligned}$$

The constant K_v is found by knowing the slip displacement must be zero at the inflection angle θ_0.

$$\begin{aligned} K_v &= \frac{1}{1+i}\left[\frac{(1+i)(\sin\theta_1 - \sin\theta_0)}{(\theta_1 - \theta_0)} - 1\right] && (2.24)\\ j_1 &= r\left[\frac{(\theta_1 - \theta)(1+i)(\sin\theta_1 - \sin\theta_0)}{\theta_1 - \theta_0} - (1+i)(\sin\theta_1 - \sin\theta)\right]. && (2.25) \end{aligned}$$

In the bottom region ($\theta < \theta_0$) , the soil moves in the same direction as the rim, thus $K_v = 0$, and the slip displacement becomes

$$j_2 = r\left[\theta_0 - \theta - (1+i)(\sin\theta_0 - \sin\theta)\right]. \tag{2.26}$$

This method has been shown to be accurate when the assumptions hold; however, this method is not well suited for vehicle dynamics simulations for mobility prediction as the assumptions severely limit the possible driving scenarios.

2.3.1 Limitations of Steady-State Approaches

The assumptions in the Wong-Reece model, used to estimate steady-state drawbar pull, tractive effort and motion resistance of a rigid, 2-D circular wheel in soft soil, are listed below. Each will be discussed in terms of limitations posed when used in conjunction with a general purpose, three-dimensional vehicle mobility simulator. A similar discussion was presented by Azimi to point out the limitations of the steady-state performance theory in relation to the mobility of lunar rovers [22, 48].

1. Normal and shear stress is uniform along the width of the wheel
2. The wheel is moving straight forward at a constant slip rate
3. Wheel velocity is parallel to flat ground
4. The soil is homogeneous and idealized as perfectly plastic

Assumption 1 immediately disallows out-of-plane wheel motion, which severely limits the range of maneuvers that can be tested in vehicle dynamics situations. Uneven terrain on left and right tires, which is an expected operating condition in soft soil, cannot be considered. Furthermore, assumption 3 aggravates this problem, as tires on slopes, or any type of non-uniform terrain cannot be considered.

Assumption 2 causes an immediate incompatibility with dynamics models, because vertical velocity will have no effect on the calculation of vertical pressure. This clearly leads to incorrect results for any type of transient vehicle maneuver where the entire vehicle is bouncing vertically, or if pitch along the center of mass occurs. Having no concept of vertical velocity also removes

the ability to calculate energy loss in the vertical direction. Assumption 2 also disallows variation in slip rates, which limits the vehicle to constant forward velocity tests.

Slip-sinkage is not included in the model. For example, a vehicle operating at 0% and 100% slip would theoretically result in the same predicted terrain sinkage, although the tire at higher slip tends to mobilize the terrain directly under the tire and cause additional sinkage due to higher shear stress typically associated with higher slip rates. Another important consideration is that slip is typically calculated on the assumption of persistent contact between the tire and terrain; however, in the general 3-D geometry case, a part of the tire may come in and out of contact with the terrain multiple times depending on the current state of the tire and terrain geometry.

Non-homogeneous terrain in any direction, vertical, longitudinal or lateral, cannot be modeled due to assumption 4. It is well known that soft soils do not have constant density nor constant soil strength at different depths. Clay at a depth of 15 cm below the surface can vary greatly from the measurement taken at a depth of 30 cm. Also, off-road terrains can have a large variety in terms of composition and thus response in a very small physical area. For example, a vehicle traversing a stream could well see the terrain change from a hard packed clay, to a moisture saturated silty loam, to a soft clay on the other side of the stream. All this soil variation can occur in a few meters, and an off-road vehicle moving at a few MPH will traverse this distance in a matter of seconds.

Tire tread geometry is not considered, which is limiting for two reasons. First, depending on the vertical sinkage of the wheel, some sections of the tire will operate in the rigid mode (lower normal pressures) and others will be in the elastic mode (higher normal pressure), a topic discussed further in Section 4.1. The mode of operation depends on: tire structure and inflation pressure, soil type and current soil compaction state, and transient dynamic vehicle maneuvers - any of which can have a large impact on the size, shape and pressure distribution of the contact patch [3]. Second, tread patterns and lug shape and size are generally not considered, at least not in terms of a vehicle dynamics context; however, there are some models that approximate the effect of lugs on overall tire thrust [58, 59].

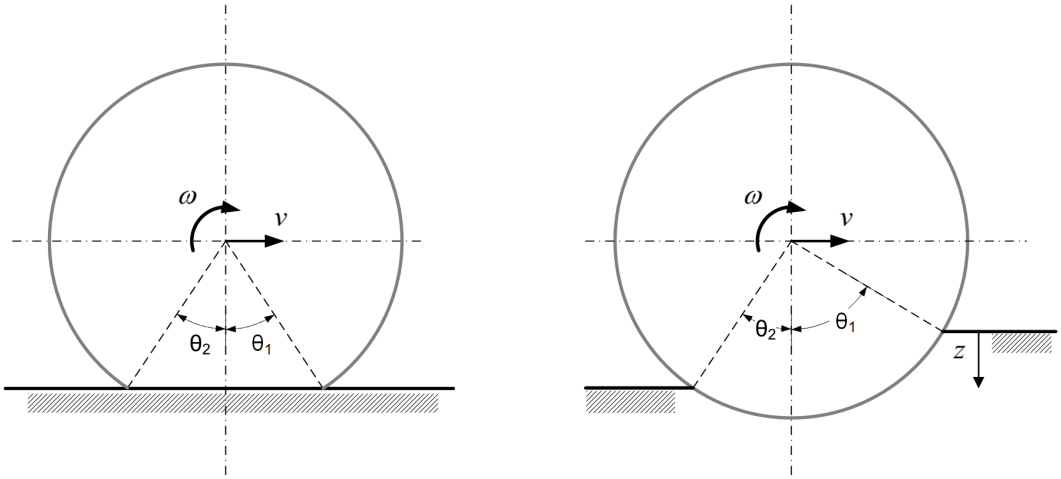

Figure 2.6: Tire operating in a pure elastic mode (left), and a perfectly rigid mode (right)

2.4 Tire/Soil Contact Patch Characteristics

The size, shape and pressure distributions of the area of contact between tire and ground is difficult to accurately calculate because the deflections of both the soil and tire contribute to the overall response, and their relative deflection magnitudes vary due to soil strength, terrain surface profile, vehicle speed, steer input, etc. There are two extreme hypotethical tire/soil operating modes, one is possibly attainable in reality and the other is not. First, consider a tire vertically loaded on a rigid, flat ground. The response of the system is entirely due to the elastic properties of the tire, shown in Figure 2.6. This can occur on unprepared terrain for very hard soils. Second, consider a flat, perfectly compliant soil; the response of the tire/soil system is entirely due to the bearing capacity of the soil. This instance is less realistic since some deflection will always be seen in a pneumatic tire due to a large vertical vehicle load applied to the wheel, and the combined stiffness of the tire belt cords and inflation pressure will be overcome at some point in the contact area.

The tire contact patch is described by both the area it encompasses as well as the stress distribution in the contact area. The simplest type of contact area is for the case of a flat rigid surface, where the tire surface conforms to the ground resulting in a two-dimensional, elliptical contact area, e.g. Figure 2.7. Lyasko determined the contact patch area of a pneumatic tire by using a

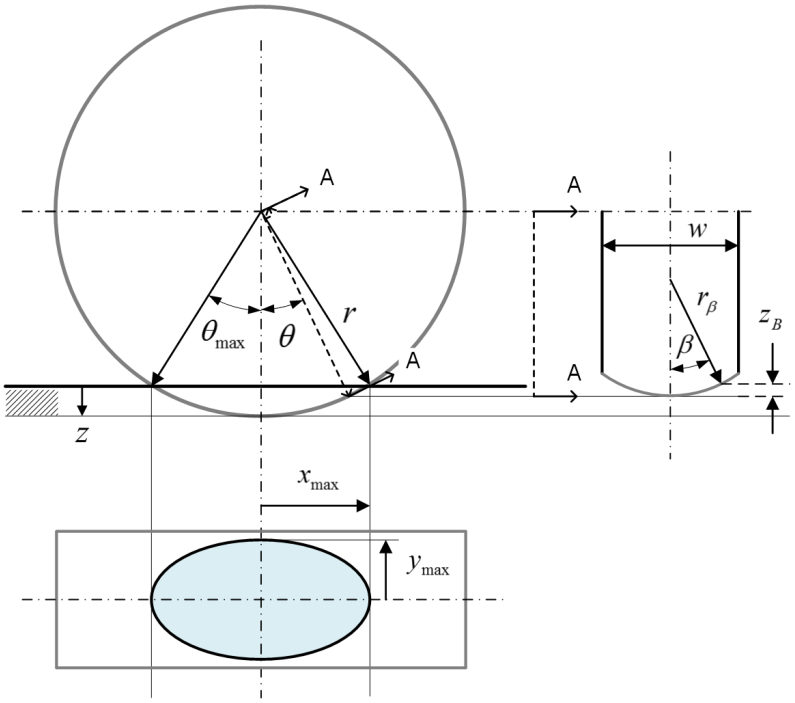

Figure 2.7: Tire surface has curvature in two planes

number of empirical relations to approximate the elliptical lengths of the area associated with the torus tire geometry [60].

When the soil becomes compliant as well, the contact area becomes three-dimensional as the soil surface deflects. Calculating the exact shape and contacts analytically is very difficult, even the case of in-plane tire motion requires physics based methods. For example, FEA is used to calculated the stress/strain in the tire and soil, and the stress and displacements from solving the boundary conditions describes the exact contact patch shape and stresses [28]. Even this detailed FE solution assumes the contact stress in the lateral direction can be well represented by a single average value; however, depending on the deflection of the tire and the strength of the soil, this may lead to an oversimplification.

Determination of the out-of-plane, or lateral, effects on the contact patch shape and stress are typically approached with experimental methods, the most comprehensive of which is given by Wulfsohn [42]. Therein, methods for experimentally determining the tire and soil deformation are reviewed, noting a lack of solutions for measuring the strain in the soil. Measurement of the strain

in the contact patch is performed by measuring the vertical and longitudinal displacement of a wire that is perpendicular to the direction of travel. Assuming no lateral soil deflection, a test function that is quadratic in both the longitudinal and lateral direction is proposed, whose coefficients are found using the experimental test results with a least squared optimization approach that constrains the test function coefficients to remain as non-imaginary and physically meaningful roots of the test function. A regression analysis was run on the test data using soil condition, tire size, inflation pressure and dynamic load as indicator variables [42]. From the data, it was seen that the contact area widens and shortens at lower soil stiffness and increase tire deflection. At large tire slip rates, the contact length increased significantly.

Using an experimental method to calculate the shape and deflections seen in the tire/soil contact patch, the tractive effort of a driven tire and the resulting soil compaction was analyzed using an assumed 2-D and 3-D contact area in [41]. A review of literature on soil/tire contact stress distributions shows that the contact pressure was constant over the width only for smooth tires at very low inflation pressures. The introduction of realistic inflation pressures, lugs/treads, soils of different strengths and various dynamic loads and slip rates typically cause the stress distribution to become non-uniform along the tire width. The stress-strain interaction due to tire loading soft soil was reviewed in [41] and it was concluded that elasticity methods alone can produce accurate stress in the soil, but Hooke's law does not predict strain well. It was found that soil dry bulk density followed increased with the logarithm of the applied pressure; however, the stress mechanism (e.g. mean normal stress, max shear stress, max octahedral stress) that best predicts bulk density change is still under debate [41].

Moisture content, shear strain, number of load cycles along with the soil material properties affect the measured stress/strain in the works cited. In detailed studies on the soil volumetric strain during tire loading, a load cycle consists of three different phases of volumetric strain: initial expansion, compaction, elastic expansion. Volumetric strain is typically limited to the surface, with the exception of very dry sand and some silts, and the areas of plastic deviatoric strain are due to tire width, contact normal pressure and shear strength of the soil. The experimental results determined the three-dimensional area which defines the soil vertical displacement and the

normal direction. Assuming all strain is volumetric and due to a semi-logarithmic stress/bulk density model, the stress distribution can be found by performing a least squares minimization with static load-deflection test data in soil. Mobility prediction is performed by using measured longitudinal displacement with Equation 2.5 and assuming maximum soil shear strength based on the Mohr-Coulomb method. Traction predictions were better when using the 3-D model, but the compaction results were similar for both 2-D and 3-D contact profiles. Dry bulk density increase was under-predicted in the top soil layer but over-predicted the depth of compaction. This led to the conclusion that the soil constitutive law was not accurate enough, a topic that remains an active area of research today [61].

Recent approaches use commercial FEA software to model the tire as an elastic structure, and the soil as a elastic-plastic solid with a Drucker-Prager modified cap model to include both the dilatation (volumetric expansion) and volumetric compaction effects for 2-D models [62, 28], and for 3-D modes in [29, 30]. The stress distribution in the contact patch is well described for the 2-D models, but only qualitatively for 3-D tire models.

Soil compaction has experimentally been shown to be less in the area of soil that was traversed by the edge of a tire when compared to the centerline [63]. An expansive review of soil compaction from agricultural traffic is performed by Raper [64], where the context is the effect of compaction and rutting on crop yields. Another review of methods to predict soil compaction due to traffic is given by Defossez [65], who analyzed semi-analytical, FEM, and hybrid methods and the required inputs to each.

2.5 Methods for Calculating Stress and Strain in Soil

It it clear that a stress-strain relationship will need to be developed based on the soil material models available, which will be used in the context of the deformable terrain models developed for the multibody simulation framework. The stress field that can be calculated due to a surface load in a semi-infinite halfspace depends on, among other factors, the assumptions of homogeneity and isotropy. Stress and strain are formed in the context of the first and second stress invariants, which describe the volumetric and shape strain contributions, respectively. Based on the derived

relations, the general form of the elastic and plastic models are formed, and a brief discussion of their various forms that result in the commonly found Drucker-Prager or Cam-Clay variants.

2.5.1 Stress in a Semi-Infinite Bounded Halfspace

The material stress/strain response of soft soil due to boundary loads differs substantially from structural mechanics in the plastic range of deformation, while the elastic range can typically be captured accurately with a linear elastic model. Elastic models used for soft soil response are either isotropic or cross-anisotropic. The simplest case assumes a homogeneous, isotropic material that behaves linear elastically to surface loads, where Boussinesq and Cerruti derived closed-form state of stress holds for any point in a semi-infinite medium due to a vertical and horizontal force on the surface. General anisotropy and cross-anisotropy will be introduced, followed by the inclusion of continuous non-homogeneity according to Frolich. Using results from Hruban and Gibson [66], it can be shown that an incompressible non-homogeneous halfspace with homogeneity that varies with depth exists. Further, it is shown that the state of stress in an incompressible homogeneous halfspace does not differ from a non-homogeneous halfspace, regardless of state of strains, which is an important characteristic that will be exploited in the resulting terramechanics model developed.

2.5.1.1 Stress Due to a Vertical Force

Boussinesq was the first to be credited with a solution to the state of stress in a bounded semi-infinite halfspace loaded by a concentrated vertical force at the surface [67]. The material in the halfspace is assumed to be perfectly elastic, homogeneous and isotropic. Under these assumptions equilibrium conditions are posed in terms of displacements, which are expressed in terms of functions of potential of varying order: ordinary, logarithmic of the first and second kinds. Using the logarithmic potential of the first kind, he was able to predict the state of stress at a given depth z and radial distance $r = \sqrt{x^2 + y^2}$ from the axis of vertical load f_V

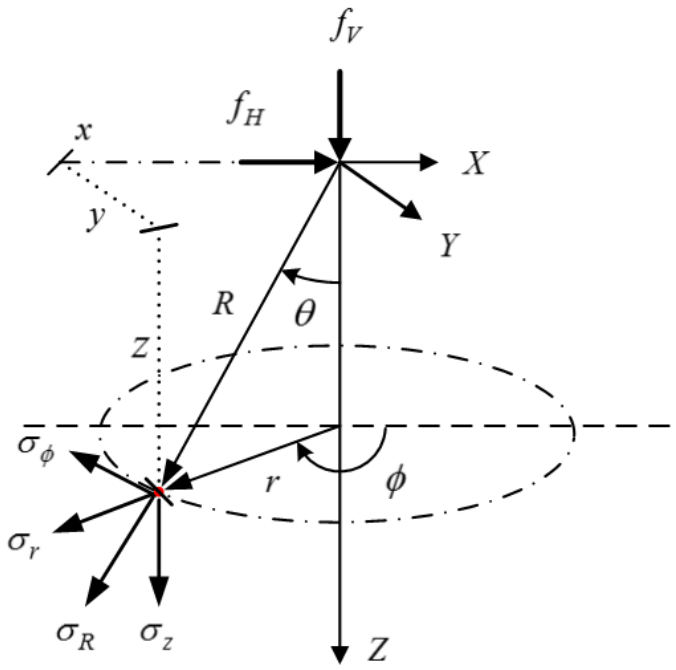

Figure 2.8: Stress at a distance from surface loads

$$\sigma_z = \frac{3f_V}{2\pi}\frac{z^3}{R^5} \tag{2.27}$$

$$= \frac{3}{2\pi}\frac{1}{\left[1+(r/z)^2\right]^{5/2}}\frac{f_V}{z^2}, \tag{2.28}$$

where $R = \sqrt{r^2 + z^2}$ and is shown in Figure 2.8.

Radial stress σ_R is best expressed using polar coordinates since it is axisymmetric,

$$\sigma_R = \frac{3f_V}{2\pi R^2}\cos\theta, \tag{2.29}$$

where $\cos\theta = {}^{z}/_{R}$ and other stress components shown in Figure 2.8 are expressed in terms of Poissons ratio μ

$$\sigma_r = \frac{f_V}{2\pi R^2}\left(\frac{3r^2 z}{R^3} - (1-2\mu)\frac{R}{R+z}\right) \tag{2.30}$$

$$\sigma_\phi = -(1-2\mu)\frac{f_V}{2\pi R^2}\left(\frac{z}{R} - \frac{R}{R+z}\right) \tag{2.31}$$

$$\tau_{rz} = \frac{3f_V}{2\pi}\frac{rz^2}{R^5} \tag{2.32}$$

Due to axisymmetric conditions, $\tau_{r\phi} = \tau_{z\phi} = 0$ and $\tau_{r\phi} = \tau_{z\phi} = 0$, where positive stresses indicate compression. Boussinesqs elasticity model can be extended to forces applied over an area by directly using integration [12]. It should be noted that the stress in the vertical direction is free of material constants, in this case the absence of Poissons ratio, and will be an important consideration in the implementation of the terrain soil model.

2.5.1.2 Stress due to a Horizontal Force

Cerruti is credited with developing methods for calculating the state of stress in a bounded halfspace due to a concentrated horizontal load on the surface [68], f_H shown in Figure 2.8. The same assumptions as before are present: the medium is elastic, homogeneous, and isotropic. As the horizontal load does not result in an axisymmetric case, the stress equations are expressed in Cartesian coordinates as reported by Feda [69]

$$\sigma_x = \frac{f_H x}{2\pi R^3}\left[\frac{3x^2}{R^2} - \frac{(1-2\mu)\,R^2}{(R+z)^2}\left(1 - \frac{y^2(3R+z)}{R^2(R+z)}\right)\right] \tag{2.33}$$

$$\sigma_y = \frac{f_H x}{2\pi R^3}\left[\frac{3y^2}{R^2} - \frac{(1-2\mu)\,R^2}{(R+z)^2}\left(3 - \frac{x^2(3R+z)}{R^2(R+z)}\right)\right] \tag{2.34}$$

$$\sigma_z = \frac{3f_H x z^2}{2\pi R^5} \tag{2.35}$$

$$\tau_{xy} = \frac{f_H y}{2\pi R^3}\left[\frac{3x^2}{R^2} + \frac{(1-2\mu)\,R^2}{(R+z)^2}\left(1 - \frac{x^2(3R+z)}{R^2(R+z)}\right)\right] \tag{2.36}$$

$$\tau_{yz} = \frac{3f_H}{2\pi}\frac{xyz}{R^5} \tag{2.37}$$

$$\tau_{zx} = \frac{3f_H x^2 z}{2\pi R^5} \tag{2.38}$$

$$\tag{2.39}$$

The stresses calculated in Equations 2.35 are only valid for points some distance from the applied force, as the soil behaves plastically in a localized area near the applied force. Further, soil does not behave isotropically, as sedimentation and overburden typically lead to an increasing Youngs modulus with soil depth. Also, soil does not typically behave as a homogeneous medium, as the material properties change as the soil is compressed and plastically deformed under a vehicle load. The solutions proposed by Boussinesq and Cerruti have been extended for a non-isotropic, non-homogeneous medium, which more accurately represents real soil behavior, described in the next section.

2.5.1.3 Stress due to Non-Isotropic Soil

An incompressible halfspace is given by a Poissons ratio of $\mu = 1/2$, which leads to $\sigma_\phi = 0$ in Equation 2.32 and leads to a purely radial propagation of stresses. The most general case of general anisotropy leads to 21 elastic constants, which requires very complicated solution procedures and is also difficult to measure experimentally. A special case of anisotropy useful in engineering practice is known as cross-anisotropy, which states that a soil mechanical response can be adequately characterized by six parameters, all of which are independent save μ_2 and μ_3

- E_v - Youngs modulus in vertical direction
- E_L - Youngs modulus in lateral plane
- μ_1 - effect of horizontal stress on horizontal strain
- μ_2 - effect of horizontal stress on vertical strain
- μ_3 - effect of vertical stress on vertical strain
- G - shear modulus of rigidity

All six parameters are non-negative, and positive strain energy defines parameter bounds as [70]

$$1 - \mu_1 - 2\mu_2\mu_3 > 0 \tag{2.40}$$

$$\mu_1 \in (-1, 1)\,. \tag{2.41}$$

Although these bounds are true for theoretically elastic materials, they do not necessarily apply in the case of real soils. The reason for including these specific parameters stems from idea that soil is formed by sedimentation, so mechanical properties should differ in the various layers in the vertical direction. In practice, typical ranges of μ_1, μ_2 and μ_3 are narrow enough where they can be ignored; thus, the distribution of σ_z only depends on the two values of Youngs modulus, E_v and E_L and their ratio, $n = {E_L}/{E_v}$, which can be found experimentally more easily than Poissons ratio μ [69].

2.5.1.4 Stress due to a Non-Homogeneous Soil

Material in the halfspace is allowed to have a Youngs modulus that differs in the lateral and vertical planes. Additionally, the value of Youngs modulus varies in the vertical direction due to the stratification of the soil. Assume the material can be treated as isotropic and incompressible ($\mu = 1/2$), leading to all stresses propagating radially. When $\mu < 1/2$, since stresses cease to be purely radial, tensile stresses appear in the soil. In soils that cannot support tension, e.g. any frictional soil that lacks cohesiveness, stresses must propagate radially. Based on the assumption of radial stress propagation, Frolich calculated the stresses as

$$\sigma_R = \frac{\nu H}{2\pi R^2}\cos^{\nu-2}\theta \tag{2.42}$$

$$\sigma_R = \frac{\nu H}{2\pi R^2}\cos^{\nu-2}\theta \tag{2.43}$$

$$\sigma_r = \frac{\nu W}{2\pi R^2}\left(\frac{r}{R}\right)^2\left(\frac{z}{R}\right)^{\nu-2} \tag{2.44}$$

$$\tau_{rz} = \frac{\nu W}{2\pi R^2}\left(\frac{z}{R}\right)^{\nu-1}\left(\frac{r}{R}\right) \tag{2.45}$$

$$, \tag{2.46}$$

where $cos\theta = z/R$ and ν is the concentration factor, which is statically indeterminate when $\nu = 3$, and is a special case that reduces to the Boussinesq stress equations, i.e. a homogeneous halfspace. Frolich showed $\nu = 3$ leads to an elastic isotropic halfspace where Youngs Modulus is constant, and $\nu = 4$ leads to a halfspace whose Youngs modulus varies linearly with depth

$$E = E_0(z/z_0)^m, \tag{2.47}$$

where z_0 is a unit length, usually the width or diameter of a loaded area, and $m = \nu - 3$. When $\nu \neq 3$ the Youngs modulus follows Equation 2.47, the halfspace material is continuously non-homogeneous, and yields an exact solution for Equation 2.49.

Feda suggests that the variation of Youngs modulus should be interpreted as the vertical effective geostatic pressure [69]

$$E = E_0\left(\frac{\gamma_0}{\gamma_w}\right)^{-m}\left(\frac{\gamma_0 z}{\gamma_w z_0}\right)^m, \tag{2.48}$$

where γ_0 and γ_w are unit weights.

2.5.1.5 Frolich Vertical Load Stress Concentration Factor

The stresses in the halfspace tend to concentrate directly under the loading axis in actual soils. The degree of concentration depends on the cohesiveness of the soil related to the soil composition and moisture content. Frolich introduced a concentration factor ν that is applied to Boussinesqs' equations that compensates for the stress concentration under the loading axis [44]. The modified vertical and radial stress equations become, respectively:

$$\sigma_z = \frac{\nu f_V}{2\pi z^2}\cos^{\nu+2}\theta \tag{2.49}$$

$$\sigma_r = \frac{\nu f_V}{2\pi R^2}\cos^{\nu-2}\theta, \tag{2.50}$$

where the value of the concentration factor varies depending on the literature referenced, and gives the elastic case seen in Equation 2.28. For example, hard, normal and soft soil can be characterized

with concentration factors of ν =3, 4, and 5, respectively, according to [71]. Alternatively, Wong [52] and Ayers [72] suggest values of ν = 4, 5 and 6 for the same soils.

The stresses calculated in Equation 2.49 and 2.50 are superimposed, as the medium is assumed to be linearly elastic, and the stresses calculated determine the total stress state at a subsurface point. Vertical stress can be expressed in radial coordinates (r, z), and an angle ϕ that describes the angle between the horizontal load vector and the location in the subsoil

$$\cos\phi = \frac{\boldsymbol{r} \cdot \boldsymbol{f_H}}{\|\boldsymbol{r}\|\|\boldsymbol{f_H}\|} \tag{2.51}$$

In other words, if the horizontal load is perpendicular to the location of the soil node, there is zero effect on the vertical soil stress which is expressed as:

$$\sigma_z = \frac{3}{2\pi} \frac{r\cos\phi}{\left[1 + (r/z)^2\right]^{5/2}} \frac{f_H}{z^3} \tag{2.52}$$

2.5.2 Soil Elasticity

From Figure 2.8, it can be seen that the state of stress at the point is simplified if symmetry is assumed in the lateral plane, i.e. $\sigma_x = \sigma_y = \sigma_r = \sigma_\phi$ depending on if Cartesian or Polar coordinates are used. This assumption is typical in soil mechanics as the testing mechanisms are typically set up in this way. Begin with the simple definition using two material parameters, Youngs modulus, E, and Poissons ratio, μ, and define the bulk and shear moduli respectively as

$$K = \frac{E}{3(1-2\mu)} \tag{2.53}$$

$$G = \frac{E}{2(1+\mu)}. \tag{2.54}$$

Define stress variables such that the bulk and shear moduli defined above can be utilized. Effective pressure, p', leads to a change in size (without a change in shape) of the element, is the same as effective stress, σ', and subtracts the pore pressure u from the absolute stress σ [73]

$$p' = \sigma' = \sigma - u. \tag{2.55}$$

The result of the compatibility equations for the virtual work associated with an incremental strain at the present state of stress allows the effective pressure to be defined in terms of the first stress invariant, I_1, which is the trace of the effective stress vector

$$p' = \frac{\sigma'_z + 2\sigma'_r}{3} = \frac{\sigma_1 + \sigma_2 + \sigma_3}{3} = \frac{I_1}{3}. \tag{2.56}$$

Define the stress associated with a change in shape of the element without a change in size or volume in a similar way

$$q = \sigma_z - \sigma_r = \sigma'_z - \sigma'_r. \tag{2.57}$$

This is known as the deviator stress, and the result of applying the compatibility equations yields the familiar form of stress, von-Mises stress, which is a function of the first and second stress invariants

$$q = \sqrt{\frac{1}{2}\sum_{i,j=1}^{3}\left(\sigma'_{ii} - \sigma'_{jj}\right)^2 + 3\tau_{ij}^2} = I_1 - \sqrt{3I_2}. \tag{2.58}$$

Define the elastic response in terms of the effective and deviator stress as

$$\begin{bmatrix} \delta\varepsilon_p \\ \delta\varepsilon_q \end{bmatrix} = \begin{bmatrix} 1/K' & 0 \\ 0 & 1/3G' \end{bmatrix} \begin{bmatrix} \delta p' \\ \delta q \end{bmatrix}, \tag{2.59}$$

where the primes on K and G indicate they are the bulk moduli in terms of the effective stresses, and there is no coupling between volumetric and distortion effects of the isotropic and elastic soil. The anisotropic elastic response, cross-anisotropy, can also be expressed in terms of the effective and deviator stresses as [74]

$$\begin{bmatrix} \delta\varepsilon_p \\ \delta\varepsilon_q \end{bmatrix} = \frac{1}{D} \begin{bmatrix} 3G* & -J \\ -J & K* \end{bmatrix} \begin{bmatrix} \delta p' \\ \delta q \end{bmatrix} \tag{2.60}$$

2.5.3 Soil Plasticity

Soft soils undergoing large vehicle-type loading conditions will experience a large amount of plastic deformation in the areas near the loading surface, and the soil cannot only be described as an elastic surface. In fact, the plasticity laws play an arguably more important role than the elasticity relationships covered. To have a complete description of irrecoverable soil response, the plasticity model should incorporate a soil yield strength function that is subject to a strain hardening (or softening, depending on the current state of stress in the soil) rule that accurately describes repeated loading effects. The loading in the soil can result in a combined elastic/plastic response, and the ratio of each type of stress/strain can be found with knowledge of a plastic potential function.

According to Wood [73], from the general matrix form of stress/strain Equation 2.59, recoverable changes in the soil volume are only affected by incremental changes in the effective stress, p'. The normal compression line of an element of soil with a logarithmic relation between effective stress and volume can be defined as

$$v = v_\lambda - \lambda \ln\left(p'\right), \tag{2.61}$$

where λ describes the slope of the elastic effective stress/volume line, and is represented for an incremental change in volume as

$$\delta v^E = -k\frac{\delta p'}{p'} \tag{2.62}$$

In the above, the superscript stands for the elastic volume change. Using the basic definition of volumetric strain $\delta\varepsilon_p = {}^{-\delta v}/_{v}$, Equation 2.62 can be transformed into the incremental elastic stress/strain as

$$\delta\varepsilon_p^E = k\frac{\delta p'}{vp'}, \tag{2.63}$$

which yields a bulk modulus value of $K' = \frac{vp'}{k}$ in Equation 2.59 that increases with the effective stress p'. Elastic shear strains do not contribute to the overall change in volume, but do contribute

to the elastic response. Since the shear modulus is a function of Poissons ratio, there are two possible approaches: assume a value for Poissons ratio or alternatively assume a value for the shear modulus. Once the plastic yield strength of the soil has been reached, a combination of elastic and plastic effects result, which are intrinsically associated with the current stress state as well as the history of plastic loading seen by the soil. This leads to the most general form of incremental volume change, where the superscripts refer to elastic and plastic changes, respectively

$$\Delta v = \Delta v^E + \Delta v^P \tag{2.64}$$

In the limit, the incremental form of plastic volumetric change with respect to an incremental change in effect preconsolidation stress is

$$\delta v^P = (\lambda - k)\frac{\delta p_0'}{p_0'}. \tag{2.65}$$

In terms of volumetric strains, the plastic component becomes

$$\delta \varepsilon_p^P = (\lambda - k)\frac{\delta p_0'}{v p_0'}. \tag{2.66}$$

Then the total volumetric strain becomes

$$\delta \varepsilon_p = k\frac{\delta p'}{v p'} + (\lambda - k)\frac{\delta p_0'}{v p_0'}. \tag{2.67}$$

Upon initiation of plastic deformation, there are three possible stress paths that can be followed

- Pure elastic rebound, according to Equation 2.61
- Pure plastic deformation, $\varepsilon p' = 0$ results in no change in volumetric strain energy
- Combined plastic/elastic response, $\delta v = 0 = \varepsilon v^E + \varepsilon v^P$

A general yield function that indicates the onset of plastic deformation which depends on the current stress state as well as the history (i.e., preconsolidation stress) of loading [73]

$$f\left(p', q, p_0'\right) = 0. \tag{2.68}$$

In practice it is typically seen that the preconsolidation pressure determines the size of the yield curve in (p', q) space [73]. Once yielding occurs, the relative ratio of elastic/plastic deformation is given by the plastic potential function

$$g\left(p', q, \xi\right) = 0. \tag{2.69}$$

where ξ serves a similar purpose as the preconsolidation pressure in the yield function, i.e. it controls the amount of the elastic/plastic incremental strain. Define the incremental plastic strains according to the potential function in terms of the volumetric and deviatoric components as

$$\delta\varepsilon_p^P = \chi\frac{\partial g}{\partial p'} \tag{2.70}$$

$$\delta\varepsilon_q^P = \chi\frac{\partial g}{\partial q} \tag{2.71}$$

where χ is a parameter associated with the strain hardening effects. The differential form of the yield function is

$$\frac{\partial f}{\partial p'}\delta p' + \frac{\partial f}{\partial q}\delta q + \frac{\partial f}{\partial p_0'}\delta p_0' = 0 \tag{2.72}$$

with the change in preconsolidation pressure being a function of both elastic and plastic shear strain as

$$\delta p_0' = \frac{\partial p_0'}{\partial \varepsilon_p^P}\delta\varepsilon_p^P + \frac{\partial p_0'}{\partial \varepsilon_q^P}\delta\varepsilon_q^P. \tag{2.73}$$

Combining the above three equations yields a solution to χ. If the yield function and plastic potential are the same, $f = g$, known as normality and is mathematically advantageous as it leads to a symmetric compliance matrix [73].

2.5.4 Drucker-Prager Cap Model

A commonly used plasticity model for soils is the Drucker-Prager modified cap model, which includes both volumetric compression and deviatoric shearing behavior [75]. There exists a critical state line in (p', q, v) space at which the material is in plastic failure at constant volume, and on either side of the critical state line exists regions of compaction and expansion [73]. Soil hardening or softening is exhibited in expansion or contraction, respectively, of the yield surface cap, usually described with an exponential density/stress function. Hardening can be described isotropically or kinematically, the latter being more accurate but more computationally expensive. In the case of a modified cap version of the Drucker-Prager model, flow rules are typically associative in the cap region, and non-associative in the transition and shear regions.

2.6 Bulldozing Effects and Soil Flow

Localized shear failure from a tire on soil typically falls under two categories. It is either directly beneath the contact surface, in which case the large shear stresses create a flow zone, or it is in the bulldozing zone near the surface in front of the tire and part of a small soil wedge that is pushed in the direction of tire travel. Simple analytical methods exist for a few idealized conditions and simulation methods are used for general purpose soil flow calculations for any transient or non-ideal conditions.

2.6.1 Bulldozing Effects

To calculate the bulldozing force required to initiate plastic flow of a soil mass along the natural shear failure plane [52], shown in Figure 2.9. A vehicle with lugged tires can approximate the increased tractive force that can be realized when the lugs initiate passive soil failure (i.e., plastic equilibrium during active tire slip) given the following assumptions: the lug is vertical and smooth, with little to no surcharge [18]. The forces resisting bulldozing are the weight of the soil and the shear forces along the failure plane. To simplify calculations, negligible friction between the soil and the tire/track interface can be assumed, resulting in a straight failure plane between the bottom

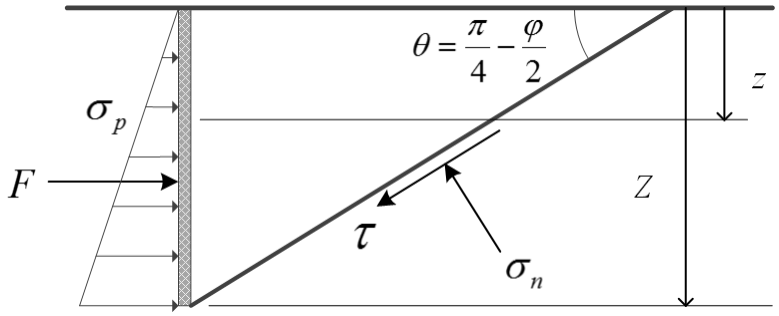

Figure 2.9: Bulldozing force generated from displacing a wedge of soil

of the tire/track and the soil surface. The angle of failure plane is given as $\theta = \frac{\pi}{4} - \frac{\varphi}{2}$, where ϕ is the soil internal friction angle.

The total force F at failure of a tire/track at depth Z shearing and displacing a soil wedge of unit weight γ and cohesive strength c is defined as

$$F_b = \int_0^Z \sigma_p dz = \int_0^Z \left(\gamma z N_\varphi + 2c\sqrt{N_\varphi}\right) dz, \tag{2.74}$$

where, $N_\varphi = \tan^2(45 + \varphi/2)$.

Assuming the bulldozing force occurs on a flat plate of width b, the total bulldozing force is integrated and found to be

$$F_b = b\left(\frac{\gamma N_\varphi Z^2}{2} + 2cZ\sqrt{N_\varphi}\right). \tag{2.75}$$

It should be noted that these are only the very simplest applications of the theory of plastic equilibrium. True applications of the theory of plasticity to soil mechanics require a more complex solution strategy than assuming a state of plastic equilibrium.

2.6.2 Soil Flow

Approaches for taking into account the soil flow due to vehicle loads are primarily empirical in nature [76] due to the complexity of the tire-terrain boundary conditions that drive the process. The boundary conditions are a function of the operating mode of the tire, in the range from no slip to complete slip, as well as the terrain conditions and soil properties. FE methods have been used

to model the soil flow by specifying the elements as either linear elastic elements in the case of applying the theory of plastic equilibrium, or more recently with critical state soil mechanics such as the Drucker-Prager cap model [62]. Typical natural terrain, such as snow, mud and organic muskeg tend to be extremely non-homogeneous and very compressible, further complicating the calculation of soil flow. To properly capture soil flow and its effects on vehicle mobility, full-resolved simulations methods that include constitutive soil material models are required to characterize the stress-strain and strain-hardening of the continuum.

2.7 Conclusions

The review of literature in Chapter 2 indicates that tire/soil interaction models to predict vehicle mobility typically fall in one of two categories: (i) empirical methods, or (ii) complex Finite Element or Discrete Element methods. Empirical methods yield a simplified steady-state 2-D solution of the tire/soil stress and strain, Section 2.3, and have been used to predict vehicle mobility with some success, Section 1.2.2, especially for rover type models with rigid wheels. However, there are a number of issues when trying to use empirical methods in conjunction with a multibody vehicle dynamics model to simulate transient acceleration or steering maneuvers, Section 2.3.1. Complex Finite Element or Discrete Element Methods are ideal to accurately simulate the stress and strain relationship in complex elasto-plastic materials, but are computationally expensive, are not easily used with a multibody dynamics vehicle model, and the constitutive models and numerical solution algorithms reamins an active area of research.

In order to calculate the three-dimensional forces and torques for a tire operating in soft soil, it is necessary to develop a dynamic interpretation of performance prediction similar to the steady-state 2-D method discussed in Section 2.3. A technique is needed that can quickly determine the contact area and contact stresses between a non-flat deformable terrain and a deformable tire based on input expected if these models were used with a multibody vehicle dynamics model. Further, the strain hardening due to repeated loading should be considered as it will impact future simulation steps in terms of both the contact patch area as well as the stress distribution through increasing the bearing capacity of compacted soil, as described in Section 2.5. It was shown that the tire inflation

pressure, pressure distribution along the width of the contact patch and soil preconsolidation bulk density were statistically significant effects when predicting net traction in Section 2.4. These are the key motivating factors behind the terrain and tire contact model development in Chapters 3 and 4, respectively.

Chapter 3

Soil Model and Terrain Database

A terrain model with two distinct layers is developed to 1) describe the soil surface geometry used to find the collision area with the tire, and 2) calculate the changes in soil stress and strain due to cyclical tire loads that causes rutting and strain-hardening. The surface of the terrain is described by tracking the height at discrete lateral and longitudinal coordinates on a grid, where the height at any intermediate coordinate is found by interpolating the height of the nearest discrete points. This results in a smooth, continuous and convex definition of the soil height, see Figure 3.1. The height at each discrete coordinate is continuously updated based on the cumulative effect of the plastic volumetric strain of the soil directly beneath the surface.

Volumetric strain of the soil is calculated by assuming the vertical normal stress in a finite volume of soil some minimum distance from the surface load can be considered the maximum principle stress. Indentation on the surface is accounted for entirely by the change in volumetric strain of the soil, as suggested by Wulfsohn [42]. Using a semi-logarithmic soil stress/bulk-density relationship, the change in bulk density due to an applied maximum normal stress is related to the change in vertical soil strain. By leveraging the method developed by Ayers and Bozdech, Section 3.2.3, an applied stress cycle is used as a basis to characterize the loading-unloading response of the finite volume of soil according to experimental evidence, which includes strain-hardening and time-dependent strain rate effects.

Although the soil very near the surface load tends to flow due to large deviatoric stresses causing localized plastic shear failure, the soil immediate adjacent to the flow zone will experience volumetric plastic strain that tends to increase the bulk density of the soil, as shown by Wulfsohn [41]. In order to find the volumetric plastic strain in the soil, the maximum principal stress of the

soil in the area affected by the vehicle loading must be found. Soil volumetric strain only in the vertical direction is considered, leading to the maximum principal stress simplifying to the vertical normal stress. The three-dimensional vertical stress field can be calculated with the Boussinesq and Cerruti equations, using the Frolich modification with steps taken to avoid numerical singularities near the surface in the terrain database as detailed in Section 3.2.3.

Contact patch forces at the tire and terrain interface are used as the input at the boundary to the soil stress calculation, and are found by first computing the contact area between the soil surface and tire geometry, then by considering the elasticity of the tire and the strength of the soil at the current time step, described in Chapter 4.1. At each simulation time step, the cumulative effect of the surface loads on the vertical normal stress of a large number of small finite volumes of soil (shown in Figure 3.1 on the right) in the area near each tire load is found using Algorithm 3.2.3. Parameter identification of the soil stress/bulk-density model is based on USDA soil material composition and USCS soil codes which identify a set of representative set of soils. The soils use coefficients derived from experimentals and are averaged to yield a best fit for a wide variety of strain-hardening soil types. A set of numerical examples for a single finite soil volume shows the model response to a set of identical load cycles. The model is shown to capture the compression/rebound, strain hardening, and time-dependent effects. Soil finite volume response within the terrain database shown in Figure 3.1 is discussed in Chapter 6 during the validation experiments. A dynamically simulated tire testing rig model to provides the inputs to the terrain model.

3.1 Terrain Surface Definition

Even when considering soil that is initially flat and homogeneous throughout, tire loads will cause plastic strain that results in volumetric compression and expansion for strain-hardening soils. This leads to changes in soil bulk density and a non-flat soil surface geometry, which requires changes in soil volume to be reflected by appropriately changing the terrain surface. Herein, the majority of the change in volume of strain-hardening soils is characterized with a vertical stress/strain model described in Section 3.2.1, where soil flow due to localized soil shear failure or bulldozing effects is neglected. This motivates a definition of soil surface heights and associated soil

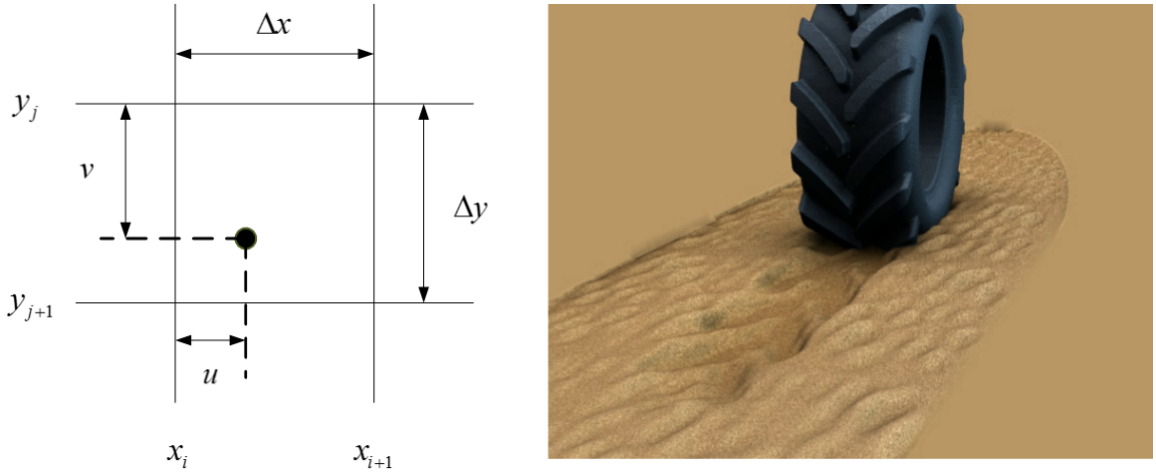

Figure 3.1: Bilinear interpolation is used to find height from the nearest four coordinates, which results in a smooth terrain surface (right)

material and derived model parameters on a discrete grid of points in terms of given longitudinal, x, and lateral, y, coordinates. Similar methods to represent a surface geometry on a regular 2-D grid are common in robotics [25], as well as for off-road terrain animation software [77] and on-road vehicle dynamics on non-flat roads [1].

The height of the terrain surface is defined globally at any coordinate that is within the database file extents in the longitudinal $[x_{\min}, x_{\max}]$ and lateral direction $[y_{\min}, y_{\max}]$, as

$$z = f\left(x, y\right). \tag{3.1}$$

The height of the terrain surface is denoted by $z(x, y)$ where x lies between the database longitudinal limits $x_{\min}$, $x_{\max}$ and y lies between the database lateral limits $y_{\min}$, $y_{\max}$. In the database, the longitudinal and lateral coordinates lie on a grid with spacings Δx and Δy shown in 3.1. If $x = x_i + u$ and $y = y_j + v$, shown in Figure 3.1, bi-linear interpolation yields

$$\begin{aligned} z(x,y) = z(x_i, y_j) + \frac{u}{\Delta x}\left(z(x_{i+1}, y_j) - z(x_i, y_j)\right) + \frac{v}{\Delta y}\left(z(x_i, y_{j+1}) - z(x_i, y_j)\right) \\ + \frac{uv}{\Delta x \Delta y}\left(z(x_i, y_j) - z(x_{i+1}, y_j) - z(x_i, y_{j+1}) + z(x_{i+1}, y_{j+1})\right). \end{aligned} \tag{3.2}$$

Each discrete coordinate maintains the undeformed and current height at the terrain surface, as well as the stress and strain of the soil directly below it, represented as a number of soil finite volumes arranged in a column shown in Figure 3.1.

The width and depth of the soil finite volume is determined by the choice of spacing on the surface grid, u and v, and the height is based on the initial vertical spacing w, shown in Figure 3.2. Strain experienced by each soil finite volume is reflected by a change in the vertical distance between each soil finite volume, and at each simulation step the cumulative strain of all the soil nodes below a coordinate determines the height at the surface.

An important implementation decision is to have enough soil finite volumes at each coordinate so the bottom-most volume, z_n, does not experience a large enough vertical stress to cause plastic strain, e.g. $\sigma_{\mathrm{a}} < \sigma_0$. This allows the vertical position of each volume in the column to be found as a function of the initial spacing and strain of the soil volumes beneath it. The spacing between adjacent subsoil nodes, $k-1$ and k is given by

$$\Delta z_{(k,k-1)} = w\left(1 - \epsilon_k\right), \tag{3.3}$$

where ϵ_k is the cumulative strain in the vertical direction of the soil volume k. Soil near the contact surface is typically in a state of localized shear failure, where the soil is actively being churned up and remolded at constant effective stress and volume [73], and is treated differently if it is closer than a calculated minimum distance, defined in Section 3.2.2.

In order to determine the height at the surface coordinates at each simulation step $z_0(x_i, y_j)$, the plastic strain ϵ_k of all the soil nodes directly below the coordinate at the surface is calculated using a semi-logarithmic stress/bulk-density relationship.

3.2 Soil Compaction Model

Each grid coordinate has a single surface node associated with it that describes the type of soil and other data, along with the total height and sinkage at that point of the terrain. Each surface voxel has a vertical column of soil finite volumes 3.2, with N_{c} points each initially spaced an equal

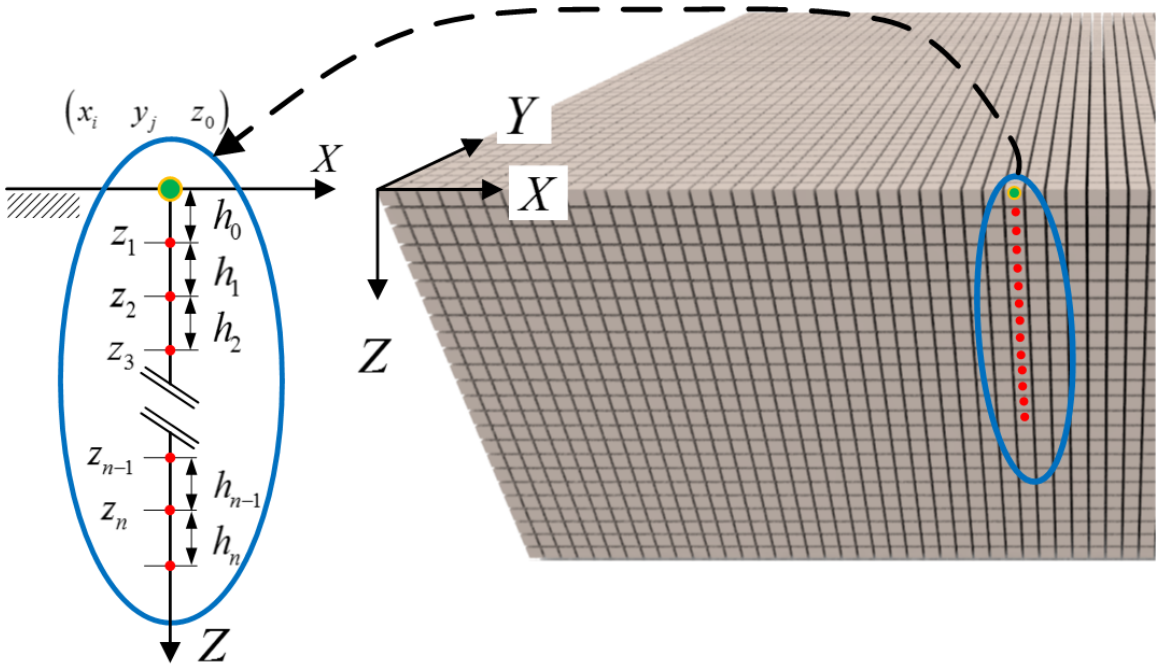

Figure 3.2: Each surface coordinate maintains the state of a number of soil finite volume nodes directly beneath it (left), shown in three-dimensions as columns (right)

distance w from one another. Each subsoil node has its own copy of the necessary variables used in the soil compaction model, and is can be thought of as a small uniaxial soil test specimen.

Soil strain is based on static calculations of elastic-plastic relationships to describe the strain hardening from repeated loading cycles. Time-dependent effects are included in the model by scaling any incremental change in strain by an empirically derived time constant, essentially limiting the maximum allowable change in strain per time step.

3.2.1 Soil Stress/Bulk Density Model

If bulk density, ρ of a soil specimen in a uniaxial compression test is plotted against $\log_{10}$ applied stress, σ_{a}, the relationship is shown to be linear for clay and silt type soils [78]. During the initial compression phase, soil particles will be rearranged and brought closer together. The straight line is also called the virgin compression curve, VCC, and the slope of that line is the compression index, C. If the soil has previously been subjected to a stress and a further stress is applied, the bulk density-stress relationship will increase along a line with a slight slope (secondary compression) until it joins with the VCC curve. The linear portion of the VCC can be described by

$$\rho = \rho_0 + C\log_{10}\left(\sigma_{\mathrm{a}}/\sigma_0\right), \tag{3.4}$$

where ρ is the computed bulk density, ρ_0 is the density at a known stress σ_0, for a given applied normal stress σ_{a}. If the VCC represents a dry soil, lines for soils at water contents less than saturation will be shifted to the left and parallel to the dry soil line. If the relationship in Equation 3.4 is known for a given water content, or degree of water saturation, curves for other water contents can be computed from the following relationship

$$\rho = \left[\rho_0 + S_{\mathrm{T}}\left(S_1 - S_0\right)\right] + C\log_{10}\left(\sigma_{\mathrm{a}}/\sigma_0\right), \tag{3.5}$$

where S_{T} is the slope of the bulk density versus degree of water saturation curve at a given stress, and S_1 is the reference degree of saturation. It scales the difference between the actual and reference moisture saturation levels, S_1 and S_0, respectively, which results in similar stresses resulting in higher increases in bulk density.

When a soil experiences a stress greater than the previous precompaction stress, a combination of elastic and plastic volumetric strain tends to cause a reduction in volume; however, after the soil reaches a peak stress, a reduction in stress tends to cause a volumetric expansion that is proportional to the total accumulated elastic strain during the load cycle. By predicting the bulk density variation due to repetitive normal loading, and assuming a majority of the deformation occurs in the vertical direction, the soil finite volume strain and impact on soil surface height can be determined along with the related net energy and power that is generated during the process. A soil element with a given height w shown in 3.2 has a vertical displacement z expressed by the following equation, which relates height to change in soil porosity

$$z = w\left(1 - (\rho_0/\rho_1)\right)\cdot, \tag{3.6}$$

where ρ_0 is the initial bulk density and ρ_1 is the final bulk density.

Time-dependent properties of the soil are needed to describe the soil response to tire loading cycles applied by a vehicle dynamics model. Rebound properties can be defined by the soil rebound index or measure of the decrease in density as the applied load is released. The time-dependent or viscous soil properties can be defined using a time constant of soil deformation based on the measured dependence on loading velocity. Compression and rebound time constants, τ_{c} and τ_{r} are defined for the soil as indicators of the time required for the bulk density ρ to change from the initial to the final value during the compression/rebound loading cycle. To establish an upper limit on soil incremental change per time step, an exponential form of the time constants is applied to the calculated change in bulk density each time step as

$$\rho^{(k+1)} = \rho^{(k)} + \Delta\rho\left(1 - e^{-t/\tau_{\mathrm{c}}}\right) \tag{3.7}$$

$$\rho^{(k+1)} = \rho^{(k)} + \Delta\rho\left(1 - e^{-t/\tau_{\mathrm{r}}}\right), \tag{3.8}$$

where the super scripts k and $k+1$ denote the time step. The determination of whether a soil volume is undergoing compression or rebound is included in the developed soil Algorithm 3.2.3. Available experimental data from Stone and Larson [79] was used to develop a regression model

for predicting the rebound constant for each terrain code as specified in [80]. The analysis produced the following equation for predicting the rebound constant for a given Grain Size Index (GSI)

$$\tau_{\mathrm{r}} = \tau_{\mathrm{c}} = 0.011 + 0.004(GSI). \tag{3.9}$$

Time constants ranging from 0.20 to 0.50 seconds are found depending on the preconsolidation stress and strain as well as the material composition and moisture levels present.

During compression, the change in bulk density is calculated by multiplying the theoretical change in bulk density, Equation 3.5, by the time-dependent compression factor, Equation 3.8. If a vehicle travels at a slower rate, the normal load is applied over a longer period of time. Thus, the bulk density increase should be greater at a lower travel speeds. This is what is expected in reality, and borne out in the numerical results on a single soil finite volume in Section 3.4.

Positive soil element vertical displacement occurs during compression when ρ_1 exceeds ρ_0 in Equation 3.5. The average compaction energy to displace the soil element vertically Δz through a given simulation timestep Δt is

$$E_c = \sigma_{\mathrm{a}} \Delta z, \tag{3.10}$$

and the approximate power required to perform the compaction is

$$P_c = E_c / \Delta t, \tag{3.11}$$

where P_c is nonzero only when compression of the soil element occurs, and is zero during rebound.

3.2.2 Vertical Soil Stress Computation

Each time step the tire surface queries the terrain to identify the terrain surface nodes in contact with the tire. Then, a set of normal pressures and shear stresses are found at each tire node, and the area associated with the tire node is used to find a set of forces acting on the terrain surface. The

Boussinesq and Cerruti equations with the Frolich modification can be applied to find the vertical pressure at any point in the soil σ_z according to Figure 2.8.

Stress in soft soil tends to concentrate directly under the loading axis in actual soils, and the degree of concentration depends on the cohesiveness of the soil and the moisture content. Frohlich introduced a concentration factor that is applied to Boussinesqs equations that compensates for the tendency for vertical stresses to concentrate around the loading axis in softer soils, discussed in Section 2.5.1.4. The vertical stress equation is converted to Cartesian coordinates,

$$\sigma_z = \frac{\nu W}{2\pi z^2}\cos^{\nu+2}(\theta) = \frac{\nu W}{2\pi R^2}\left(\frac{z}{R}\right)^{\nu}, \tag{3.12}$$

where the value of the concentration factor varies depending on the literature referenced, $\nu = 3$ gives the elastic case and the upper limit is $\nu = 6$ for extremely soft soils. The effect of the Frolich concentration parameter on the superimposed Boussinesq and Cerruti contributions to σ_z by a single point load is shown in two dimensions in Figure 3.3.

While closed form solutions exist for simple loading conditions such as flat plates with constant pressure, pressure distributions of tire loads on soft soil are complex and cannot be be expressed as easily integrated functions. Saint Venants principle is used to break the load into a number of point loads, and the overall effect on the soil is found via superposition [69] from Equations 3.12 and 2.35 from each point force at the surface.

As reported in the literature review in [42], the contact patch is complex and non-uniform in terms of size, shape and pressure distribution. Further, the boundary forces will change in time, and may be non-smooth as well. To attain accuracy better than 95% at a given depth using Saint Ventant's method, z, the dimension of the length between applied forces must be smaller than $1/3$ of the depth [81].

Due to the typical soil failure zone residing at shallow depths, stresses at the surface are calculated differently than the other points in the soil. Stresses calculated by Equations 3.12 and 2.35 become unrealistic as $\|\boldsymbol{R}\| \to 0$ in Figure 2.8. This motivates setting bounds on the calculations of stresses in the halfspace, i.e. each individual point in the subsoil considers the contribution of

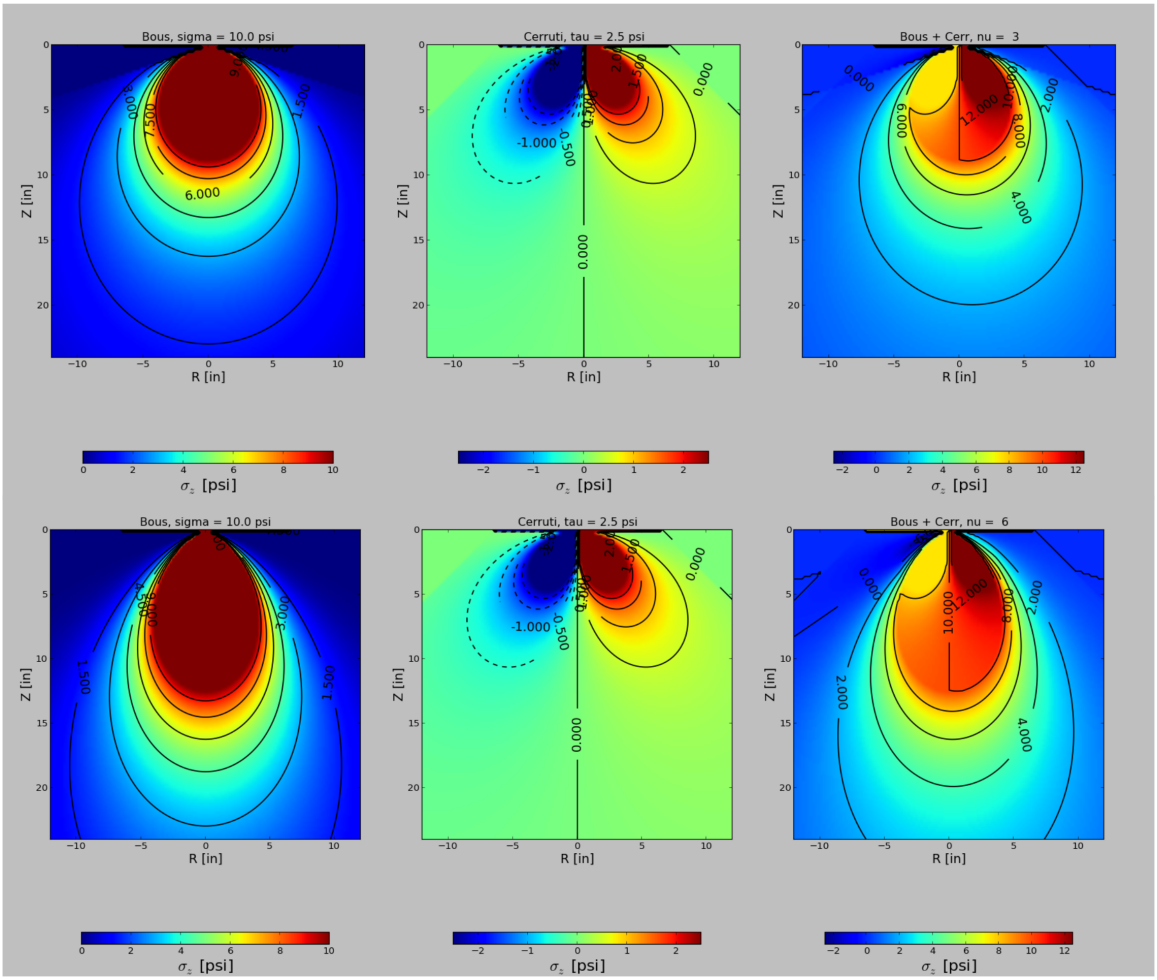

Figure 3.3: σ_z calculated using Equation 3.12 with $\nu = 3$ (top) and $\nu = 6$ bottom

surface forces to the vertical stress in the medium only if the distance between the point in the subsoil is at least a distance of $R_{\min}$ from any given surface load,

$$\sigma_z^i = \begin{cases} \sigma_{\text{surf}} \text{ if } R < R_{\min} \\ \sum_{i=1}^{N_\text{f}} \sigma_{z,i\text{F}} + \sigma_{z,i\text{C}} \text{ else} \end{cases} \tag{3.13}$$

where $\sigma_{z,\text{F}}$ and $\sigma_{z,\text{C}}$ are the Frolich and Cerruti stress equations, respectively, and N_f is the total number of concentrated forces applied to the surface.

3.2.3 Soil Element Compaction Algorithm

Combining the methods described in this chapter, it is possible to calculate the effect of a number of forces, applied to the surface of the terrain, on the vertical stress and strain of the soil at some minimum distance from the surface. This is accomplished by tracking the cumulative effect of each force on each soil element. A total of N_f forces, $\boldsymbol{f} = (f_x, f_y, f_z)^T$, act on the surface. They are contained in matrix $\boldsymbol{F} = (\boldsymbol{f}_0, \boldsymbol{f}_1, ..., \boldsymbol{f}_{N_\text{f}-1})$. Each has a corresponding global position $\boldsymbol{r}_f = (r_x, r_y, r_z)^T$ stored in the matrix $\boldsymbol{R}_f = (\boldsymbol{r}_{f,0}, \boldsymbol{r}_{f,1}, ..., \boldsymbol{r}_{f,N_\text{f}-1})$ and shown in Figure 2.8.

Depending on the type of soil at each force location, the Frolich stress concentration factor ν will vary, possibly at each force in $\boldsymbol{F}$. A single soil node with global coordinates $\boldsymbol{r}_{\text{node}}$ has its stress computed as the sum of the contributions from the vertical and horizontal force components $\boldsymbol{F}$, granted the relative location of the surface force is smaller than a threshold value.. For a valid force, the vertical stress contribution can be computed according to Figure 2.8, and the steps required to compute the overall sstress on the node is summarized in the follow Algorithm.

ALGORITHM SUBSOIL STRESS($\boldsymbol{F}$, $\boldsymbol{r}_F$, $\boldsymbol{\nu}$, N_f, $\boldsymbol{r}_{\text{node}}$)

(1) $\sigma_z = 0$

(2) **for** $k := 0$ **to** N_f

(3) $\quad \boldsymbol{r}_k = \boldsymbol{r}_{\text{node}} - \boldsymbol{R}_f(k)$

(4) $\quad z = \boldsymbol{r}_k(z)$

(5) $\quad r_\text{H} = \sqrt{\boldsymbol{r}_k(x)^2 + \boldsymbol{r}_k(y)^2}$

(6) $\quad f_\text{v} = \boldsymbol{F}_k(z)$

(7) $f_{\mathrm{H}} = \sqrt{\boldsymbol{F}_k(x)^2 + \boldsymbol{F}_k(y)^2}$

(8) **if** $z > z^\star$ and $r_{\mathrm{H}}^2 \leq (\nu + 1)z^2$

(9) $\sigma_{z,\mathrm{Frolich}} = \frac{f_{\mathrm{v}} \nu_k z^{\nu_k}}{2\pi \|\boldsymbol{r}_k\|^{\nu+2}}$

(10) $\sigma_{z,\mathrm{Cerruti}} = \frac{3 f_{\mathrm{H}} r_{\mathrm{H}} \cos(\phi)}{2\pi z^3 \left(1 + \left(\frac{r_{\mathrm{H}}}{z}\right)^2\right)^{5/2}}$

(11) $\sigma_z = \sigma_z + \left(\sigma_{z,\mathrm{Frolich}} + \sigma_{z,\mathrm{Cerruti}}\right)$

(12) **endfor**

(13) **return** σ_z

A typical applied stress cycle is assumed to monotonically increase from $\sigma_z = 0$ to a maximum stress and bulk density of $\sigma_{\max}$ and $\rho_{\max}$, respectively, then decreases back to zero stress in a similar fashion. The volumetric strain is perfectly plastic, and no change in bulk density occurs until the applied stress calculated by Algorithm 3.2.3 reaches a value greater than the previous maximum stress, known as the preconsolidation stress σ_0. When the bulk density increases, it is limited to a rate of compaction according to τ_{c}. After the maximum stress is reached, the applied stress monotonically decreases according to the rebound time constant, τ_{r} in Equation 3.9, and the rebound soil constant R, where volumetric expansion occurs until the load is entirely removed. To prevent sudden volumetric expansion due to quickly removed loads, the maximum rate at which bulk density can expand is $\Delta_\rho(\max)$. This represents an empirically derived constant that is approximated as 0.02 [g/cm^3], but should be scaled appropriately based on the simulation time step and the actual rebound rates observed if field test data is available. The amount of expansion accumulates during the unloading cycle and is used to progressively reduce the expansion that occurs in the next step, until the limit is reached. The new preconsolidation stress and density are then set at the end of a completed stress cycle when the rebound timer, t_{reb} is active and the applied stress reaches zero. Water saturation effects are included in ρ_{S}, the current bulk density of the soil is ρ, the height of the soil finite volume is H at the current time step, with a cross sectional area of A (e.g. the terrain surface grid size), reb is the rebound constant and the simulation time step size is h.

SOIL BULK DENSITY($\sigma_z, \sigma_0, \rho, \rho_{\max}, \rho_0, \Delta_{\rho 2}, C, \mathrm{reb}, \tau_{\mathrm{c}}, \tau_{\mathrm{r}}, \mathrm{t_{reb}}, \rho_{\mathrm{S}}, \mathrm{h}, \mathrm{H}, \mathrm{A}$)

(1) $\rho = \rho_0 + \rho_S + C \log_{10} \sigma_z/\sigma_0$

(2) **if** $\rho > \rho$

(3) Compression

(4) $\rho = \rho + (\rho - \rho)\,(1 - \exp(-h/\tau_c))$

(5) $\Delta z = (1 - \rho/\rho)\, H$

(6) $E = \Delta z \sigma_z A$

(7) $\rho_{\max} = \rho$

(8) **else if** $\sigma_z < \sigma_{\max}$

(9) Rebound

(10) $t_{\text{reb}} = t_{\text{reb}} + h$

(11) **if** $\rho_{\max} - \rho_0 > 2\text{reb}$

(12) $\Delta_\rho = \Delta_\rho(\max)$

(13) **else**

(14) $\Delta_\rho = (\rho_{\max} - \rho_0)\,/2$

(15) **if** $\Delta_{\rho 2} < \Delta_\rho$

(16) $\rho_c = (\Delta_\rho - \Delta_{\rho 2})\,(1 - \exp(t_{\text{reb}}/\tau_r))$

(17) $\rho = \rho - \rho_c$

(18) $\Delta z = (1 - \rho/\rho)\, H$

(19) $\Delta_{\rho 2} = \Delta_{\rho 2} + (\rho - \rho)$

(20) **else**

(21) Stress is the same

(22) $\rho = \rho$

(23) **else**

(24) Stress is the same

(25) $\rho = \rho$

(26) **if** $\sigma_z = 0$ and $t_{\text{reb}} > 0$

(27) End of load cycle

(28) $\sigma_0 = \sigma_0 10^{(\rho - \rho_0 - \rho_S)/C}$

(29) $\rho_{\max} = \Delta_{\rho 2} = t_{\text{reb}} = \sigma_{\max} = 0$

(30) **return** $\rho, \rho_{\max}, \sigma_0, \rho_0, \Delta_{\rho 2}, t_{\text{reb}}, \Delta z, E$

3.3 Soil Parameter Identification

Ayers and Bozdech [40] collected test data available in the literature for various soil compositions under uniaxial loading. The pressure/bulk-density relationship is established for a soil given its USCS composition and moisture saturation level. Additional tests that measure the time-dependent effects of the experiment are used to identify the model parameters associated with the viscosity of the process. Soil material parameters in Equation 3.5 and time-constant in Equation 3.8 are found using a linear regression on available test data in the literature.

To find the compression index, C, the clay content methods developed by Larson [78] are used by combining the curves developed for temperate region soils and highly weatherized soils. The result is a second order polynomial that relates C to the percent clay. Similarily, an applied pressure of 98 [kPa] determines the preconsolidation bulk-density, ρ_0, which is also a second order polynomial in terms of the clay percentage.

The effect of moisture differs for fine grained and coarse grained soils. To find S_{T} for fine grained soils, a second order polynomial which is a function of the percent silt is used. Alternatively, for coarse grained soils, S_{T} is found as a second order polynomial as a function of the percent clay, as suggested in [82].

Soil shear strength model parameters in Equation 2.3 and the shear deformation modulus, K in Equation 2.5, can also be found as a function of soil material composition. Friction angle and soil cohesion, ϕ and c, respectively, are found as a linear combination of the clay index, grain size index and RCI average. Shear deformation modulus, K, is found as a linear combination of the clay index and grain size index.

For example, a common clay with type CH according to the Unified Soil Classification System (USCS) is composed of 73.3% clay, 13.3% silt, and 13.4% sand, with clay and grain size indices of 5.0, an average grain size of 0.352 [mm] and an average RCI of 80. According to the model

Table 3.1: Soil bulk density and shear stress model parameters for clay, silt and clay soil

ϕ [deg]	c [kPa]	K [cm]	ρ_0[g/cm^3]	C[g/cm^3]	S_{T}[g/cm^3]	R[g/cm^3]
14.3	25.3	8.0	0.882	0.43	0.0053	0.031
24.3	0	20	1.334	0.36	0.0029	0.022
14.3	25.3	8.0	0.882	0.43	0.0053	0.031

proposed by Ayers and Bozdech, the model parameters for the soil compaction and shear stress models are listed in the first row of Table 3.1.

For a silty loam, USCS type 'ML', composed of, 13.6% clay, 61.5% silt and 24.9% sand, clay index of 0.93, grain size index 2.63 and the same moisture and RCI average as the clay yields the model parameters listed in the second row in Table 3.1. For a sandy soil, type 'SW' composed of, 6.9% clay, 2.3% silt and 90.8% , clay index of 0.47 and grain size index of 0.75 and the same moisture and RCI average as the clay results in the third row.

3.4 Finite Soil Volume Example Results

This section discusses an example of a test load being repeatedly applied to a single soil finite volume. This example tests the response of the soil model to a directly applied load, in Equation 3.5. The stress cycle is applied three times to the soil with a maximum stress of 350 kPa, operating in USCS CL type soil, traveling at a constant rate of 1.0, 2.0 and 3.0 m/s. Soil composition is 47.2% clay, 24.0% silt and 28.9% sand, with a clay index of 3.21 and a grain size index of 2.32. This yields a compression index $C = 0.5133$ g/cm^3, initial bulk density $\rho_0 = 1.266$ g/cm^{3}preconsolidation bulk density $\rho_0 = 1.204$ and stress $\sigma_0 = 98.0$ kPa.

Soil bulk density is plotted for the 1 m/s stress cycle, shown in Figure 3.4. Volumetric strain and change in bulk density does not begin immediately when the load is applied, it begins when the applied stress is greater than the preconsolidation stress, $\sigma > \sigma_0$. Rebound does not occur immediately after the max applied stress is reached, but instead begins when the applied load again drops below the preconsolidation stress.

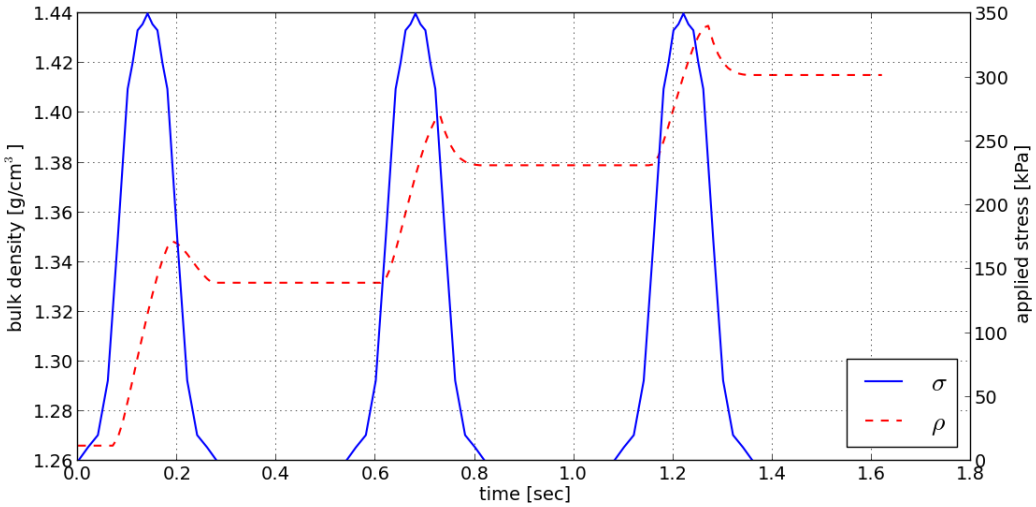

Figure 3.4: Bulk density as a function of time, 1 m/s vehicle speed

Table 3.2: Total soil vertical displacement, Energy and Peak Power at various vehicle speeds

Speed [m/s]	$\Delta\rho$ [g/cm^3]	Energy [kJ/m^3]	Power [kW/m^3]	ρ_0^e [g/cm^3]	σ_0^e [kPa]
0.5	0.2508	71.66	197.92	1.517	201.3
1	0.1652	53.17	235.9	1.431	165.3
2	0.08797	33.76	271.5	1.354	138.4
3	0.05432	24.70	293.4	1.321	128.1
4	0.05099	19.26	305.5	1.317	127.1
5	0.04556	15.82	313.3	1.311	125.5

The greatest change in strain occurs during the first load cycle, and is less each subsequent cycle due to strain hardening of the model. Strain hardening is reflected in the increase in preconsolidation stress and bulk density at the end of each load cycle, see the bottom two plots in Figure 3.5. Strain energy and power during the stress cycle are shown in Figure 3.5. They both decrease in magnitude each subsequent load cycle. Maximum power and energy are achieved just before the maximum applied load is reached, leading to most of the compaction energy being accumulated during the first half of the applied load cycle. This is due to a combination of the incremental strain being dependent on the rate of change of the applied load, which results in larger incremental strains per step, with the time-dependent effects in Equation 3.8.

Slower vehicle speed increases the bulk density of the volume of soil at a slower rate initially; however, the increased duration of the applied load results in a much greater overall plastic deformation, as shown in Figure 3.6. This is reflected in the cumulative compaction energy and peak power shown in Table 3.2, where the higher vehicle speed results in a slightly higher peak power but a much lower total change in bulk density.

For three vehicle speeds, dry bulk density change, energy, peak power and final values of preconsolidation bulk density and strain are shown in Table 3.2. Each entry in Table 3.2 is plotted as a function of the vehicle speed, with the results shown in Figure 3.7. The relationship between vehicle speed and the cumulative change in bulk density, $\Delta\rho$, is non-linear where at higher

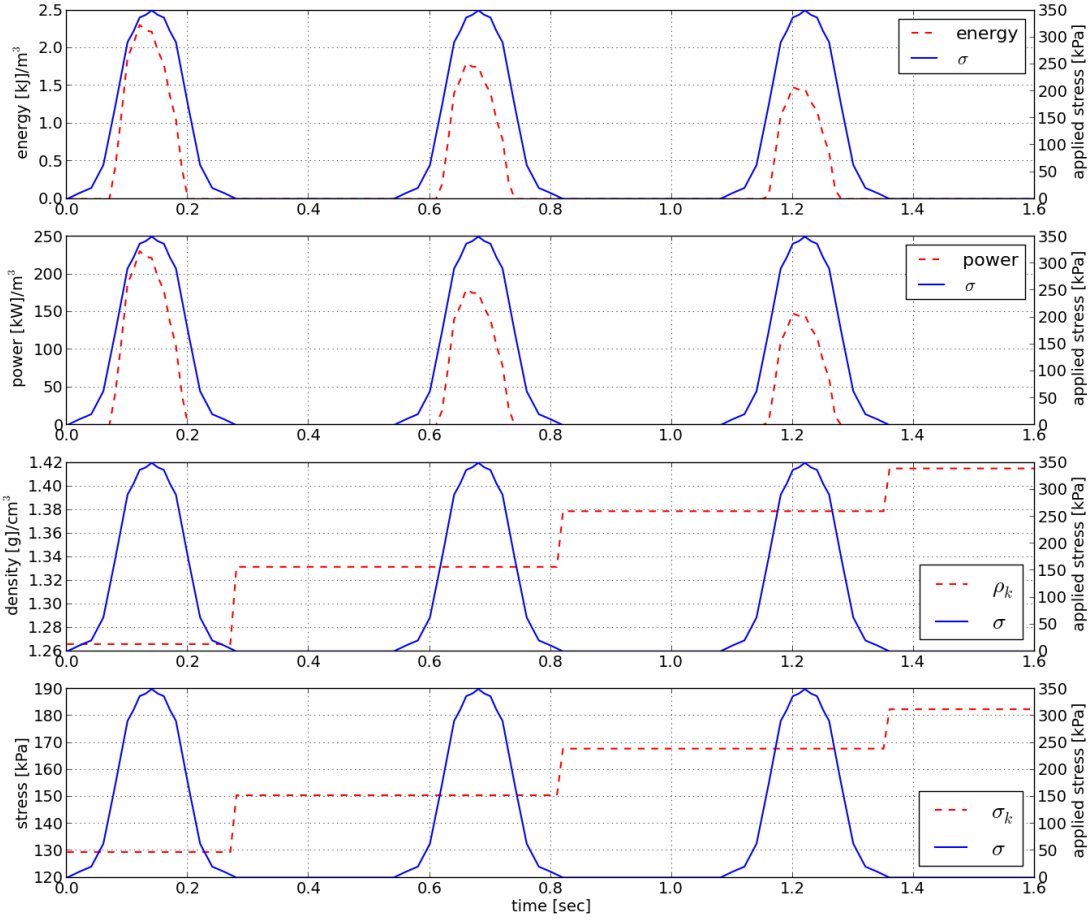

Figure 3.5: USCS CL type soil (top to bottom): compaction energy and power, preconsolidation bulk density and stress

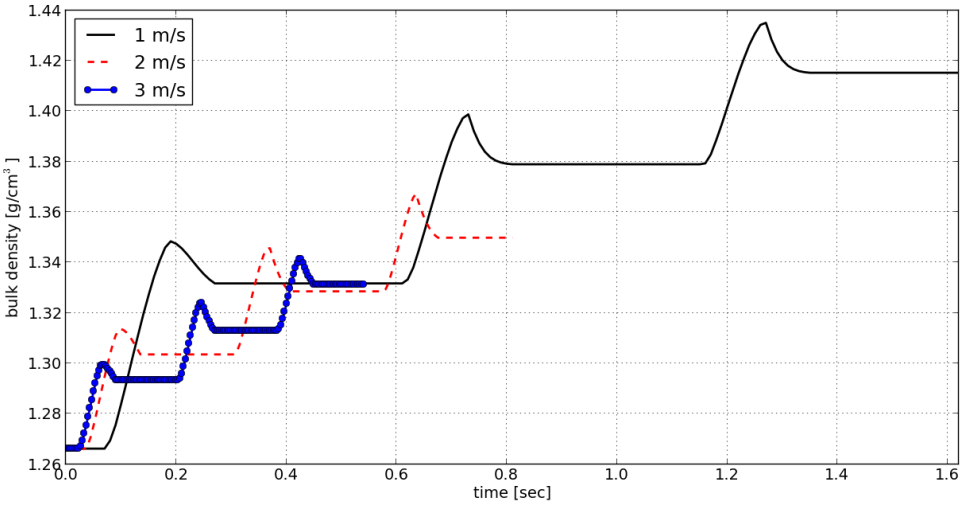

Figure 3.6: CL soil, bulk density as a function of time, 1, 2 and 3.0 m/s vehicle speed

speeds the slope becomes smaller. This trend, also be seen in the net compaction energy and final preconsolidation stress σ_0 and bulk density ρ_0, is a combined effect of the semi-logarithmic stress/bulk-density relationship and the time-constant scaling effect. Peak power is the only output that can be fitted with a linear curve reasonably well.

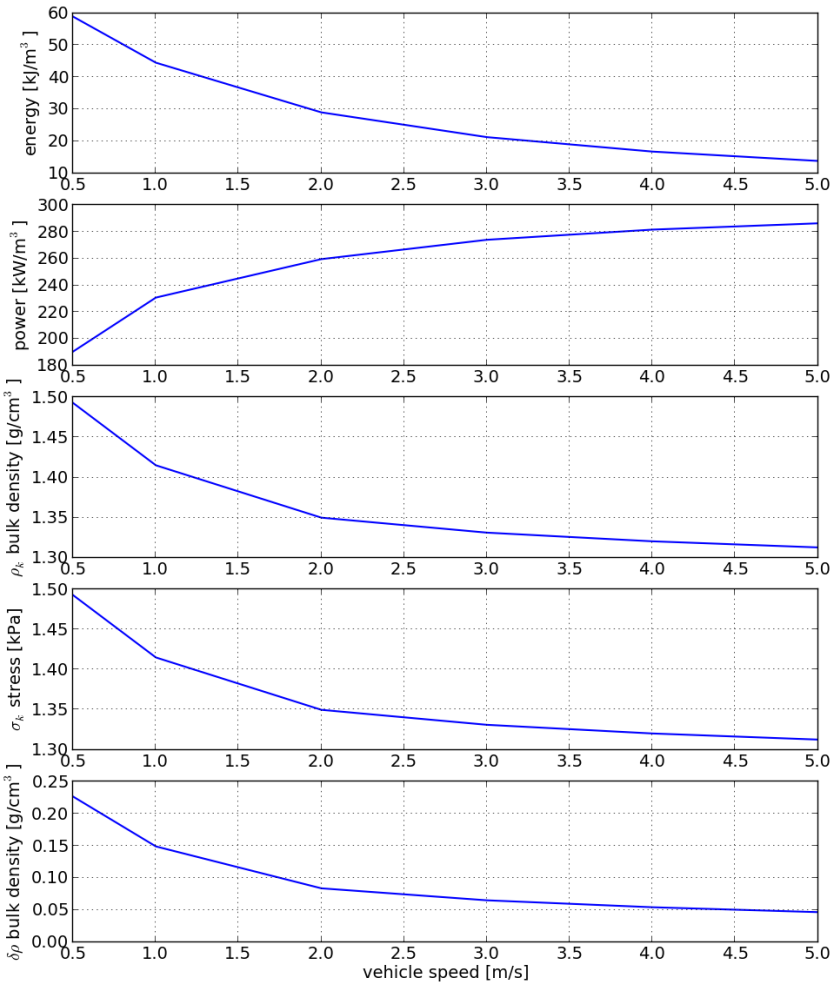

Figure 3.7: CL soil (top to bottom): total compaction energy, peak power, net change in bulk density and final preconsolidation density and final preconsolidation stress

Chapter 4

Tire/Terrain Contact Model

Using the definition of a continuous terrain surface from Section 3.1, a contact model is developed to find the three-dimensional contact area as well as the reaction normal and shear stresses for a tire interfaced to a vehicle dynamics model following the STI, Section 2.1.1. Calculation of the reaction force and torque on the wheel rigid body results in a dynamic prediction of tire/soil performance in three dimensions.

A collision detection algorithm is developed to find the contact area between a tire and the terrain surface based on a point cloud representation of the tire surface. A local coordinate system is applied to each tire node to define the normal vector and shear stress plane based on the undeflected tire geometry. Reviewing existing models and experimental results for calculation of the tire normal and shear stress, simplifying assumptions are made that lead to a quasi-static normal pressure calculation at each tire node in contact with the terrain. An simplified elastic tire method is combined with the local bearing capacity of the soil to lead to an elastic-plastic calculation of normal pressure. Shear stresses are assumed independent of the normal pressure, and are found using the shear strength of the soil and the accumulated shear displacement of each tire node in contact.

The contact model assumes the contact surface can be found based on the undeflected shape of the tire where the height of each tire node is checked against the current terrain surface height at the node's (x, y) coordinate. Typical assumptions for tire shapes include a cylinder and a torus and both are investigated when developing and fitting the tire model parameters to data. As shown by Wulfsohn [42], net traction and soil compaction values are more accurate when the contact patch area is considered a 3-D shape with curvature in two directions rather than a 2-D approximation.

This is clearly shown when the cylindrical and toroidal tires normal pressures are plotted in 3-D and compared against results reported in the literature, discussed in Section 2.4.

The form of the elastic spring function used to define the elastic tire is not known but test functions are evaluated using wheel load-deflection data that is readily available, using a least-squares method to find a best fit for the parameters of each particular spring test function. For a torus shaped tire, the optimal radius of the lateral cross-section can be found based on additional test data, typically the maximum contact width as a function of wheel deflection. It is shown that the torus shaped tire yields more accurate contact pressures when compared to a cylinder shaped tire. Most importantly, the resulting prediction of performance of the tire-terrain contact model is found in three-dimensions (e.g., returns three reaction forces and moments on each wheel) based on input expected from a vehicle dynamics model using the Standard Tire Interface, Section 2.1.1.

4.1 Contact Patch Model

According to Svendenius, tread deformations are fast and small when compared with carcass deformations and are normally considered quasi-static [83]. This is bolstered by the fact that the terrain will deform appreciably; thus, the tread or lugs will most likely sink into the terrain and be affected by the large damping and can be treated as static with respect to the tire belt dynamics. Most wheeled vehicles operate on deformable soil at low speeds, typically in the range of 1 or 2 m/s, minimizing the influence of the tire belt or carcass dynamics, allowing the tire-soil contact forces to be calculated with a quasi-static contact patch model. Pneumatic tires exhibit significantly different contact patch characteristics when operating on rigid and soft surfaces, shown in Figure 2.6.

On a flat, rigid surface, the contact patch acts in a two-dimensional area, the normal pressure is always orthogonal to the road surface plane. A large normal pressure spike is seen at the boundary of the contact area thus leading to large amounts of tire belt bending in that region. Thus, the dynamics of a dynamic tire is completely determined by the structural characteristics of the tire. This is an example of a purely elastic tire operating mode is the limit at which there is zero deflection in the road surface, and 100% deflection occurs in the tire, shown in Figure 2.6

In very soft soil, the tire will sink as the bearing capacity of the soil is less than the pressure exerted by the tire. This leads to a much larger contact area, which is typically not flat with tires, and needs to be described in three-dimensions. There are usually lower pressure spikes at the boundary of the contact patch area since the contact pressures are distributed over a larger area, relieving the large bending effects in the tire belt. In soft soil these pressure spikes are generally limited to the sides of the tire, as shown by Berg [84].

This can be compared with the elastic operating mode, where the normal pressure spikes are caused by the large bending strains at the contact boundary. In very soft soil the boundary pressure spikes are due to the tire punching into the terrain rather than belt bending. The bearing capacity of strain hardening soil increases as it is compacted at depth, and eventually increases to the point where the tire behaves in the elastic operating mode.

The three-dimensional shape of the contact surface more closely resembles that of an unloaded tire, depending on the relative stiffness of the tire and soil. On rigid surfaces such as pavement the contact patch is two dimensional, resulting in a flattening of the portion of the tire in contact with the ground. This has a non-negligible impact on the direction of the tire surface normal direction when comparing the shape of an unloaded and loaded tire. However, in the case of soft-soil the contact surface is no longer flat, but rather is three-dimensional since the tire sinks into the terrain.

While there will be some flattening of the tire due to larger normal pressure occurring at a greater soil depth, the combination of a three-dimensional contact area with an increased contact area (when comparing to a tire on a rigid surface) means there will be much less change in the tire shape between the unloaded and loaded configurations. Experimental methods by Upadhayaya and Wulfsohn have shown that a three-dimensional tire-soil contact patch much better represents the compaction effects of a tire loading soft soil [42]. In fact, the contact surface was best described with curvature in both the longitudinal and lateral directions, as the derived function was quadratic in those directions. This leads to the natural definition of the tire or contact surface geometry to resemble that of a torus.

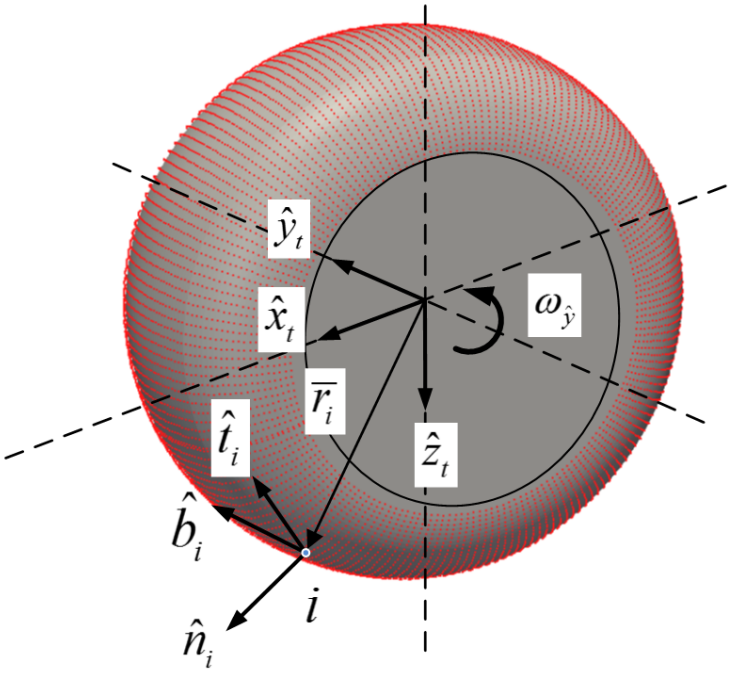

Figure 4.1: Tire nodes and a locally defined coordinate system

4.1.1 Collision Detection

The first step in finding the contact stresses is to perform a collision detection to find the area of contact between the tire and terrain. A tire geometry represented as a surface is discretized into many small triangles. Each small triangle has a local coordinate system associated with it, attached to the geometric center of the triangle. This point is referred to as a tire node. A given tire node i that resides at the surface of the tire, shown in Figure 4.1, has global coordinates $\boldsymbol{r}_i = (x_i, y_i, z_i)^T$, and is defined to be in contact with the terrain if the global height of the point on the undeformed tire surface is below the height on the terrain surface given by Equation 3.6.

With positive z is defined as vertically downwards, the gap function for tire node i, shown schematically in Figure 4.2, is written as

$$\Phi_i(r_i) = z_i - z\left(x_i, y_i\right). \tag{4.1}$$

This leads to a constraint on the contact pressures of each node on the tire surface, $\boldsymbol{\sigma_i}$, defined as a complementarity condition with the gap function as

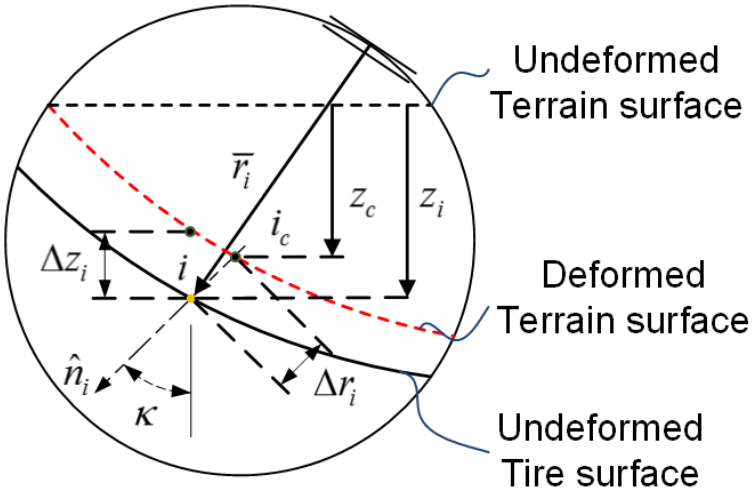

Figure 4.2: A single tire node in contact, in the tire x-z plane

$$0 \leq \sigma_i \perp \Phi_i\left(\boldsymbol{r}_i\right) \geq 0 \tag{4.2}$$

4.1.2 Tire Surface Node Local Reference Frame Definition

The direction the normal pressure on the tire surface acts at each discrete contact point is found by utilizing localized tire and terrain geometry. At each discrete point, the normal pressure is calculated by assuming it acts in the direction of the locally defined undeformed tire normal direction, $\hat{\boldsymbol{n}}_{\boldsymbol{i}}$, which itself is defined with respect to the tire coordinate system. The unique transformation matrix is defined at each tire nodal point as

$$\boldsymbol{A_i} = \left[\begin{array}{ccc} \hat{\boldsymbol{t}}_i^T & \hat{\boldsymbol{b}}_i^T & \hat{\boldsymbol{n}}_i^T \end{array} \right] \tag{4.3}$$

Shear stress is defined in the planes $\hat{\boldsymbol{t}}_i^T$ and $\hat{\boldsymbol{b}}_i^T$, which are orthogonal to the tire node normal direction. The contact pressure of tire node i has two shear and one normal component in the direction of the local unit vectors of Equation 4.3

$$\bar{\boldsymbol{\sigma}}_{\boldsymbol{i}} = \left(\begin{array}{ccc} \tau_{\mathrm{t}} & \tau_b & \sigma_{\mathrm{n}} \end{array} \right)^T. \tag{4.4}$$

4.1.3 Normal Pressure-Calculation

For a given collision k between the surface of the terrain and tire node i, the radial penetration distance between the terrain surface and the undeformed tire geometry, Δr_i shown in Figure 4.2, is defined along the tire node local normal direction. The normal pressure is found by assuming each tire node acts as an elastic spring, which is a function of only Δr_i in the tire node coordinate system

$$\sigma_{\mathrm{n}} = f\left(\Delta r_k\right). \tag{4.5}$$

The functional definition of Equation 4.5 is found in the next subsection by fitting a number of trial functions to tire load/deflection test data by using a least squares method.

From the collision detection step, the point on the terrain surface, i_c is found by a simple iterative process. It can be imagined that the soil deforms much more slowly than the tire, and that the tire contact surface will conform to the surface of the terrain. First, find the magnitude of the normal pressure at point i_c according to Equation 4.5, with the caveat that the normal pressure must be less than or equal to the bearing capacity of the soil, which can be approximated using the classical Bekker pressure-sinkage formula

$$\sigma_{\mathrm{bc}} = k_{\mathrm{e}}(z_{\mathrm{c}})^n, \tag{4.6}$$

where parameters k_{e} and n are found from field pressure plate tests of the soil using a Bevameter or another similar device. If the normal pressure found from the elastic spring is greater than the bearing capacity of the soil, $\sigma_{\mathrm{n}} > \sigma_{\mathrm{bc}}$, the point along the locally defined tire normal direction line is found where the two pressures are in equilibrium, $\tilde{i}_c$. The angle between the local tire coordinate system normal direction, $\hat{\boldsymbol{n}}_i$, and the tire local vertical direction, $\hat{\boldsymbol{z}}_{\mathrm{t}}$, κ_i shown in 4.2, is used to find the total height below the surface of the undisturbed terrain as

$$\tilde{z}_c = z_c + \left(\Delta r_i - \Delta \tilde{r}_i\right) \sin\left(\kappa_i\right), \tag{4.7}$$

where $\Delta \tilde{r}_i$ is the new radial penetration distance at node i that satisfies the equilibrium condition.

Parameters for the elastic spring function, Equation 4.5, are found for a given tire at different inflation pressures by using manufacturer tire testing data. The maximum normal pressure is limited by the vertical deflection of the point on the terrain surface using the classical Bekker/Reece flat plate pressure-sinkage relations. This results in the true point of contact between the tire and terrain lying on the line between points i and i_c shown in Figure 4.2.

The procedure for solving the normal pressure for a single tire node using the collision detection results is summarized in Algorithm 4.1.3:

ALGORITHM CONTACT NORMAL PRESSURE($\Delta r_i, \kappa, z_c, k_e, n$)

(1) $\sigma_{\mathrm{n}} = f(\Delta r_i)$

(2) $\sigma_{\mathrm{bc}} = k_e \left(z_c\right)^n$

(3) **if** $\sigma_{\mathrm{n}} > \sigma_{\mathrm{bc}}$

(4) $\quad \sigma_{\mathrm{n}} = f(\Delta \tilde{r_i})$

(5) $\quad \tilde{z}_c = z_c + (\Delta r_i - \Delta \tilde{r_i}) \sin(\kappa)$

(6) $\quad \sigma_{\mathrm{bc}} = k_e (\tilde{z}_c)^n$

(7) $\quad \sigma_{\mathrm{n}} - \sigma_{\mathrm{bc}} = 0$

(8) **return** $\sigma_{\mathrm{n}}, \Delta \tilde{r_i}$

4.1.4 Shear Stress Calculation

The standard SAE definition for wheel slip rate can be expressed as

$$s = \frac{r\omega_{\mathrm{cm},y} - v_{\mathrm{cm},x}}{v_{\mathrm{cm},x}}, \tag{4.8}$$

where $v_{\mathrm{cm},x}$ is the longitudinal component of the wheel velocity vector, r is the tire rolling radius, and $\omega_{\mathrm{cm,y}}$ is the angular velocity of the wheel about the spin axis shown in Figure 4.1. If the tire geometry is rigid and has a uniform radius, this definition is sufficient to find the slip displacement for a tire operating at steady-state in the entire contact area.

There are two distinct limitations to using Equation 4.8, i.e., the rolling radius is assumed constant and $s \to \infty$ as $v_{\mathrm{cm},x} \to 0$.

In the case of a non-steady state, non-rigid tire with a non-uniform rolling radius, an incremental slip velocity approach is used to find the instantaneous slip velocity at each locally defined tire nodal coordinate system, and the incremental slip is found by multiplying the slip velocity in the shear plane by the timestep size. The total slip is accumulated for the duration that the tire belt node is in contact with the terrain.

Define the tire slip displacement vector in the tire node local coordinate system

$$\bar{\boldsymbol{s}} = \begin{pmatrix} s_{\mathrm{t}} & s_b & s_n \end{pmatrix}^T. \tag{4.9}$$

The local tire nodal coordinate system $\boldsymbol{A_i}$ is used to define a local slip plane in terms of the binormal and tangent directions shown in Figure 4.1. The incremental slip displacement in the tire node normal direction is actually associated with the normal stress, which is orthogonal to the slip plane and does not contribute to the shear stress binormal components are included in the shear calculations.

For a given time step, m, the tire node slip vector is updated incrementally as the tire local nodal coordinate system typically has a substantial change in orientation through the duration of contact, and also because the tire node radial deflection $\Delta\tilde{r}_i$ impacts the rolling radius

$$\bar{\boldsymbol{s}}_i^m = \bar{\boldsymbol{s}}_i^{m-1} + h\bar{\boldsymbol{v}}_i^m, \tag{4.10}$$

where $\bar{v}_i^m$ is the instantaneous velocity expressed in the tire belt node local coordinate system, which is found by using the tire rigid body velocities and the location of the node with respect to the wheel center of mass.

The local position of tire node i depends on the undeflected node position, $\bar{\boldsymbol{r}}_{\boldsymbol{i,0}}$, and the radial displacement of the elastic spring found from Equation 4.5

$$\bar{\boldsymbol{r}}_i = \bar{\boldsymbol{r}}_{i,0} - \hat{\boldsymbol{n}}_i\Delta\tilde{r}_i \tag{4.11}$$

The global velocity of tire node i is calculated as

$$\boldsymbol{v}_i = \boldsymbol{v}_{\mathrm{cm}} + \boldsymbol{A}_{\mathrm{t}}\tilde{\bar{\boldsymbol{\omega}}}_{\mathrm{t}}\bar{\boldsymbol{r}}_i, \tag{4.12}$$

where $\tilde{\boldsymbol{\omega}}_{\mathrm{t}}$ is the skew-symmetric angular velocity of the tire expressed in the local tire coordinate system, $\boldsymbol{A}_{\mathrm{t}}$, shown in Figure 4.1, defined as

$$\boldsymbol{A}_t = \begin{bmatrix} \hat{\boldsymbol{x}}_t & \hat{\boldsymbol{y}}_t & \begin{pmatrix} 0 & 0 & 1 \end{pmatrix}^T \end{bmatrix}. \tag{4.13}$$

The velocity is expressed in terms of the tire node local coordinate system as

$$\bar{\boldsymbol{v}}_i = \boldsymbol{A}_i^T \boldsymbol{A}_{\mathrm{t}}^T \boldsymbol{v}_{\mathrm{cm}} + \boldsymbol{A}_i^T \tilde{\boldsymbol{\omega}}_{\mathrm{t}} \bar{\boldsymbol{r}}_i. \tag{4.14}$$

The magnitude of the shear stress on the tire belt node is found using the Janosi-Hanamoto equation [11], using the magnitude of the cumulative slip displacement of the node in the shear plane as $j_i = \sqrt{s_t^2 + s_b^2}$

$$\tau_i = (c - \sigma_i \tan\phi)\, e^{-j_i/K}. \tag{4.15}$$

Parameters associated with the Mohr-Coulomb shear strength, c and $\tan\phi$, are based on the soil in contact with tire node i at the current time step. The shear modulus K remains constant through the duration of contact. The above slip displacement and shear stress are calculated for each tire node in persistent contact with the soil, i.e., it was in contact with the terrain during the previous simulation time step), and is summarized in Algorithm 4.1.4. The variable with an $over\bar{b}ar$ denotes a value with respect to the local tire node coordinate system, Equation 4.3, calculated for time step m with stepsize h. As the tire node coordinates are expressed with respect to the tire coordinate system, the tire velocities and orientation matrix are also used, $\boldsymbol{v}_{\mathrm{t}}, \tilde{\boldsymbol{\omega}}$ and $\boldsymbol{A}_{\mathrm{t}}$, respectively. The magnitude of the shear stress is expressed in

ALGORITHM CONTACT SHEAR STRESS($\bar{\boldsymbol{s}}_i^{m-1}, \bar{\boldsymbol{r}}_i, \boldsymbol{A}_{\mathrm{t}}, \boldsymbol{v}_{\mathrm{t}}, \tilde{\boldsymbol{\omega}}_{\mathrm{t}}, h, \sigma_{\mathrm{n}}, c, \phi, K, \mu_s$)

(1) $\bar{\boldsymbol{v}}_i^m = \boldsymbol{A}_i^T \boldsymbol{A}_{\mathrm{t}}^T \boldsymbol{v}_{\mathrm{t}} + \boldsymbol{A}_i^T \tilde{\boldsymbol{\omega}} \bar{\boldsymbol{r}}_i$

(2) $\bar{\boldsymbol{s}}_i^m = \bar{\boldsymbol{s}}_i^{m-1} + h \bar{\boldsymbol{v}}_i^m$

(3) $j_i = \sqrt{s_{\mathrm{t}}^2 + s_{\mathrm{b}}^2}$

(4) $\tau_{\mathrm{mc}} = c + \sigma_{\mathrm{n}} \tan(\phi)$

(5) $\tau_{\max} = \min\left(\tau_{\mathrm{mc}}, \sigma_{\mathrm{n}} \mu_s\right)$

(6) $\bar{\tau} = \tau_{\max}\left(1 - e^{j_i/K}\right)$

(7) $\bar{\tau_{\mathrm{t}}} = \bar{\tau} s_{\mathrm{t}} / \sqrt{(s_{\mathrm{t}}^2 + s_{\mathrm{b}}^2)}$

(8) $\bar{\tau_{\mathrm{b}}} = \bar{\tau} s_{\mathrm{b}} / \sqrt{(s_{\mathrm{t}}^2 + s_{\mathrm{b}}^2)}$

(9) **return** $\bar{\tau}_{\mathrm{t}}, \bar{\tau}_b$

4.2 Elastic/Plastic Contact Model

Under the assumption that the tire contact patch shape resembles that of the undeformed tire, an elastic radial spring tire model is used to find the normal stress between the tire and the terrain surface. If the tire moves at a relatively slow velocity and no extreme transient events occur, a quasi-static elastic-plastic contact patch model can be used to calculate the contact area and the normal stresses based on the combined elastic behavior of the tire with the plastic limit of the soil bearing capacity limiting the stress values. To simplify the analysis, the tire cord belt mass is neglected, and the points on the tire surface are allowed to displace in the radial direction independently when they are in contact with the terrain surface.

At one extreme, when the soil bearing capacity is very large the problem reduces to solving the forces due to the elastic displacement of the tire belt nodes. Assuming this is the case with a terrain surface that is flat yields the conditions present in a typical tire load/deflection experiment. Manufacturer data is readily available and is used in this analysis to fit the elastic spring model parameters for tires of varying inflation pressures. Note that the tire inflation pressure accounts for 85% to 90% of a tires load carrying capacity; while the tire structure accounts for remaining portion [85].

Even assuming the tire surface displaces only in the radial direction, it is not clear what the best functional form for Equation 4.5 would be. Experimental load-deflection data for a pneumatic tire will allow the tire radial spring functions and parameters to be identified in the case of using a cylindrical and torus as tire shapes. Typical tire load/deflection data is collected on a rigid flat surface, and the area of the tire in contact with the surface deflects to conform to the flat shape, changing the normal direction to the vertical. It will be shown that an undeformed tire with cylinder geometry does a poor job of estimating the width of the tire contact, and also does not accurately

describe the contact area as the terrain becomes increasingly firm. Additional experimental data available for the contact patch length, width and area for certain inflation pressures can be used to define the undeflected shape as a torus with an optimal radius. The radius of curvature of the cross-section of the tire is found which minimizes the least-squares error between the deflection and maximum contact width data available for a tire with a 35 psi inflation pressure.

4.2.1 Cylinder Tire Geometry

This approach leverages a least squares approach to minimize the error between the manufacturer load/deflection data with simplified cylindrical tire geometry, shown in Figure 4.3. Cylindrical tire geometry gives a constant tire width, w, and a cross sectional area $A = 2xw$. The total area depends on the deflection of the tire and the longitudinal coordinate can be defined as a function of the angle from the vertical $x = r\sin\theta$. This leads to a differential area of $dA = 2wr\cos\theta d\theta$. As the pressure acts in the normal direction with respect to the undeformed tire, the total vertical load can be expressed as a function of the tire center of mass vertical displacement z_{cm}

$$F(z_{\mathrm{cm}}) = \int_A \sigma_{\mathrm{n}}\cos\theta dA = 2wr\int_{\theta=0}^{\theta=\theta_r} \sigma_{\mathrm{n}}\cos^2\theta d\theta. \tag{4.16}$$

The simplest case is that of a linear elastic spring. Using notation from Figure 4.3,

$$\sigma_{\mathrm{n}}(\theta) = a\Delta k, \tag{4.17}$$

where a is the identified spring rate in pressure per distance. Solving for Δk in terms of the tire radius, deflection and angle, Equation 4.16 becomes

$$F(z_{\mathrm{cm}}) = 2wra\int_{\theta=0}^{\theta=\theta_r} \left[r\cos^2\theta - (r - z_{\mathrm{cm}})\cos\theta\right]d\theta \tag{4.18}$$

To allow for arbitrarily complex spring function forms, a least squares method is used to minimize the error between the calculated load for a given deflection. Here we use manufacturer data for a typical truck tire, a Goodyear 37x12.5-R 16.5 Wrangler MT, at inflation pressures of 15 and

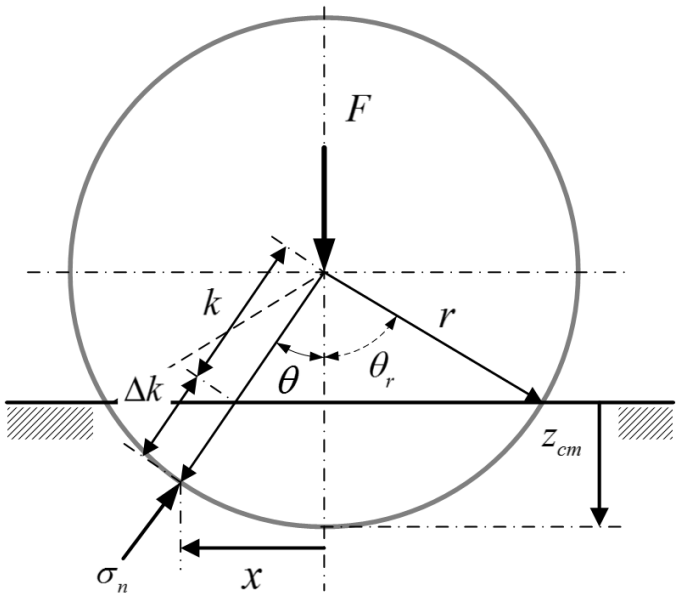

Figure 4.3: Simplified tire geometry used for elastic tire parameter fitting procedure

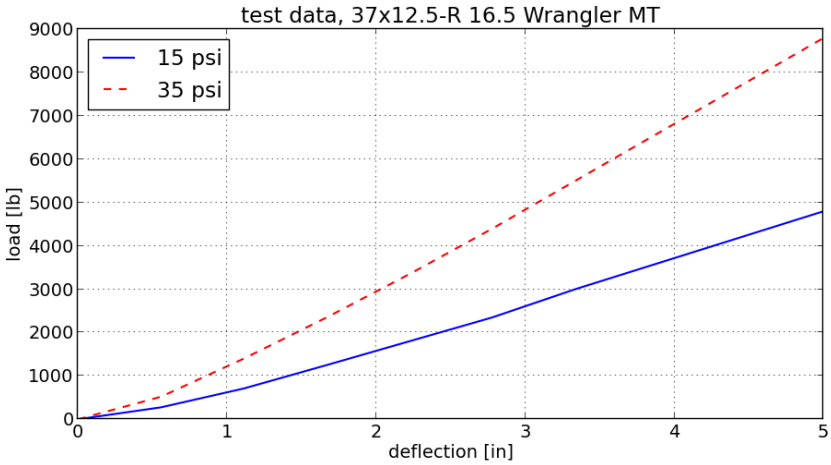

Figure 4.4: Load vs. deflection test data for Goodyear Wrangler MT at two inflation pressures

35 psi, see Figure 4.4. Higher inflation pressure leads to larger loads for a given tire deflection. A number of spring functional forms were investigated, including linear, quadratic, and power. The minimization function is

$$\min \sum_{j=1}^{N_{\mathrm{p}}} \left(F_j - F(z_{\mathrm{cm,j}})\right)^2, \tag{4.19}$$

for a number of chosen experimental data points, N_{p}, where F_j is the experimentally measured load and $F(z_{\mathrm{cm,j}})$ is the result of computing the load from the model for a given value of experimental deflection using Equation 4.16.

The optimization scheme will yield the best-fitting parameters of the spring function form selected. In the case of a linear spring, Equation 4.18, the optimal values for a tire with inflation pressures of 15 and 35 psi are $a = 7.99$ and 14.7, respectively. The optimal linear spring stiffness yields a good match between the model and experimental data for inflation pressures of 15 and 35 psi, shown in Figures 4.5 and 4.6.

Additional data for the contact patch maximum width, length and area as a function of deflection is also available at the 35 psi inflation pressure. Comparing the values used in the model, it can be seen assuming an undeformed cylindrical shape yields larger values for all three cases, as seen in Figure 4.7. The model overestimates the contact patch width and area, and underestimates

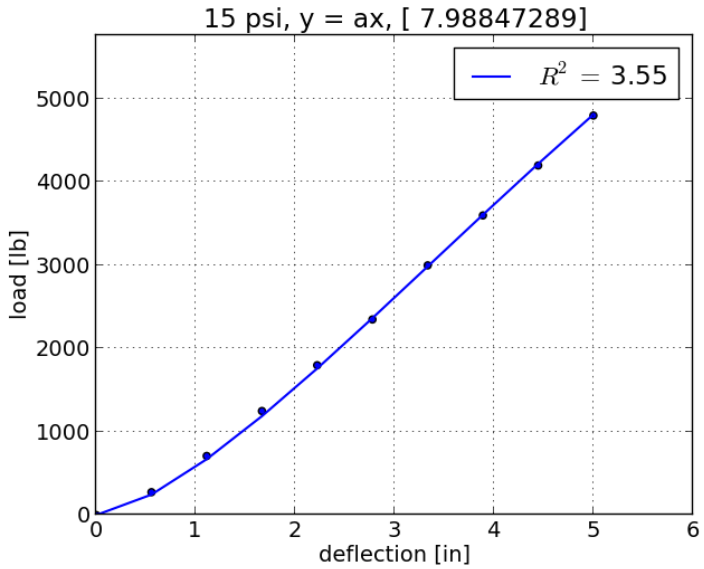

Figure 4.5: Wheel load/deflection data points and fitted deformable tire model, cylinder tire at 15 psi

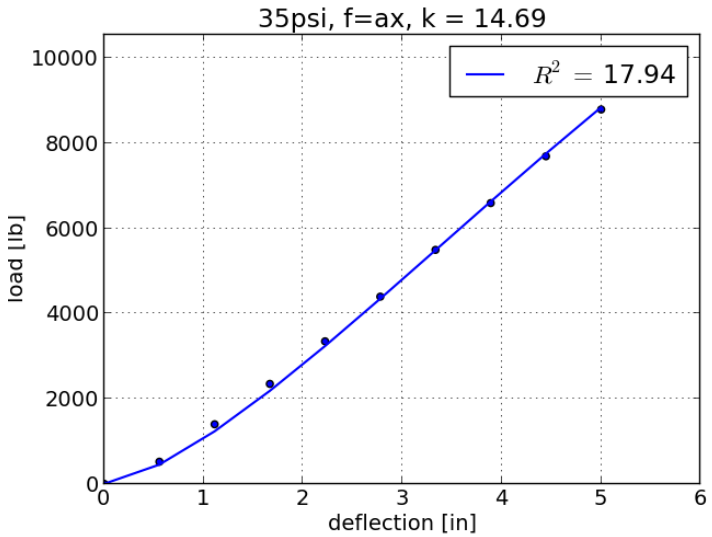

Figure 4.6: Wheel load/deflection data points and fitted deformable tire model, cylinder tire at 35 psi

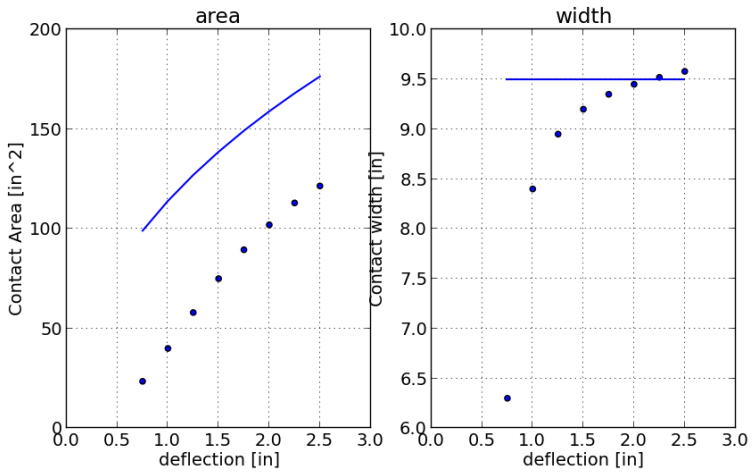

Figure 4.7: Contact area and width vs. wheel deflection data and the corresponding cylinder model predictions

the normal pressure magnitudes in the limit that the soil model becomes highly compressed and acts as a rigid, flat surface.

An elliptical contact patch shape can be obtained by defining a second radius and sweeping the cross section with a circular arc, resulting in a torus tire shape. Using a torus for an undeflected shape will help alleviate the overestimation of the contact area, and leads to a more natural contact area, see Figure 4.8. The optimal radius of curvature of the torus is selected based on the width data shown in Figure 4.7, as explained in the next section.

4.2.2 Torus Tire Geometry

An additional parameter, β, is defined that gives curvature to the cross section of the tire. This leads to an increased contact width as vertical tire deflection increases, which is seen from the experimental data in Figure 4.7. Typically, the maximum tire contact width is recorded during wheel load/deflection tests for one inflation pressure. This allows for a simple least squares method to determine the optimal radius in the cross-section r_β, by comparing the width predicted by a torus on a flat plate, $y_{\max,j}$, with the width data, w_j

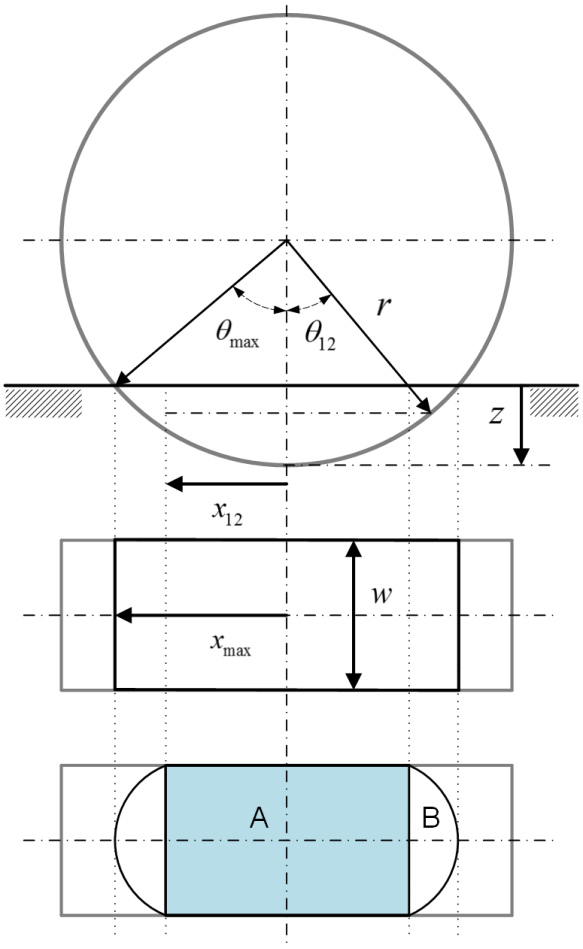

Figure 4.8: Tire contact areas on a flat surface for a cylinder (middle) and torus shaped (bottom)

$$\min \sum_{j=1}^{N_{\mathrm{p}}} \left(y_{\max,j} - w_j\right)^2 . \tag{4.20}$$

The tire belt node location and surface normal is now locally defined as a function of both θ and β, shown in Figure 4.9; however, the spring deflection is still only considered in the radial direction (e.g., the tire x-z plane) when calculating the tire normal pressure.

Using the maximum tire contact width data for a typically encountered range of tire deflections (0.75 to 2.5) inches, a least squares approach is used to find the optimal radius in the tire cross-section, r_β , shown in Figure 4.9. Assuming a maximum contact width of 9.5 inches, the optimal radius is $r_\beta = 8.43$ inches and the calculated max wheel width for the torus wheel geometry shows better agreement with the experimental data, shown in Figure 4.10.

Due to the curvature in the tire cross section, for a given wheel deflection a torus tire shape leads to overall radial spring deflections smaller than those predicted by a cylinder tire shape. The normal direction does not always point in the radial direction and now has a lateral component, which also contributes to an increased elastic spring stiffness. The integral used to find the vertical force in the least squares method to identify the optimal linear spring constant, Equation 4.19, is modified to account for the dimension added by the torus tire shape.

Shown in Figure 4.11, the contact area of a torus tire and flat ground is either a single ellipse (for small wheel deflections), or a rectangular section with two elliptical caps. For the given wheel deflection and torus radius, the max swept angle in the cross section is

$$\beta_{\max} = \cos^{-1}\left(\frac{r_\beta - z}{r_\beta}\right). \tag{4.21}$$

This allows for the maximum theoretical lateral length from the wheel centerline to be found as

$$y_{\max} = r_\beta \sin\left(\beta_{\max}\right). \tag{4.22}$$

If the maximum lateral length calculated is greater than half the width of the tire the contact area is made up of two distinct shapes, shown on the left in Figure 4.11. First, the length of the

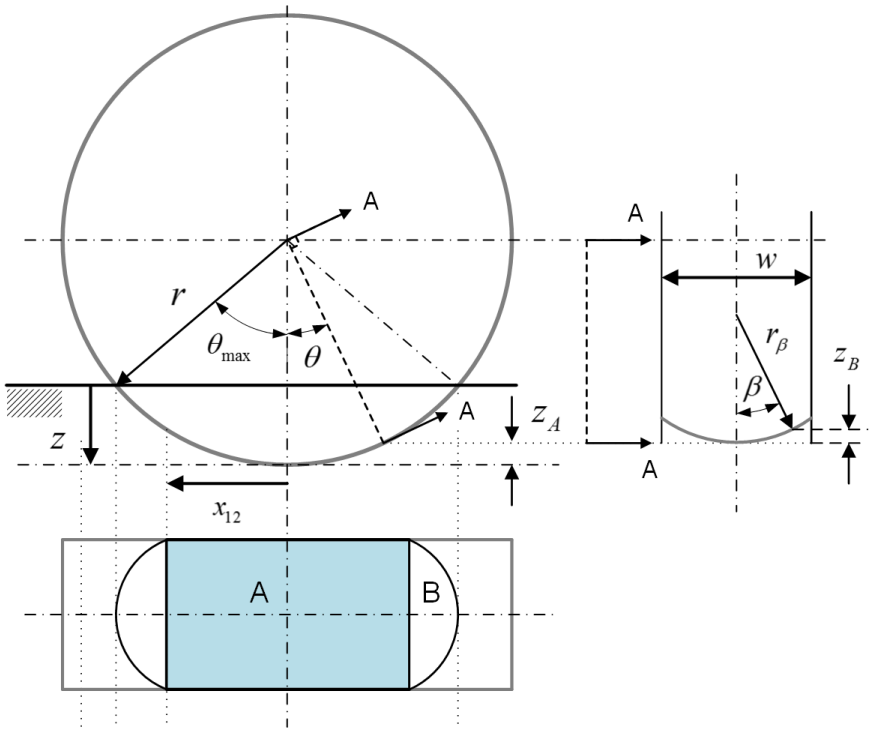

Figure 4.9: Torus shaped tire contact area and cross section

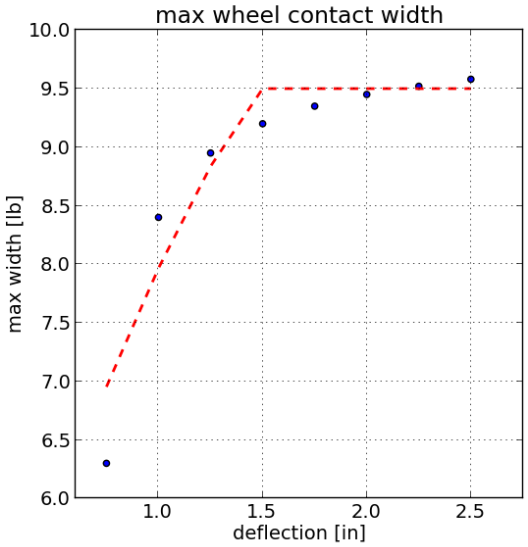

Figure 4.10: Contact width vs. wheel deflection data compared to model using a torus

rectangular section is found. The integral for contact area A has a limited cross section angle, found by setting y_{max} equal to half the width of the tire,

$$\beta'_{\max} = \sin^{-1}\left(\frac{b}{2r_\beta}\right). \tag{4.23}$$

The boundary between A and B is found by knowing that at the maximum swept angle, $\beta'_{\max}$, the global vertical height of the cross section sweep, z_B added to the vertical height from the sweep of the angle θ_{12}, z_A shown in 4.11, equals the wheel deflection, $z_{12} = z_A + z_B$. The angle which defines the boundary between areas A and B is

$$\cos\theta_{12} = \frac{r - z}{r - r_\beta\left(1 - \cos\beta_{\max}\right)}. \tag{4.24}$$

The normal pressure acts normal to the tire surface, which is now a function of both θ and β. Therefore, the wheel load is found by integrating the normal pressure over the area defined by both angles

$$F_z = \int \sigma_{\mathrm{n}} \cos\theta \cos\beta dA \tag{4.25}$$

$$= \iint \left(\sigma_{\mathrm{n}} \cos^2\theta \cos^2\beta\right) d\beta\, d\theta \tag{4.26}$$

For integral A, the angles are swept over the rectangular cross section from 0 to θ_{12} and $\beta'_{\max}$. Due to symmetry, the vertical force contribution is

$$F_z^A = 4r\left(r_\beta\right) \int_0^{\theta_{12}} \int_0^{\beta'_{\max}} \left(\sigma_{\mathrm{n}} \cos^2\theta \cos^2\beta\right) d\beta d\theta. \tag{4.27}$$

Integral B sweeps the remaining amount of θ, and the upper bound for β is a function of θ. Also, an elliptical contact area is seen in this contact

$$F_z^B = \pi r\left(r_\beta\right) \int_{\theta_{12}}^{\theta_{\max}} \int_0^{\beta(\theta)} \left(\sigma_{\mathrm{n}} \cos^2\theta \cos^2\beta\right) d\beta d\theta. \tag{4.28}$$

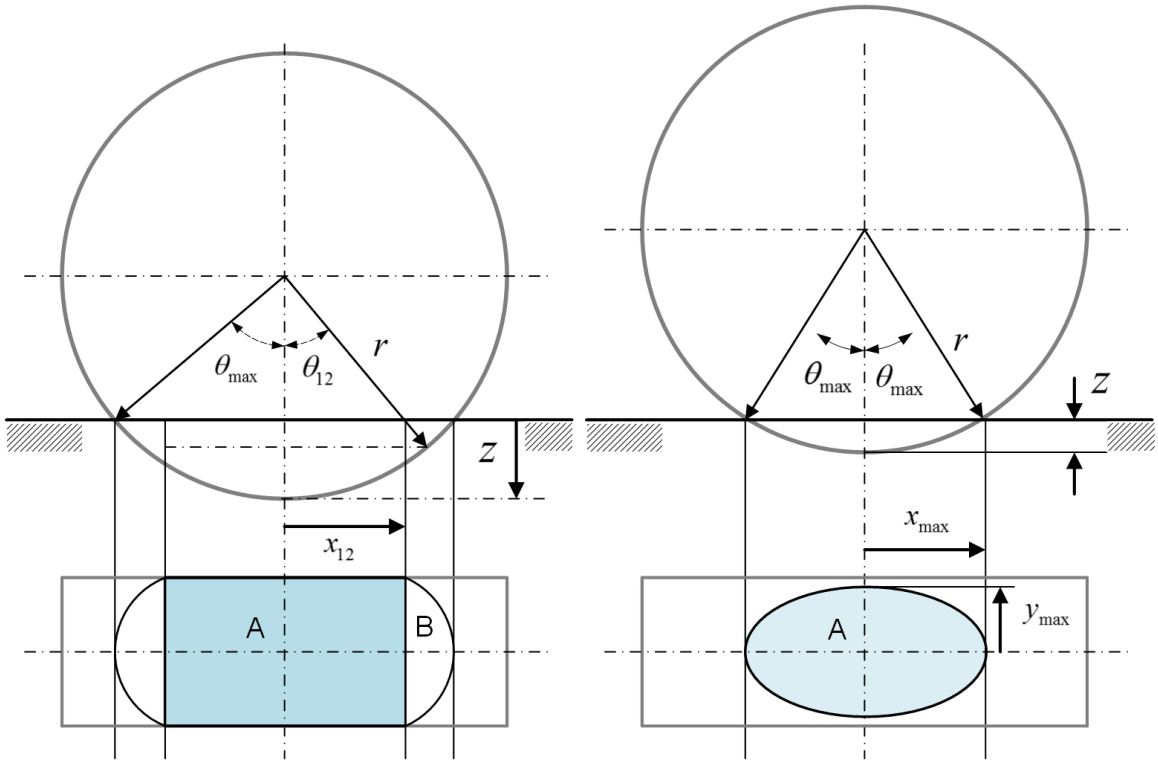

Figure 4.11: Torus tire shape leads to two distinct contact areas on flat ground

In the second case, the maximum lateral length swept by the torus falls within the width of the tire, which allows the use of a single integral to calculate the vertical force. This is similar to Equation 4.28, except the entire range of θ is swept

$$F_z^C = \pi r \left(r_\beta\right) \int_0^{\theta_{\max}} \int_0^{\beta(\theta)} \left(\sigma_{\mathrm{n}} \cos^2\theta \cos^2\beta\right) d\beta d\theta. \tag{4.29}$$

Finally, the radial spring displacement used to find the normal pressure, Equation 4.5, is found in terms of θ and β

$$\Delta k(\theta, \beta) = r - \frac{r - z}{\cos\theta} - r_\beta \left(1 - \cos\beta\right). \tag{4.30}$$

Performing the optimization procedure to identify the spring stiffness value for a given spring function, Equation 4.19, and using the appropriate integrals to compute the vertical force, a quasi-static normal pressure model is generated for a tire based on its inflation pressures and geometric dimensions.

4.3 Dynamic Tire Performance Prediction

Once the optimal elastic spring function parameters and the torus cross-section radius are calculated, the tire normal and shear pressures in the contact patch at any simulation time step can be found. This allows a dynamic interpretation of tire/soil performance for the overall wheel thrust, motion resistance and torque.

Each tire node has a normal $\boldsymbol{\sigma}_i$ and shear pressure $\boldsymbol{\tau}_i$ acting in orthogonal planes and expressed in global coordinates. The area of each tire node is scaled by the ratio of the radial displacement to the undeflected radial length, e.g. $A_i = A_{i,0} \frac{\|\bar{\boldsymbol{r}}_i\|}{\|\bar{\boldsymbol{r}}_{i,0}\|}$. The force vector on the tire center of mass is calculated as a sum of the normal and shear components of all the nodes, N_{c}, in contact during this time step as

$$\boldsymbol{f}_{\text{wheel}} = \int (\boldsymbol{\sigma} + \boldsymbol{\tau}) dA \tag{4.31}$$

$$= \sum_{i=0}^{N_{\text{c}}} (\boldsymbol{\sigma}_i + \boldsymbol{\tau}_i) A_i. \tag{4.32}$$

Tire contact stress distributions where the normal pressure direction does not necessarily point through the wheel spin axis leads to a different formulation when compared to 2.13. Again the contributions from all the tire nodes in contact with the soil are summed after taking the cross product of the local position $\boldsymbol{r}_i$. Stresses $\boldsymbol{\sigma}_i$ and $\boldsymbol{\tau}_i$ are orthogonal to one another and are combined.

$$\bar{\boldsymbol{t}}_{\text{wheel}} = \int (\boldsymbol{\sigma} \times \bar{\boldsymbol{r}}_i + \boldsymbol{\tau} \times \bar{\boldsymbol{r}}_i) dA \tag{4.33}$$

$$= \sum_{i=0}^{N_{\text{c}}} (\boldsymbol{\sigma}_i + \boldsymbol{\tau}_i) \times (\bar{\boldsymbol{r}}_i) A_i. \tag{4.34}$$

If soil is initially flat and homogeneous throughout, operating at steady-state, e.g. s in Equation 4.8 is constant and $v_{z,t} = 0$ in Figure 4.1, a direct comparison to the Wong/Reece steady-state solution discussed in Section 2.3 can be made. Chapter 6 compares the results yielded against numerical predictions as well as experimental results for a tire in clay from [41] both in terms of wheel mobility prediction and the soil stresses and strains.

Chapter 5

Terrain Software Implementation and Co-Simulation with Dynamics Engine

5.1 Background and Overview of Terrain Software Framework

This chapter details the terrain database implementation and software framework developed to create a co-simulation environment to enable accurate mobility simulations with a multibody dynamic tire or vehicle. Parts of the terrain database models were originally developed by the author during the development of the Vehicle Terrain Interaction Model (VTIM), a US-Army STTR funded project that was a collaboration between TARDEC/MechSim/Universities of Tennessee and Wisconsin-Madison [86]. The project goal was to create a physics-based deformable terrain model to be used with an existing real-time vehicle dynamics ride-motion simulator [87] to enable off road mobility simulations with an arbitrarily complex tire model, e.g., [88]. Software existed to represent the terrain surface geometry using satellite imagery and contained methods to efficiently query the height and terrain properties to resolve local high-fidelity terrain surface data, as required by a real-time simulator [89]. Methods were developed to approximate the real-time wheel/soil interaction through utilizing empirical numerics developed at ERDC for soft soil and snow [90].

Terrain models were developed as a standalone C++ based API using the existing terrain geometry database functionality. New methods were implemented to calculate the stress and strain in the 3-D areas around tire loads according to the methods developed by Ayers and Bozdech, outlined in Section 3, for a single soil element. These methods were extended by providing a contact patch

model for tires described in Section 4, that utilized a torus shaped tire shape to calculate the collision area with the terrain surface. Each tire is calibrated according to experimental wheel vertical load/deflection data and max contact width data typically available from the manufacturer. The normal pressure, subsequently calculated by balancing the local tire elastic forces with the bearing capacity of the soil specified using classical pressure-sinkage terramechanics relations detailed in Section 2.2.1, is used to generate a 3-D contact stress profile. This allows the overall wheel torque, drawbar pull, motion resistance, thrust, as well as lateral force and moment effects, to be calculated dynamically for each tire and be integrated into a dynamic vehicle model to be used in handling and mobility simulations.

The vehicle model and API plug-in manager are contained within the Chrono framework, described in the next section. At each simulation time step, each wheel of the vehicle performs a query of the terrain database to determine the dynamic tire reaction forces and torques. In the background, the terrain database uses the resolved contact patch forces as an input to the terrain stress and strain model. Any changes in soil volumetric strain causes the surface of the terrain to deform according to the soil models described in Section 3.2.3. The co-simulation interface between the multibody vehicle dynamics engine and the terrain database is exposed by Chrono, which contains the vehicle model and solves the system EOMs at each step using its DVI solvers.

Parallel computing is utilized to address a number of computational bottlenecks encountered in the compute intensive calculations, e.g. to find the three-dimensional stress field in the soil due to a tire load. Hardware acceleration leveraging parallel CPU and GPU cores is applied where appropriate, depending on task- and data-parallel type computations. Scaling analyses are run that show a strong scaling trend as the number of parallel CPU cores is increased. GPU acceleration is targeted at specific data-parallel soil stress calculations, but when enabled is shown to have a considerable effect on reducing the overall computation time of a terrain database query. Finally, details on hiding inherent overhead, or 'latency' from initiating GPU functions (due to requiring time-consuming global memory transfers at the start) is discussed in terms of an asynchronous threading technique that begins the CPU to GPU memory transfer as soon as possible, resulting in modest time-savings.

5.2 Integration with Dynamics Engine via Co-Simulation

Chrono is a C++ Software Development Kit (SDK) that allows for dynamic system modeling and simulation, and has been used in the past to simulate simple vehicles [91], as well as handle rigid-body friction and contact with arbitrarily complex geometry [92]. Other uses of Chrono can be found in [93, 31, 32], and the software framework is available as open-source code on Github [94]. A brief description of the modeling methodology of the rigid body system with bilateral and unilateral constraints is given, followed by a discussion of where the exchange of information occurs between Chrono and the terrain database in terms of the rigid body system Equations of Motion (EOM). The co-simulation method is classified as a multi-rate Gauss-Seidel type [95], where the global time step is determined by the much stiffer multibody system, which is variable and typically in the range of $H_{\max} = 0.5$ to 1 milliseconds.

5.2.1 Multibody Dynamics Equations of Motion

The multibody dynamics EOMs in the Chrono software libraries are based on a Differential Variational Inequality (DVI) formulation which has been documented and evaluated by a number of authors, [92, 96, 97, 98, 99]. A feature of this type of approach is the ability to solve rigid body dynamics problems involving friction and contact in the tens of millions of bodies range [32]. This is enabled through using modeling and numerical solution algorithms that can run well on advanced parallel hardware as explained in [100, 99]. The following summary of the multibody system EOMs in Chrono is derived from the full description detailed by Heyn [32].

A system of rigid bodies can interact through contact, friction, joints and force functions. Each body is described in absolute Cartesian coordinates with its center of mass global position $\boldsymbol{r} = (x, y, z)^T$ and orientation described by a quaternion $\boldsymbol{\epsilon} = (\epsilon_0, \epsilon_1, \epsilon_2, \epsilon_3)^T$ as a generalized coordinate $\boldsymbol{q} = \left(\boldsymbol{r}^T, \boldsymbol{\epsilon}^T\right)^T$. Similarly, each body has a corresponding global velocity coordinate, $\dot{\boldsymbol{q}} = \left(\dot{\boldsymbol{r}}^T, \dot{\boldsymbol{\epsilon}}^T\right)^T$, and acceleration $\ddot{\boldsymbol{q}} = \left(\ddot{\boldsymbol{r}}^T, \ddot{\boldsymbol{\epsilon}}^T\right)^T$. Rotational velocity is more easily understood in terms of a body local coordinate system at the center of mass as $\bar{\boldsymbol{\omega}}$, and a body generalized velocity $\boldsymbol{v} = \left(\dot{\boldsymbol{r}}^T, \bar{\boldsymbol{\omega}}^T\right)^T$ is related to $\dot{\boldsymbol{q}}$ using a linear mapping $\dot{\boldsymbol{q}} = \boldsymbol{T}(\boldsymbol{q})\boldsymbol{v}$ [101].

The mass matrix $\boldsymbol{M}$ is diagonal and constant due to the choice of the centroidal reference frames for generalized coordinates. External forces and torques are expressed as $\boldsymbol{f}\left(t, \boldsymbol{q}, \dot{\boldsymbol{q}}\right)$. The second order differential equations that describe the EOMs of the system are described as $\boldsymbol{M}\dot{\boldsymbol{v}} = \boldsymbol{f}\left(t, \boldsymbol{q}, \dot{\boldsymbol{v}}\right)$ [101].

Bilateral constraints allow joints to be modeled which results in limiting the relative or absolute kinematic motion of bodies, thus removing Degrees of Freedom (DOF) from the system. A bilateral constraint B is expressed as an algebraic constraint applied to the generalized coordinates of a body as $\boldsymbol{g}\left(\boldsymbol{q}, t\right) = \boldsymbol{0}$. The number of DOFs removed varies from zero to six depending on the type of joint. Bilateral constraints can also be enforced on the velocity level as $\nabla_q \boldsymbol{g}^T \boldsymbol{T}\left(\boldsymbol{q}\right)\boldsymbol{v} + \frac{\partial \boldsymbol{g}}{\partial t} = 0$ [97].

In the case where no rigid body contacts are present, the Equations of Motion with only bilateral constraints and external forces are expressed as

$$\dot{\boldsymbol{q}} = \boldsymbol{T}\left(\boldsymbol{q}\right)\boldsymbol{v} \tag{5.1}$$

$$\boldsymbol{M}\left(\boldsymbol{q}\right)\dot{\boldsymbol{v}} = \boldsymbol{f}\left(t, \boldsymbol{q}, \boldsymbol{v}\right) - \boldsymbol{g}_{\boldsymbol{q}}^T\left(\boldsymbol{q}, t\right)\lambda \tag{5.2}$$

$$\boldsymbol{g}\left(\boldsymbol{q}, t\right) = \boldsymbol{0} \tag{5.3}$$

Unilateral constraints can also be added to model contact and friction, but this feature is not a main concern of the present work and is omitted. However, they are included in the full set of DVI EOMs for contextual purposes, Equations 5.4-5.8, as the solution to the time-stepping scheme is heavily focused on solving the large optimization problems posed.

For a given time t and time-step l, denote the current system position and velocity vectors as $\boldsymbol{q}^{(l)}$ and $\boldsymbol{v}^{(l)}$. The goal is to find the solution to the problem in order to advance to the next time step, $t^{(l+1)} = t^{(l)} + h$, given a known time step size h. The time discretized EOMs leverage an over-relaxation scheme specified by Anitescu and Tasora [96], where the relevant terms include the generalized velocity linear transform, Newton's 2nd law and the bilateral constraints in Equations 5.4 through 5.8, respectively.

$$\boldsymbol{q}^{(l+1)} = \boldsymbol{q}^{(l)} + h\boldsymbol{T}\left(\boldsymbol{q}^{(l)}\right)\boldsymbol{v}^{(l+1)} \tag{5.4}$$

$$\boldsymbol{M}\left(\boldsymbol{v}^{(l+1)} - \boldsymbol{v}^{(l)}\right) = h\boldsymbol{f}\left(t^{(l)}, \boldsymbol{q}^{(l)}, \boldsymbol{v}^{(l)}\right) - \boldsymbol{g}_{\boldsymbol{q}}^{T}\left(\boldsymbol{q}^{(l)}, t\right)\lambda + \sum_{i=1}^{N_c}\left(\boldsymbol{\gamma}_{i,n}\boldsymbol{D}_{i,n}^{T} + \boldsymbol{\gamma}_{i,u}\boldsymbol{D}_{i,u}^{T} + \boldsymbol{\gamma}_{i,w}\boldsymbol{D}_{i,w}^{T}\right) \tag{5.5}$$

$$\frac{1}{h}\boldsymbol{g}\left(\boldsymbol{q}^{(l)}, t\right) + \boldsymbol{g}_{\boldsymbol{q}}^{T}\boldsymbol{T}\left(\boldsymbol{q}^{(l)}\right)\boldsymbol{v}^{(l+1)} + \boldsymbol{g}_t = \boldsymbol{0} \tag{5.6}$$

$$0 \leq \frac{1}{h}\Phi_i\left(\boldsymbol{q}^{(l)}, t\right) + \boldsymbol{D}_{i,n}^{T}\boldsymbol{v}^{(l+1)} \perp \boldsymbol{\gamma}_{i,n} \geq 0, \quad i = 1, 2, \ldots, N_c \tag{5.7}$$

$$\left(\boldsymbol{\gamma}_{i,u}, \boldsymbol{\gamma}_{i,w}\right) = \underset{\sqrt{\gamma_{i,u}^2+\gamma_{i,w}^2} \leq \mu_i \gamma_{i,n}}{\arg\min} \left(\boldsymbol{\gamma}_{i,u}\boldsymbol{v}^{(l+1)^T}\boldsymbol{D}_{i,u} + \boldsymbol{\gamma}_{i,w}\boldsymbol{v}^{(l+1)^T}\boldsymbol{D}_{i,w}\right) \tag{5.8}$$

The rigid body frictional contact is described in the Equations 5.7 and 5.8 and is incorporated into Equation 5.5, as additional force terms containing the contact impulses $\boldsymbol{\gamma}$ and tangent space transformation matrices $\boldsymbol{D}_i$. The complementarity condition in Equation 5.7 indicates that either bodies are in contact and there is a non-zero normal reaction impulse $\boldsymbol{\gamma}_{i,n}$, else there is no contact impulse if the bodies are not in contact. Contact friction is contained in the minimization objective function in Equation 5.8 and represents a static Coulomb friction model. The two terms multiplied by $\frac{1}{h}$ in Equations 5.6 and 5.7 are stabilization terms for the bilateral and unilateral constraints, respectively.

If there are no rigid body frictional contacts in the system, as is the case when running the validation studies in Chapter 6, then the EOMs reduce to the classical multibody definition, shown in time-continuous form in Equations 5.1-5.3.

$$\boldsymbol{q}^{(l+1)} = \boldsymbol{q}^{(l)} + h\boldsymbol{T}\left(\boldsymbol{q}^{(l)}\right)\boldsymbol{v}^{(l+1)} \tag{5.9}$$

$$\boldsymbol{M}\left(\boldsymbol{v}^{(l+1)} - \boldsymbol{v}^{(l)}\right) = h\boldsymbol{f}\left(t^{(l)}, \boldsymbol{q}^{(l)}, \boldsymbol{v}^{(l)}\right) \tag{5.10}$$

$$\frac{1}{h}\boldsymbol{g}\left(\boldsymbol{q}^{(l)}, t\right) + \boldsymbol{g}_{\boldsymbol{q}}^{T}\boldsymbol{T}\left(\boldsymbol{q}^{(l)}\right)\boldsymbol{v}^{(l+1)} + \boldsymbol{g}_t = \boldsymbol{0} \tag{5.11}$$

5.3 Execution Flow Diagram, Single Terramechanics Step

The two developed Application Programming Interfaces (API) modularize the terrain and tire models in order to allow for an arbitrarily complex tire model to be used. As shown in the high-level execution flow diagram, 5.1, at any point in time the tire can query the terrain for the current terrain surface profile usually to determine tire-terrain forces due to contact. This new feature allows for the inclusion of tire models that calculate the tire-terrain contact forces and pressure distributions based on the current state of the tire and terrain geometry. The size and shape of the terrain area queried at each time step is automatic and optimized based on the position, orientation and velocity of each traction element. Generally, the tire-terrain collision detection calculates forces at a higher fidelity than is needed by the terrain. Thus, the hundreds or thousands of contact points and forces are consolidated onto the terrain surface according to the terrain grid spacing being used in the terrain model. Once the tire loading forces are known for the terrain, they are used as an input to the soil compaction model used to describe the three-dimensional soil stress-strain resulting from the external vehicle load [42]. The stress and strain (both elastic and plastic) are computed for the volume of affected soil (along with numerous other state variables), the terrain height profile is then updated and the next time step ensues.

5.4 Parallel Computing

Although the methods embraced to represent the tire/soil interaction are simplified from their full form, yet when using a terrain grid spacing to accommodate the smallest feature on the tire results several computational bottlenecks. Herein they are addressed through parallel computing. Two avenues are explored to increase the computation speed of key sections of the simulation by utilizing both parallel CPU and GPU hardware. First, the calculation of the soil vertical stress field each time step is performed using sequential, parallel CPU and fully CPU/GPU parallel implementations. Large speed-ups are gained when using GPU computing in targeted sections of the simulation. Second, it was observed that the computational bottleneck shifted from the soil stress

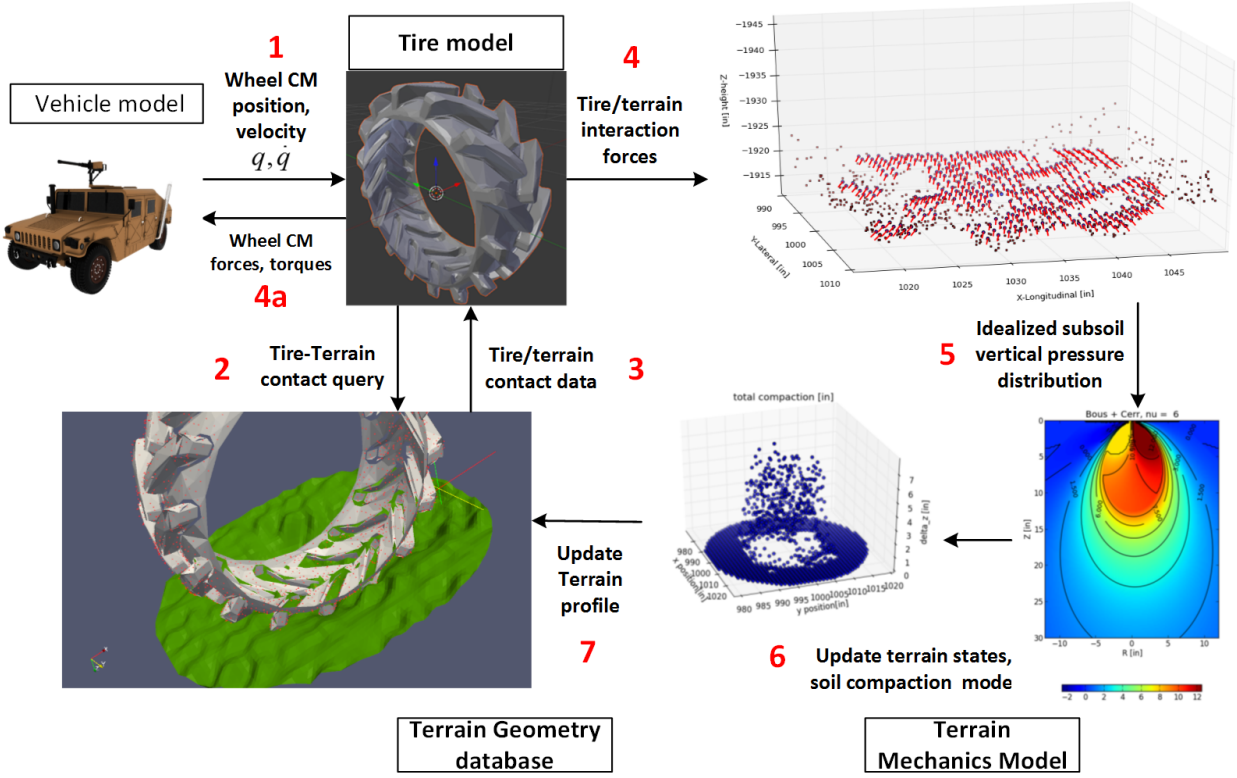

Figure 5.1: Steps in the simulation loop with a vehicle model

computation to the moving of data to and from the GPU global memory. An asynchronous parallel simulation loop is designed and implemented, which advances certain parts of the simulation and preemptively begins the transfer of memory to/from the GPU before the CUDA functions are invoked. It is seen that the latency inherent in large memory transfers to and from the CPU RAM to the GPU global memory can be curtailed using this sort of simulation task parallel approach.

5.4.1 Soil Stress Acceleration with Parallel CPU and GPU Computing

Representing the terrain volumetrically as shown in Figure 3.2 with element sizes small enough to accommodate the fidelity of the tire geometry results in a heavy computational burden. In general, the subsoil stress calculations need to be performed at each point in the soil volume being analyzed and for each contact force point on the soil due to the applied load. For example, a simulation with a 1x1 inch surface grid resolution and a tire with diameter/width of 56.5/20.5 inch, respectively, queries approximately 1950 terrain surface nodes, 59,000 subsoil volumes with anywhere from 100 to 1000 contact forces considered at the terrain surface. For higher terrain fidelity, a 0.4x0.4 inch surface resolution can be used, where results in 12,400 terrain surface node queries, 370,830 subsoil nodes with anywhere from 400-4,000 contact forces at the boundary. It is evident that the number of calculations scales $O(N^2)$ with an increase in terrain grid resolution.

Due to the nature of the equations above, it can be seen that the terrain geometry is spatially independent, that is, the terrain in one area does not depend upon that in another. The same is true for the individual tire elements. This means that calculations on different areas of the terrain and different elements of the tire can be done in parallel. It does not matter when or where the calculations for each area are performed, as long as they are all finished before moving on to the next set of calculations. Calculations performed on each subsoil volume are the same (albeit with different data), therefore the GPU is a good option to help accelerate these types of bottlenecks. GPU hardware and software both use the NVIDIA CUDA framework for calculations and the Thrust library for memory management. Operations that were task parallel, but not data parallel were accelerated using parallel CPU units, using the OpenMP standard. A schematic is shown in

Figure 5.2, where the parallel sections on both the CPU and GPU hardware are highlighted with a 'stack' of tiles representing the data/tasks being executed in parallel.

A comparison of the total run times for the CPU and GPU implementations for a five second simulation with a 50ms time step for grid resolutions ranging from 0.5x0.5 inch to as large as 3x3 inches is shown in Figure 5.3. The CPU simulations were performed on a machine with four 16 core AMD Opteron 6274 processors, allowing for 64 simultaneous threads. The GPU simulations were performed on a machine with an Nvidia Tesla C2070 and two six core Intel Xeon E5-2630 processors. It can clearly be seen that the GPU is faster than the CPU for finer resolution grids - those with a larger number of subsoil volumes.

The runtime required for a simulation is roughly proportional to the product of the number of subsoil volumes and tire contact points; i.e., the total number of stress calculations performed. It can clearly be seen that the GPU is approximately 8-9x faster than the OpenMP CPU approach, on average. Given that the previous figure shows the GPU to only be about 4x faster for the entire simulation at the given terrain grid resolution indicates that the GPU implementation has reached a point where the overhead of the rest of the simulation code is taking up more time than the subsoil stress calculations. It should be noted that timings reported here include the overhead of moving the subsoil node data to and from the GPU.

5.4.2 Asynchronous Simulation Timestep in Parallel

An execution flow chart for using the API functions calls sequentially is shown in Figure 5.2. It begins with the vehicle model, which is contained in Chrono as a multibody dynamics model. At each time step each tire individually makes a terrain database query. The database goes through all the motions for each tire query. The resulting force/torque on the wheel spindle is passed back to the vehicle model, where it is used as an external force acting on the vehicle wheel axles.

An advantage of using the developed model is that individual components involved in a terrain query are not necessarily dependent on one another. While it is true that calculating the soil stress and strain is dependent on the contact pressure model, which depends on the collision detection, which is in turn dependent on the geometry query of the terrain surface. The true point of coupling

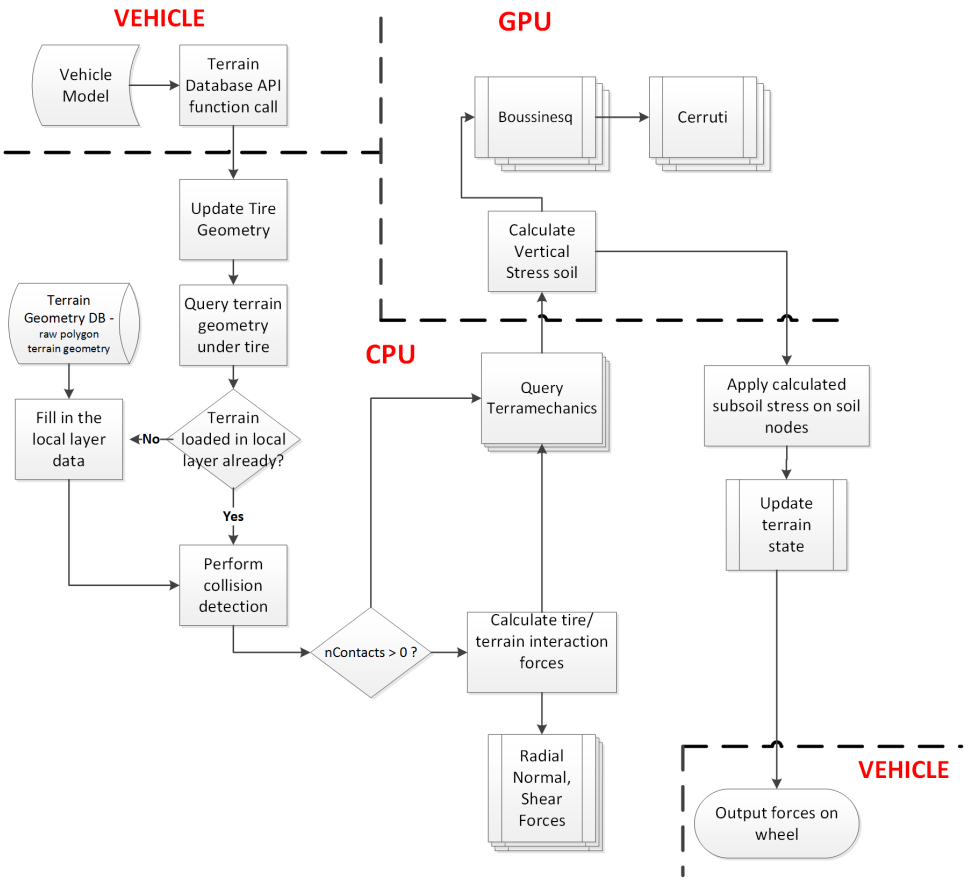

Figure 5.2: Execution flow for a single terrain query, run in parallel using CPU and GPU acceleration

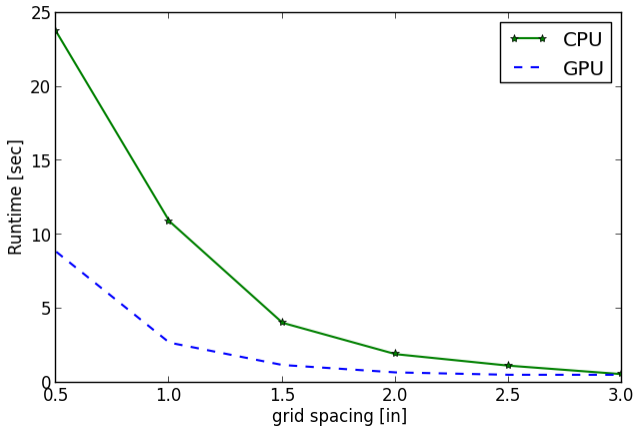

Figure 5.3: Total runtime for a 5 second single tire simulation, different terrain grid spacing

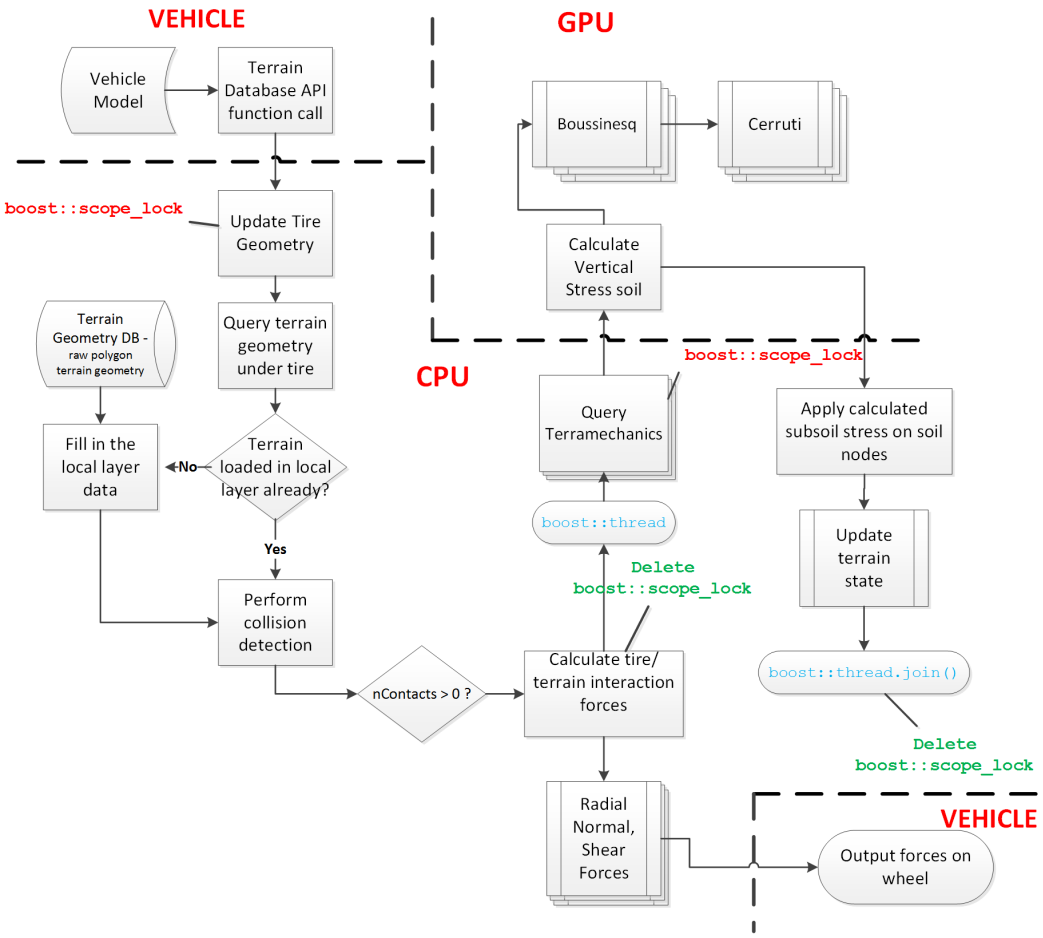

Figure 5.4: Execution flow, asynchronous execution of the computation offloaded to the GPU hardware

between the tire and terrain actually ends once the contact pressure is calculated. At that point, there is no reason to wait until the contact patch forces are passed to the terrain and the soil concludes the calculation of stress and strain. The tire only needs the contact patch forces to find the resultant force and torque on the wheel hub and passes the result back to the vehicle to allow the multibody model to continue its solution procedure immediately.

Using multi-threading, it becomes possible to minimize unnecessary waiting for the terrain database to complete the compute intensive task of finding the pressure and strain in the soil. In this case, a multi-threading package allows easy creation of scope locks, shown in Figure 5.4, disallowing future function calls by the vehicle simulator until the scope is left by completing the terramechanics function call. Other parts of the simulation continue working while the section is offloaded to the GPU hardware, results are computed and returned for the next simulation step.

Chapter 6

Validation

The soil and tire models developed are intended to be used with a dynamically driven tire in a multibody vehicle simulation framework, herein referred to as the ”dynamic tire” method. Under steady-state in-plane operating conditions comparisons can be drawn with the seminal performance prediction methods by Wong and Reece [13, 14], herein referred to as the ”WR” method. Results for normal and shear stress can be used to validate the general patterns of the contact patch model developed when tires are kinematically driven at specified steady-state slip rates. Overall wheel mobility prediction numerics including thrust, motion resistance and torque, formally defined in Equation 2.13 validate the results produced by the model under similar operating conditions..

Experimental results for a tire in soil reported by Wulfsohn and Upadhyaya are used and compared to simulation results in terms of the soil compaction and drawbar pull [42, 41]. Values reported by Wulfsohn with known soil classification data available from the USDA and other sources are used as inputs for a soft, tilled clayey loam and a similar soil that is firm. Soil model parameter identification of a Yolo clayey loam is performed for both tilled and firm soil conditions using methods from Section 3.3.

Analysis of experimental variance showed that tire size, inflation pressure, loading and soil condition were statistically significant when calculating net traction of a driven agricultural tire, which leads to the choice of low and high values for each variable in the experiments [41]. Tire sizes include 18.4R38 (narrow) and 24.5R32 (wide), with inflation pressures of 85 kPa (12.3 psi) and 125 kPa (18.1 psi), under loads of 1837 and 2755 kg. Net traction of of each of these combination of variables is experimentally found in [41] at a low and high slip rate, and can be compared with directly with the results produced by the dynamic tire.

Deformable tire model parameter identification is performed using tire size and load/deflection curves at the two inflation pressures as inputs. Relevant data is available from the tire manufacturer and also discussed in [42]; however, the max contact width as a function of deflection was not reported, so the data used in the example in Section 4.2.2 is scaled relative to the actual tire widths and range of deflections. A number of tests functions that describe the elastic tire pressure as a function of radial deflection, Equation 4.5, are examined to find the best functional type to accurately represent the extreme case where the soil is flat and rigid. Using a square root function leads to the lowest least squares error, Equation 4.19; however, a linear function is chosen for simplicity and also because the least squares error is not significantly larger.

An initially flat terrain is tested using the dynamic in-plane testing rig model described in Section 6.3.1. Simulation results at steady-state slips rates are compared to the 2-D WR method as well as the experimental results reported in [42, 41]. Drawbar pull is shown to agree well with both the WR and experimental results, with the dynamic tire predicting higher values based on a larger contact area. This is borne out in the normal and shear contact pressure distribution plots. The dynamic tire contact normal and shear stress along the centerline of the tire as a function of θ is shown in Figure 2.5. Significant differences in drawbar pull were seen in the tilled soil at low tire inflation pressures when compared with the experimental results in [41]. This is due to the presence of lugs on the actual tire, which leads to much larger experimental drawbar pull values at both low and high wheel slip rates.

Required torque is compared between the WR and dynamic tire model, showing good agreement in most cases. Differences stem from the larger contact area that is calculated with the developed contact models. Total rut volume shows relatively good agreement when compared to the experimental values in [41]; however, the field data had large variances in the measured total rut volume.

The dynamic tire is driven at constant slip rates to provide results for validation purposes; however, any valid multibody dynamic modeling element can be used to drive the wheel. First, an angular velocity is applied to the wheel at progressively higher values, followed by a constant applied wheel torque.

6.1 Firm and Loose Yolo Clay Loam Parameter Identification

Material composition of the Davis Yolo Loam used for validation is identified with a description of the tilled and firm soil reported by Wulfsohn and Upadhyaya [42, 41]. The bulk density of the sample at the surface is used to identify the soil model parameters using the method developed by Ayers and Bozdech [40] discussed in Section 3.3. To verify the accuracy of the model parameters identified, a test load is repeatedly applied to a single soil element, and the stress, bulk density, volumetric compaction energy and power are compared for the tilled and firm soil.

The tilled soil has an average initial bulk density and standard deviation of $\rho_{0,\mathrm{t}} = 1200.2 \pm 41.7 kg/m^3$ or 1.2002 g/cm^3. The firm soil was tested at two dates, and the mean of the average initial bulk density and standard deviation yields $\rho_{0,\mathrm{f}} = 1449.1 \pm 86.7 [kg/m^3]$ or 1.449 g/cm^3.

Material composition of the soil is not specified in terms of the Unified Soil Classification System (USCS) in the reference; however, the USDA has an extensive set soil description series available online, which includes a Yolo Series. Described as a clayey loam in the aforementioned experimental results, another set of soil mechanics experiments is detailed in [102], citing a CL type USCS soil classification, which is used for the loose clay loam. Classification of soils found in this area also indicate soils with less clay content and more silt content which are USCS MH or ML type soils. The firm Yolo loam is considered an MH type soil, as ML types have more sand than clay, which is not the case for these types of soils.

6.1.1 Loose Clay Loam

A representative tilled clayey loam soil is composed of 47.1% clay, 24.0% silt and 28.9% sand, with clay index of 3.21. Mean grain size is 0.76 mm, leading to a grain size index of 2.32. For the tilled soil, the compression index is $C = 0.5133$ [g/cm^3], with preconsolidation bulk density ρ_k = 1.20 [g/cm^3] and stress σ_k = 95.93 [kPa]. Moisture effects were ignored, i.e. $\rho_S = 0$. The rebound index $\mathrm{reb} = 0.02028$ [g/cm^3].

The behavior of the tilled soil model is shown by applying three identical stress cycles from 0 to 350 kPa with varying cycle time duration based on assumed vehicle speeds in the range of 0.5

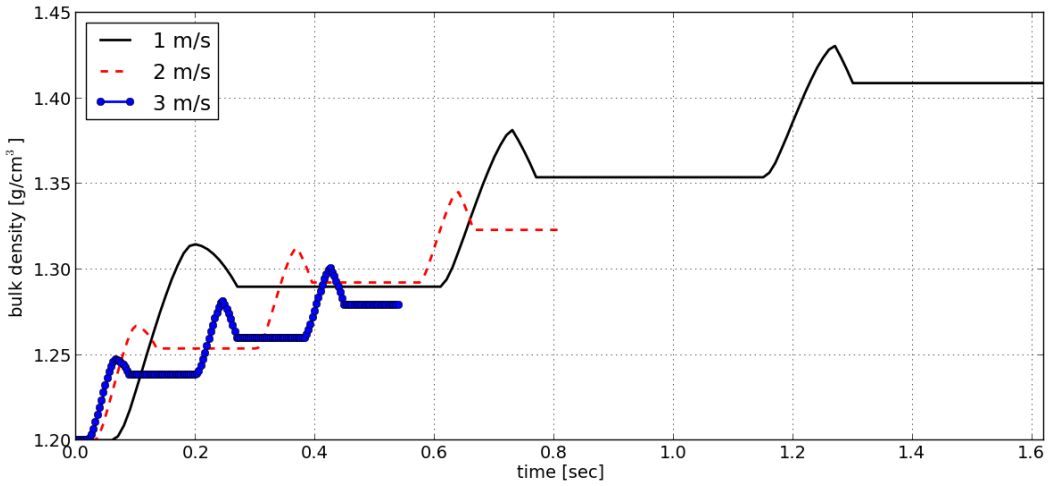

Figure 6.1: Loose Yolo loam bulk density, 1, 2 and 3.0 m/s vehicle speed

m/s to 5 m/s, similar to the approach in Section 3.4. The bulk density is shown for three vehicle speeds in Figure 6.1, where the largest increases in bulk density occur at lower vehicle speeds and on the first cycle.

Compaction power and energy per step is shown at the 1 m/s vehicle speed in Figure 6.2, along with the preconsolidation stress and bulk density after each load cycle.

The total change in bulk density, energy, peak power and final values of preconsolidation bulk density and stress for a range of vehicle speeds is shown in Figure 6.3.

Loose loam shows behavior similarities with the USCS CL type soil analyzed in Section 3.4. Soil shear strength parameters used in Algorithm 4.1.4 are constant and found experimentally in [41] for both soil types. For the firm loam, $c = 7.1$ [kPa], internal friction angle $\phi = 21.17$ [deg] and shear modulus $K(mean \pm SD) = (1.06 \pm 0.29)$ [cm]. This is compared to the values calculated by the model for the loose soil, $c_{ref} = 26.91$ [kPa], $\phi_{ref} = 16.60$ [deg], $K_{ref} = 1.25$ [cm], which is not used when experimental values from shear tests are available. Also, appropriate pressure/sinkage parameters must be used, although they play a less important role in the overall mobility model and only define the maximum soil bearing capacity in Algorithm 4.1.3. For the loose soil, a clayey loam with Bekker parameters $k_c = 41.6$ [kN/m^{n+1}], $k_\phi = 2471$ [kN/m^{n+2}],

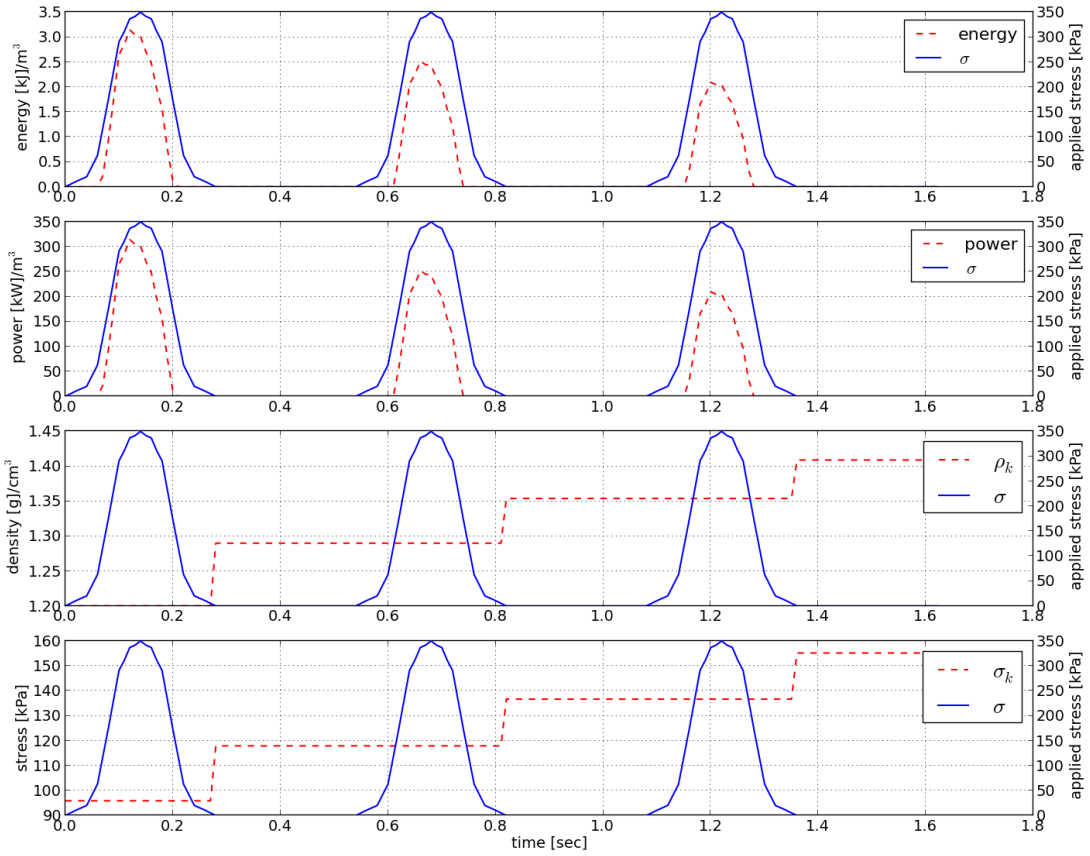

Figure 6.2: Loose Yolo loam (top to bottom): compaction energy per step, power, preconsolidation density and stress at 1 m/s vehicle speed

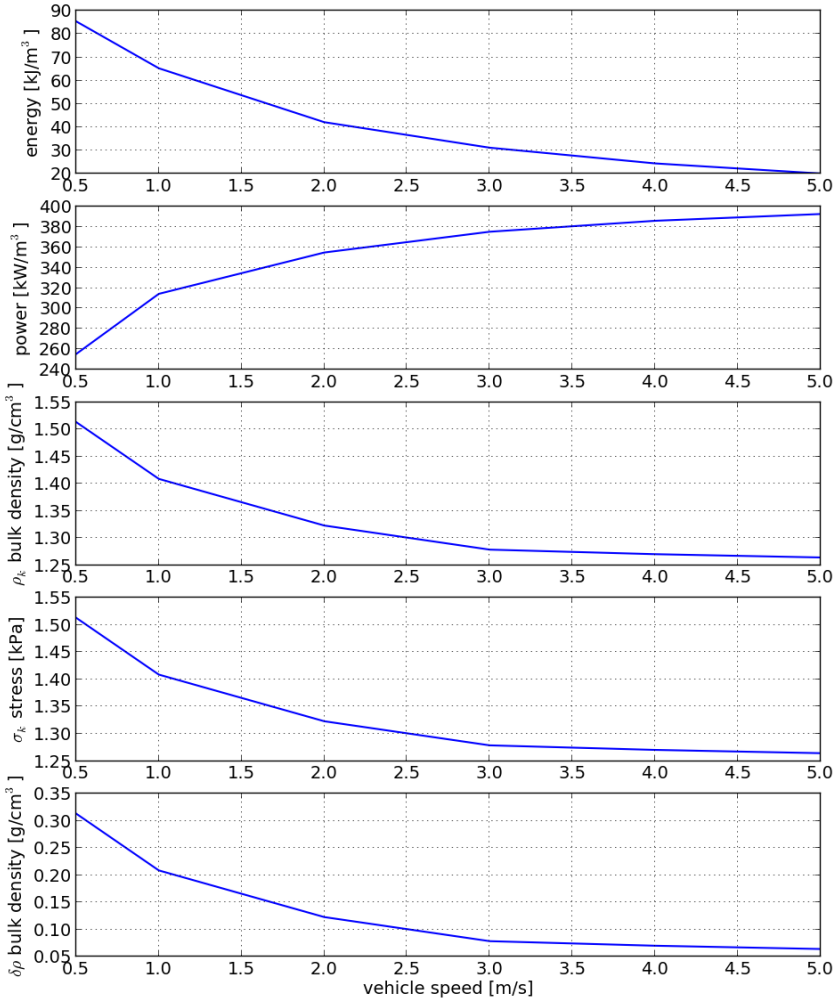

Figure 6.3: Loose Yolo loam (top to bottom): Compaction energy, peak power, final preconsolidation density and stress and net change in bulk density

$n = 0.73$ is used, with corresponding Reece parameters $k'_c = 121.1$ [kPa], $k'_\phi = -4.2$ [kPa/m] [18].

6.1.2 Firm Clay Loam

A USCS MH soil type is representative of firm loam soil and found in the same geographical area as the loose tilled soil. It is composed of 34.8% clay, 50.0% silt and 15.2% sand, with clay index 2.38, mean grain size of 0.4125 mm, with a grain size index of 4.27. The firm soil has an initial density $\rho = 1.504$ [g/cm^3], the compression index is $C = 0.4921$ [g/cm^3], with preconsolidation bulk density ρ_k = 1.20 [g/cm^3] at the reference stress stress σ_k = 98.1 [kPa], moisture effects were ignored, e.g. $\rho_S = 0$ and a rebound index $\mathrm{reb} = 0.02808$ [g/cm^3].

As before, the behavior of the soil model is shown by applying three identical stress cycles from 0 to 350 kPa with varying cycle time duration based on assumed vehicle speeds in the range of 0.5 m/s to 5 m/s. The bulk density is shown for three vehicle speeds in Figure 6.4, for both types of soil. As before, the largest increases in dry bulk density occur at lower vehicle speeds and on the first cycle.

Total increase in dry bulk density shows the difference between the two soils, where the tilled soil saw a total increase of 0.2088 [g/cm^3] compared to the firm soil increase of 0.04739 [g/cm^3], a difference by a factor of 4.4. These results indicate that the contact patch calculated on the firm soil will more closely resemble that of a tire on flat ground, where the tilled soil will exhibit much more sinkage leading to a contact area with more pronounced curvature.

Compaction power and energy is shown at the 1 m/s vehicle speed in Figure 6.2, with the preconsolidation stress and bulk density after each load cycle for both the tilled and firm soils. Power and energy per step curves have similar shapes for both soils, but as the firm soil deforms much less the peak power and net compaction energy are both about 2.5 times less than that of the tilled soil, seen in the top two rows of Figure 6.5. It is reasonable to expect the overall compaction energy will lead to a lower performance prediction for any tire operating in the tilled loam.

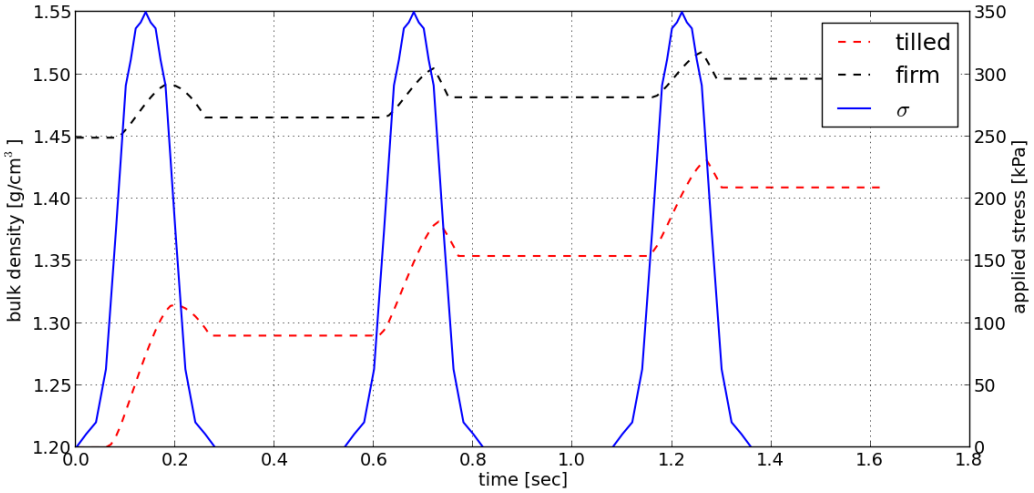

Figure 6.4: Tilled and firm loam dry bulk density, 1 m/s vehicle speed

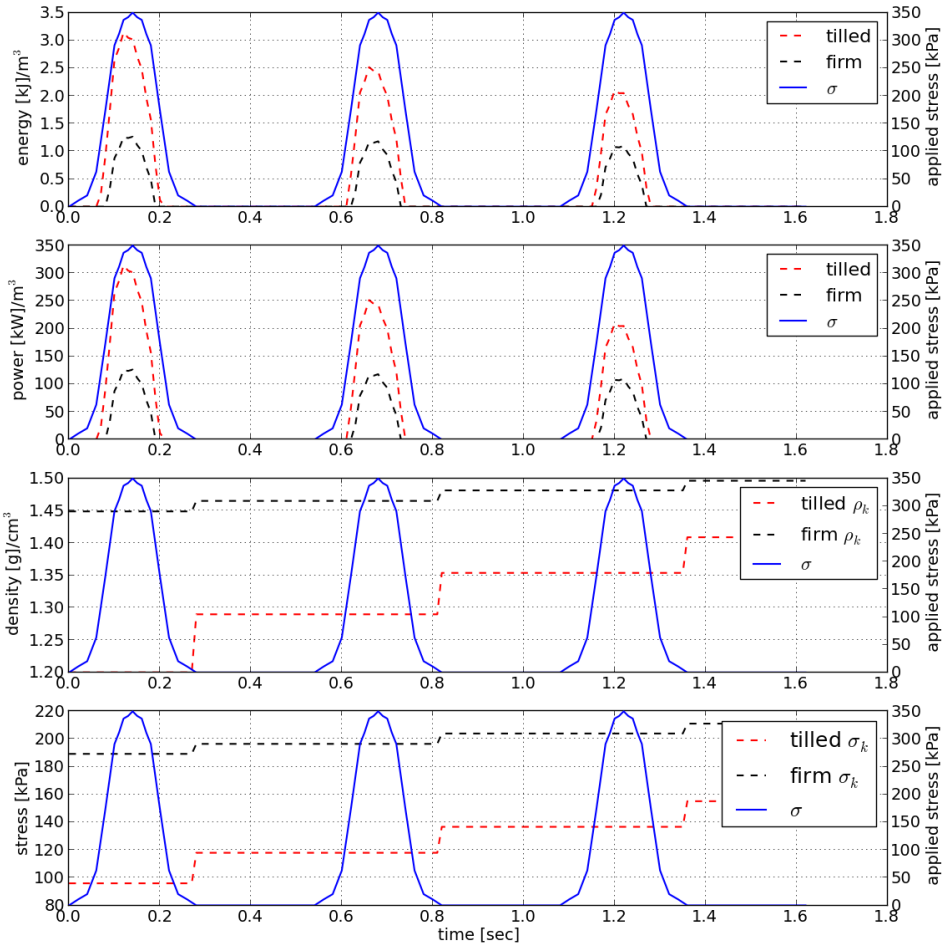

Figure 6.5: Tilled and firm Yolo loam (top to bottom): compaction energy, power and preconsolidation density and stress

The total change in bulk density, energy, peak power and final values of preconsolidation bulk density and stress for a range of vehicle speeds is shown in Figure 6.6. Each entry in Table 3.2 is plotted as a function of the vehicle speed, with the results shown in Figure 6.6.

For the firm loam, the average of the two experimentally derived constants in [41] is used for shear cohesive strength, $c = 35.72$ kPa, internal friction angle $\phi = 23.13$ deg and shear modulus $K(mean \pm SD) = (1.06 \pm 0.52)$ cm. This is compared to the values calculated by the model for the firm soil, $c_{ref} = 0$ kPa, $\phi_{ref} = 21.14$ deg, $K_{ref} = 1.61$ cm A Loam is used to represent the bearing capacity of the firm soil, with Bekker parameters $k_c = 66.0$ kN/m^{n+1}, $k_\phi = 4486$ kN/m^{n+2}, $n = 1.02$ is used, with corresponding Reece parameters $k'_c = 55.3$ kPa, $k'_\phi = 4292$ kPa/m [18].

6.2 Tire Contact Model Parameter Identification

Tire model parameter identification is carried out in two steps. First, the radius of the curve that describes the cross section of the torus, r_{Beta} is found for each tire size using Equation 4.20. Next, the elastic spring constant is found for each inflation pressure using Equation 4.19.

Optimization for equations that call for a minimization is performed using MINPACK's hybrd algorithm [103]; only the function is specified and the integration is performed numerically to allow any type of test function for Equation 4.5 to be used. The absolute solver tolerance is scaled relative to the magnitude of the input wheel load data. Depending on the configuration of the contact area on a flat plate, see Figure 4.11, the overall calculated vertical force resulting from the normal stress in the contact patch requires either one or two sets of integrals. Each is solved numerically with a Gauss Quadrature method, where the absolute error tolerance is also scaled as a function of the wheel load data.

6.2.1 Narrow Tire, Low Inflation Pressure

Maximum contact width/wheel deflection data, shown in 6.7, was adapted from a Wrangler truck tire by adjusting the max width and range of deflections to match the contact width and deflections experimentally obtained by [42] for each tire in tilled soil. The narrow 18.4R38 tire at an inflation pressure of 85 kPa had a reported max width of 57.5 cm on tilled loam under a dynamic

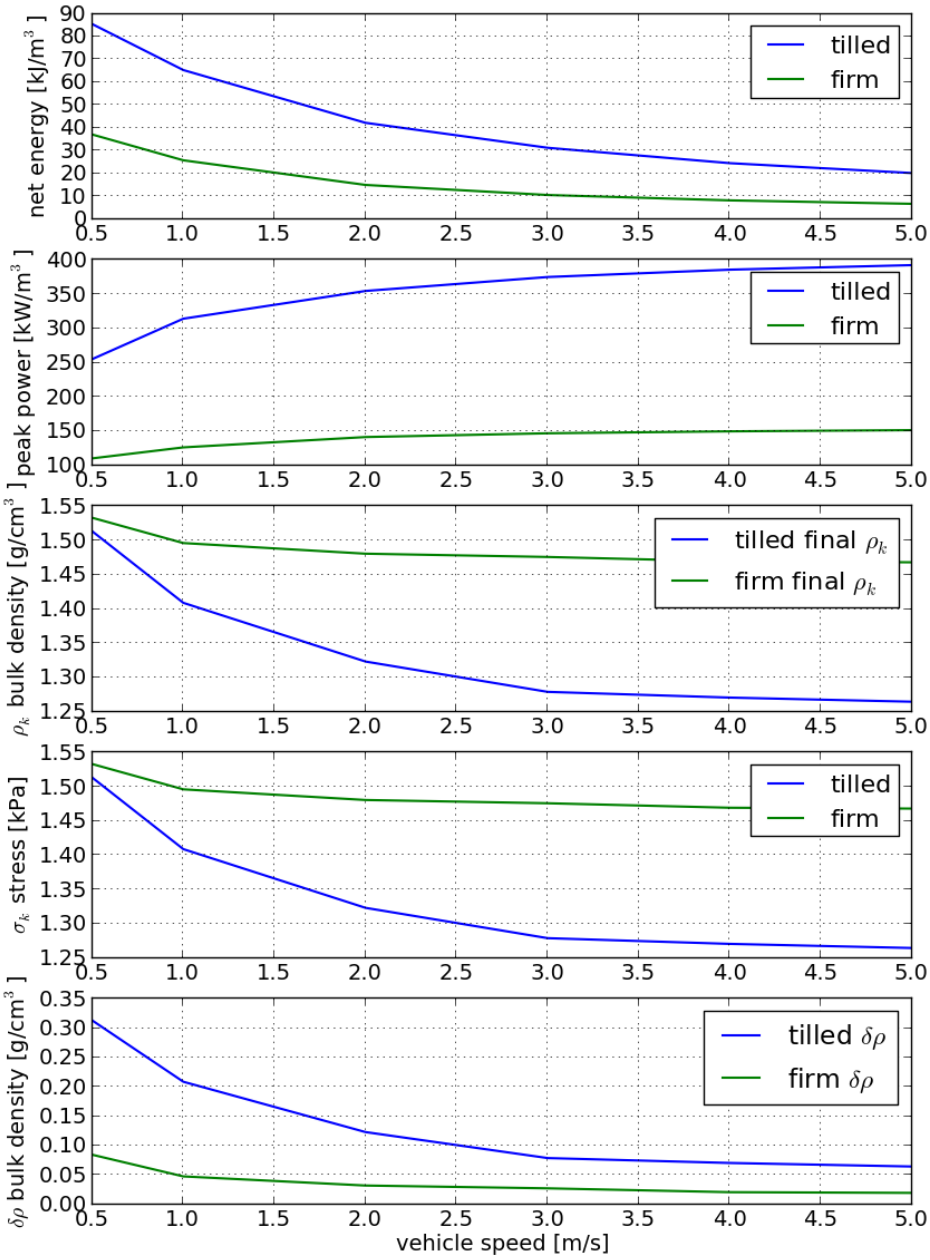

Figure 6.6: Tilled and firm Yolo loam (top to bottom): compaction energy, peak power, final preconsolidation density and stress, and total change in bulk density

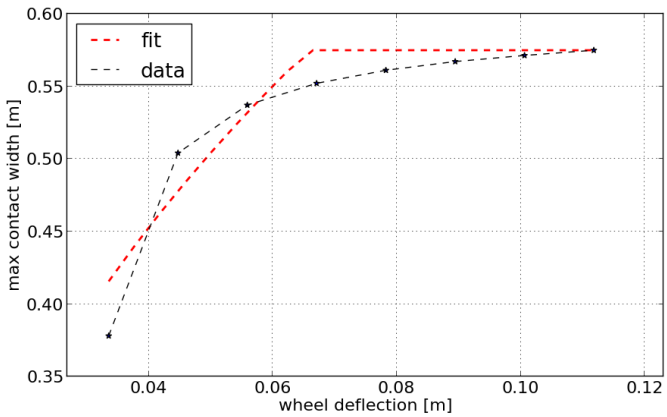

Figure 6.7: Max contact width during wheel load/deflection test, 18.4R38 tire 85 kPa inflation pressure

load of 27 kN, leading to a cross section radius, $r_\beta = 66.10$ cm, found using the Least Squares method described in Equation 4.20, and using a diameter of 1.82 meters for the large agricultural tires.

Both low and high inflation pressures are used to create two sets of tire model parameters for the 18.4R38 tire. Wheel load/deflection tests at two inflation pressures, 85 kPa and 125 kPa, are shown in Figure 6.8.

The optimal elastic spring function constant(s) in Equation 4.5 are found at the lower inflation pressure of 85 kPa, for a range of functional forms for pressure as a function of radial displacement. Using a number of trial spring function forms, including: linear, square root, 2nd and 3rd order polynomials, and combinations of these types of functions, the best fitting parameters are found and used to calculate the model's vertical force according to Equation 4.26, then plotted against the measured wheel force at each wheel deflection, shown in Figure 6.9. It is clear from the plot that the best function for the spring is $\sigma_n = a\sqrt{x}$.

Although the possible range of tire belt radial displacements in reality is known, the model may experience much larger local displacements due to some unforseen simulation circumstances. The possible optimal parameters in Equation 4.5 are limited to being positive reals for this reason. Functional forms and their optimal parameters according to the least squares model fit are shown

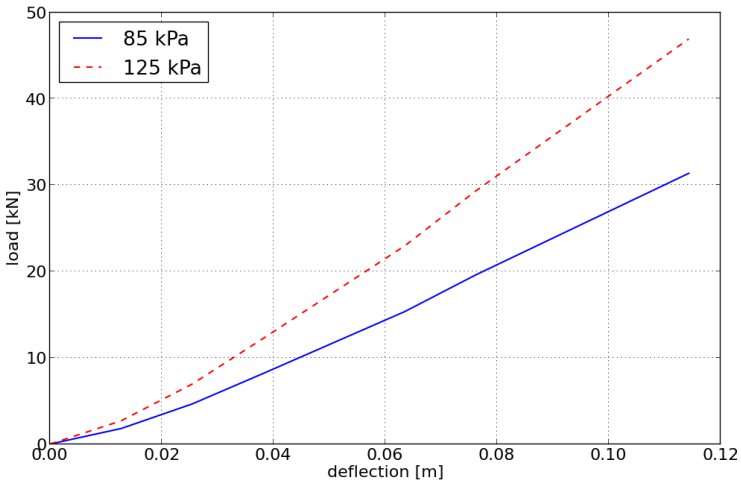

Figure 6.8: Wheel load/deflection data, 18.4 R38 tire 85 kPa inflation pressure

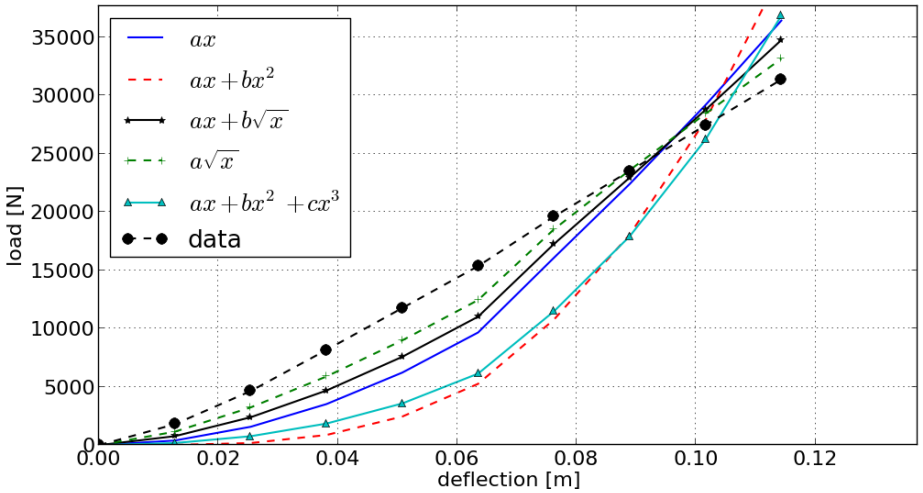

Figure 6.9: Wheel load/deflection data compared to fitted model with optimal parameters, 18.4 R38 tire, 85 kPa inflation pressure

Table 6.1: Optimal parameters for trial spring functions, 18.4R38 tire 85 kPa inflation pressure

Function type	$\sigma_n = f(x)$ form, [Pa]	Optimal $(p_0, p_1, ...) * 10^5$	Error $*10^3$
Linear	$p_0 x$	13.14	31.77
Quadratic	$p_0 x + p_1 x^2$	(7.433, 86.30)	41.81
Linear/Sqrt	$p_0 x + p_1 \sqrt{x}$	(2.289, 2.889)	16.69
Sqrt	$p_0 \sqrt{x}$	3.469	13.88
3rd order Polynomial	$p_0 x + p_1 x^2 + p_2 x^3$	(6.991, 74.45, 72.90)	43.02

in Table 6.1, along with the cumulative error calculated when fitting the model to the data using the optimal parameters.

Using the optimal parameters for the square-root function, $\sigma_n = p_0 \sqrt{x}$, and the cross sectional dimension r_β, the normal stress at 0.1 meter vertical wheel displacement on a flat rigid surface is plotted, which corresponds to a wheel vertical load of 26,950 N. The cylindrical tire shape is plotted as a reference to the torus normal contact stress distribution, as it is the method to describe the contact stress distribution in the Wong-Reece method, detailed in Section 2.3, which is used as a baseline for steady-state dynamics simulations.

The difference in representing the tire geometry with a 2-D approximation is seen in the normal stress distributions for a cylinder and torus shaped tire using shown in Figure 6.10. Curvature in the $x - y$ cross section dimension from the torus shape lowers the tire radial displacement when in contact with a flat surface as the distance from the tire centerline is increased. The torus tire has a similarly large pressure spike near the edges of the contact patch, although less severe than the cylinder case. The stress profile in the tire $x - y$ plane is shown in Figure 6.11.

6.2.2 Narrow Tire, High Inflation Pressure

The narrow 18.4R38 tire had a reported max width of 53.5 cm on tilled loam under a dynamic load of 27 kN at the higher inflation pressure of 125 kPa. A higher inflation pressure prevents tire deflection under similar loads, which would reduce the flattening effect which is seen in the lower maximum contact width with the higher tire inflation pressure. The tire $x - y$ plane cross section

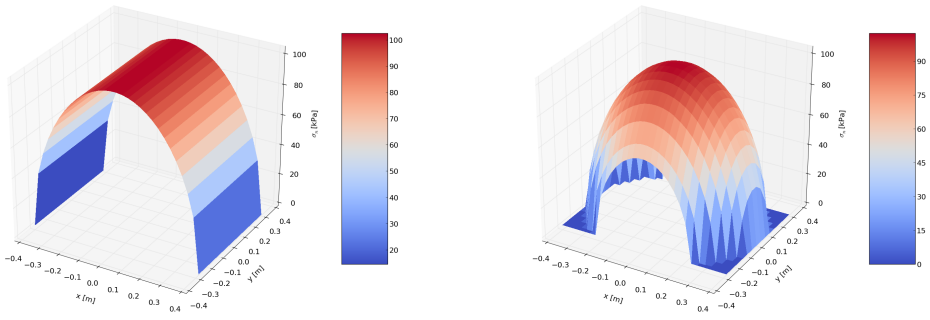

Figure 6.10: Tire normal stress at 0.1 m wheel deflection, 18.4R38 tire 85 kPa, cylinder (left) and torus (right)

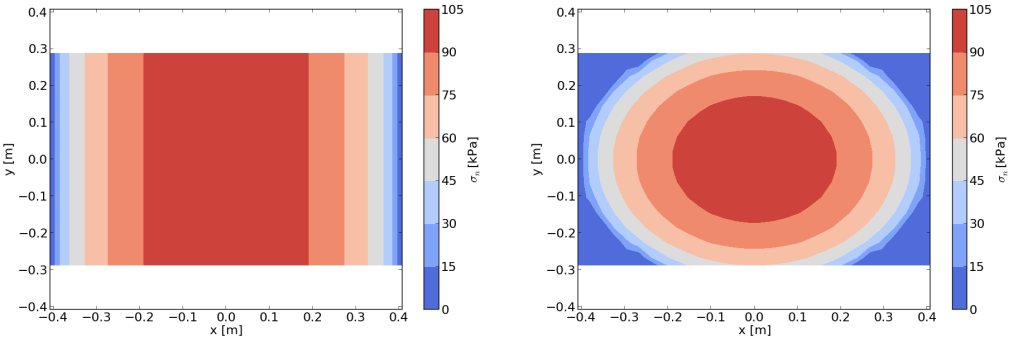

Figure 6.11: Tire normal stress at 0.1 m wheel deflection, 18.4R38 tire 85 kPa, top view, cylinder (left) and torus (right)

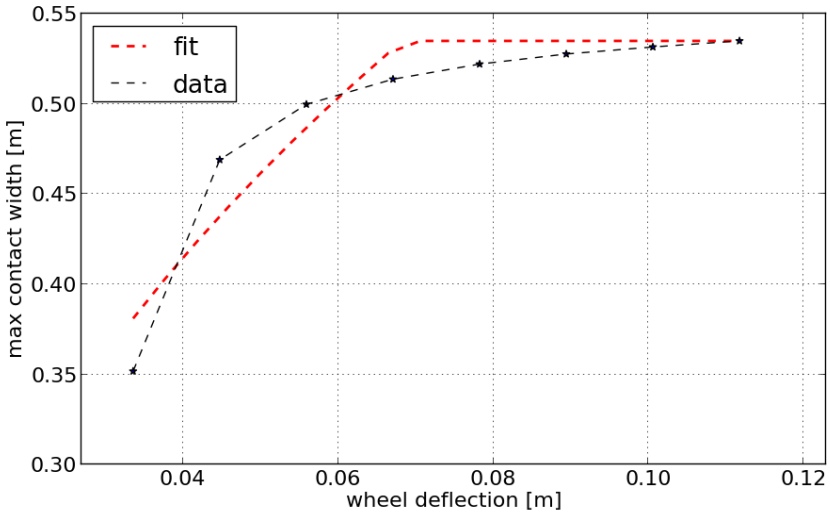

Figure 6.12: Max contact width during wheel load/deflection test, 18.4R38 tire, 125 kpa inflation pressure

radius, $r_\beta = 55.82$cm, is found using the Least Squares method described in 4.20 with the fitted model and max contact width shown in Figure 6.12. The contact width plots are similar at both inflation pressures.

The optimal elastic spring function constant(s) in Equation 4.5 are found at the higher inflation pressure of 125 kPa, for a range of functional forms shown in Figure 6.13. It is clear from the plot that the best function for the spring is again $\sigma_n = a\sqrt{x}$.

Functional forms and their optimal parameters according to the least squares model fit for the 125 kPa inflation pressure are shown in Table 6.2, along with the cumulative error calculated when fitting the model to the data using the optimal parameters. Here the third order polynomial is allowed to have negative coefficients, as it is not selected to be used.

Using the optimal parameters for the square-root function, $\sigma_n = p_0\sqrt{x}$, and the cross sectional dimension r_β, the normal stress at 0.1 meter vertical wheel displacement is plotted for both the cylinder and torus shaped tires, shown in 3-D in Figure 6.14 and a top view in 2-D in Figure 6.15.

A clear difference between the low and high inflation pressures are the higher spring coefficients. In the case of the chosen square-root spring function, low and high inflation pressures

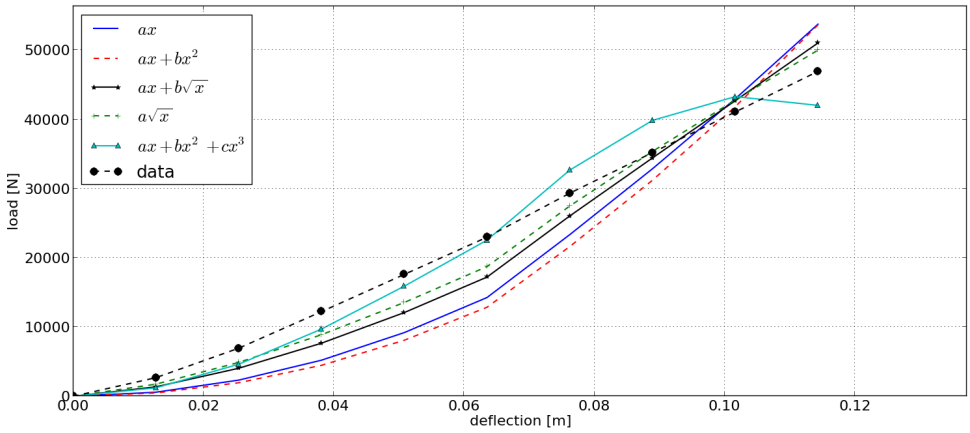

Figure 6.13: Wheel load/deflection data compared to fitted model with optimal parameters, 18.4 R38 tire 125 kPa

Table 6.2: Optimal parameters for trial spring functions, 18.4R38 tire 125 kPa

Function type	$\sigma_n = f(x)$ form, [Pa]	Optimal $(p_0, p_1, ...) * 10^5$	LS Error $*10^3$
Linear	$p_0 x$	21.21	47.90
Quadratic	$p_0 x + p_1 x^2$	(16.83, 53.11)	53.78
Linear/Sqrt	$p_0 x + p_1 \sqrt{x}$	(6.859, 3.597)	29.85
Sqrt	$p_0 \sqrt{x}$	5.345	21.47
3rd order Polynomial	$p_0 x + p_1 x^2 + p_2 x^3$	(46.19, -211.0, -1709)	23.55

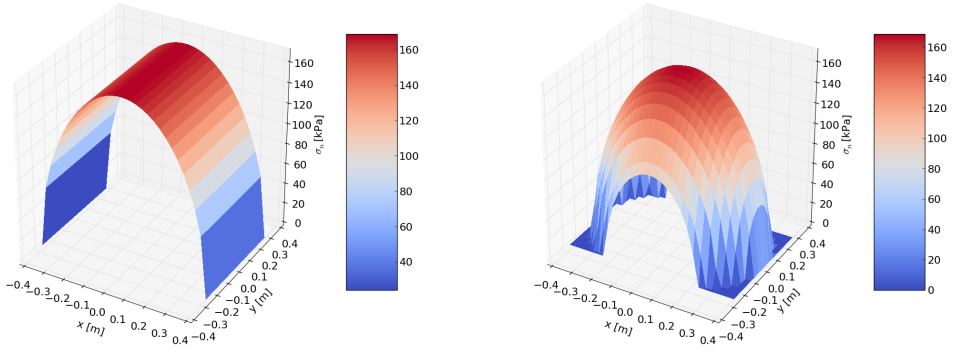

Figure 6.14: Tire normal stress at 0.1 m wheel deflection, 18.4R38 tire 125 kPa, cylinder (left) and torus (right)

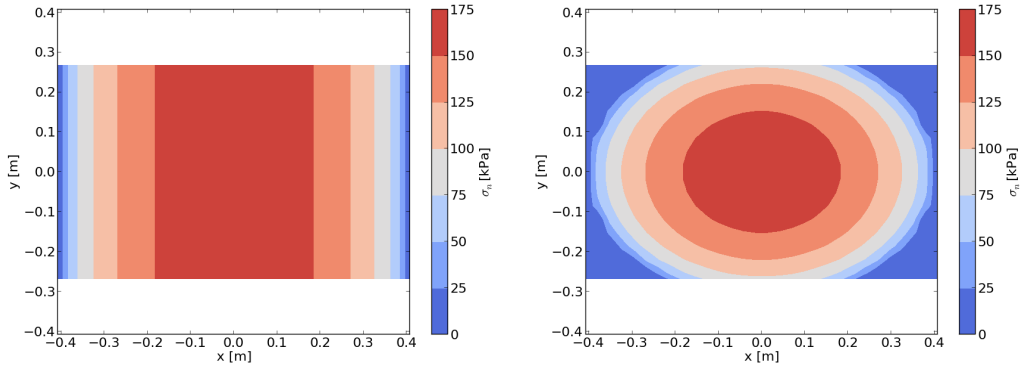

Figure 6.15: Tire normal stress at 0.1 m wheel deflection, 18.4R38 tire 125 kPa, top view, cylinder (left) and torus (right)

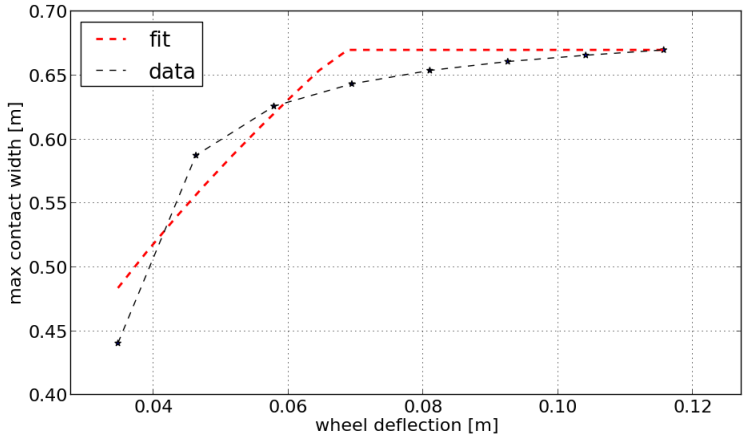

Figure 6.16: Max contact width during wheel load/deflection test, 24.5R32 tire, 85 kPa inflation pressure

yielded coefficients of 3.469 and 5.345 10^5, respectively. The normal contact pressures of the cylinder and torus shaped tires on flat ground are very similar in shape, the most notable difference being in the maximum normal pressure achieved at the higher inflation pressure.

6.2.3 Wide Tire, Low Inflation Pressure

A wider 24.5R32 tire has a reported max width of 67 cm, leading to a cross section radius $r_\beta = 86.06$ cm which is larger when than the narrower 18.4R38 tire, correctly predicting a greater increase in contact width with wheel deflection.

The fitted model and max contact width is illustrated in Figure 6.16, showing good agreement with the experimentally measured maximum contact width.

The optimal elastic spring function constant(s) in Equation 4.5 are found for a range of functional forms shown in Figure 6.17. It is clear from the plot that the best function for the spring is again $\sigma_n = a\sqrt{x}$.

Functional forms and their optimal parameters according to the least squares model fit are shown in Table 6.3, along with the cumulative error calculated when fitting the model to the data using the optimal parameters. Here the third order polynomial is allowed to have negative coefficients, as it is not selected to be used.

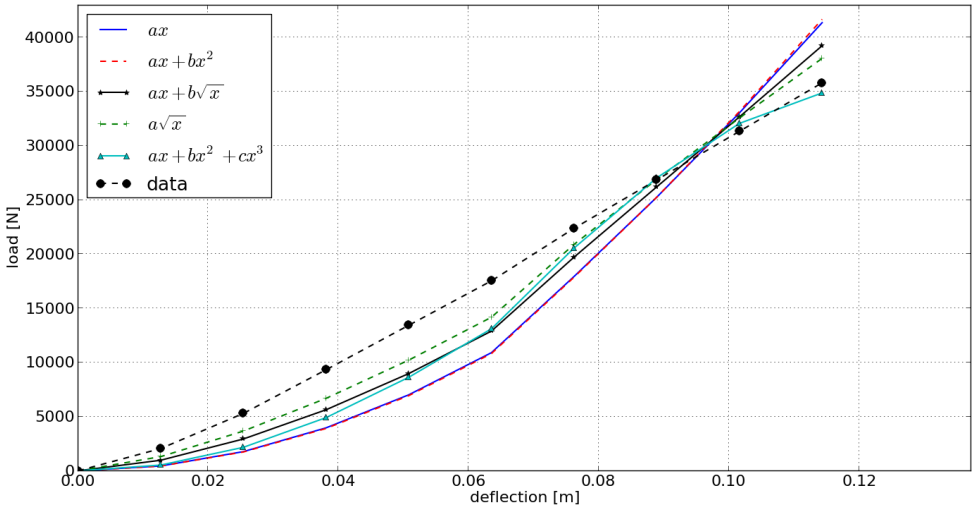

Figure 6.17: Wheel load/deflection data compared to fitted model with optimal parameters, 24.5 R32 tire 85 kPa

Table 6.3: Optimal parameters for trial spring functions, 24.5R32 tire 85 kPa

Function type	$\sigma_n = f(x)$ form, [Pa]	Optimal $p_0, p_1, ...) * 10^5$	LS Error $*10^3$
Linear	$p_0 x$	12.69	36.84
Quadratic	$p_0 x + p_1 x^2$	(12.37, 5.075)	37.61
Linear/Sqrt	$p_0 x + p_1 \sqrt{x}$	(4.830, 1.947)	24.28
Sqrt	$p_0 \sqrt{x}$	3.155	16.59
3rd order Polynomial	$p_0 x + p_1 x^2 + p_2 x^3$	(14.39, 97.73, -1619)	21.96

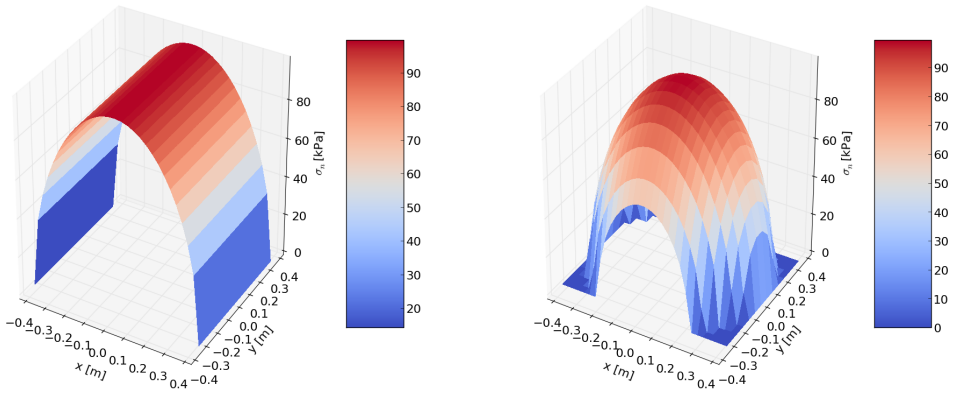

Figure 6.18: Tire normal stress at 0.1 m wheel deflection, 24.5R32 tire 85 kPa, cylinder (left) and torus (right)

Using the optimal parameters for the square-root function, $\sigma_n = p_0\sqrt{x}$, and the cross sectional dimension r_β, the normal stress at 0.1 meter vertical wheel displacement is plotted for both the cylinder and torus shaped tires, shown in 3-D in Figure 6.18 and a top view in 2-D in Figure 6.19.

The larger maximum contact width and larger value of r_β leads to a flatter contact stress distribution in the narrow 24.5R32 tire, when comparing Figure 6.18 to the narrow 18.4R38 tire at the same inflation pressure in Figure 6.10. The wider tire also exhibits a lower average normal stress overall at deflections of 10 and 20 cm, as shown in Figures 6.20 and 6.21, when comparing the stress along the centerline of the tire.

6.3 Driven Wheel Validation Results

Models used for validation include narrow and wide tires, 18.4R38 and 24.5R32, at two inflation pressures, 85 kPa and 125 kPa, on loose and firm clayey loam soil conditions in a dynamic soil bin testing environment contained in the Chrono dynamics software. A driven tire exercises the software containing the contact and soil models developed. At constant slip rates direct comparisons are made with the classical 2-D plastic equilibrium steady-state methods by Wong and Reece [13, 14] (herein referred to as the ”WR” method) in terms of the overall wheel performance, e.g.

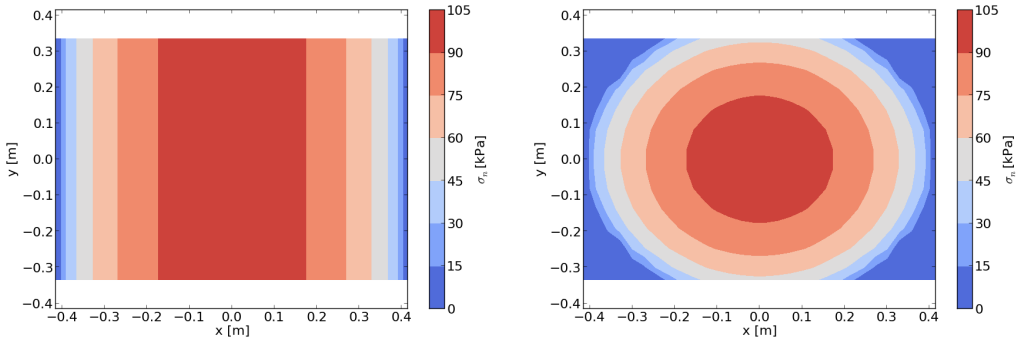

Figure 6.19: Tire normal stress at 0.1 m wheel deflection, 24.5R32 tire 85 kPa, top view, cylinder (left) and torus (right)

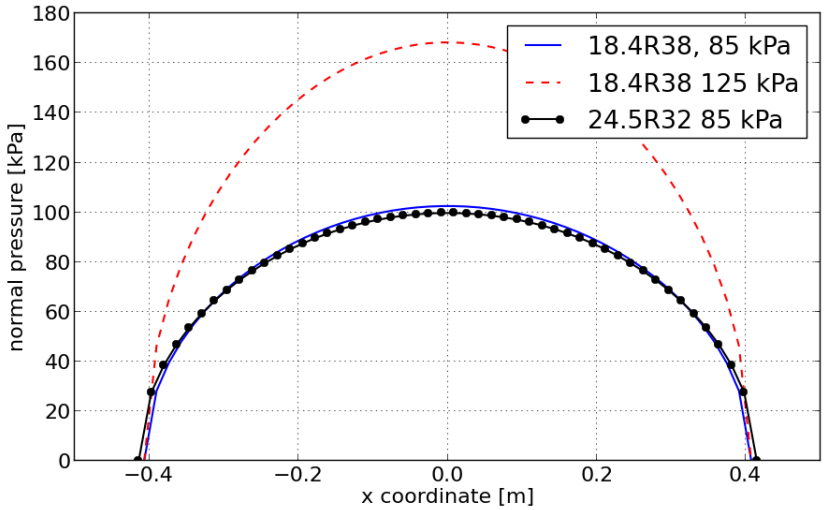

Figure 6.20: Tire normal stress at 0.1 m wheel deflection along tire length, torus tires

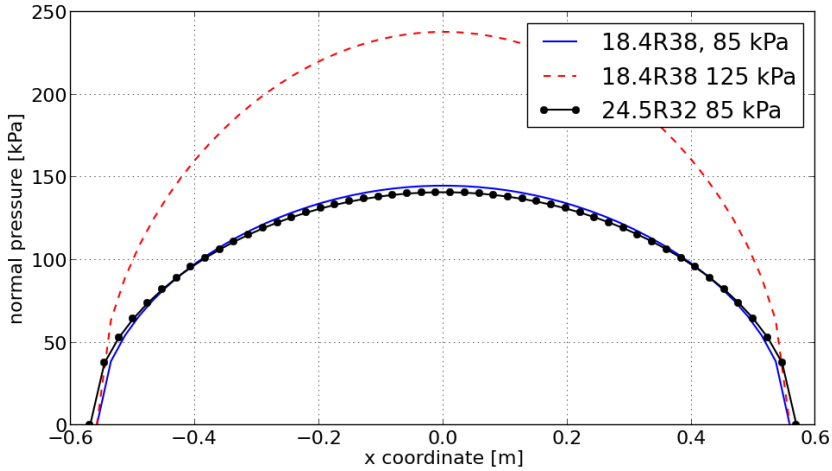

Figure 6.21: Tire normal stress at 0.2 m wheel deflection along tire length, torus tires

drawbar pull, motion resistance, driving torque and wheel sinkage. Wheel performance was predicted and measured under these conditions for a dynamic 3-D contact patch by Wulfsohn [42, 41], allowing out-of-plane stress distribution effects to be considered in the overall wheel performance at steady slip conditions. Further comparisons are made by comparing the contact area and stress distributions at low and high slip rates with both 2-D and 3-D experimental references in [42].

Wheel slip rate, Equation 4.8, is used as an input to the reference models; in the dynamic model this could be more than one combination of forward velocity and wheel angular velocity. For all simulations, the wheel begins at rest and is allowed to settle in the soil, and both the angular velocity and linear velocity are ramped to a value of 1. Progressively higher angular velocities are applied as a motion to the wheel until the desired slip rate is reached, as defined by Equation 4.8.

Low to high slip rates are considered in the range of 5% to 30%, respectively, and steady state slips are established at a few points for each combination of tire size, inflation pressure, soil type and dynamic load.

6.3.1 Dynamic Tire Soil Bin Model

A soil bin testing rig is meant to emulate the in-plane dynamic response of a quarter car by including a sprung mass to the tire and wheel. A multibody model of this device was built in Chrono, which consists of three rigid bodies, 1) the tire body, 2) wheel spindle, and 3) sprung mass, two force elements and three kinematic constraints, shown in Figure 6.22. The spindle is constrained to the tire with a revolute joint at the tire center of mass, with the axis of rotation aligned to be orthogonal to the tire's plane of motion. A spring and damper force is present between the spindle and the sprung mass whose rates are based on the shocks of a large truck. The sprung weight is constrained to the spindle with a translational joint along the global vertical direction. The sprung weight is constrained to the ground to only allow in-plane motion of the three bodies. This is accomplished with an Oldham style joint, which allows the weight to have two translational degrees of freedom (up/down, forward/backward) only; all three rotation parameters are not allowed to change on the sprung mass.

The mass of the spindle and wheel rigid bodies are each 5% of the total system mass, and the sprung mass contains the other 90%. Inertia for the wheel body is based on assuming the mass is equally distributed and the shape is a cylinder with dimensions based on the width and height of the rim associated with each tire.

A tire is driven by applying the wheel angular velocity and forward velocity as a motion between the spindle and wheel rigid bodies. Each wheel angular velocity is applied for 2 seconds of simulation time to allow steady-state motion to develop in the dynamic model. Thrust, motion resistance and drawbar pull are calculated based on output from the contact normal and shear stresses calculated in the three dimensional contact patch, shown in Figure 6.23.

As the applied angular velocity is increased from zero to 2 rad/sec, the forward velocity is held constant and the tire is only allowed a dynamic degree of freedom in the vertical direction.

6.3.2 Driven Wheel Performance

Validation of the model begins with the simplest case of steady in-plane wheel motion for the overall wheel performance prediction values. Wheel thrust is defined as the cumulative force acting in the forward direction as the result of the shear generated in the contact patch. Motion resistance is defined as the cumulative force acting in the opposite direction of travel as the result of the normal forces generated in the contact patch. Drawbar pull is the difference between the two values, and dictates the towing capacity of the vehicle at a given slip rate.

Using the Wong-Reece method, Equation 2.13 describes the two-dimensional steady-state interpretation of wheel performance. According to Wong and Reece, a rigid, circular wheel operating at steady-state velocity and slip conditions can shave these values solved over a range values of slip values as described in Section 2.3. At each steady-state slip value, the contact angle θ_1 is iteratively solved for assuming the exit angle θ_2 is zero (e.g., soil rebound is not considered). Thus each wheel size will have four sets of performance predictions for the range of simulations considered, two for each soil type and two for each dynamic load. Note that inflation pressure is not considered in this analysis as the wheel is considered rigid with this method.

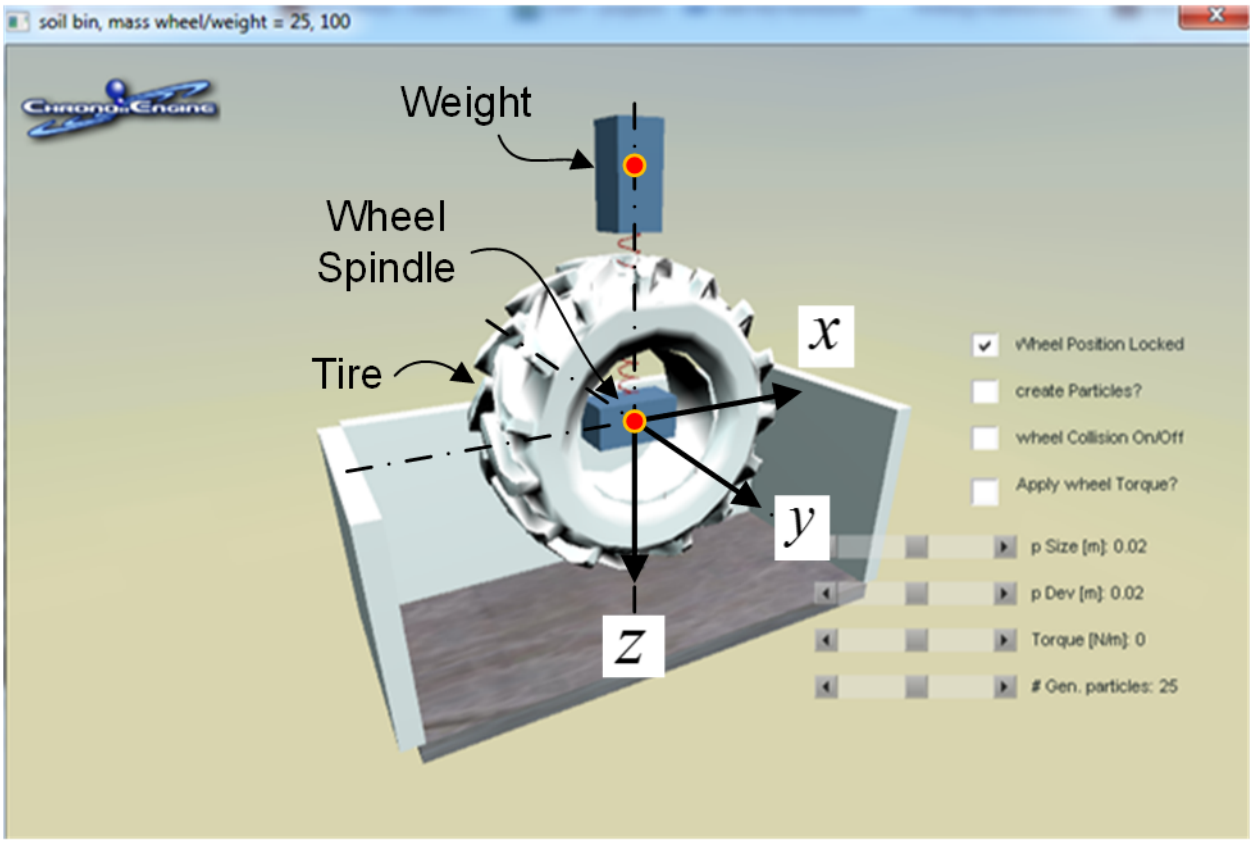

Figure 6.22: Multibody dynamic tire soil bin model used in validation experiments

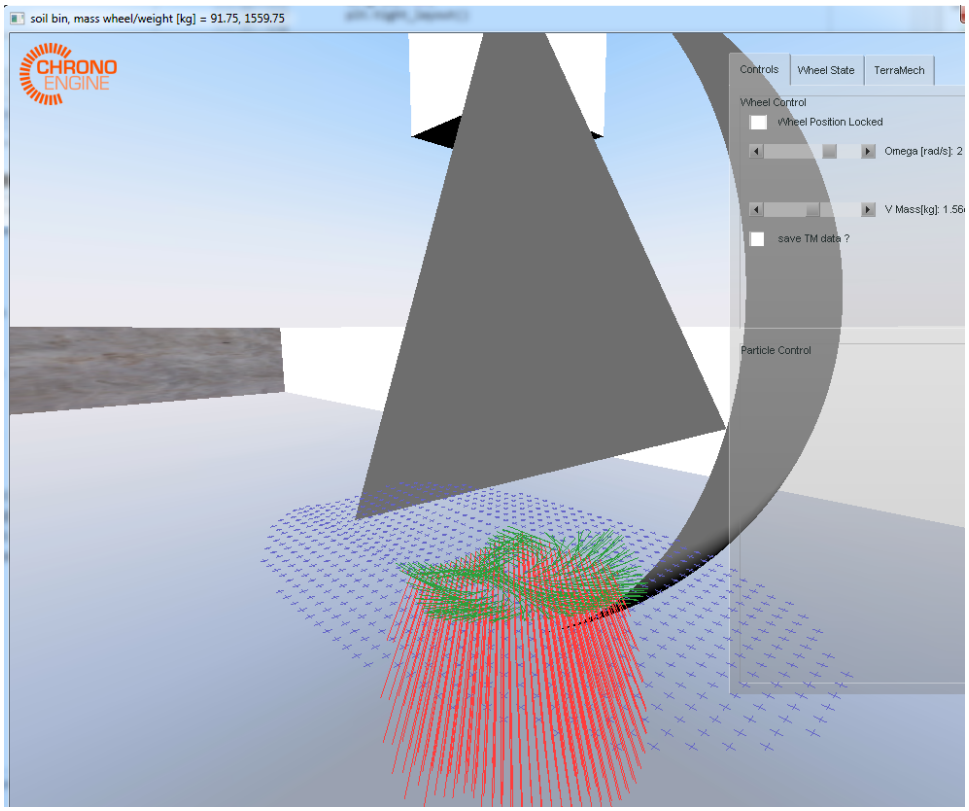

Figure 6.23: Dynamic tire driven with an applied rotational and linear velocity, normal (red) and shear (green) contact pressures shown as vectors

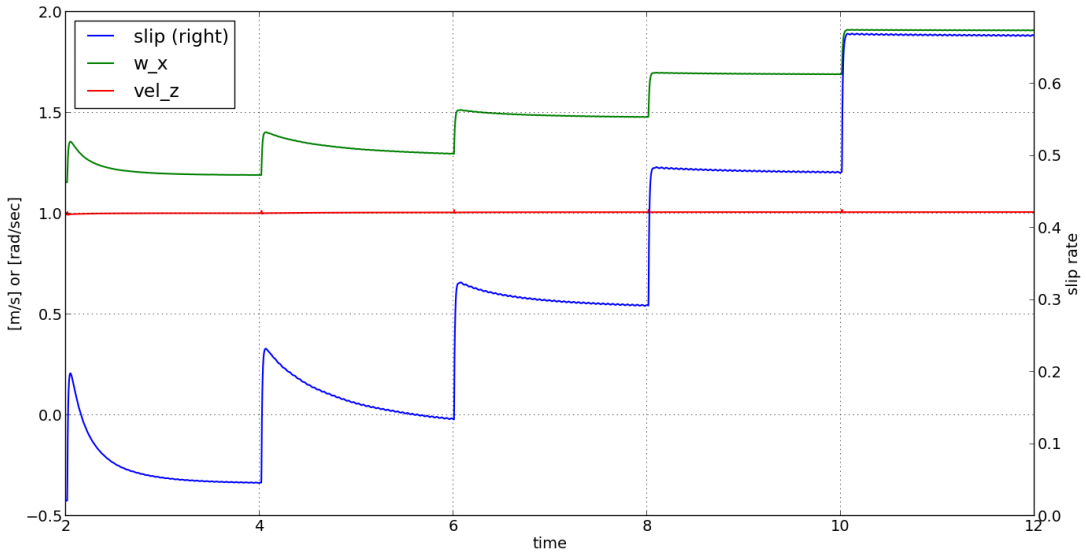

Figure 6.24: Slip ratio, wheel angular and forward velocities for a 18.4R38 tire at 85 kPa inflation pressure

Table 6.4: Pressure-sinkage parameters [18]

Soil type	k_c [kPa/m^{n-1}]	k_ϕ [kPa/m^n]	n	c_1	c_2
Tilled	6.8	1134	0.85	0.43	0.32
Firm	66.0	4486	1.0	0.18	0.32

The tilled and firm Yolo clay loam soils have their shear strength characteristics documented in [42]; however there is no indication of vertical pressure/sinkage tests performed to identify the empirical parameters in Equation 2.1. Representative clay and loam soils have these soil-specific parameters fitted as reported in [18] for North Gower Clay Loam and Greenville Loam. They result in a following set of values for the tilled and firm soils, Table 6.4. For a driven wheel, two additional empirical parameters are required, where c_1 and c_2 in Equation 2.19 are based on reported values in [13]. Pressure-sinkage plots for a flat plate with assumed minimum plate width $b = 20$ inches is shown in Figure 6.25.

6.3.2.1 Driven Tire Performance, Tilled Soil, 85 kPa Inflation Pressure

Performance results of the narrow 18.4R38 tire on the tilled soil are shown for small and large mass that correspond to wheel loads of 18 kN and 27 kN, respectively. First, the results according to the Wong-Reece 2-D steady-state equilibrium approach are presented for the drawbar pull, wheel torque and overall wheel sinkage for the parameters listed in Table 6.4.

These are compared to the results obtained when the dynamically driven tire has a constant forward velocity of 1 m/s applied with a motion. A constant angular velocity is applied over a long enough duration of simulation time for the dynamic model to reach a quasi-steady-state value, as the change in slip as defined by Equation 4.8 approaches zero. Steady-state performance can then be compared to the WR methods for thrust, motion resistance, drawbar pull, torque and sinkage as a function of wheel slip rate.

At the smaller 18 kN load, thrust, H, and motion resistance R are shown in Figure 6.26 as a function of slip ratio calculated using the WR method. Here it can be seen that drawbar pull D increases with slip ratio due to the thrust increasing at a faster rate than motion resistance, which

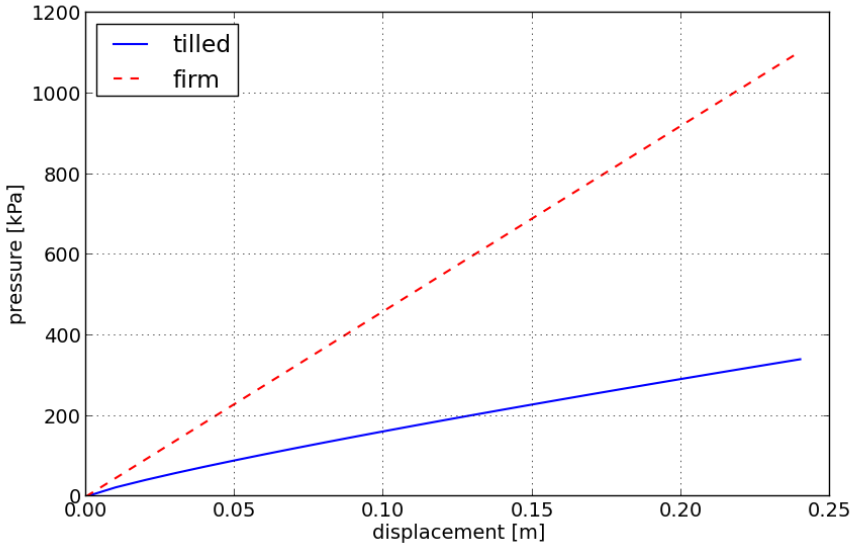

Figure 6.25: Pressure-sinkage of a flat plate, width = 57 cm

stays fairly constant through a large range of slip ratios. Shear stress near the bottom of the wheel, τ_2 has the largest impact on the overall drawbar pull.

The dynamic tire has the same performance predictions defined in Equation 4.32, which are found as a function of slip at steady state and shown in Figure 6.27. At higher slip rates, thrust increases substantially then levels off, and motion resistance actually decreases somewhat, due to the time-constant effect of the soil strain model. Drawbar pull is predicted to increase from 3.5 kN at 10% slip to 6.0 kN at 70% slip for the dynamic tire. This can be compared with the results from the 2-D WR model, Figure 6.26, where the drawbar pull increases from 2.9 to 3.6 kN at slip rates from 10% to 70%, showing good agreement between the models. Larger drawbar pull at similar slip rates is expected for the dynamic tire model, since the deformable tire and soil rebound characteristics lead to larger contact patch areas.

Using the same 18.4R38 tire type and inflation pressure of 85 kPa, drawbar pull was measured by Wulfsohn [41] in a tilled loam soil for a dynamic weight of 17.8kN. At 1.2% slip drawbar pull was 4.9 kN, and at 27% slip drawbar pull was 9.71 kN (where dynamic load varied somewhat at 17.6 kN). This is compared to an estimated 1 kN drawbar pull at 1.2% slip and 5.5 kN at 27% slip using the dynamic tire model, which can almost definitely be attributed to the presence of lugs in the actual tires. Here it becomes clear that the additional tractive effects of treads and lugs should be included in the model, possibly using Equation 2.75 or some variation thereof to include the additional tractive effort these features provide.

In the WR method, required input torque is based solely on the shear stress terms, as the rigid tire geometry and normal stress directions lead to no net torque on the wheel. Torque at a range of slip ratios is shown in Figure 6.28, where τ_1 is the shear stress developed in the front part of the contact patch, $\theta > \theta_m$, and τ_2 is the shear developed in the bottom section of the wheel. As the slip ratio is increased, the required input torque in the front of the contact patch is reduced, while the bottom part of the wheel increases the wheel torque at a faster rate. Wheel sinkage is plotted as a function of slip rate, and assuming there is little to no piling of soil in front of the tire, it is not surprising that sinkage increases with slip ratio as shown in Figure 6.29.

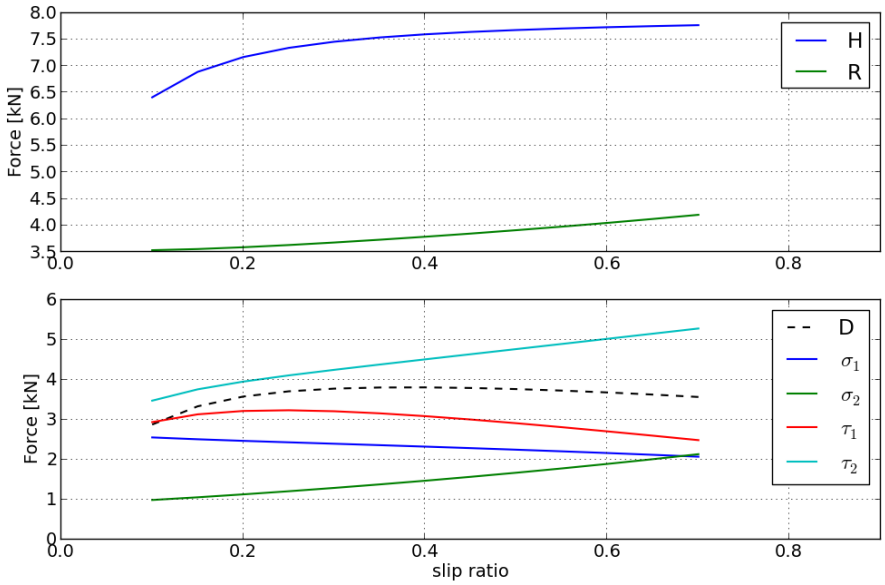

Figure 6.26: WR thrust, motion resistance (top) and drawbar pull, tilled soil, 18 kN load, 18.4 R38 tire

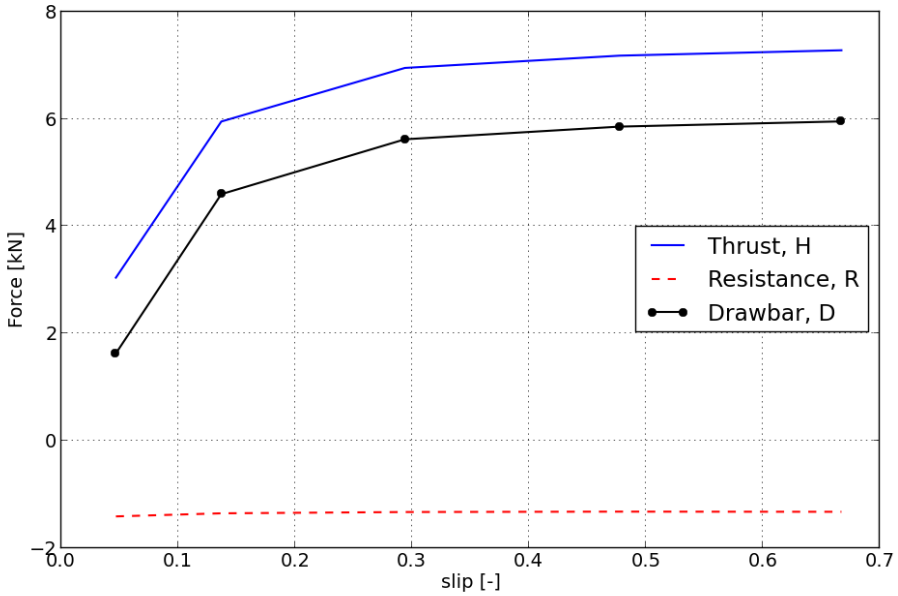

Figure 6.27: Dynamic tire thrust, motion resistance and drawbar pull, tilled soil, 18 kN load, 18.4R38 tire, 85 kPa inflation pressure

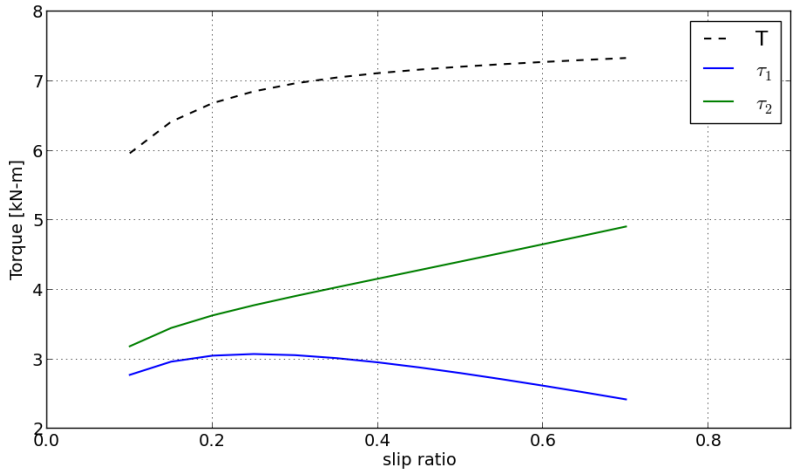

Figure 6.28: WR wheel torque and shear stress, tilled soil, 18 kN load, 18.4R38 tire, 85 kPa inflation pressure

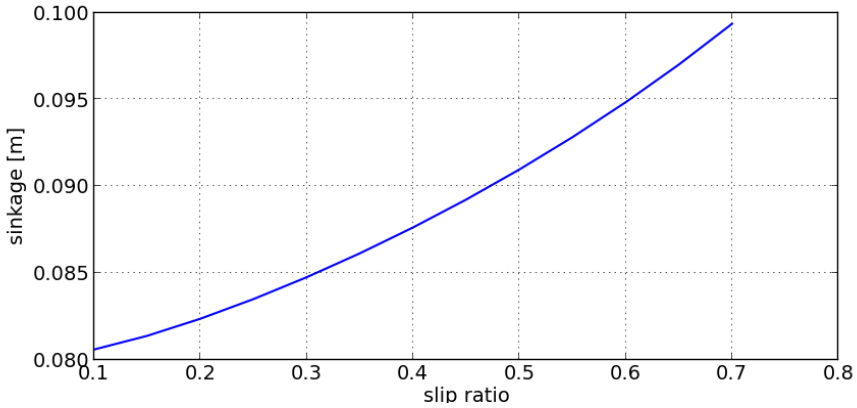

Figure 6.29: WR wheel sinkage, tilled soil, 18 kN load, 18.4R38 tire

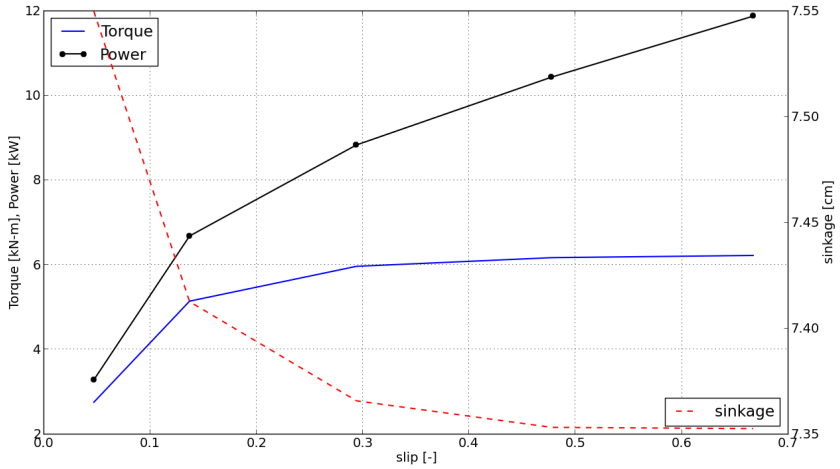

Figure 6.30: Dynamic tire torque, power and sinkage, tilled soil, 18 kN load, 18.4R38 tire, 85 kPa inflation pressure

Results for Torque and sinkage of the WR method is compared to the results of the dynamic tire in Figure 6.30. The WR model predicts a net wheel torque of 6.0 and 7.3 kN-m at wheel slips of 10 and 70%, respectively. This is compared to the results of the dynamic tire which yields torques of 4.3 and 6.2 kN-m at slip rates of 10 and 70%, respectively. The WR model predicts larger shear stress in the contact patch at lower slips, but good agreement is seen at higher slip rates.

Another trend is that the overall sinkage of the wheel decreases with increased angular velocity, which indicates that in cohesive and strain-hardening soils the time duration that a load is applied to the surface of the soil has arguably a more significant impact than increased sinkage at higher slips.

The total volumetric strain experienced by the soil is assumed to be caused by vertical compaction only, and the total volumetric compaction of all the terrain grid nodes in the active contact patch is summed to find the total contact patch strain. Total compaction shown as a function of slip is seen in Figure 6.31, with values of 0.0078 and 0.0071 m^3. This value is compared to the experimental results reported in [41], who reported a rut volume of 0.00321 and 0.0121 m^3 at slip rates of 1.2 and 27.0 %, respectively. Here the difference is again attributed to the effect of lugs in the experimental case.

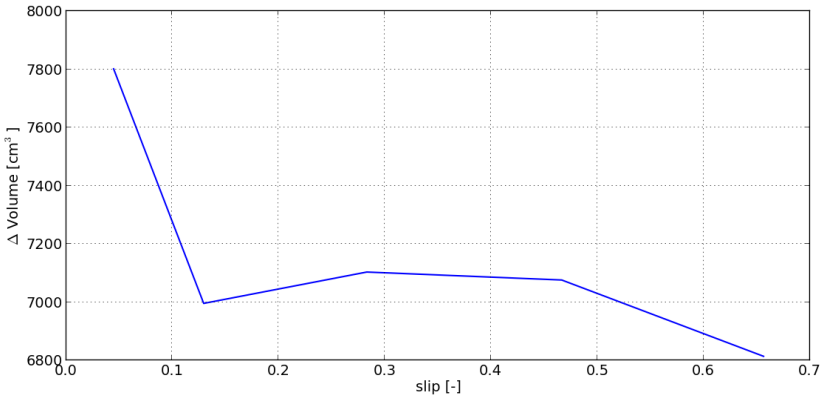

Figure 6.31: Volumetric strain of soil grid nodes in active contact with the dynamic tire, tilled soil, 18 kN load, 18.4R38 tire, 85 kPa inflation pressure

The weight is increased from 18kN to 27 kN, again using the 18.4R38 tire at 85 kPa in tilled soil. First, the WR method is used to calculate thrust and motion resistance, plotted as a function of slip ratio in Figure 6.32.

The dynamic tire is tested at the higher weight and drawbar pull, motion resistance and thrust, shown in Figure 6.33 is first compared to the WR method. The WR method calculates that drawbar pull is 3.7 and 3.8 kN at 10 and 70% slip, respectively. The dynamic tire results show a drawbar pull of 3.6 kN and 7.7 kN at 10 and 70 % slip, respectively, showing good agreement at lower slip rates.

Comparing these values to those experimentally found by Wulfsohn [41], who reported drawbar pull of 7.1 and 14.4 kN at slip ratios of 7.2 and 21.9%, respectively. The effect of lugs in the physical tests leads to a large predicted increase in the drawbar pull due to the lack of lug effects in the dynamic tire contact model.

Required torque to drive the more heavily loaded tire at a variety of slip rates according to the WR method is shown in Figure 6.32. Wheel sinkage shows a similar curve trend for the large 27 kN load when compared to the smaller 18 kN load, with the exception of higher sinkage in general being observed for the larger load, shown in Figure 6.35.

The dynamically driven tire at the higher 27 kN load is compared to the WR model, which calculates required wheel torques of 9.2 and 10.5 kN-m at slip rates of 10 and 70%, respectively. This is compared to the dynamic tire model, with wheel torques of 7.1 and 15.6 kN-m at slip rates of 10 and 54%, respectively, shown in Figure 6.36, with good agreement with the WR model.

Total volumetric compaction is compared to the experimental results in [41] at the higher 27 kN load, with reported values of 0.0070 and 0.017 m^3 at slip rates of 7.2 and 21.9%, respectively. This is compared to the results of the dynamic tire model which yields compaction volumes of 0.016 and 0.015 m^3, plotted against slip rate in Figure 6.37.

A similar analysis is carried out for the wider 24.5R32 tire, on the same tilled loam soil at both small and large vertical loads. At the smaller 18 kN load, thrust, H, and motion resistance R are shown in Figure 6.38 as a function of slip ratio using the WR method.

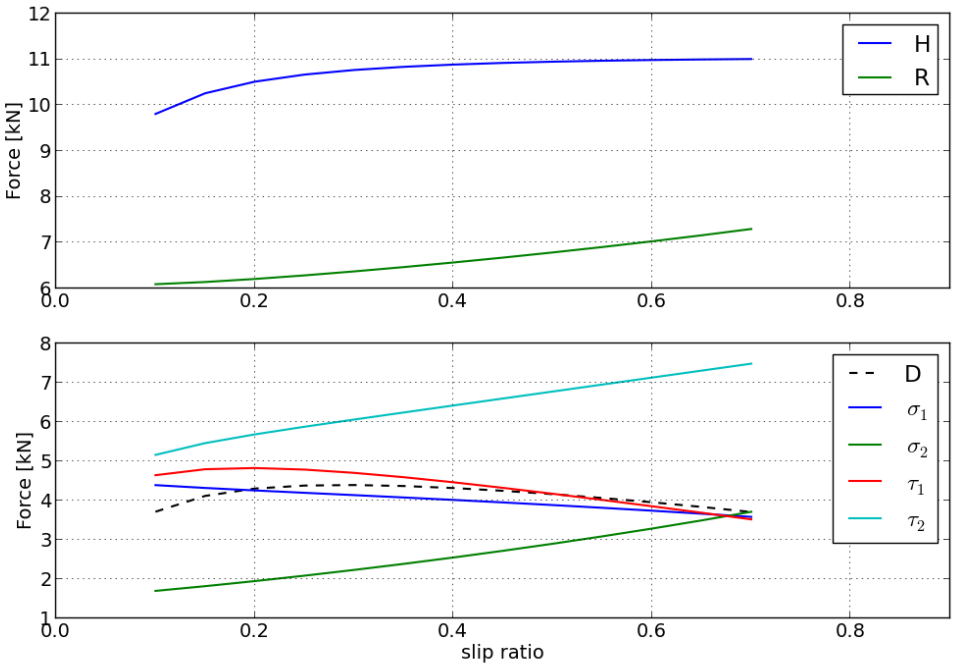

Figure 6.32: WR thrust, motion resistance (top) and drawbar pull, tilled soil, 27 kN load, 18.4 R38 tire

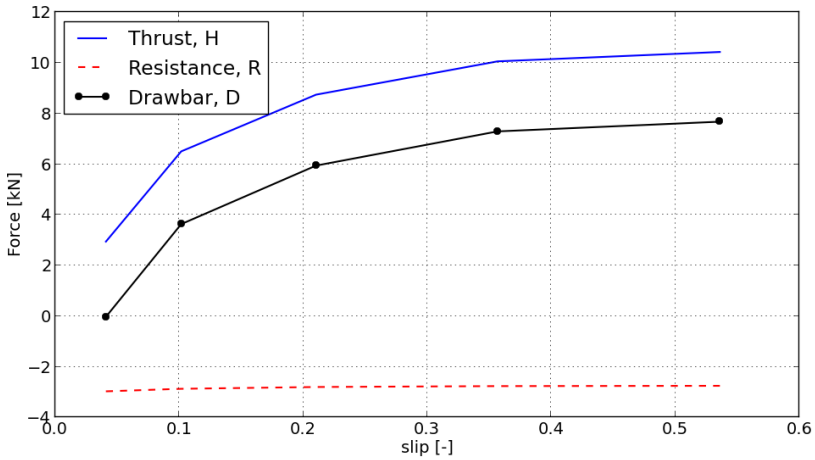

Figure 6.33: Dynamic tire thrust, motion resistance and drawbar pull, tilled soil, 27 kN load, 18.4R38 tire, 85 kPa inflation pressure

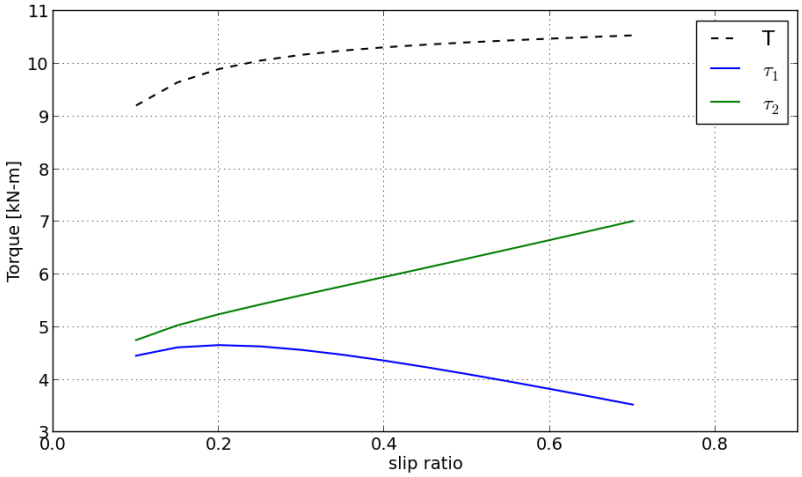

Figure 6.34: WR wheel torque, tilled soil, 27 kN load, 18.4R38 tire

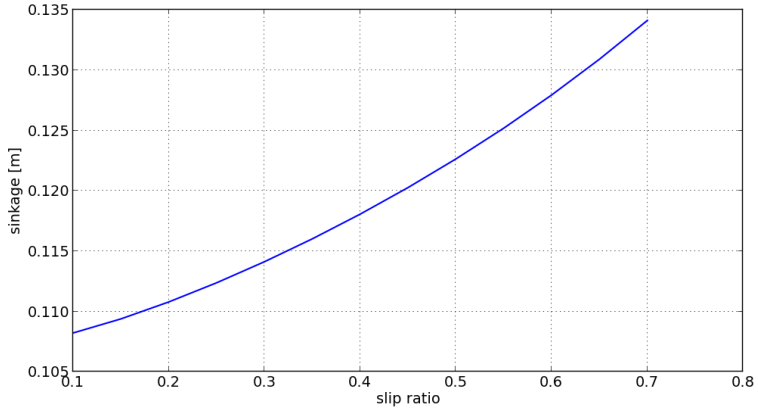

Figure 6.35: WR wheel sinkage, tilled soil, 27 kN load, 18.4R38 tire

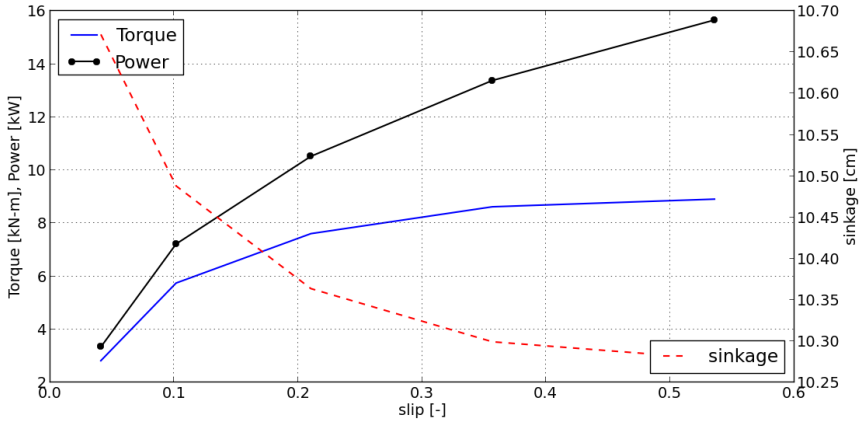

Figure 6.36: Dynamic tire torque, power and sinkage, tilled soil, 27 kN load, 18.4R38 tire, 85 kPa inflation pressure

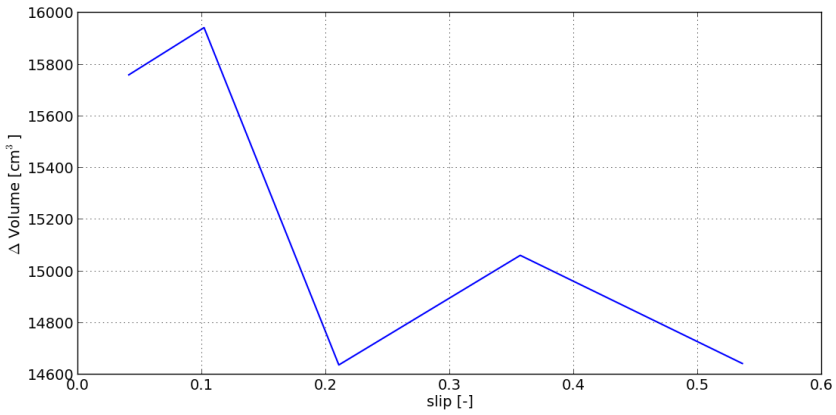

Figure 6.37: Volumetric strain of soil grid nodes in active contact with the dynamic tire, tilled soil, 27 kN load, 18.4R38 tire, 85 kPa inflation, 85 kPa inflation pressure

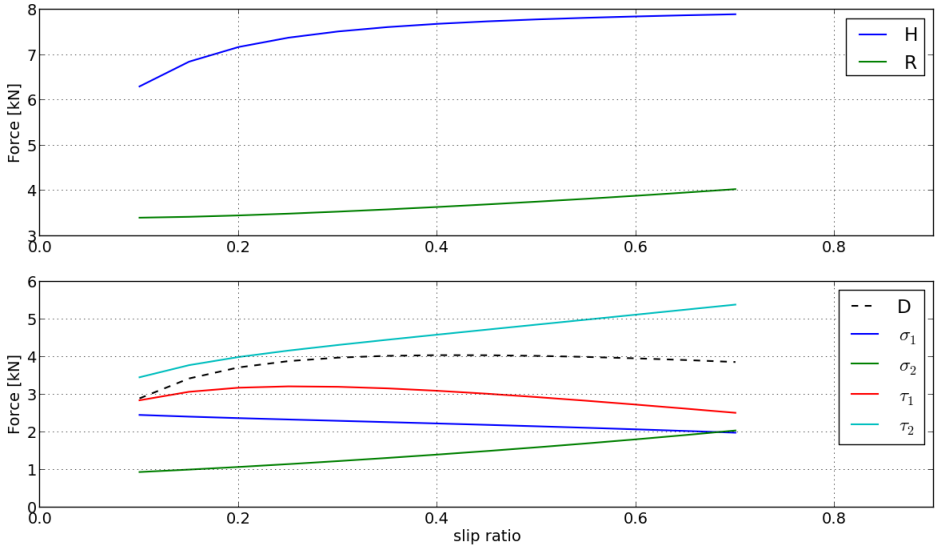

Figure 6.38: WR thrust, motion resistance (top) and drawbar pull, tilled soil, 18 kN load, 24.5 R32 tire

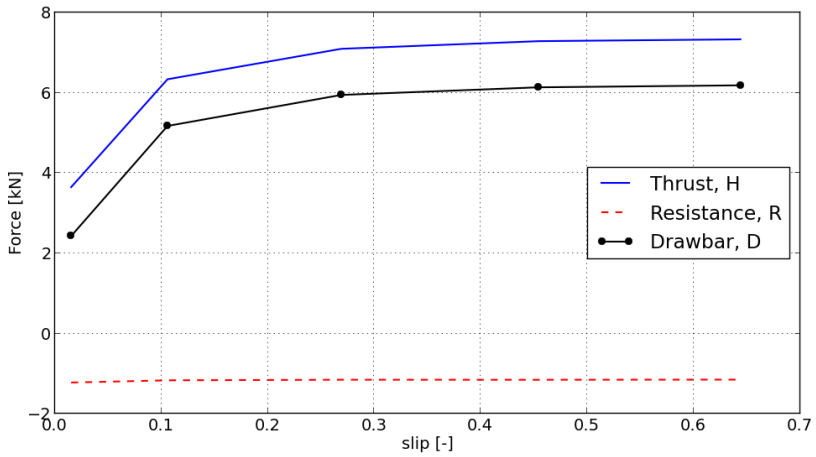

Figure 6.39: Dynamic tire thrust, motion resistance and drawbar pull, tilled soil, 18 kN load, 24.5R32 tire, 85 kPa inflation pressure

For comparison, the WR method predicts drawbar pull of 3.0 and 4.0 kN at slip rates of 10 and 70 %, respectively. The wider 24.5R32 dynamic tire yields drawbar pull of 5.0 and 6.2 kN at slips rates of 10 and 70%, respectively. The dynamic tire drawbar pull is plotted against slip rate in Figure 6.39, and shows good agreement.

Experimental drawbar pull results of 5.1 and 9.7 kN at slip rates of 6.4 and 31.8%, respectively, for this tire type are reported in [41]. These are compared to the dynamic tire with drawbar pull of 3.9 and 6.0 kN at those slip rates, again highlighting the importance of including lug effects on the shear developed in the contact patch.

Torque at a range of slip ratios according to the WR method is shown in Figure 6.40. Wheel sinkage is plotted as a function of slip rate, and assuming there is little to no piling of soil in front of the tire, it is not surprising that sinkage increases with slip ratio as shown in Figure 6.41.

The wider dynamic tire has required wheel torque, sinkage and power shown as a function of slip in Figure 6.42, with calculated torque of 5.5 and 6.5 kN-m at slip rates of 10 and 70%, respectively. These values are compared to the WR model, with calculated torques of 5.6 and 7.2 kN-m at the same wheel slips, again showing good agreement between the torques at low and high slip rates.

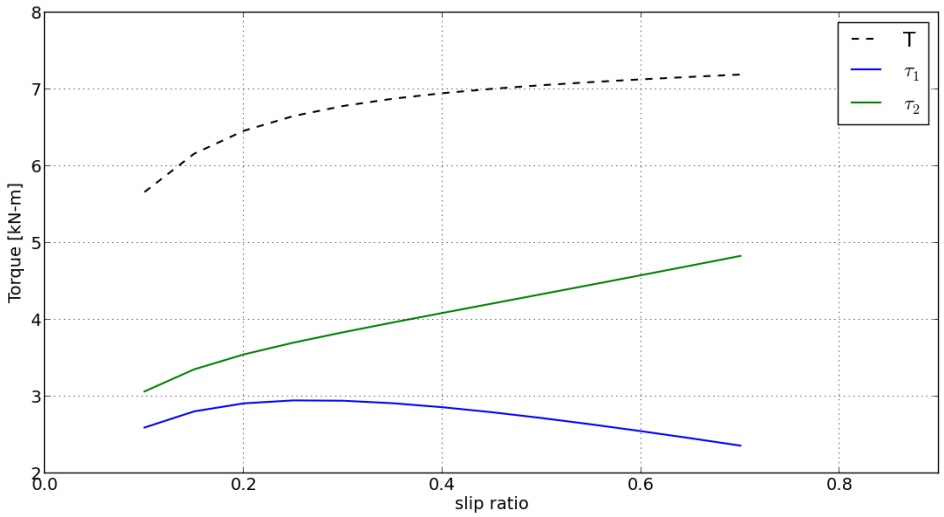

Figure 6.40: WR wheel torque, tilled soil, 18 kN load, 24.5R32 tire

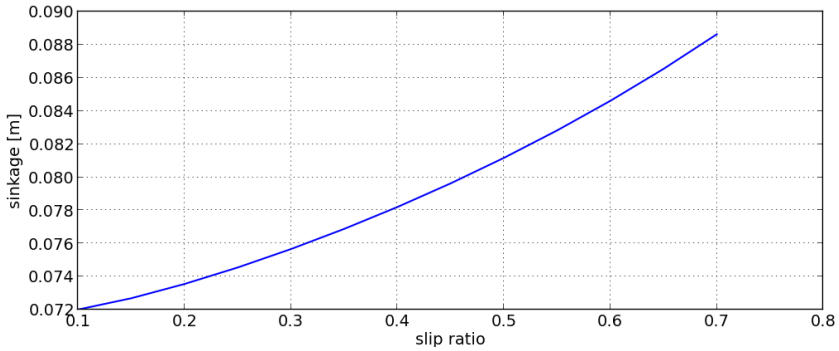

Figure 6.41: WR wheel sinkage, tilled soil, 18 kN load, 24.5R32 tire

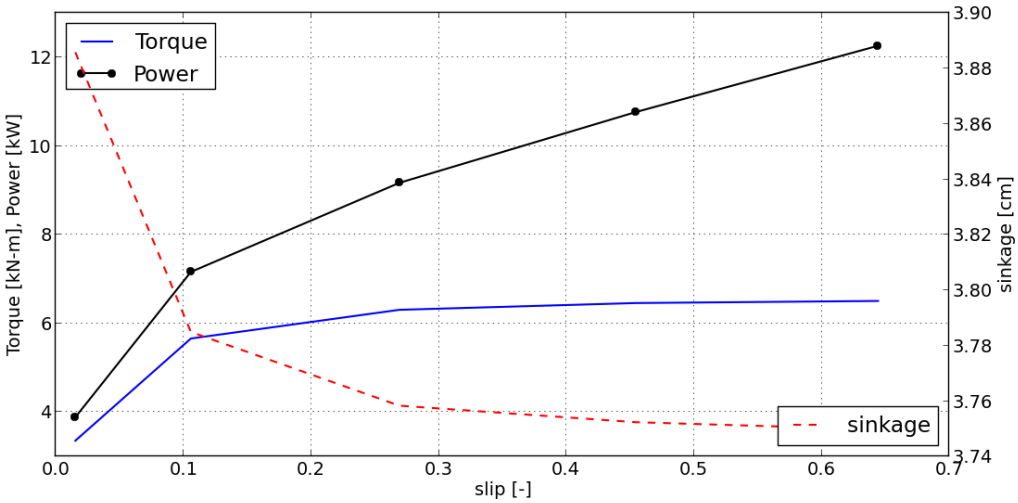

Figure 6.42: Dynamic tire torque, power and sinkage, on tilled soil, 18 kN load, 24.5R32 tire, 85 kPa inflation pressure

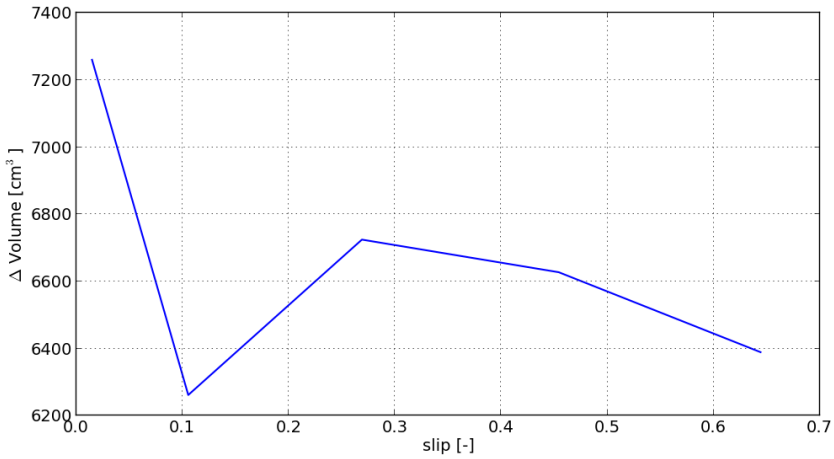

Figure 6.43: Volumetric strain of soil grid nodes in active contact with the dynamic tire, tilled soil, 18 kN load, 24.5R32 tire, 85 kPa inflation, 85 kPa inflation pressure

Total volumetric compaction is compared to the experimental results in [41] for the wider tire, with reported values of 0.0089 and 0.016 m^3 at slip rates of 6.4 and 31.8%, respectively. This is compared to the results of the dynamic tire model which yields compaction volumes of 0.0068 and 0.0067 m^3, plotted against slip rate in Figure 6.43. The overall compaction values show agreement that is satisfactory.

The wider tire is analyzed at the larger 27 kN load, thrust and motion resistance are plotted as a function of slip ratio, with drawbar pull shown with individual integral terms shown in Figure 6.44.

For comparison, the WR method calculates drawbar pull of 3.7 and 4.2 kN at slip rates of 10 and 70 %, respectively. The dynamic tire results in drawbar pull of 5.3 and 8.3 kN at slip rates of 10 and 52%, respectively, showing good agreement.

Required torque to drive the tire as a function of slip rate is shown in Figure 6.44 using the WR method. Wheel sinkage for the larger load is shown in Figure 6.47.

For comparison, the WR method calculates required wheel torques of 8.7 and 10.2 kN-m at slip rates of 10 and 70%, respectively. The dynamic tire results in wheel torques of 7.1 and 9.4 kN-m at slip rates of 10 and 52%, respectively, shown in Figure 6.48.

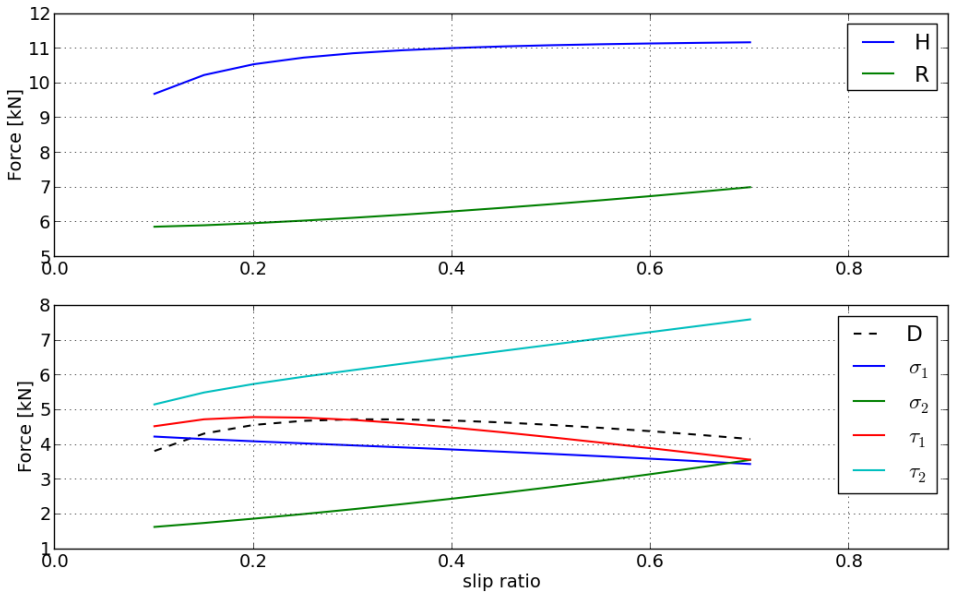

Figure 6.44: WR thrust and motion resistance (top) and drawbar pull with individual terms (bottom), tilled soil, 27 kN load, 24.5 R32 tire

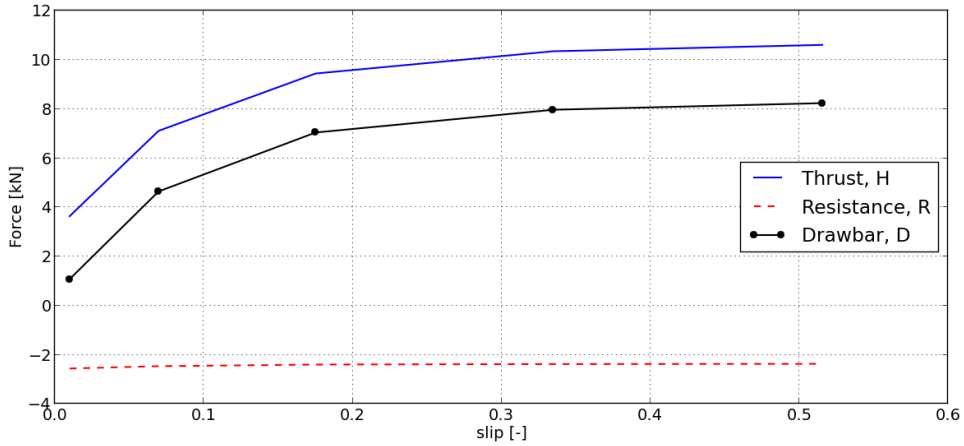

Figure 6.45: Dynamic tire thrust, motion resistance and drawbar pull, tilled soil, 27 kN load, 24.5R32 tire, 85 kPa inflation pressure

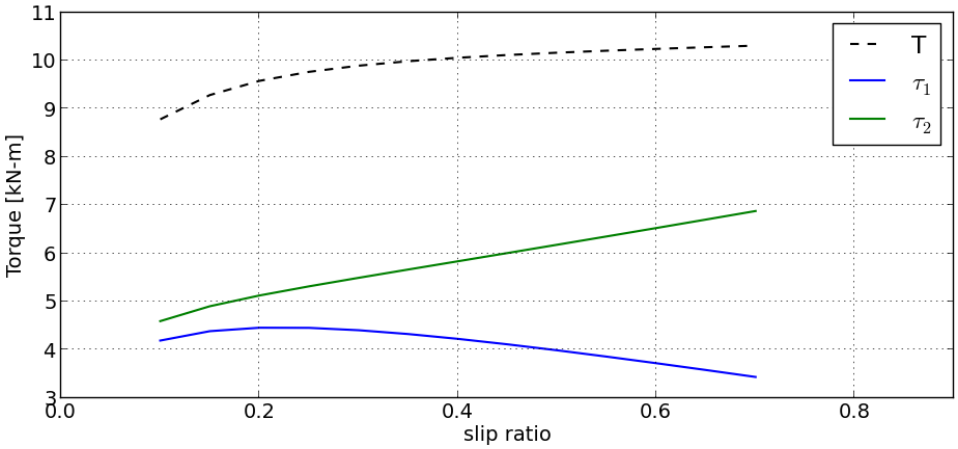

Figure 6.46: WR wheel torque, tilled soil, 27 kN load, 24.5R32 tire

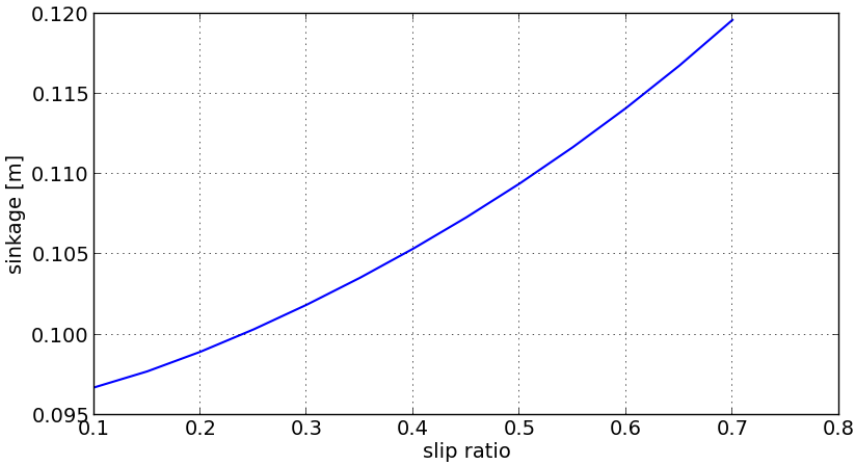

Figure 6.47: WR wheel sinkage, tilled soil, 27 kN load, 24.5R32 tire

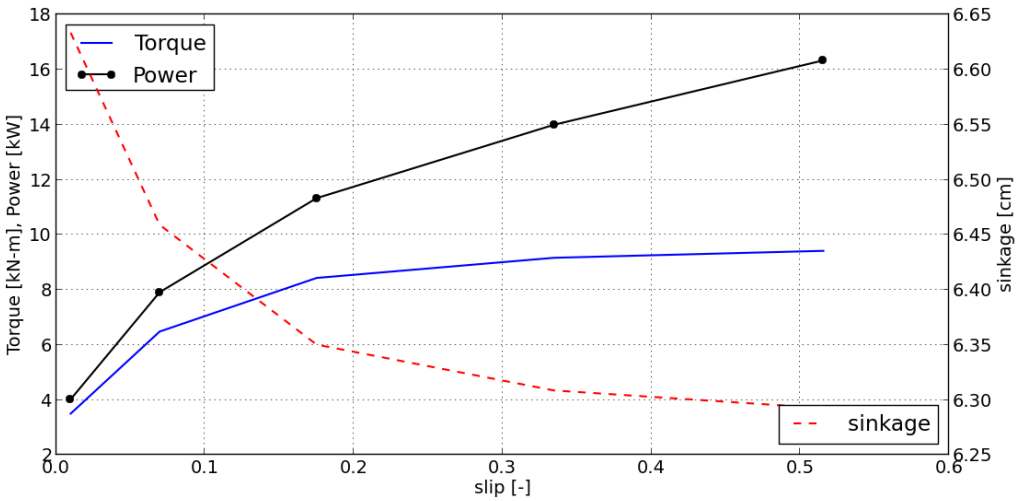

Figure 6.48: Wheel torque, power and sinkage, tilled soil, 27 kN load, 24.5R32 tire, 85 kPa inflation pressure

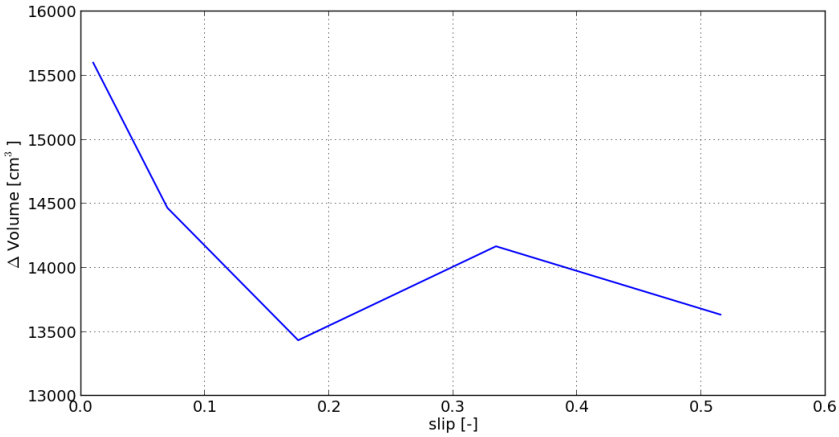

Figure 6.49: Volumetric strain of soil grid nodes in active contact with the dynamic tire, tilled soil, 27 kN load, 24.5R32 tire, 85 kPa inflation, 85 kPa inflation pressure

Total volumetric compaction is compared to the experimental results in [41] for the wider tire at the higher load, with reported values of 0.012 and 0.0066 m^3 at slip rates of 5.8 and 31.6%, respectively. This is compared to the results of the dynamic tire model which yields compaction volumes of 0.0068 and 0.0067 m^3, plotted against slip rate in Figure 6.49. The overall compaction values show agreement that is satisfactory.

6.3.2.2 Driven Tire Performance, Tilled Soil, 125 kPa Inflation Pressure

The narrow 18.4R38 tire is tested at a higher inflation pressure of 125 kPa, which affects the tire spring constant identified during the tire parameter identification, Section 6.2.2. Thus only the dynamic tire model will have different mobility performance and contact stress results at a higher inflation pressure. The dynamic tire is compared to the experimental results in [41] for a tilled loam soil with an applied vertical load of 18kN. Experimental drawbar pull is 1.5 and 8.6 kN at slip rates of 3.1 and 27.9%, respectively Comparing the dynamic tire drawbar pull of 1.4 and 5.3 kN, at slip rates of 4 and 27.9%, respectively, shows good agreement with the field tests run at the higher inflation pressures.

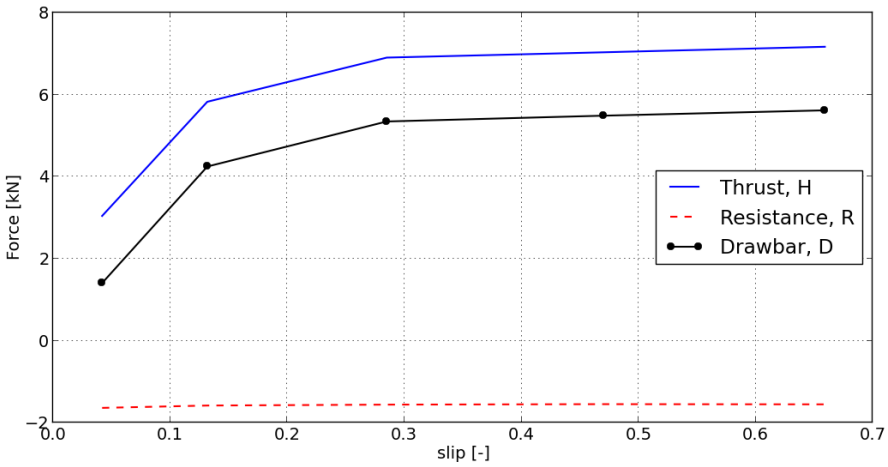

Figure 6.50: Dynamic tire, thrust, motion resistance and drawbar pull, tilled soil, 18 kN load, 18.4R38 tire, 125 kPa inflation pressure

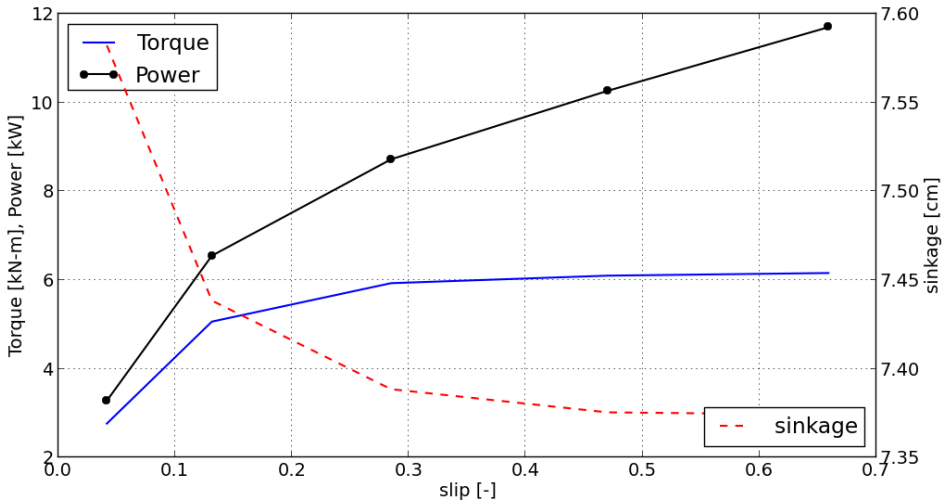

Figure 6.51: Dynamic tire torque, power and sinkage, tilled soil, 18 kN load, 18.4R38 tire, 125 kPa inflation pressure

The wheel torque, sinkage and power is not recorded in the experimental results in [41], but are reproduced using the dynamic tire test rig at an inflation pressure of 125 kPa shown in Figure 6.51.

Total soil compaction in the contact patch for the 125 kPa inflation pressure dynamic tire is shown as a function of slip in Figure 6.52. Experimental results reported in [41] at the higher inflation pressure yield rut volumes of 0.0018 and 0.0057 m^3 at slip rates of 3.1 and 27.9 %, respectively. The dynamic tire shows volumetric compression of 0.0077 and 0.0074 m^3 at slip rates of 4.4 and 27.9%, respectively. A large variance in the experimental values leads to the conclusion that the relative amount of soil compaction is correct.

Comparisons are drawn between the dynamic tire model results at low and high inflation pressures of 85 kPa. Drawbar pull shows very similar values for both inflation pressures at low slip rates; however, at high slip rates it is clear that the lower inflation pressure leads to slightly higher drawbar pull. Required wheel torque is seen to be nearly identical between the tires at the two inflation pressures, which is likely due to the fact that structural tire effects are not considered, where the hysteresis of an under-inflated tire would lead to a larger required wheel torque in reality. Wheel sinkage is higher at the lower inflation pressure, but likely due to the increased elastic deflection

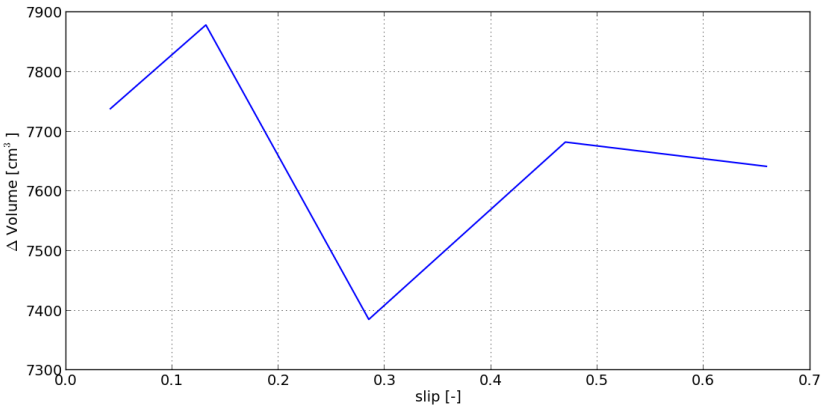

Figure 6.52: Volumetric strain of soil grid nodes in active contact with the dynamic tire, on tilled soil, 18 kN load, 18.4R38 tire, 125 kPa inflation pressure

of the deformable tire model. Soil volumetric compaction in the contact patch is slightly higher at the higher inflation pressure, due to the higher normal stresses generated by the tire model.

6.3.2.3 Driven Tire Performance, Firm Soil

Performance results of the narrow 18.4R38 tire on the firm soil with parameters specified in Table 6.4 are shown for the smaller 18 kN wheel load. Thrust, H, and motion resistance R are shown in Figure 6.53 as a function of slip ratio using the WR method.

For comparison, the WR method predicts drawbar pull of 5.0 and 7.5 kN at slip rates of 10 and 70%, respectively. The dynamic tire results show drawbar pull of 6.9 and 8.4 kN at slip rates of 10 and 60%, respectively, shown in Figure 6.54. Good agreement is seen, with the dynamic tire model once again predicting a larger drawbar pull when compared to the WR method.

Experimental average drawbar pull of 5.9 and 10.1 kN at average slip rates of 1.4 and 23.3% in [41] are compared to the dynamic tire model values of 2.5 and 8.1 kN at slip rates of 4.4 and 23.3%, respectively. Again, drawbar pull of the experimental results is higher than the dynamic tire model due to the added tractive effort provided by the lugs.

The wheel torque at a range of slip ratios is shown in Figure 6.55, for the WR method. Wheel sinkage is plotted as a function of slip rate, and assuming there is little to no piling of soil in front of the tire, it is not surprising that sinkage increases with slip ratio as shown in Figure 6.56.

For comparison, the WR method yields wheel torques of 6.5 and 9.3 kN at slip rates of 10 and 70%, respectively. This is compared to the results of the dynamic tire, shown in Figure 6.57 which yields torques of 6.3 and 7.5 kN-m at slip rates of 10 and 70%, respectively. In the case of the firm soil, good agreement is seen at higher slip rates between the models.

Total volumetric compaction predicted by the dynamic tire is shown as a function of slip in Figure 6.58, with values of 0.0030 and 0.0028 m^3 at slip rates of 5 and 30%, respectively.

The experimental results in [41] do not include a measurement of rut volume for the firm soil. However, maximum rut depth was measured to be 27 and 65 mm at slip rates of 1.4 and 23.3%, respectively. This is compared to the change in sinkage of 10 mm between slip rates of 5 and 23.3% for the dynamic tire shown in Figure 6.57.

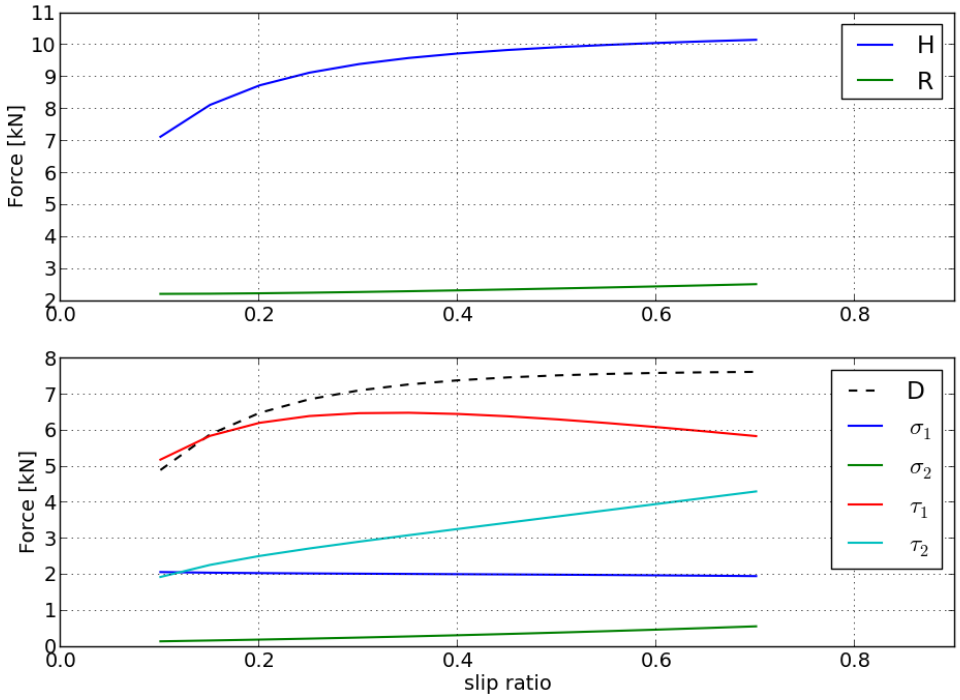

Figure 6.53: WR thrust, motion resistance (top) and drawbar pull, firm soil, 18 kN load, 18.4 R38 tire

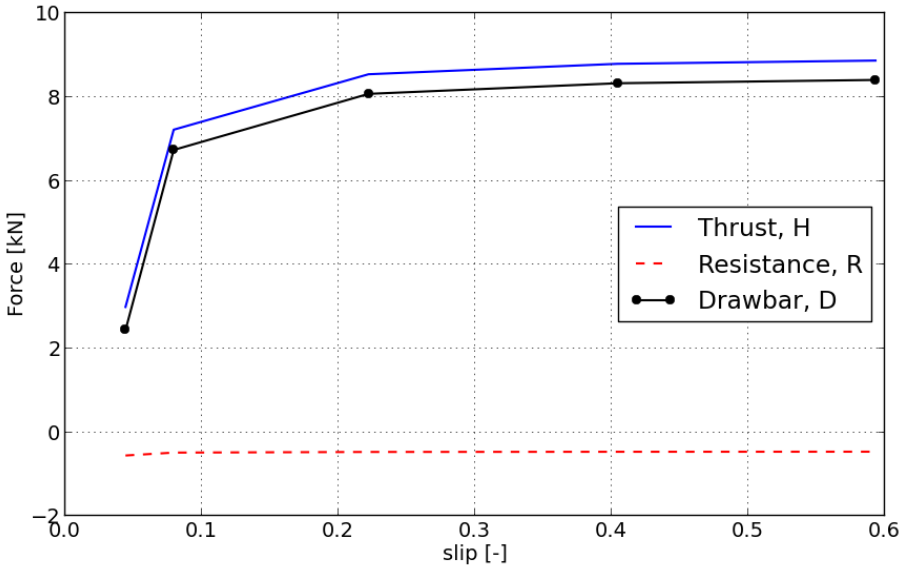

Figure 6.54: Dynamic tire thrust, motion resistance and drawbar pull, firm soil, 18 kN load, 18.4 R38 tire, 85 kPa inflation pressure

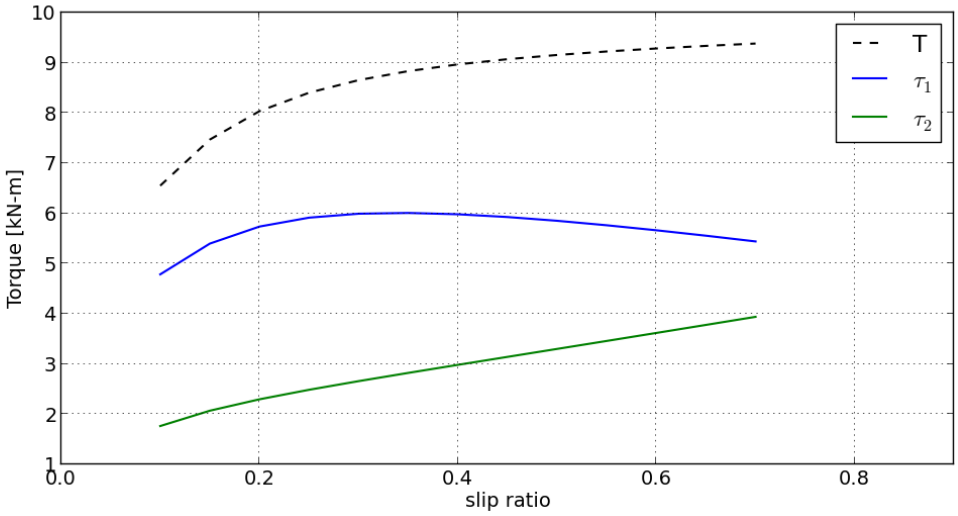

Figure 6.55: WR wheel torque, firm soil, 18 kN load, 18.4R38 tire

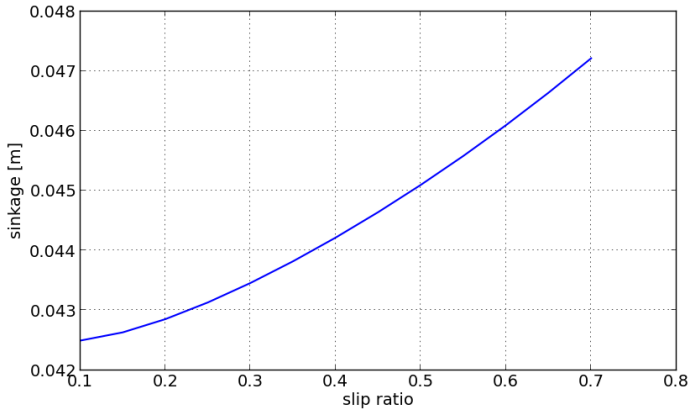

Figure 6.56: Wheel sinkage, firm soil, 18 kN load, 18.4R38 tire

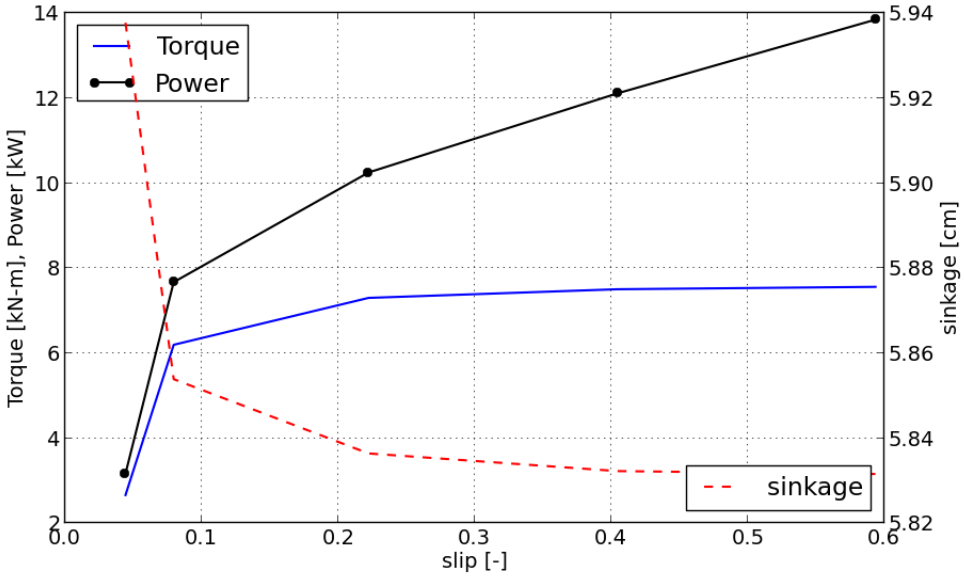

Figure 6.57: Dynamic tire torque, power and sinkage vs. slip rate, firm soil, 18 kN load, 18.4R38 tire, 85 kPa inflation pressures

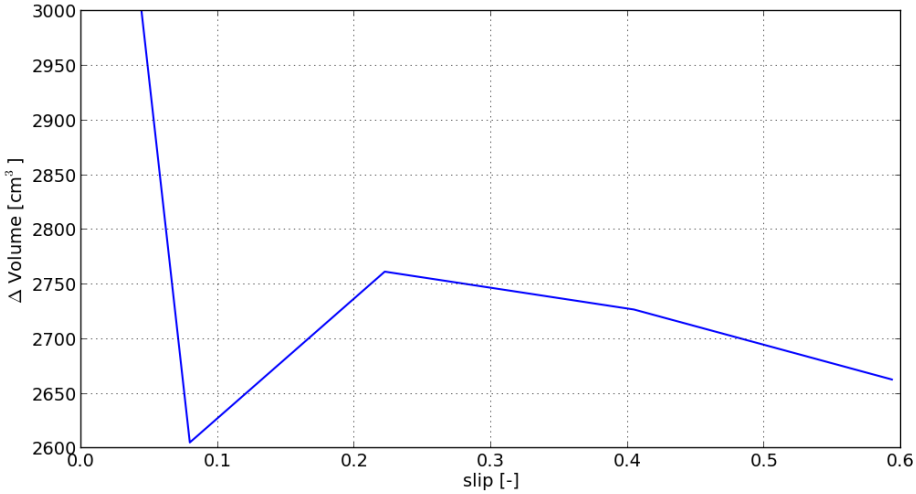

Figure 6.58: Volumetric strain of soil grid nodes in active contact with the dynamic tire, firm soil, 18 kN load, 18.4R38 tire, 85 kPa inflation pressure

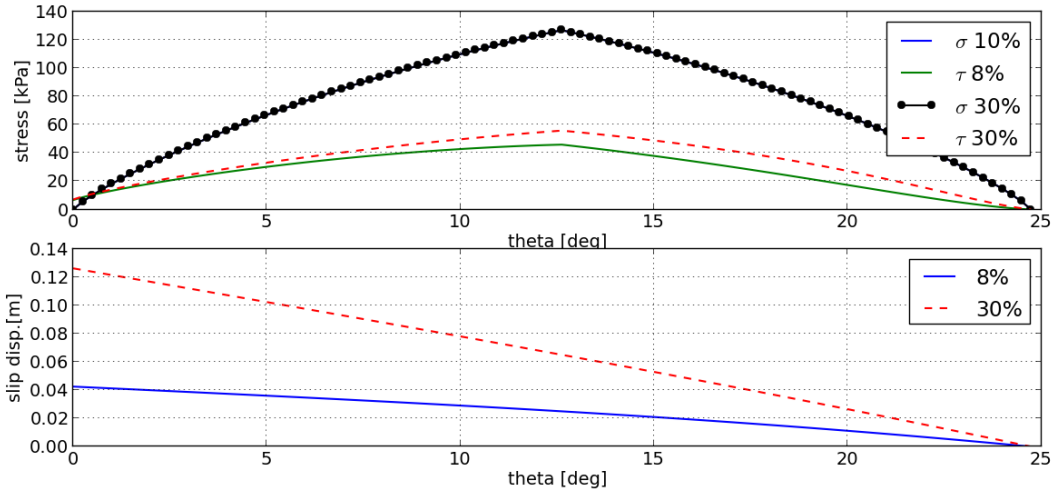

Figure 6.59: WR normal and shear stress at a low and high slip rate, tilled soil, 18 kN load, 18.4R38 tire

6.3.3 Driven Wheel Contact Stress

Performing the steady-state solutions as described by Wong and Reece for driven wheels [13] yields a set of contact and maximum stress angles, θ_1 and θ_m, respectively, for each combination of soil, wheel and load. The normal and shear stresses along the centerline of the wheel can be plotted for any given slip ratio, where only the shear distribution differs for each solution set, as shown in Figure 6.59 for the 18.4R38 tire on soft tilled soil with a total vertical load of 18 kN.

This is compared with the contact stress of a dynamically driven tire, where a constant linear velocity of 1 m/s is applied and the applied angular velocity is varied to yield a range of slip rates. The tire node normal and shear stress are shown along the centerline of the tire in Figure 6.60, for three steady-state wheel slip rates of 4.8, 22.2 and 59.3%, respectively. Similar to the WR contact stress distributions, the chief difference between the stress profiles is the shear stress distribution.

For the narrow 18.4R tire driven on a tilled loam, the load of 18 kN can be compared with a larger weight of 27 kN using the WR method. The contact stress distribution for the normal and shear can again be plotted at both low and high slip rates in Figure 6.61.

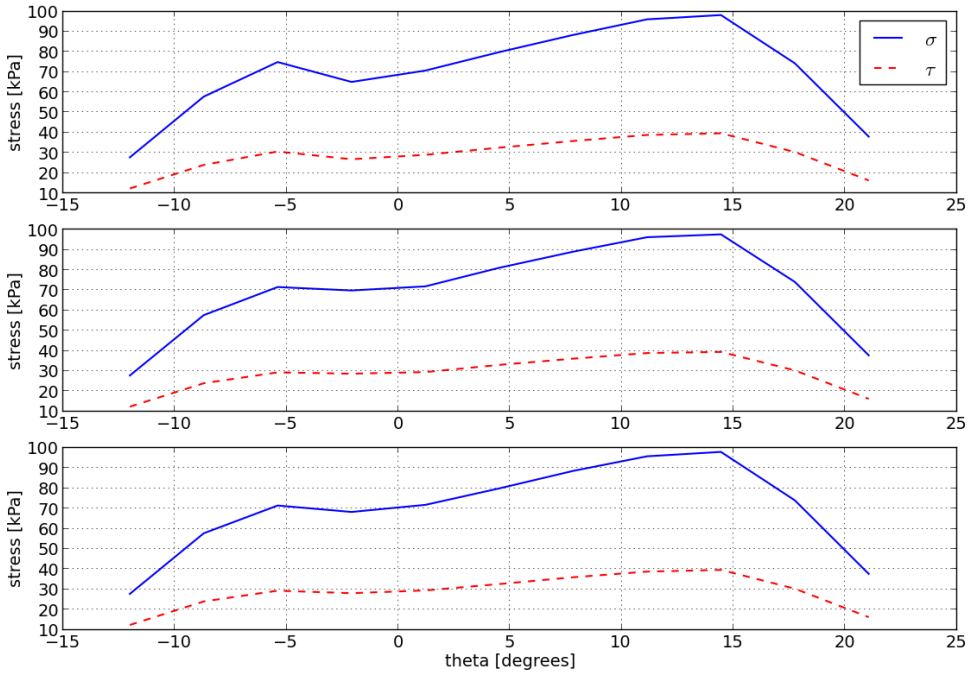

Figure 6.60: Dynamic tire normal and shear stress, wheel slip rates of 4.8, 22.2 and 59.3% (top to bottom), tilled soil, 18 kN load, 18.4R38 tire, 85 kPa inflation pressure

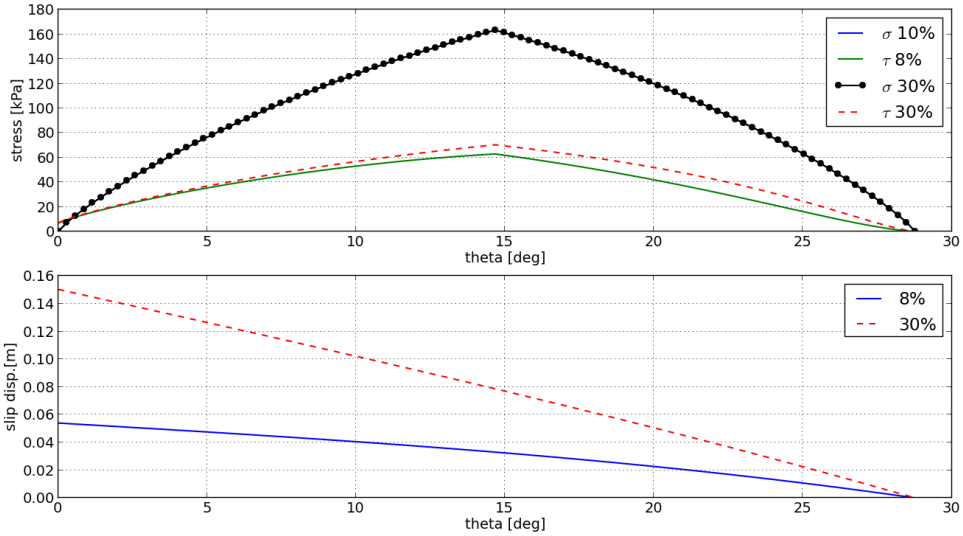

Figure 6.61: WR normal and shear stress at a low and high slip rate, tilled soil, 27 kN load, 18.4R38 tire

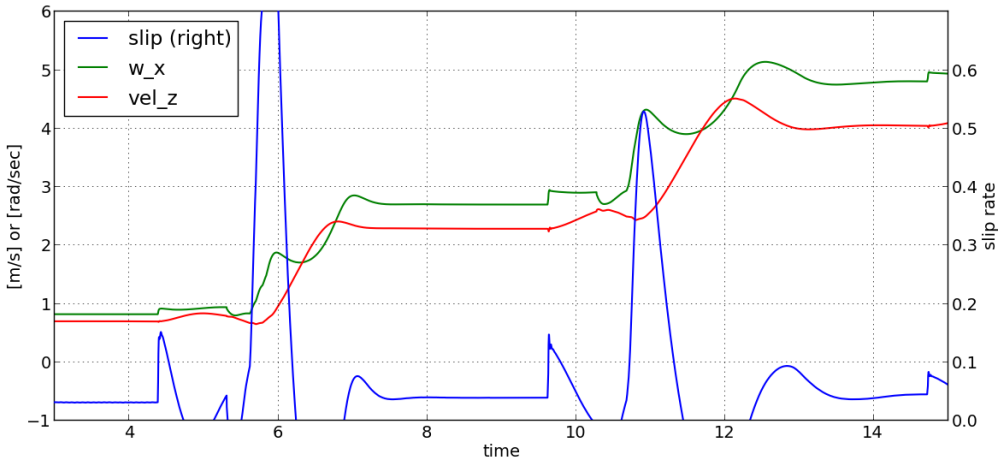

Figure 6.62: Dynamic tire slip rate, wheel angular velocity and forward velocity, applied wheel angular velocities of 1, 3 and 5 rad/sec, tilled soil, 18 kN load, 18.4R38 tire, 85 kPa inflation pressure

A contrasting driving method for the dynamic tire is illustrated, where only the wheel angular velocity is specified and the forward acceleration is achieved through the drawbar pull until steady-state in terms of the forward velocity is reached. Applied wheel angular velocities of 1, 3 and 5 rad/sec results in the wheel angular velocity and forward velocity shown in Figure 6.62.

Contact stress distribution along the centerline of the tire at each applied angular velocity is shown in Figure 6.63. As the applied wheel angular velocity rate and resulting forward velocity increases, the normal stress goes through three distinct distribution types. First, at very low applied wheel angular velocities, the stress is closer to uniform along the length of the contact patch. At higher velocities, the normal stress moves towards the front of the wheel as the front of the tire encounters soil quickly enough where it cannot deform before large elastic tire stresses result. At the highest velocities the normal stress becomes more evenly distributed as the tire passes over the soil quickly enough to avoid large amounts of soil sinkage.

The closest comparison between a tire on a real vehicle and the dynamically driven tire is to use an applied torque at the wheel spindle. A constant torque of 1600 N-m is applied to the wheel of a 18.4R38 tire at 85 kPa inflation pressure under a 18 kN vertical load. No comparison can be

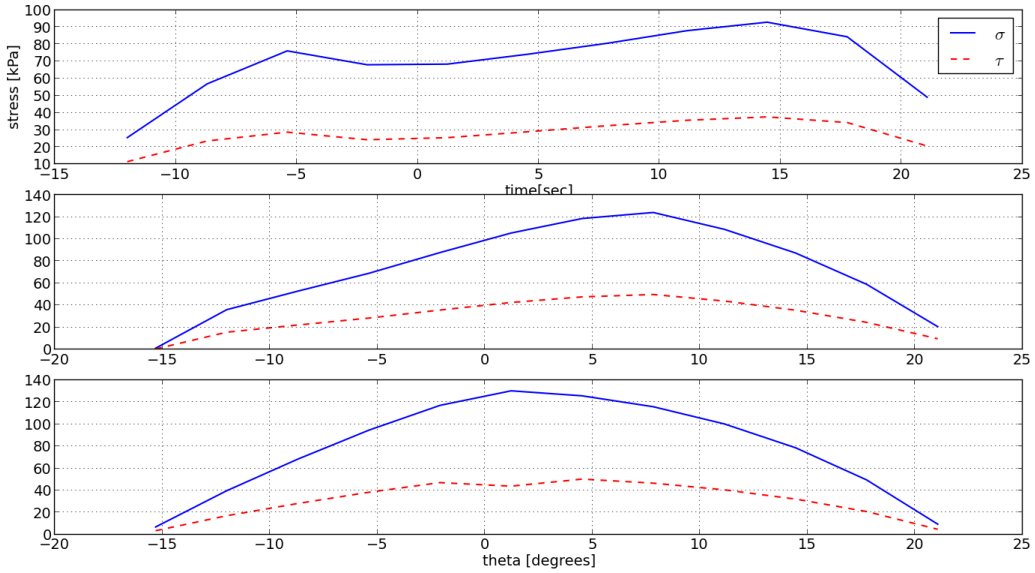

Figure 6.63: Dynamic tire normal and shear stress, applied wheel angular velocities of 1, 3 and 5 rad/sec, tilled soil, 18 kN load, 18.4R38 tire, 85 kPa inflation pressure

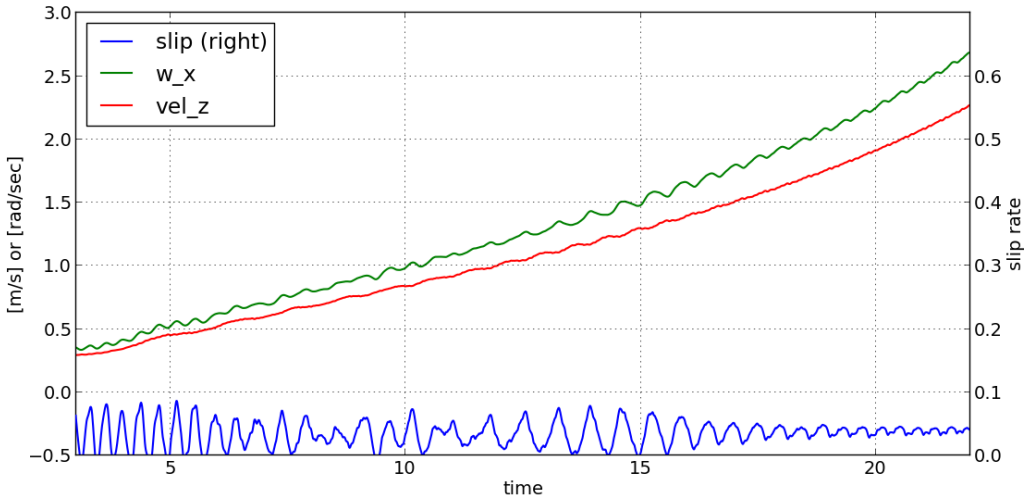

Figure 6.64: Slip ratio, wheel angular and forward velocities for a 18.4R38 tire at 85 kPa inflation pressure driven and applied torque of 1600 Nm

made with the experimental or WR methods for a dynamic wheel driven by a torque, so we are free to select any sort of non-flat terrain surface geometry to investigate the effects on the performance. The undeformed height of the terrain surface nodes are offset based on a Non-uniform rational B-spline (NURBS) implementation by Reid and detailed in [89] to give the terrain surface a visually bumpy texture. The constant torque results in continual acceleration of the wheel, and the effect of initializing the terrain with a bumpy surface can be seen in the oscillating response of the wheel slip rate, see Figure 6.64.

Wheel forward acceleration is due to a positive drawbar pull generated, shown in Figure 6.65. The bumpiness on the surface of the terrain is clearly evident in the curves for wheel thrust, motion resistance and drawbar pull. Frequency of vibrations are based on the vehicle speed and the wavelength of the NURBS superimposed on the terrain surface.

Contact normal and shear stress along the centerline of the of the tire at simulation times of 4, 12 and 20 seconds are shown in Figure 6.66. These simulation times correspond to wheel forward velocities of 0.34, 1.01 and 1.91 m/s, respectively. Both normal and shear stress distributions are clearly strong functions of the wheel forward velocity, indicated by Figure 6.66. This is the case

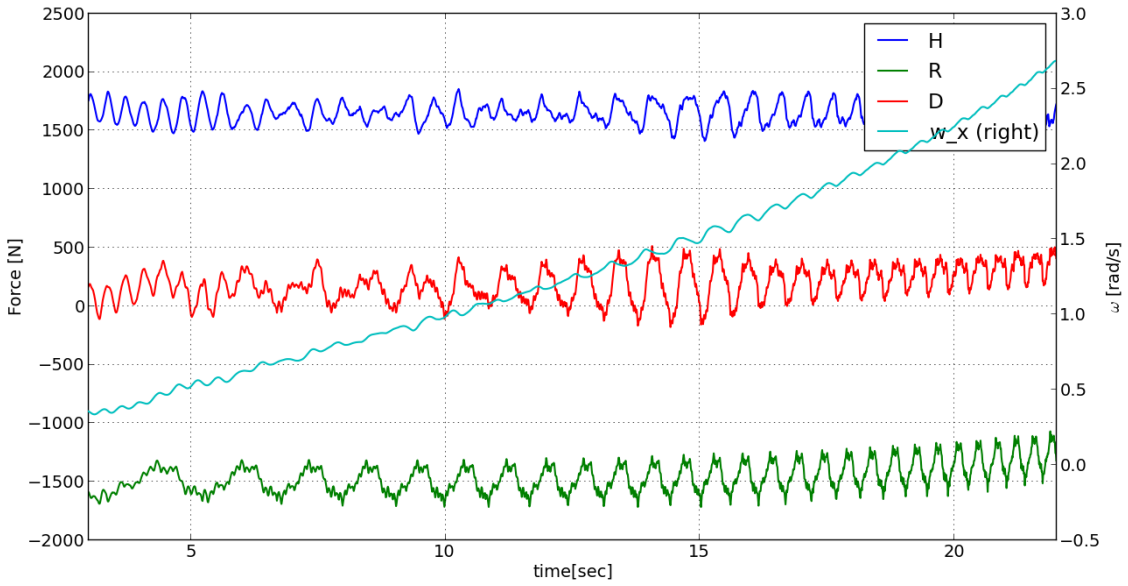

Figure 6.65: Dynamic tire thrust, motion resistance, drawbar pull and wheel angular velocity, tilled soil, 18 kN load, 18.4R38 tire, 85 kPa inflation pressure, 1600 N-m applied torque

even though the slip rate oscillated around 5% and seems to play no significant role in the amount of traction achieved by the tire driven with an applied torque.

6.4 Conclusions

The soil and tire models developed have parameters fitted based on those used in the experimental reports in [42], for two tire sizes, at two inflation pressures, operating at two soil compositions with a small and large system mass. Effects of inflation pressure on the 3-D contact stress profile on a flat, rigid surface were significant in both terms of absolute stress achieved as well as the stress distribution. The deformable tire model developed in Chapter 4, is tested using a variety of spring functions as trial inputs to the least squares parameter fitting method. When the spring is assumed to deform only in the radial direction (e.g., orthogonal to and passing through the wheel spin axis), tire pressure as a function of the square root of deflection results in the best fit. For the validation efforts the follow, a linear elastic spring is used for simplicity.

Validation efforts were aimed at the overall wheel in-plane mobility, which includes thrust, motion resistance, drawbar pull and the required driving torque for a specified wheel slip, Equation 4.8. A multibody dynamic tire testing rig was developed in the Chrono dynamics software and compared to the 2-D steady-state plastic equilibrium approach proposed by Wong and Reece [13, 14]. Good agreement was seen between the models for both the overall drawbar pull and required torque as a function of slip. However, due to the larger contact area of the dynamic tire model, motion resistance did not increase with the slip rate, unlike the WR model, which led to differences between drawbar pull at higher slip rates.

The tire and soil models were selected to allow a direct comparison with the experiments carried out by Wulfsohn and Upadhyaya [42, 41] in terms of the drawbar pull and the total change in soil volume associated with rutting. Good agreement in relative terms was seen, except in the case of a loose soil with a tire at low inflation pressure. In this case the large lugs had a significant effect on providing additional thrust to the physical tire. It is clear that adding a layer to the tire model that considers these lug forces would be a beneficial addition to the developed software.

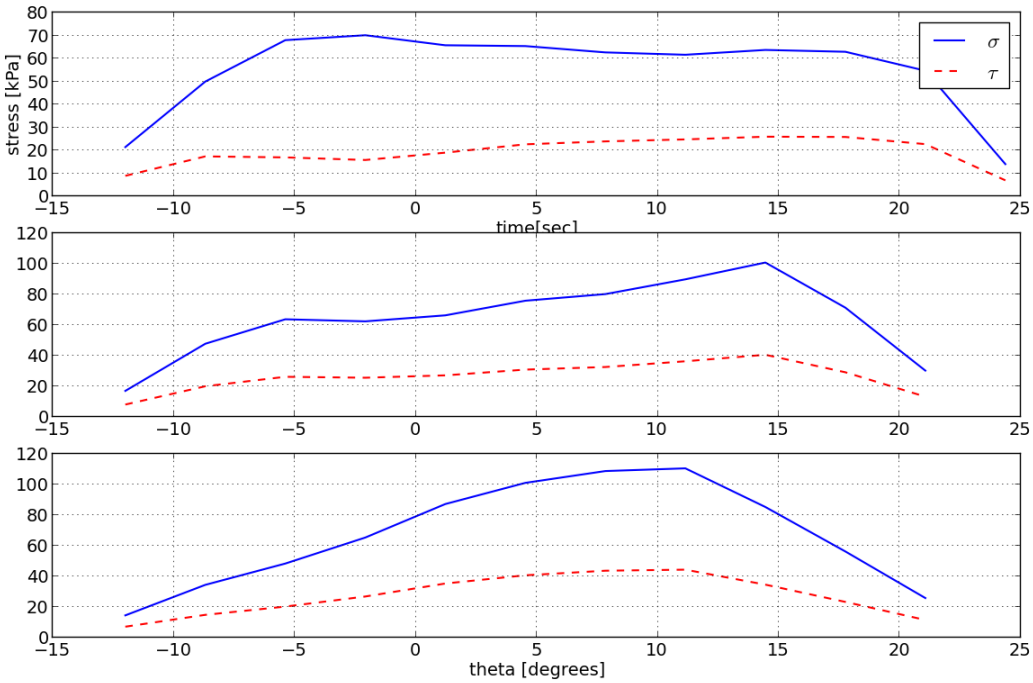

Figure 6.66: Dynamic tire normal and shear stress, tilled soil, 18 kN load, 18.4R38 tire, 85 kPa inflation pressure, 1600 N-m applied torque

The benefits of having a general purpose multibody representation of the tire and soil system is that the tire can be driven any number of ways as shown in Section 6.3.3. Rather than specify a slip rate, the dynamic tire was driven with a specified wheel angular velocity only. It was shown that the contact stress distributions vary substantially at different applied wheel angular velocities. This indicates that the current methods of considering the performance prediction as a function of slip does not include the entire picture. Specifying both the wheel forward and angular velocities adds a layer of fidelity that is needed when general purpose mobility scenarios are to be simulated. This is demonstrated when the tire has a constant torque applied to the wheel, leading to steady acceleration. As the tire gained velocity, the contact normal and shear stress distributions along the centerline of the tire were shown to differ significantly, owing to the dynamic nature of the simulation.

Chapter 7

Demonstration of Technology and Future Work

The newly developed contact and terrain are focused on allowing out of plane motion and repeated loading effects, which are expected when mobility simulations with realistic driver steering input are performed. Repeated loading of the soil is tested using the soil bin developed by driving forwards and backwards at a constant applied angular velocity. The response of each successive pass on the in-plane performance prediction, e.g. drawbar pull and torque, overall wheel sinkage and contact stresses is be analyzed.

One benefit of the contact model developed in Chapter 4 is that the deformable tire model can be replaced by any tire geometry that accurately describes the undeformed contact surface of the tire. A lugged agricultural tire with complex geometry represented with a triangle mesh is substituted for the torus shaped tire, and the results of the lugs on the response of the terrain is shown in Section 7.2.

A representative off-road multibody truck model is created in Chrono based on a detailed realistic full-vehicle HMMWV model created in the COTS ADAMS/Car [43]. It is a simplified 9-body model, but retains the overall vehicle mass and inertia values, as well as important suspension kinematic details, such as hard points locations, kinematics constraints and force elements. Simple out of plane motion is simulated using a full-vehicle model in order to exhibit the potential of the developed methods to capture the dynamic effects of general 3-D maneuvers on deformable soil. Straight-line acceleration/braking, turning and lane changes are a few of the planned maneuvers to simulate in the near future in which the motion of an entire vehicle is simulated and the response of the chassis is analyzed along with the performance prediction of the entire vehicle, e.g. required driving torque, vehicle towing capacity, etc.

7.1 Repeated Loading

The dynamic tire soil testing rig developed in the Chrono multibody dynamics engine and detailed in Section 6.3.1 uses the tire model parameters derived for the 18.4R32 tire at 85 kPa inflation pressure, with soil parameters derived for the tilled Yolo loam soil in Chapter 6, and is loaded with a sprung mass of 2753 kg.

An applied angular velocity is applied to drive the tire back and forth over a common section of soil. To keep the dynamic system stable, the angular velocity is ramped from the positive to negative value of the spin rate. An applied wheel angular velocity of 3 rad/sec is used to drive the wheel, and the overall wheel drawbar pull and torque are analyzed, along with the sinkage on each pass and the stress distributions on different passes.

The forward velocity, spin rate and slip rate is plotted in Figure 7.1 for a total of 5 passes, where the dynamic effects of changing the direction of the testing rig is evident in the noise of the slip rate.

Total wheel sinkage is shown with wheel spin rate in Figure 7.2, where the average sinkage at each successive pass is approximately: 13.2, 15.3, 16.4, 16.9, 17.2 and 17.4 cm. These results highlight the strain-hardening effect of the combined soil and tire models, where the change in sinkage after each pass is 2.1, 1.1, 0.5, 0.3 and 0.2 cm.

Contact normal and shear stress along the centerline of the tire at quasi-steady-state conditions is shown at three different passes, numbers 1, 3 and 5 in Figure 7.3. First, the contact angle is greatest on the first pass at about 33 degrees, whereas the contact angles on the 3rd and 5th passes are about 23 and 22 degrees, respectively. Second, the shape of the normal and shear stress distributions changes from a profile with two areas of maximum normal stress in the first pass, to a fairly uniformly distribution on the 5th pass. Maximum normal and shear stresses also increase with each pass.

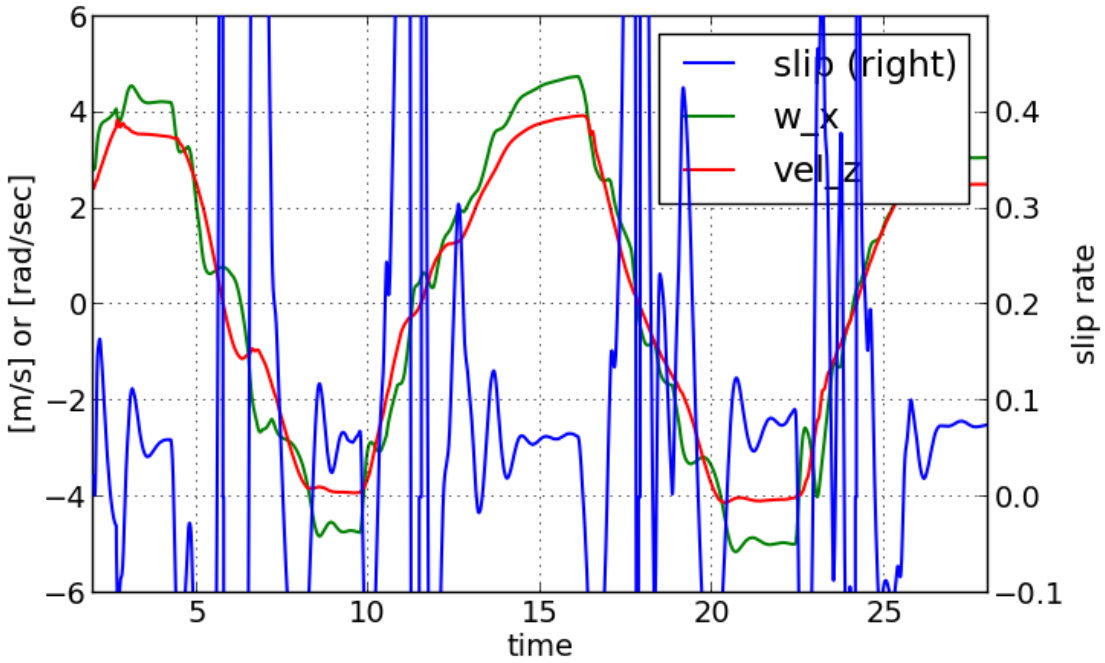

Figure 7.1: Repeated loading effects on dynamic forward velocity, wheel spin and slip rates, 3 rad/sec angular velocity, on tilled soil, 27 kN load, 18.4R38 tire

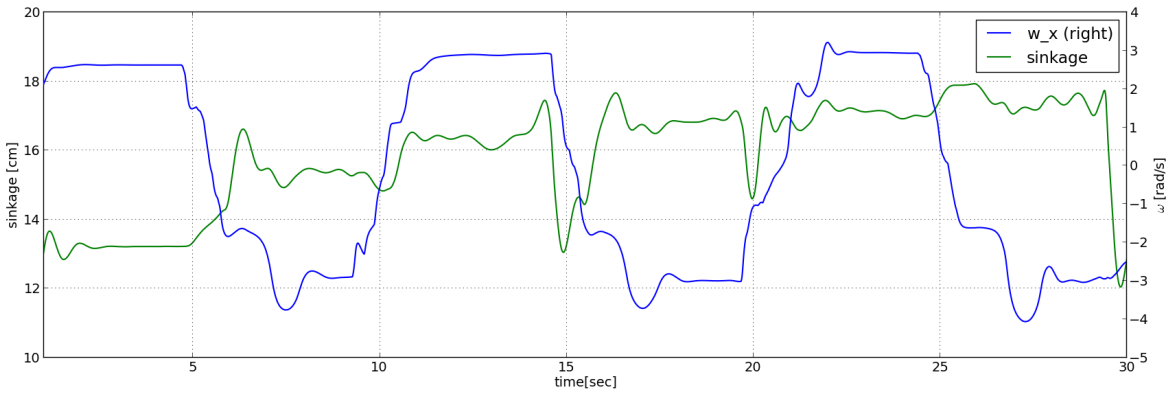

Figure 7.2: Repeated loading effects on wheel sinkage, 3 rad/sec angular velocity, on tilled soil, 27 kN load, 18.4R38 tire

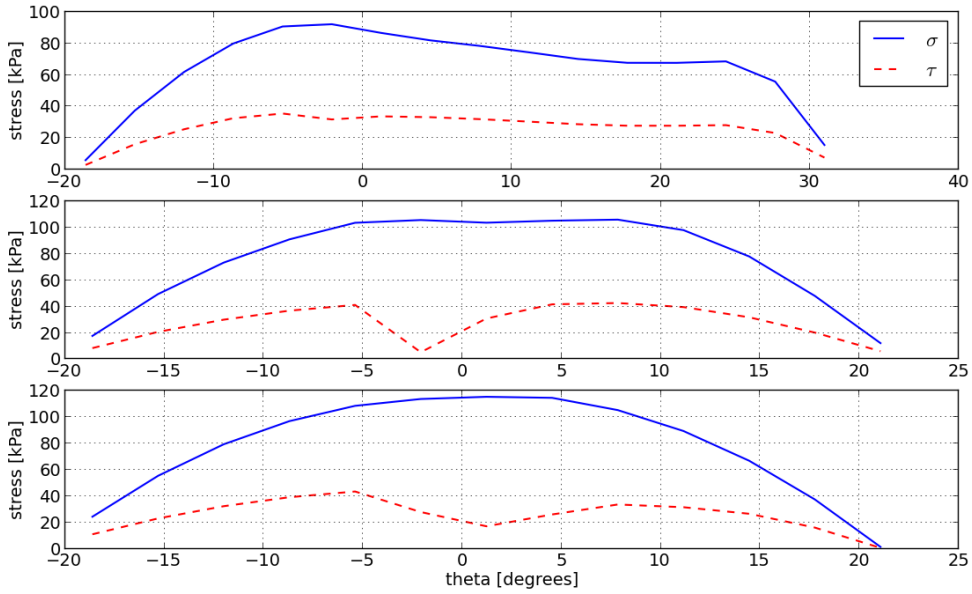

Figure 7.3: Repeated loading effects on contact normal and shear stress, pass number 1, 3 and 5, 3 rad/sec angular velocity, on tilled soil, 27 kN load, 18.4R38 tire

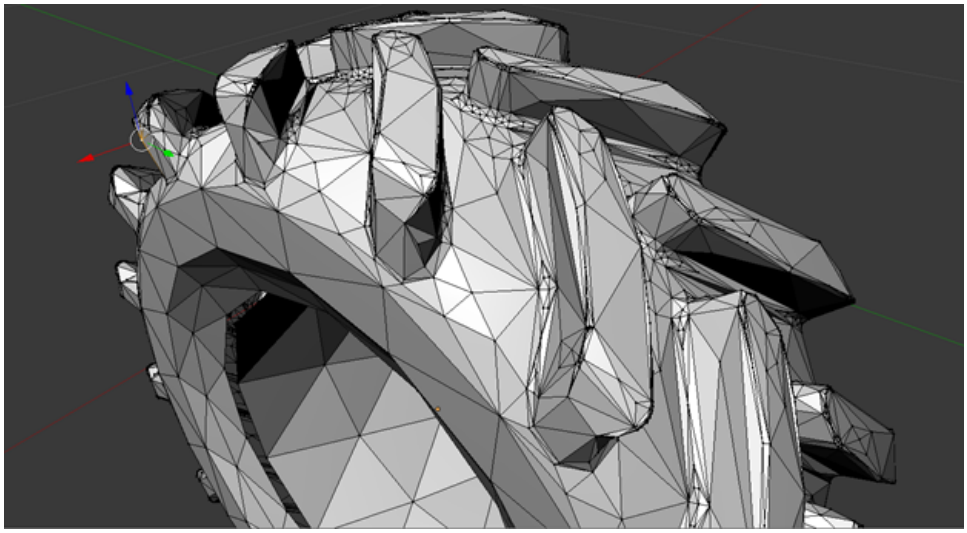

Figure 7.4: Tire geometry surface represented with a triangulation

7.2 General Tire Geometry

One of the benefits of the soil model accepting arbitrary force inputs at the surface is that any type or shape tire can be used, provided a constitutive normal and shear contact force can be derived from the available data. For example, an agricultural tire with a lugged surface is shown in Figure 7.4, where the surface is represented as a set of triangles.

Careful selection of the faces that contribute to the contact forces with the ground leads to a set of triangle faces with normals that are roughly orthogonal to the spin axis. The triangle faces define the tire node surfaces used in the normal stress calculation. Sides and faces of the lugs significantly affect the tractive ability of a vehicle by providing additional forces that shear and bulldoze the soil surrounding it. A similar deformable tire model is used to find the normal stresses, and the typical shear stress-shear displacement relations still hold on the triangle faces. The result of applying this tire to the soil model is shown in Figure 7.5, where the lugged pattern is clearly seen due to the increased sinkage.

The soil model is not limited to calculating the response from a tire, any traction element (or part of the vehicle) can be used as long as a contact force model is established and the order of operations discussed in Section 5.3 is followed.

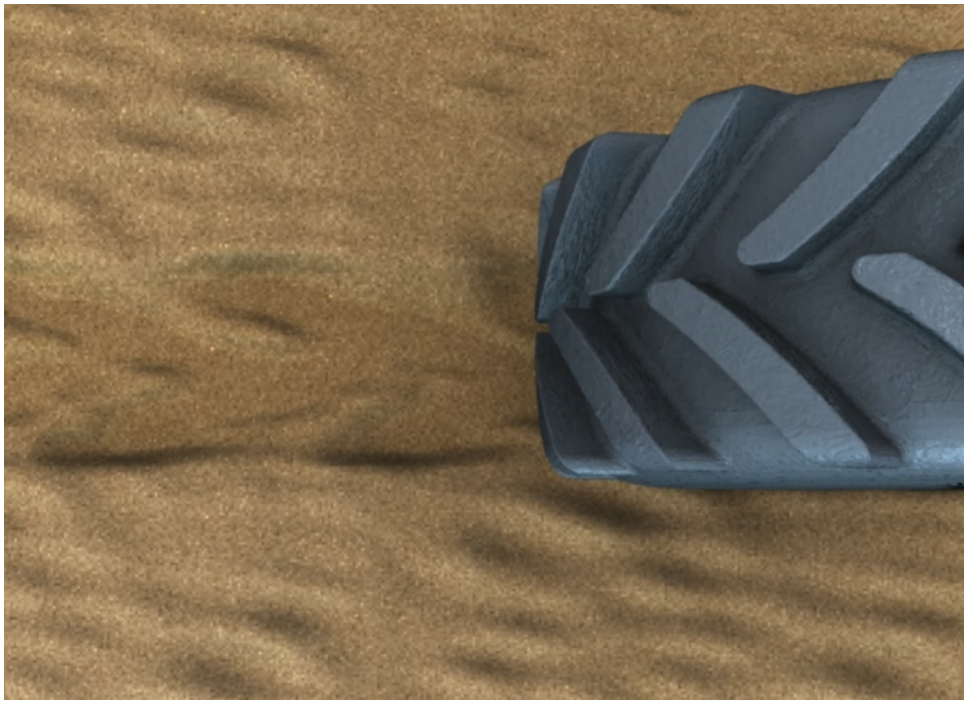

Figure 7.5: Lugged Tire and resulting footprint

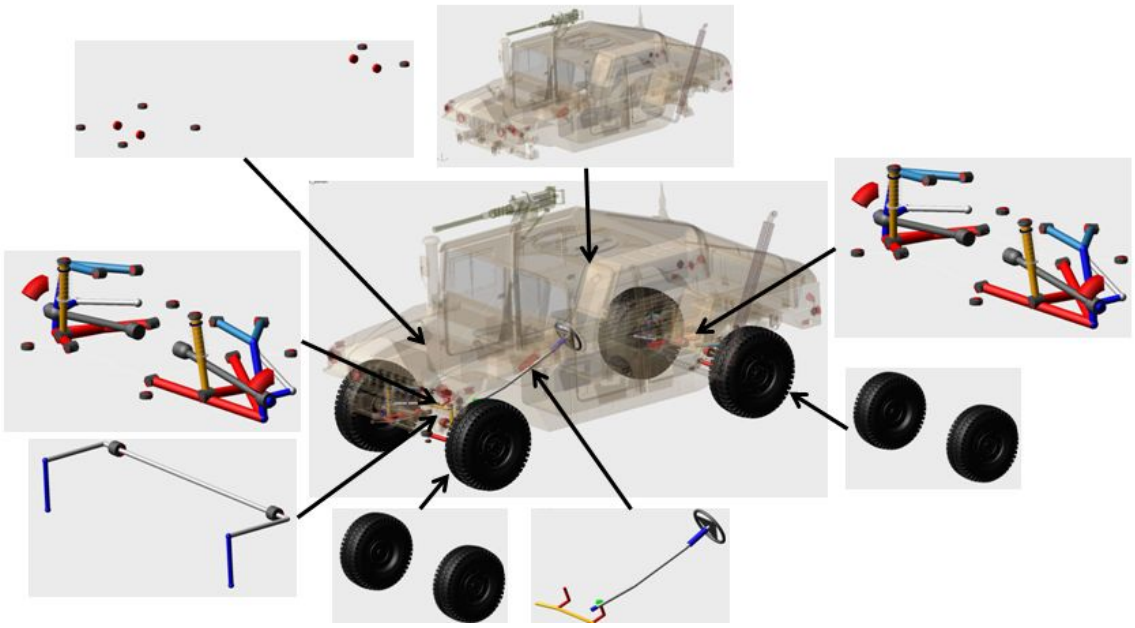

Figure 7.6: Multibody dynamics full-vehicle model in ADAMS/Car, shown as an assembly of subsystems

7.3 HMMWV Vehicle Dynamic Model

The original full-vehicle multibody HMMWV modeled in ADAMS/Car includes the following subsystems: chassis, front and rear suspension, anti-roll bar, steering, brakes, powertrain and four wheels. Note that only the wheels but not the tires are present in the multi-body vehicle model. A third-party software was used to represent the structural response of the elastic tire through co-simulation of a lumped mass-beam tire model. The suspension control arms are connected to the chassis with compliant bushing elements, and all four wheels are driven and receive equal power. The vehicle is shown in Figure 7.6 with the chassis geometry partially transparent to show the location of the subsystems that are combined to make the full vehicle assembly.

This model is typical of a combined multibody vehicle and tire model to perform mobility simulations to understand how the vehicle handles operating under a range of driver inputs (including steering, throttle and braking) on rigid road geometry and obstacles. The complexity of these mobility models is typically in the hundreds of modeling elements, including rigid bodies,

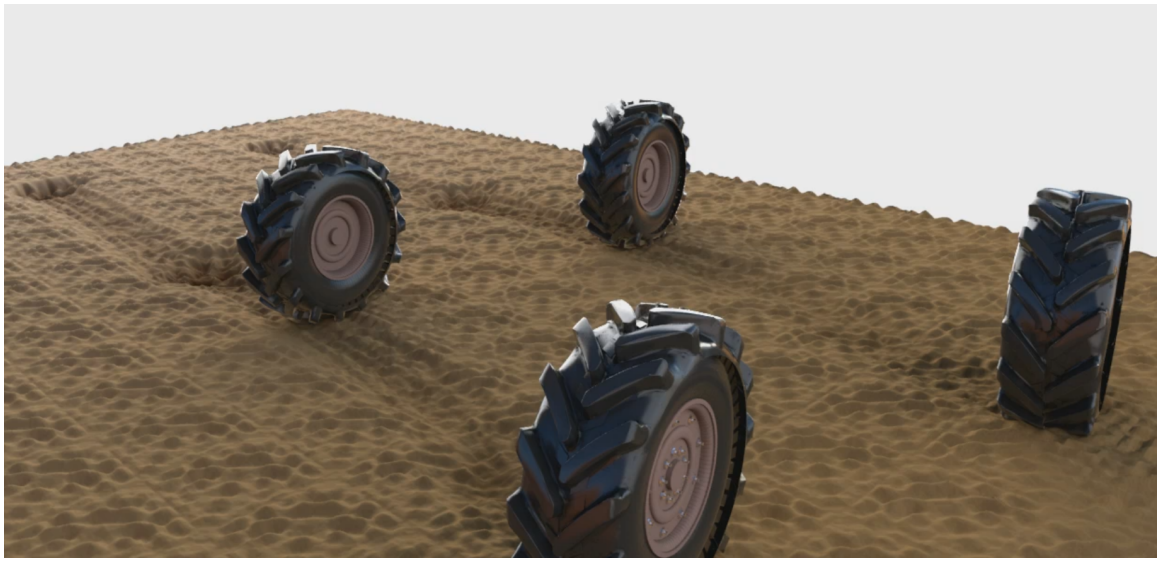

Figure 7.7: Multibody dynamic full-vehicle model on soft soil

kinematic constraints, force elements and motions. Simulation run-times are near real-time if no special modeling elements are present (Finite Elements, Controls, Contact and Impact, etc.).

As a first investigation into the response of a full multi-body vehicle model on the developed contact force and terrain models, a simplified 9 body vehicle model is developed. A chassis is constrained to four bodies representing the suspension uprights for each tire. Each upright constraint includes four massless links to the chassis to model the kinematics of the upper and lower control rods of each suspension subsystem. Each upright has a spring/damper connected to the chassis to represent the shocks. Each spindle has a wheel body constrained to it via a revolute joint; these wheels are the recipient of the reaction forces calculated by the terrain models.

An example of the four wheels of the vehicle on the soft soil database is shown in Figure 7.7, where only the tires are shown with the terrain surface. The footprint of the tires can clearly be seen as it slides down the inclined surface, and the geometry and path of the ruts effects the dynamic response of the vehicle.

Simulations similar to those run for the validation experiments in Section 6 could be applied to the full vehicle, to predict the full vehicle drawbar pull, or required torque to maintain a certain speed in a soft soil. Repeated loading effects involving a convoy of vehicles would provide

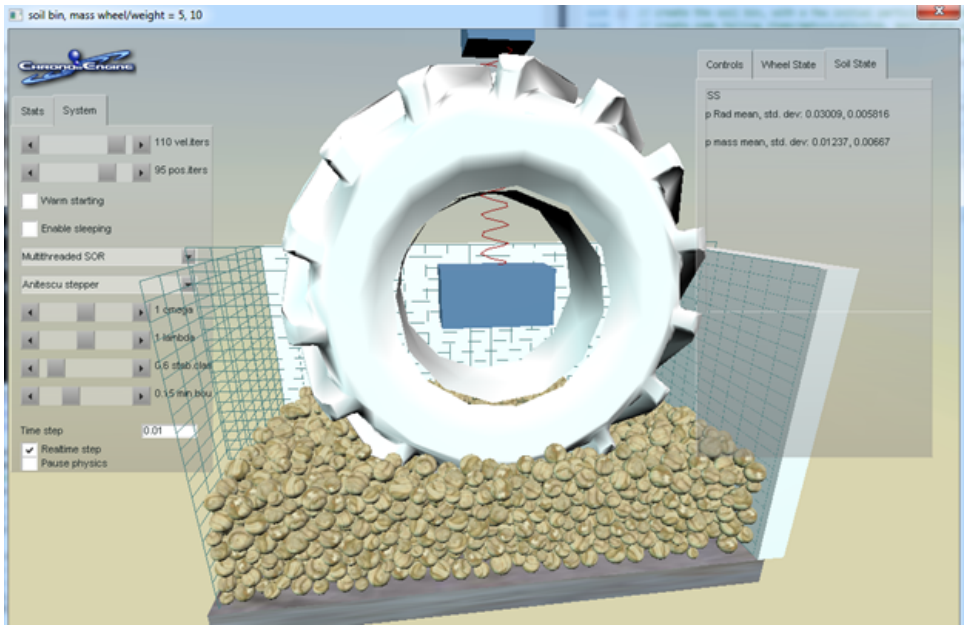

Figure 7.8: Multibody tire testing rig, soil modeled with rigid bodies

interesting results on the mobility requirements of the first, 10th, and so, vehicle to pass a broken trail.

7.4 Current Research

The dynamic in-plane tire testing rig can be used with other modeling components already present in Chrono, where the soil model is replaced by a system of rigid particles interacting through contact and friction, which can also be used to model tire/soil interaction, but on a much finer scale as shown in Figure 7.8.

These types of discrete element methods are ideal for frictional sandy and grainy type soils that are near incompressible and tend to flow rather easily. As shown in Figure 7.9, the dynamics between the tire and the particles in the contact patch is extremely complex and creates shear failure planes that require many particles to capture accurately. Research to understand how to generate constitutive material models that are physically accurate needs to be undertaken before these types of models can be used in the design cycle with efficiency and confidence. However,

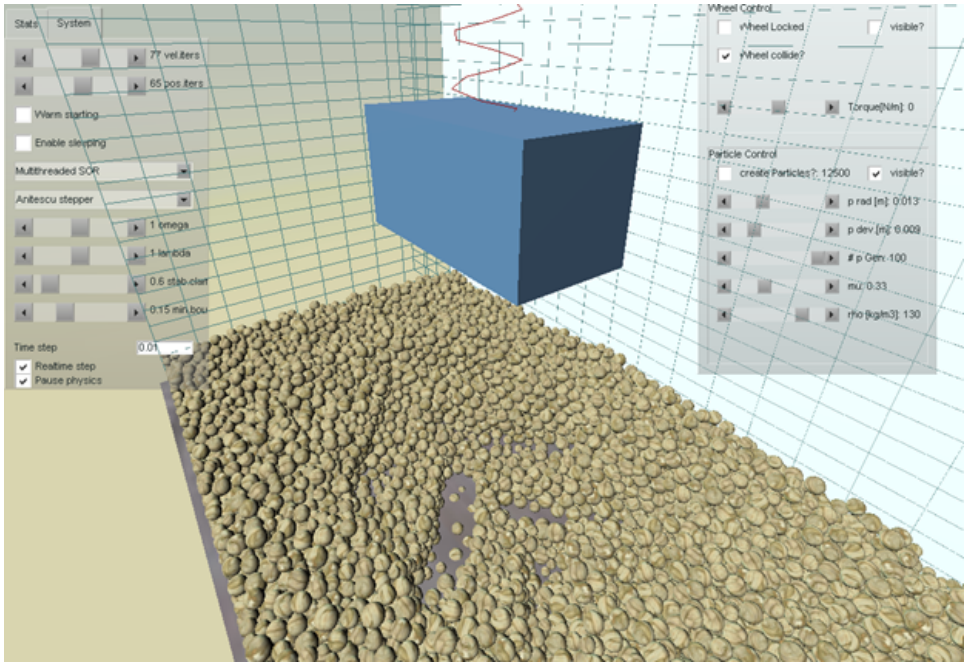

Figure 7.9: Lugged tire (not shown) footprint, soil modeled with rigid bodies

fully physics-based methods such as these offer the broadest range of applications and operating conditions when considering off-road mobility scenarios to be simulated.

7.5 Future Work

The terrain surface was allowed to deform due to soil strain but for model development purposes was considered initially flat. As shown in Section 7.3, the terrain surface can have the discrete coordinate heights set using B-Splines to describe the bumpiness and waviness in the lateral and longitudinal directions [89]. Typically the size of these obstacles is small in comparison to the tire size and overall soil vertical deflections and they serve a mostly visual purpose. Macro-scale terrain obstacles such as hills, inclines, large ditches or riverbeds, or change in surface grade have a large impact on vehicle dynamics when the road is considered rigid, as discussed in [93] and [43]. In fact, the software can easily be extended to enable accurate generation of terrain topography based on satellite imagery, e.g. digit elevation models, or polygonal representations. To

facilitate fast and efficient storage and querying of the terrain surface, a quad-tree type data structure is maintained that dynamically initializes soil coordinates and soil finite volumes the first time it is encountered, then swaps areas of the terrain in and out of local memory depending on their proximity to the vehicle. Dynamic initialization of terrain data will involve one extra step, where the initial terrain height is referenced from an external database for a given (x, y) coordinate on the terrain surface.

Further investigation into the calculation of the initial density as a function of depth below the surface is motivated by the experimental results in [41], where tilled and firm clayey loam soil saw significant deviation in dry bulk density with depth. Is the current model sufficient in assuming the initial dry bulk density of the soil is homogeneous when calculating the dynamic tire performance, or does the non-homogeneous behavior need to be considered? In the developed terrain model, it is possible to initialize each soil finite volume using different initial conditions and soil model parameters, allowing non-homogeneous soil to be analyzed using these methods.

The use of a structural tire model can accommodate the inclusion of the tire belt and carcass dynamics by extending the contact model in Chapter 4 to apply the calculated normal and shear stress to the tire surface nodes rather than calculating the overall reaction forces and torques on the wheel, Section 4.3. Initial development of a 2-D Finite Element elastic ring tire model based on the Absolute Nodal Coordinate Formulation was developed in MATLAB to evaluate the model proposed by Sugiyama [104] for this purpose. Lumped mass-spring-damper tire models are popular for handling and noise-vibration-harshness analysis in commercial software, and could be used as well [1, 45], granted they adhere to the Standard Tire Interface. Depending on the frequency response range of interest, different tire models are appropriate for on-road vehicle dynamics analysis, ranging from simple to highly-complex [47, 46]. A similar taxonomy for selecting an appropriate tire model in terramechanics simulations will be developed, with the caveat that the method for representing the soil can vary greatly, from empirical methods [12] to mesh-free continuum methods to capture compressibility and mass flow effects [36, 37, 105].

Methods for developing DVI particle-based representations of soils, sands and gravels under vehicle type loads is underway in the Simulation Based Engineering Lab (SBEL), modeling both

dry-frictional material as well as cohesive soils. Validation efforts led by Melanz, [93], investigate the simulation stability and convergence issues and how to determine specific material properties (e.g., bulk density) through shear box virtual testing. Extremely transient maneuvers or very flowable/weak soils that cause extensive localized soil shear failure would benefit from being able to utilize this type of tire/soil model. Issues are present on the computational side as well; in order to integrate this type of particle model into a usable terrain geometry database requires continuous to discrete model homogenization techniques to be developed and validated.

Many other applications outside of vehicle mobility and tire/soil interaction can be realized using the developed methods. Machine instrument/soil interaction could be used to virtually test bulldozers and other earth moving equipment, while simultaneously being used to assess the wheel/-track and ground interaction effects as well. Mining equipment including any type of shovel or dredging device could leverage these methods, with an opportunity to investigate fracture mechanics models in particle systems of varying composition, strength and particle size, shape or distribution when being dug or drilled.

High Performance Computing allows large particle systems to be simulated, so esoteric studies like those investigating the Terradynamics of desert animals [106] can be extended to a 3-D model where out-of-plane effects can be investigated. Space related applications include rover mobility on planetary surfaces, or asteroid drilling analysis [107].

Chapter 8

Conclusions

8.1 Summary of Work and Contributions

In lieu of using computationally expensive and complex FEM or DEM models, a tire-terrain contact model was developed which is quasi-static but incorporates both tire elastic properties and soil plastic strength into the calculation of contact stresses, 4. The tire model is built in conjunction with a terrain model that maintains the terrain surface height and the state of the soil affected by loading. This allows strain-hardening and rebound to be incorporated into the soil response, which is necessary to accurately capture both the contact patch and resulting soil compaction as detailed by [42] and discussed in Section 2.4.

These models were implemented into a set of C++ libraries that are integrated into existing software solutions for modeling and simulating multibody vehicle dynamics. Profiling was performed and many parts of the developed terrain models are accelerated using parallel CPU and GPU hardware, and speedups on the order of 9x were seen when increasing the number of parallel CPU cores from 1 to 24; GPU speedups of over 5x were achieved as the fidelity of the terrain was increased (e.g., more calculations per time step) as described in Section 5.4.

Model parameter identification was based on a Least Squares approach with available tire and soil experimental data in Chapter 6. The Python source code used in the analysis is available on author's Github page [108]. The soil and tire models developed have parameters fitted based on those used in the experimental reports in [42, 41], for two tire sizes, at two inflation pressures, operating at two soil compositions with a small and large system mass.

The deformable tire model developed in Chapter 4, is tested using a variety of spring functions as trial inputs to the least squares parameter fitting method to find the best fitting form to Equation 4.5. When the spring is assumed to deform only in the radial direction (e.g., orthogonal to and passing through the wheel spin axis), tire pressure as a function of the square root of deflection results in the best fit. For the validation efforts the follow, a linear elastic spring was used for simplicity.

The model was validated by comparing overall wheel in-plane mobility, which includes: thrust, motion resistance, drawbar pull and the required driving torque, at a range of specified wheel slips, Equation 4.8. A multibody dynamic tire testing rig was developed in the Chrono dynamics software and compared to the 2-D steady-state plastic equilibrium approach proposed by Wong and Reece [13, 14]. Good agreement was seen between the models for both the overall drawbar pull and required torque as a function of slip. However, due to the larger contact area of the dynamic tire model, motion resistance did not increase with the slip rate, unlike the WR model, which led to differences between drawbar pull at higher slip rates. The developed model showed an improvement over the 2-D steady-state Wong/Reece method described in Section 2.3 by allowing general 3-D motions and torques to dynamically drive the tire.

The tire and soil models were selected to allow a direct comparison with the experiments carried out by Wulfsohn and Upadhyaya [42, 41]. Good agreement was seen in general, except for a handful of tests at low inflation pressure in soft soil, where the tire lugs contribute a significant extra amount of tractive effort. It is clear that adding a layer to the tire model that considers lug forces would be a beneficial addition to the developed software.

Rather than specify a slip rate, the dynamic tire was driven with a specified wheel angular velocity only. It was shown that the contact stress distributions vary substantially at different applied wheel angular velocities, indicating that considering the performance prediction as a function of slip only does not fully capture the wheel velocity effects. A number of additional features of the developed tire and terrain models were discussed in Chapter 7, including non-flat terrain and out of plane motion of a simplified vehicle model with four wheels. Also, any type of tire or traction

element geometry definition can be used, allowing tracked vehicles or parts of the chassis in the contact model.

The specific accomplishments of this work are:

- Developed and implemented a deformable terrain model for use in multibody vehicle mobility simulations. Allows for transient and out-of-plane driving scenarios such as braking or lane-change maneuvers.
  - Developed a method to approximate the vertical stress field due to an arbitrary normal and shear stress distribution applied to the soil surface.
  - Developed a method to track plastic volumetric strain based on loading-unloading cycles. Collaboration with University of Tennessee yielded a method to identify the soil model parameters based on soil mechanical experimental data.
  - Implemented the above algorithms in the context of a terrain database that is integrated to a multibody dynamics software engine, Chrono. Multibody models simulated include the tire testing rig used for the validation studies, as well as the simple vehicle model.
  - Alleviated the computational bottlenecks by leveraging parallel CPU/GPU hardware support in key locations of the algorithms.
- Developed and implemented a contact patch model to complement the deformable terrain model for vehicles with pneumatic tires. Specifically considered non-uniform normal and shear stress in the lateral tire direction, to better describe the non-symmetric contact stress distributions of an agricultural tire operating on soft soil in [42].
  - Developed a method to calculate normal stress distribution for soil-tire contact based on the contact geometry, deformable tire effects and the bearing capacity of the soil.
  - Developed a method to calibrate the deformable tire model parameters based on the inflation pressure from readily available manufacturer tire load-deflection test data. Also calibrated tire contact geometry cross-section dimension based on related test data.

  - Implemented these models into the vehicle simulation framework in a similar way as the terrain model.

- Validated results of single tire in-plane performance prediction with both Wong-Reece analytical results as well as experimental data in terms of drawbar pull, motion resistance, thrust, and wheel torque as a function of wheel slip.

- Validated results of single tire in-plane contact stress distributions based on the Wong-Reece analytical methods.

- Demonstration of technology includes analysis of repeated-loading effects, the ability to drive the tire dynamically with an applied torque, ability to use general traction element geometry, and the terrain surface to be initialized as a non-flat surface.

LIST OF REFERENCES

[1] M. Gipser. Ftire - the tire simulation model for all applications related to vehicle dynamics. *Vehicle System Dynamics*, 45(139-151):139–151, 2007.

[2] J. Madsen, D. Ghiocel, D. Gorsich, D. Lamb, and D. Negrut. A stochastic approach to integrated vehicle reliability prediction. In *ASME 2009 International Design Engineering Technical Conferences and Computers and Information in Engineering Conference*, pages 2035–2047. American Society of Mechanical Engineers, 2009.

[3] C. Harnisch, B. Lach, R. Jakobs, M. Troulis, and O. Nehls. A new tyre-soil interaction model for vehicle simulation on deformable ground. *Vehicle System Dynamics*, 43:384–394, 2005.

[4] J. Slattengren. Utilization of adams to predict tracked vehicle performance. *SAE transactions*, 109(2):1–7, 2000.

[5] K. Iagnemma, C. Senatore, B. Trease, R. Arvidson, K. Bennett, A. Shaw, F. Zhou, L. Van Dyke, and R. Lindemann. Terramechanics modeling of mars surface exploration rovers for simulation and parameter estimation. In *ASME IDETC*, 2011.

[6] K. Xia and Y. Yang. Three-dimensional finite element modeling of tire/ground interaction. *International journal for numerical and analytical methods in geomechanics*, 36(4):498–516, 2012.

[7] A. A. Rula and C. J. Nuttall Jr. An analysis of ground mobility models (anamob). Technical Report AEWES-TR-M-71-4, Army Engineer Waterways Experiment Station, Vicksburg MS, 1971.

[8] R. B. Ahlvin and P. W. Haley. *NATO Reference Mobility Model: Edition II. NRMM User's Guide*. US Army Engineer Waterways Experiment Station, 1992.

[9] M. G. Bekker. *Introduction to terrain-vehicle systems*. University of Michigan Press, Ann Arbor, MI, 1969.

[10] A. Reece. Principles of soil-vehicle mechanics. *Proceedings of the Institution of Mechanical Engineers: Automobile Division*, 180(1):45–66, 1965.

[11] Z. Janosi and B. Hanamoto. The analytical determination of drawbar pull as a function of slip for tracked vehicles in deformable soils. In *Proc of the 1st int conf mech soil–vehicle systems. Turin, Italy*, 1961.

[12] M. G. Bekker. *Theory of land locomotion; the mechanics of vehicle mobility*. University of Michigan Press, Ann Arbor,, 1956.

[13] J. Y. Wong and A. R. Reece. Prediction of rigid wheel performance based on the analysis of soil-wheel stresses part i. performance of driven rigid wheels. *Journal of Terramechanics*, 4(1):81–98, 1967.

[14] J.-Y. Wong and A. R. Reece. Prediction of rigid wheel performance based on the analysis of soil-wheel stresses: Part ii. performance of towed rigid wheels. *Journal of Terramechanics*, 4(2):7–25, 1967.

[15] M. Lyasko. Multi-pass effect on off-road vehicle tractive performance. *Journal of Terramechanics*, 47(5):275–294, 2010.

[16] G. Meirion-Griffith and M. Spenko. A modified pressure-sinkage model for small, rigid wheels on deformable terrains. *Journal of Terramechanics*, 48(2):149–155, 2011.

[17] G. Meirion-Griffith and M. Spenko. A pressure-sinkage model for small-diameter wheels on compactive, deformable terrain. *Journal of Terramechanics*, 50:37–44, 2012.

[18] J. Y. Wong. *Terramechanics and off-road vehicles*. Elsevier, 1989.

[19] I. Schmid. Interaction of vehicle and terrain results from 10 years research at ikk. *J. of Terramechanics*, 32(1):3–26, 1995.

[20] B. Trease, R. Arvidson, R. Lindemann, K. Bennett, F. Zhou, K. Iagnemma, C. Senatore, and L. Van Dyke. Dynamic modeling and soil mechanics for path planning of the mars exploration rovers. In *ASME IDETC*, pages 755–765. American Society of Mechanical Engineers, 2011.

[21] B. Chan, N. Thompson, C. Sandu, and H. Dankowicz. A novel tire-soil interaction model for simulation of off-road vehicles. In *Proc. of the 15th Conference of the ISTVS*, volume 16, pages 25–29, 2005.

[22] A. Azimi, J. Kovecses, and J. Angeles. Wheel-soil interaction model for rover simulation based on plasticity theory. In *Intelligent Robots and Systems (IROS), 2011 IEEE/RSJ International Conference on*, pages 280–285. IEEE, 2011.

[23] D. Rubinstein and J. L. Coppock. A detailed single-link track model for multi-body dynamic simulation of crawlers. *Journal of Terramechanics*, 44(5):355–364, 2007.

[24] H. Shibly, K. Iagnemma, and S. Dubowsky. An equivalent soil mechanics formulation for rigid wheels in deformable terrain, with application to planetary exploration rovers. *Journal of Terramechanics*, 42(1):1–13, 2005.

[25] B. Schafer, A. Gibbesch, R. Krenn, and B. Rebele. Planetary rover mobility simulation on soft and uneven terrain. *Vehicle System Dynamics*, 48(1):149–169, 2010.

[26] J. Hambleton and A. Drescher. Modeling wheel-induced rutting in soils: indentation. *Journal of Terramechanics*, 45(6):201–211, 2008.

[27] J. Hambleton and A. Drescher. Modeling wheel-induced rutting in soils: Rolling. *Journal of Terramechanics*, 46(2):35–47, 2009.

[28] C. W. Fervers. Improved FEM simulation model for tiresoil interaction. *Journal of Terramechanics*, 41(2):87–100, 2004.

[29] S. Shoop. *Finite Element Modeling of Tire-Terrain Interaction*. Thesis, University of Michigan, 2001.

[30] K. Xia. Finite element modeling of tire/terrain interaction: Application to predicting soil compaction and tire mobility. *Journal of Terramechanics*, 48(2):113–123, 2011.

[31] J. Madsen, D. Lamb, T. Heyn, and D. Negrut. GPU-based high performance parallel simulation of tracked vehicle operating on granular terrain. In *SAE World Congress*, pages 05–22, 2010.

[32] T. Heyn. *On the Modeling, Simulation and Visualization of Many-Body Dynamics Problems with Friction and Contact*. PhD thesis, University of Wisconsin - Madison, 2013.

[33] H. Nakashima and A. Oida. Algorithm and implementation of soil-tire contact analysis code based on dynamic fe-de method. *Journal of Terramechanics*, 41(2):127–137, 2004.

[34] H. Nakashima, H. Fujii, A. Oida, M. Momozu, H. Kanamori, S. Aoki, T. Yokoyama, H. Shimizu, J. Miyasaka, and K. Ohdoi. Discrete element method analysis of single wheel performance for a small lunar rover on sloped terrain. *Journal of Terramechanics*, 47(5):307–321, 2010.

[35] M. A. Knuth, J. Johnson, M. Hopkins, R. Sullivan, and J. Moore. Discrete element modeling of a mars exploration rover wheel in granular material. *Journal of Terramechanics*, 49(1):27–36, 2012.

[36] H. Bui, R. Fukagawa, K. Sako, and O. Shintaro. Lagrangian meshfree particles method (sph) for large deformation and failure flows of geomaterial using elastic-plastic soil constitutive model. *Int. J. of Numer. Anal. Meth. Geomech.*, 32:1537–1570, 2008.

[37] H. H. Bui and R. Fukagawa. An improved sph method for saturated soils and its application to investigate the mechanisms of embankment failure: Case of hydrostatic pore water pressure. *International Journal for Numerical and Analytical Methods in Geomechanics*, 37(1):31–50, 2013.

[38] B. J.-Y. Chan. *Development of an off-road capable tire model for vehicle dynamics simulations*. PhD thesis, Virginia Polytechnic Institute and State University, 2008.

[39] I. Shmulevich. State of the art modeling of soiltillage interaction using discrete element method. *Soil and Tillage Research*, 111(1):41–53, 2010.

[40] P. Ayers, G. Bozdech, J. Freeman, A. Reid, and J. O'Kins. Soil engineering property determination for military vehicle terrain interaction model. In *ASABE Annual International Meeting*, 2012.

[41] D. Wulfsohn and S. K. Upadhyaya. Prediction of traction and soil compaction using three-dimensional soil-tyre contact profile. *Journal of Terramechanics*, 29(6):541–564, 1992.

[42] D. Wulfsohn and S. Upadhyaya. Determination of dynamic three-dimensional soil-tyre contact profile. *J. of Terramechanics*, 29(4-5):433–464, 1992.

[43] J. Madsen. *A Stochastic Framework for Ground Vehicle Simulation*. Thesis, University of Wisconsin - Madison, 2009.

[44] H. B. Pacejka and E. Bakker. The magic formula tyre model. *Vehicle system dynamics*, 21(51):1–18, 1992.

[45] A. Gallrein and M. Baacker. CDtire: a tire model for comfort and durability applications. *Vehicle System Dynamics*, 45(S1):67–77, 2007.

[46] P. Lugner, H. Pacejka, and M. Plochl. Recent advances in tyre models and testing procedures. *Vehicle System Dynamics*, 43(6-7):413–436, 2005.

[47] D. Ammon. Vehicle dynamics analysis tasks and related tyre simulation challenges. *Vehicle System Dyna*, 43:30–47, 2005.

[48] A. Azimi, J. Kovecses, and J. Angeles. Wheel-soil interaction model for rover simulation and analysis using elastoplasticity theory. *IEEE Ttransactions on Robotics*, 29:1271–1288, 2013.

[49] Vehicle dynamics terminology, standard j 670. *Society of Automotive Engineers*.

[50] A. Riedel. Standard tire interface. *TYDEX Working Group, December*, 1996.

[51] M. G. Bekker. *Off-the-road locomotion; research and development in terramechanics*. University of Michigan Press, Ann Arbor,, 1960.

[52] J. Y. Wong. *Theory of ground vehicles*. J. Wiley, New York, N.Y., 2nd edition, 1993.

[53] B. Hanamoto and E. H. Jebe. Size effects in the measurement of soil strength parameters. Report, Army Tank-Automotive Command - Warren, MI, 1963.

[54] K. Terzaghi. *Soil mechanics in engineering practice*. John Wiley & Sons, 1996.

[55] D. Schuring and R. Emori. Soil deforming processes and dimensional analysis. Report, SAE, 1964.

[56] V. Kacigin and V. Guskov. The basis of tractor performance theory. *J. of Terramechanics*, 5(3):43–66, 1968.

[57] J. Wong and J. Preston-Thomas. On the characterization of the shear stress-displacement relationship of terrain. *Journal of Terramechanics*, 19(4):225–234, 1983.

[58] A. Grecenko. Thrust and slip of a low-pressure tire on compressible ground by the compression-sliding approach. *Journal of Terramechanics*, 47(4):249–259, 2010.

[59] A. Grecenko. Compression-sliding approach: Dependence of transitional displacement of a driving element on its size and load. *Journal of Terramechanics*, 48(5):325–332, 2011.

[60] M. Lyasko. The determination of deflection and contact characteristics of a pneumatic tire on a rigid surface. *Journal of Terramechanics*, 31(4):239–246, 1994.

[61] T. Keller and M. Lamande. Challenges in the development of analytical soil compaction models. *Soil and Tillage Research*, 111(1):54–64, 2010.

[62] C. Liu and J. Wong. Numerical simulations of tire-soil interaction based on critical state soil mechanics. *J. of Terramechanics*, 33(5):209–221, 1996.

[63] T. R. Way, T. Kishimoto, H. Allen Torbert, E. C. Burt, and A. C. Bailey. Tractor tire aspect ratio effects on soil bulk density and cone index. *Journal of terramechanics*, 46:29–34, 2009.

[64] R. Raper. Agricultural traffic impacts on soil. *Journal of Terramechanics*, 42:259–280, 2005.

[65] P. Defossez and G. Richard. Models of soil compaction due to traffic and their evaluation. *Soil & Tillage Research*, 67(67):41–64, 2002.

[66] R. Gibson. Some results concerning displacements and stresses in a non-homogeneous elastic half-space. *Geotechnique*, 17:58–67, 1967.

[67] J. Boussinesq. Application des potentiels a l'etude de l'equilibre et du mouvement des solides elastiques. *Gauthier-Villars, Paris*, 1885.

[68] V. Cerruti. Ricerche intorno all'equilibrio de corpi elastici isotropi. *Reale Accademia dei lincei*, 13, 1881-1882.

[69] J. Feda and Z. P. Bazant. *Stress in subsoil and methods of final settlement calculation*. Developments in geotechnical engineering. Elsevier Scientific Pub. Co., Amsterdam ; New York, 1978.

[70] H. G. Poulos and E. H. Davis. Elastic solutions for soil and rock mechanics. 1974.

[71] A. J. Koolen and H. Kuipers. *Agricultural soil mechanics*. Springer-Verlag, 1983.

[72] P. Ayers and J. Van Riper. Stress distribution under a uniformly loaded rectangular area in agricultural soils. *Trans. of the ASAE*, 34(3):706–710, 1991.

[73] D. M. Wood. *Soil behaviour and critical state soil mechanics*. Cambridge University press, 1990.

[74] J. Graham and G. Houlsby. Anisotropic elasticity of a natural clay. *Geotechnique*, 33(2):165–180, 1983.

[75] L. Resende and J. B. Martin. Formulation of drucker-prager cap model. *Journal of Engineering Mechanics*, 111(7):855–881, 1985.

[76] L. Karafiath and E. Nowatzki. *Soil Mechanics for Off-Road Vehicle Engineering*. Trans. Tech Publications, Aedermannsdorf, Switzerland, 1978.

[77] Y. He, J. Cremer, and Y. Papelis. Real-time extendible-resolution display of on-line dynamic terrain. In *Graphics Interface*, 2002.

[78] W. Larson, S. Gupta, and R. Useche. Compression of agricultural soils from eight soil orders. *Soil Sci. Soc. Am. J.*, 44:450–457, 1980.

[79] J. Stone and W. Larson. Rebound of five one-dimensionally compressed unsaturated granular soils. *Soil Sci. Soc. Am. J.*, 44:819–822, 1980.

[80] P. Ayers, G. Bozdech, J. Freeman, A. Reid, and J. O'kins. Development of a dynamic visco-elastic vehicle-soil interaction model for rut depth, energy and power determinations. In *17th Intr. Conf. of the ISTVS*, 2011.

[81] D. W. Taylor. Fundamentals of soil mechanics. *Soil Science*, 66(2):161, 1948.

[82] S. Gupta and W. Larson. Estimating soil water retention characteristics from particle size distribution, organic matter percent, and bulk density. *Water Resources Research*, 15:1633–1635, 1979.

[83] J. Svendenius and M. Gafvert. A semi-empirical dynamic tire model for combined-slip forces. *Vehicle System Dynamics*, 44(2):189–208, 2006.

[84] G. E. V. Berg and W. R. Gill. *Pressure distribution between a smooth tire and soil*. American Society of Agricultural Engineers, 1959.

[85] A. N. Gent and J. D. Walter. Pneumatic tire. Report, NationalHighway,Traffic and-SafetyAdministration, 2006.

[86] J. Madsen, D. Negrut, A. Reid, A. Seidl, P. Ayers, G. Bozdech, J. Freeman, and J. OKins. A physics-based vehicle/terrain interaction model for soft soil off-road vehicle simulations. *SAE International Journal of Commercial Vehicles*, 5(1):280–290, 2012.

[87] S. A. Shoop, P. W. Richmond, and J. Lacombe. Overview of cold regions mobility modeling at crrel. *Journal of Terramechanics*, 43:1–26, 2006.

[88] D. Negrut and J. S. Freeman. Dynamic tire modeling for application with vehicle simulations incorporating terrain. *SAE International Congress & Exposition*, 2013:06–05, 1994.

[89] M. Morrison, R. Romano, A. Reid, and D. Gorsich. High-frequency terrain content and surface interactions for off-road simulations. Report, SAE, 2004.

[90] P. W. Richmond, R. A. Jones, D. C. Creighton, and R. B. Ahlvin. Estimating off-road ground contact forces for a real time motion simulator. *SAE transactions*, 113(2):325–332, 2004.

[91] A. Tasora. Real-time simulation of a racing car. In *9th International Workshop on Research and Education in Mechatronics, Bergamo, Italy*. Citeseer, 2008.

[92] H. Mazhar, T. Heyn, A. Pazouki, D. Melanz, A. Seidl, A. Bartholomew, A. Tasora, and D. Negrut. Chrono: a parallel multi-physics library for rigid-body, flexible-body, and fluid dynamics. *Mech. Sci.*, 4(1):49–64, 2013.

[93] D. Melanz, H. Mazhar, and D. Negrut. A multibody dynamics-enabled mobility analysis tool for military applications. In *SAE World Congress & Exhibition*, 2014.

[94] A. Tasora, D. Negrut, and et al. Project chrono. github.com, 2014.

[95] M. Busch and B. Schweizer. Numerical stability and accuracy of different co-simulation techniques: Analytical investigations based on a 2-Dof test model. In *Proceedings of the IMSD*, pages 71–83, 2010.

[96] A. Tasora and M. Anitescu. A fast ncp solver for large rigid-body problems with contacts, friction and joints. *Multibody Dynamics: Computational Methods and Applications*, 12:45, 2008.

[97] M. Anitescu and A. Tasora. An iterative approach for cone complementarity problems fornonsmooth dynamics. *Computational Optimization and Applications*, 47(2):207–235, 2010.

[98] A. Tasora and M. Anitescu. A matrix-free cone complementarity approach for solving large-scale, nonsmooth, rigid body dynamics. *Computer Methods in Applied Mechanics and Engineering*, 200(5):439–453, 2011.

[99] D. Negrut, A. Tasora, H. Mazhar, T. Heyn, and P. Hahn. Leveraging parallel computing in multibody dynamics. *Multibody System Dynamics*, 27(1):95–117, 2012.

[100] D. Negrut, A. Tasora, M. Anitescu, H. Mazhar, T. Heyn, and A. Pazouki. Solving large multi-body dynamics problems on the GPU. *GPU Gems*, 4:269–280, 2011.

[101] E. J. Haug. *Computer Aided Kinematics and Dynamics of Mechanical Systems*. Allyn and Bacon, 1989.

[102] N. Wagner and J. Zayas. Soil properties of yolo loam. Technical report, UC - Berkeley Civil & Environmental Engineering, 2011.

[103] J. J. More, B. S. Garbow, and K. E. Hillstrom. User guide for minpack-1. Technical report, CM-P00068642, 1980.

[104] H. Sugiyama and Y. Suda. Non-linear elastic ring tyre model using the absolute nodal coordinate formulation. *Proc. IMechE Part K: J. Multi-body Dynamics*, 223:211–219, 2009.

[105] T. Blanc and M. Pastor. A stabilized smoothed particle hydrodynamics, Taylor-galerkin algorithm for soil dynamics problems. *International Journal for Numerical and Analytical Methods in Geomechanics*, 37(1):1–30, 2013.

[106] C. Li, T. Zhang, and D. Goldman. A terradynamics of legged locomotion on granular media. *Bulletin of the American Physical Society*, 58:1408–1412, 2013.

[107] H. Mazhar, M. Quadrelli, T. Heyn, J. Madsen, and D. Negrut. Using a granular dynamics code to investigate the performance of a helical anchoring system design. In *Earth and Space*, pages 274–283. ASCE, 2012.

[108] J. Madsen. pyterramechanics. https://github.com/jcmadsen/pyTerramechanics, 2014.